VRIJE UNIVERSITEIT

Validating the performance of a Raman laser spectrometer (RLS) instrument under Martian conditions

ACADEMISCH PROEFSCHRIFT

ter verkrijging van de graad Doctor aan
de Vrije Universiteit Amsterdam,
op gezag van de rector magnificus
prof.dr. F.A. van der Duyn Schouten,
in het openbaar te verdedigen
ten overstaan van de promotiecommissie
van de Faculteit der Aard- en Levenswetenschappen
op maandag 25 november 2013 om 15.45 uur
in de aula van de universiteit,
De Boelelaan 1105

door

Khadijeh Motamedi Mohammadabadi

geboren te Esfahan, Iran

promotor: prof.dr. G.R. Davies
copromotor: dr. A.P.M.C.A.M.G. Colin

To My Father

CONTENTS

Scope of thesis

Summary/Samenvatting

Chapter 1: Introduction to Mars

Chapter 2: Raman and Laser induced breakdown Spectrometer (RLS)

Chapter 3: Manufacture and design of a new Mars atmosphere simulation chamber

Chapter 4: The effect of ambient temperature and composition on the Raman study of olivine: implications for the stoichiometric changes

Chapter 5: Raman study of hydrated sulphates and carbonates under Martian conditions with the RLS instrument

Chapter 6: RLS capabilities under Martian conditions; current and future perspectives

Scope of thesis

Two of the most fundamental questions faced by scientists are the origin of life and if life exists outside of planet Earth.There are a several extra-terrestrial locations where it has been suggested that life may have or could still survive:

- Mars (Levin et al., 1962; Houtkooper and Schulze-Makuch, 2010)
- Venus (schulze- Makuch and Irwin, 2004)
- Moons of Jupiter: Europa (Reynolds et al., 1983; Chyba and Philips, 2002), Ganymede and Callisto (Lipps et al., 2004)
- Moons of Saturn: Titan (McKay and Smith, 2005) and Enceladus (McKay et al., 2008).

With the ever increasing discovery of exoplanets, there have even been attempts to search for evidence of life outside our Solar System. The search for life on exoplanets is limited to the spectroscopic detection of possible life-indicator gases (O_2, O_3, H_2O, CO and CH_4), which may indicate the existence, past or present, of living organisms (Hedge and Kaltenegger, 2013). The huge distances to exoplanets and limitations in technology are barriers that pose a challenge in the search for life beyond Earth.

Within the Solar System so far there have been a couple of bodies accessible for *in situ* measurements,such as the Moon, Mars and near-Earth objects such as asteroids (Abell et al., 2009). Of these, Mars is the focus of attention in the search of life. This thesis represents a small portion of the on-going work contributing to the ExoMars mission to Mars, ESA's first mission of the Aurora programme.

Obtaining a better understanding of Mars geologic history and the search for evidence of past or present life on Mars are the principal objectives of the ExoMars mission. Water plays an essential role in supporting all types of terrestrial life forms (Chyba and Philips, 2002); consequently the scientific focus of most Martian missions is to search for evidence of water (Malin and Edgett, 2000). In addition, in the context of postulated future manned missions to the planet, an "on-site" source of H_2O would be crucial. Quantifying the amount of water on the planet's surface, its spatial distribution and its occurrence, either as liquid or ice or bound in hydrated silicate or sulphate minerals such as clay and sulphates is therefore a key requirement of instrumentation on current and future Mars missions (Grady, 2008; Poulet et al., 2005; Ehlmann et al., 2011).

A combined Raman-laser induced breakdown spectroscopy (LIBS) (RLS) instrument was initially chosen as one of the instruments of the Pasteur analytical package of the ExoMars rover (Rull et al., 2012). As such it was proposed to be one of the most important analytical tools on the mission being a first contact instrument. Raman spectrometry would be used to characterise mineralogy and organic compounds and simultaneously, the LIBS would determine multi-elemental compositions of minerals (Ahlers, et al., 2008). The combination of mineralogy and compositional data had the capability to both constrain the location of water and understand petrogenetic processes that form rocks and minerals. Due to scaling back of the ExoMars mission, the RLS has been replaced by a Raman only instrument. However, the potential powerful analytical capability of a combined RLS system is widely recognised and development of a RLS continues in the context of potential future missions to both Mars and Moon (Laan et al., 2009).

The fundamental aim of this PhD thesis is to rigorously evaluate the performance of an elegant breadboard RLS instrument under Mars analogue conditions. Specifically we aim to test the functionality of the instrument under varying temperature conditions and quantify the difference in Raman data produced under terrestrial and Martian conditions. Therefore after an introduction of the planet Mars in chapter one, the RLS instrument and the theoretical background of Raman and LIBS techniques are introduced in chapter two. The accuracy of the RLS instrument's performance needs to be determined under Martian conditions before sending this instrument to Mars. This will be further explained in chapter two. To determine the RLS instrument performance under Martian conditions, it was essential to design, manufacture and test a Mars Atmosphere Simulation Chamber (MASC) to reproduce the atmospheric conditions of Mars. The testing and operation of the MASC therefore became the first objective of this PhD research and will be explained in chapter three. The final objective of this PhD research was to assess the effectiveness of the RLS instrument in obtaining Raman spectra from different minerals under Martian conditions. Hence, chapters four and five will describe the possible influence of temperature and pressure on mineral Raman spectra at Martian conditions. Finally in chapter six, a review of the RLS performance is given and some recommendations will be suggested to improve the performance of the RLS instrument.

Summary

Obtaining a better understanding of Mars' geologic history and the search for evidence of past or present life on Mars are the principal objectives of ESA's first mission of the Aurora programme, ExoMars. Water plays an essential role in supporting all types of terrestrial life forms; consequently a major scientific focus of most Martian missions is to search for evidence of water. In addition, in the context of postulated future manned missions to the planet, an "on-site" source of H_2O would be crucial. Quantifying the amount of water on the planet's surface, its spatial distribution and its occurrence, either as liquid or ice or bound in hydrated silicate or sulphate minerals such as clay and sulphates is therefore a key requirement of instrumentation on current and future Mars missions.

A combined Raman-laser induced breakdown spectroscopy (LIBS) (RLS) instrument was initially chosen as one of the instruments of the Pasteur analytical package of the ExoMars rover. As such it was proposed to be one of the most important analytical tools on the mission being a first contact instrument. Raman spectrometry would be used to characterise mineralogy and organic compounds and simultaneously, the LIBS would determine multi-elemental compositions of minerals. The combination of mineralogy and compositional data had the capability to both constrain the location of water and understand petrogenetic processes that form rocks and minerals. Due to scaling back of the ExoMars mission, the RLS has been replaced by a Raman only instrument. However, the potential powerful analytical capability of a combined RLS system is widely recognised and development of a RLS continues in the context of potential future missions to both Mars and Moon.

This PhD project is designed to determine the optimum analytical strategy for the Raman and Laser Induced Breakdown Spectroscopy (LIBS) (RLS) instrument on Mars. Therefore, the first objective of this PhD research was to design, manufacture and test a Mars Atmosphere Simulation Chamber (MASC) large enough for instrument testing and capable of reproducing the atmospheric conditions of Mars. The MASC is a temperature and atmosphere controlled chamber (200 l). In order to reproduce Mars' atmosphere and temperature inside the MASC, an innovative heating-cooling system was coupled to a vacuum and gas control system. The MASC chamber can simulate planetary atmospheres and by doing so we are able to perform *in situ* sample analysis and test the performance of space instruments.

The second objective of this PhD research was to validate the performance of the RLS instrument within the MASC under Martian conditions. Therefore, the RLS instrument was installed inside the MASC and the performance of the RLS instrument was evaluated and tested. The performance of the spectrometer was initially assessed based on the calibrations of the spectrometer at different temperatures. For the calibration, visible light (~400– 800 nm) was directed at the RLS instrument to localise the position of the visible spectrum on the charge coupled device (CCD) and the visible spectrum from 660 to 800 nm was used for Raman analyses for this research. The calibration established that the position of the spectrum on the CCD was influenced by the temperature of the spectrometer. We conclude that the prism of the RLS instrument was significantly affected by thermal changes. In other word, the most probable causes of the change in the position of the orders on the CCD are (the

unwanted) movement of the prism or (unwanted) change(s) in the properties of the prism due to thermal expansion. A key observation is that the spectrum did not shift horizontally on the CCD so that wavelength calibrations were not affected. From these observations we conclude that the grating was not affected by temperature. Consequently, we can summarise that the RLS instrument can be operated under Martian atmospheric conditions provided that temperature variations only vary in the range +10 to -20 °C.

The final objective of this PhD research was to assess the effectiveness of the RLS instrument in obtaining Raman spectra from different group of minerals under Martian conditions. The results of the experiments show that the influences of temperature and pressure on mineral Raman spectra were not detected at Martian conditions. In fact, the different structures of minerals result in distinct Raman spectra. Importantly it has been shown that it is possible to use detect changes in Raman spectra using the RLS instrument to determine compositional variations of specific mineral groups, e.g. Mg– Fe substitution in olivine. However, the poor identification of a group of minerals by the RLS instrument confirm that, the RLS instrument is far less effective at producing and detecting Raman signals than commercially available instruments; e.g., Renishaw InVia Raman microscope.

We recommend extensive further testing of the RLS instrument and the newly designed Raman-only instrument for ExoMars on samples that will be more typical of Mars's surfaces. The work carried out to date, although under Martian conditions, was essentially under laboratory conditions. More rigorous assessments of the effects of variable grain size and surface morphology are needed. This is because the intensity of the Raman peak is determined not only by instrument optics, but also by the sample properties. The influence of the crystals properties (such as grain size, surface relief, colour and absorption coefficient) on the peaks intensity needs to be studied.

We evaluated key aspects of performance of the RLS instrument that were sub-optimal and made a series of suggestions for improvement of RLS instrument's performance for future planetary missions.

Recommendation	Goal
- Select a suitable stable Raman laser source	- Accurate and reproducible Raman spectra
- Increase the laser power	- Improving the detection limits of minerals
- Decrease the RLS instrument spot size	- Ability to identify minerals of small grain size
Improving the RLS optical design - Re-design spectrometer - Shorter optical fibres - Use less connectors	- To increase SNR and optical transmission
- Improve the CCD cooling system	- Increasing SNR (decrease thermal noise)
- Change the angle of the grating or apply a shorter wavelength laser source	- To expand the Raman spectral range to above 3000 cm^{-1} to include water

Coupled with the proposed improvements above we are confident that the use of a combined Raman-LIB spectrometer will be a valuable addition to the contact instrument package of future planetary missions.

Nederlandse samenvatting

De ExoMars missie is de eerste ruimtemissie binnen het Aurora programma van de Europese ruimtevaartorganisatie ESA. De belangrijkste wetenschappelijke doelen van deze missie zijn het beter begrijpen van de geologische geschiedenis van Mars, en de zoektocht naar de vroegere of huidige aanwezigheid van leven op Mars. Omdat de aanwezigheid van vloeibaar water essentieel is voor het bestaan van leven op Aarde, wordt bij Marsmissies het zoeken naar leven gelijkgesteld aan het zoeken naar water ('follow the water'). Naast wetenschappelijke redenen voor een zoektocht naar water op Mars is er ook een praktische reden. Als er ook nu nog water of ijs aanwezig is in de bovenste grondlagen van Mars, zou dat toekomstige bemande missies naar Mars vergemakkelijken.

Een van de belangrijkste taken van veel instrumenten op huidige en toekomstige Marsmissies is dan ook om nauwkeuriger gegevens te verzamelen over de hoeveelheid water op het oppervlak van Mars, over de verspreiding van dat water, en over de vorm waarin het water is opgeslagen (als vloeistof, ijs, of als watermoleculen in waterhoudende silicaten of zwavelhoudende mineralen zoals klei of sulfaten.

Een instrument dat Raman spectroscopie combineert met laser-geinduceerde breakdownspectroscopie (Raman-LIBS Spectrometer/RLS) maakte aanvankelijk deel uit van het Pasteur instrumentpakket op de ExoMars rover. Dit instrument was een van de belangrijkste in het pakket, omdat gesteentemonsters als eerste door dit instrument zouden worden geanalyseerd. Ramanspectroscopie zou gebruikt worden om de mineralogie en organische bestanddelen van monsters te karakteriseren. Tegelijkertijd zou de LIBS techniek gebruikt worden om de chemische samenstelling van de mineralen te bepalen. Door de combinatie van mineralogische en chemische informatie zouden zowel de aanwezigheid van water als de petrogenetische processen die ten grondslag lagen aan de vorming van de aanwezige gesteenten bestudeerd kunnen worden. Door het beperken van de ExoMars missie is het RLS instrument inmiddels vervangen door een Raman spectrometer. Niettemin wordt de toegevoegde waarde van een gecombineerd RLS systeem nog steeds breed onderschreven. De ontwikkeling van een RLS wordt daarom momenteel voortgezet met het oog op toekomstige missies naar zowel Mars als de Maan.

Dit promotie-onderzoek had tot doel een optimale analyse-strategie te ontwikkelen voor metingen met een gecombineerd Raman-LIBS instrument (RLS) op het Marsoppervlak. Om dit doel te bereiken is eerst een test-faciliteit ontworpen en gebouwd (MASC, Mars Atmosphere Simulation Chamber), waarin de atmosferische omstandigheden op het oppervlak van Mars kunnen worden nagebootst. MASC is een cylindrisch vat met een volume van 200 liter met een innovatief verwarmings- en koelsysteem, gekoppeld aan een vacuum/gasinlaat systeem. In de MASC faciliteit kunnen de temperatuur, gassamenstelling, en druk op het Marsoppervlak worden nagebootst. Instrumenten kunnen in het vat bij realistische condities *in situ* analyses uitvoeren en zo getest worden.

Na constructie van de MASC faciliteit is het RLS instrument getest onder Martiaanse omstandigheden. De RLS is in het MASC vat gemonteerd, en de prestaties van het instrument zijn ge-evalueerd. Het effect van veranderingen in omstandigheden op de prestaties van de RLS zijn eerst bestudeerd aan de hand van spectrometer calibraties bij verschillende temperaturen. Voor de calibratie werd gemeten waar zichtbaar wit licht met golflengtes tussen de 400 en 800 nm geprojecteerd werd op de CCD detector van de spectrometer. Het deel van het spectrum tussen 660 en 800 nm werd gebruikt voor Raman analyses. De calibratie gaf aan dat de positie van het spectrum op de CCD duidelijk veranderde bij verandering van de temperatuur van de spectrometer, waarschijnlijk door verschuiving of vormverandering van het gebruikte prisma. Een belangrijke observatie is dat het spectrum niet horizontaal verschuift op de CCD, waardoor golflengte-calibraties niet beinvloed worden. Samenvattend concluderen we dat het RLS instrument op Mars gebruikt kan worden, mits temperatuurvariaties beperkt blijven tot het gebied tussen +10 en -20 °C.

Ten slotte is de werking van het RLS instrument bij Marscondities getest door het meten van Raman spectra van een reeks mineralen. De resultaten van deze metingen geven aan dat er geen significante effecten zijn van temperatuur en atmosferische druk op de Raman spectra. Wel is aangetoond dat variaties in de chemische samenstelling van mineralen binnen een bepaalde groep leiden tot meetbare veranderingen in de Raman spectra van het RLS instrument bij Marscondities. Zo kan de magnesium:ijzer verhouding in olivijn bepaald

worden aan de hand van Raman spectra. Het Raman signaal van sommige mineralen is te zwak bij gebruik van het RLS instrument, terwijl dezelfde mineralen een duidelijk Raman signaal geven als commerciele Raman apparatuur wordt gebruikt.

In vervolgstudies zouden metingen gedaan moeten worden aan monsters die representatiever zijn voor de bodem op Mars. Hoewel de metingen in het werk beschreven in dit proefschrift plaats hebben gevonden onder Marscondities, konden niet alle aspecten van metingen op Mars nagebootst worden. Zo is een systematische studie naar het effect van korrelgrootte, mineraalkleur, en korrelmorfologie op Raman spectra nodig. De werking van het RLS instrument was submoptimaal in verschillende opzichten. De volgende adviezen voor het verbeteren van het instrument komen voort uit dit promotie-onderzoek:

- Een stabielere Raman laser is nodig om nauwkeurige en reproduceerbare Raman spectra te verkrijgen
- De laserstraal moet intenser worden om de detectielimieten te verbeteren
- De spotgrootte van de laserstraal moet verkleind worden zodat kleinere mineraalkorrels kunnen worden geanalyseerd
- Signaal-ruis verhouding en optische transmissie kunnen verbeterd worden door het optische ontwerp te verbeteren met (a) een andere spectrometer (b) kortere optische vezels (c) minder connectoren.
- De koeling van de CCD zou verbeterd kunnen worden. Ook dit leidt tot verbetering van de signaal-ruis verhouding.
- Om watergehaltes te meten met Raman spectroscopie moet de golflengte van de laserbron verlaagd worden.

De uitkomsten van dit onderzoek geven aan dat een gecombineerd Raman-LIBS instrument een zeer nuttig, veelzijdig instrument kan zijn voor toekomstige landermissies naar de Maan en Mars.

Chapter 1: Introduction to Mars

Contents

1.1 Introduction to the planet Mars

Mars is the closest planet to Earth. It is known as the "Red Planet" due the presence of iron oxide on the surface. It is the fourth planet in our solar system relative to the Sun. Mars also has two small moons that are named Phobos and Deimos. They orbit the planet at a relatively close distance of 9377 and 23436 km respectively.

Mars is a rocky differentiated planet like Earth divided into a crust, a mantle and a core. Figure 1.1 shows the internal structures of Mars and Earth.
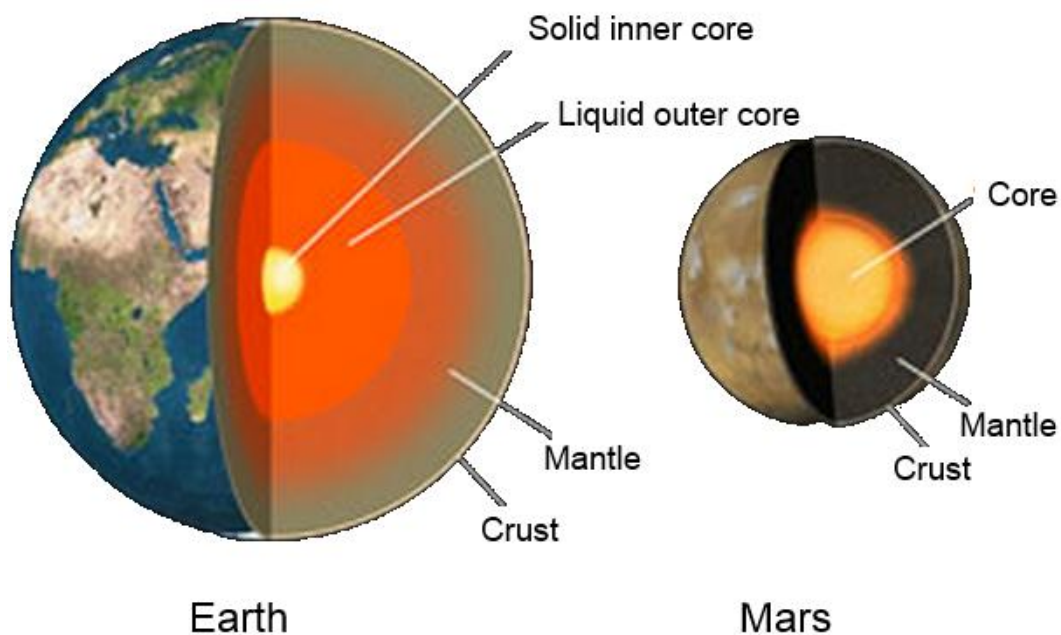
Figure 1.1. The internal structure of Mars and Earth (modified from http://www.rationalskepticism.org).

Mars diameter (3390 km) is approximately half that of Earth's. Due to its lower mass its surface gravity is about three times less than on Earth.

Mars rotates about its own axis in 24 hours, 39 minutes and 35 seconds, which is a solar day. Because Mars is more distant from the sun, it takes longer to orbit around the sun. Mars completes an orbit in 669 Martian days. Table 1.1 contains a summary of the comparison of physical parameters of the planets Mars and Earth.

Parameters	Mars	Earth	Ratio (Mars/Earth)
Mass (10^{24} kg)	0.64185	5.9736	0.107
Volume (10^{10} km^3)	16.318	108.321	0.151
Equatorial radius (km)	3396.2	6378.1	0.532
Core radius (km)	1700	3485	0.488
Mean density (kg/m^3)	3933	5515	0.713
Surface gravity (m/s^2)	3.71	9.80	0.379
Black-body temperature (K)	210.1	254.3	0.826
Incident flux (W.m^{-2})	600	1400	0.428
Surface temperature (°C)	-63 (-133 to +27)	15 (-89 to +60)	-
Surface pressure (mbar)	6 to 10	1013	-
Moon(s)	Phobos and Deimos	The Moon	-
Distance to the Sun (10^6km)	228 (1.5AU)	150 (1AU)	-

Table 1.1. Comparison of the major physical parameters of Mars and Earth.

1.2   Present climatic conditions at the Mars surface

In this section Martian environmental conditions are reviewed. This introduction is essential as we need to simulated these conditions in MASC to determine the RLS instrument performance under Martian conditions.

1.2.1   Mars' atmosphere

The Mars atmosphere is approximately 100 times thinner than on Earth. It consists of approximately 95% carbon dioxide. Table 1.2 shows the exact Martian atmospheric compositions.

	Mars	Earth
CO_2	95.32	0.039
N_2	2.7	78.084
Ar	1.6	0.934
O_2	0.13	20.946
CO	0.08	4.0673
H_2O	0.021	0.40 in entire atmosphere, typically 1–4 at surface
Ne	0.00025	0.001818
Kr	0.00003	0.000114
Xe	0.000008	0.000009
O_3	0.000003	0.0000006

Table 1.2. Comparison of the atmospheric compositions of Mars and Earth (in percent)(Kieffer et al., 1992).

1.2.2   Temperature and climate at the Mars surface

Due to the thin atmosphere, Mars is not able to retain much of the heat from sunlight. Most of the heat comes from the ground after it absorbs solar radiation. The Martian atmosphere does not have enough absorption or greenhouse capability to contribute to the warming of the surface. On Earth the presence of water and carbon dioxide in its atmosphere are the most common contributors of the greenhouse effect, Fig. 1.2. When sunlight comes through the atmosphere, some solar radiation is reflected from the Earth's surface and as a result sunlight energy is sent back to the atmosphere. However, sunlight radiation is partially absorbed at the Earth's surface and in the atmosphere. This radiation warms up the planet and is later re-emitted as infrared (thermal) radiation. The presence of water and carbon dioxide in Earth's atmosphere leads to the absorption of some of this infrared radiation. These characteristics are the main contributors to the planets greenhouse effect, which is demonstrated in Fig. 1.2.
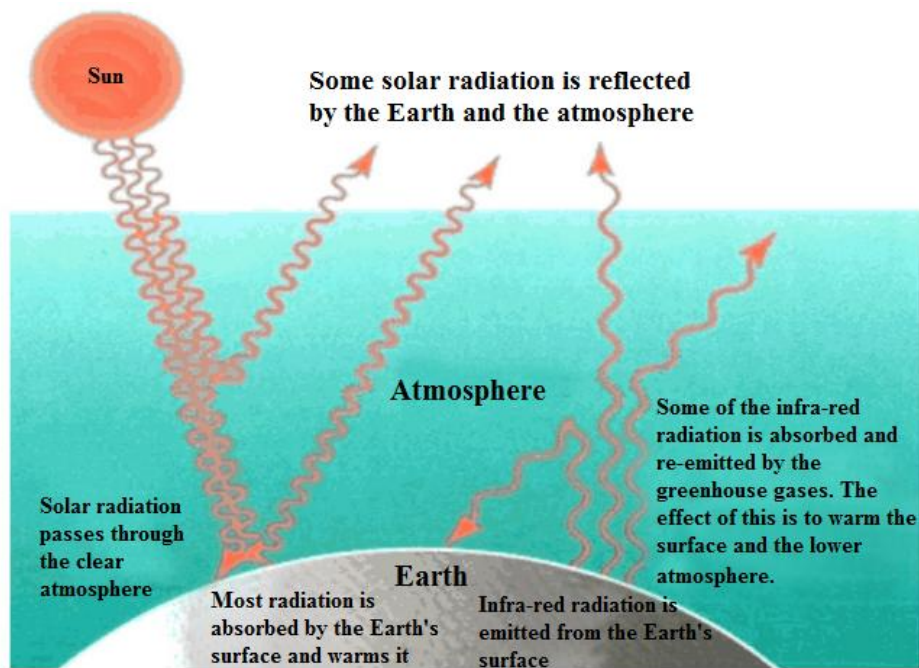
Figure 1.2. The greenhouse gases trap some of the reflected solar heat in the atmosphere and raise the average temperature of the Earth's surface from about -21 °C to about +14 °C
(modified from http://www.is.wayne.edu/MNISSANI/A&S/greenhou.htm).

The average temperature on Mars is about -60 °C. As Mars orbits around the sun with a tilt angle of 25.19° on its rotational axis, Mars has seasons like Earth (Earth has a tilt angle of 23.44°). Because Mars is further away from the sun, seasons are longer. In the Northern Hemisphere, spring lasts seven months, while summer and fall are both about six months long, and winter only four months long (Earth months). According to the Mars Orbiter camera, in the summer the temperature can reach ~ 30 °C at the equator, while in the winter the temperature drops to ~-130 °C at the poles (Grady, 2008).

Rovers and landers have provided precise temperature records at local sites on Mars, for instance the Curiosity rover has been performing daily measurements since 2012. These data show there is a diurnal temperature variation of more than 80 °C. The thin Martian atmosphere cannot retain the heat during the night. Figure 1.3 reports the data collected by the Curiosity rover between august 2012 and February 2013 at the Gale Crater.

However, the diurnal temperature change can be narrowed to only about 10 °C during periods of dust storm (Sheehan, 1996).
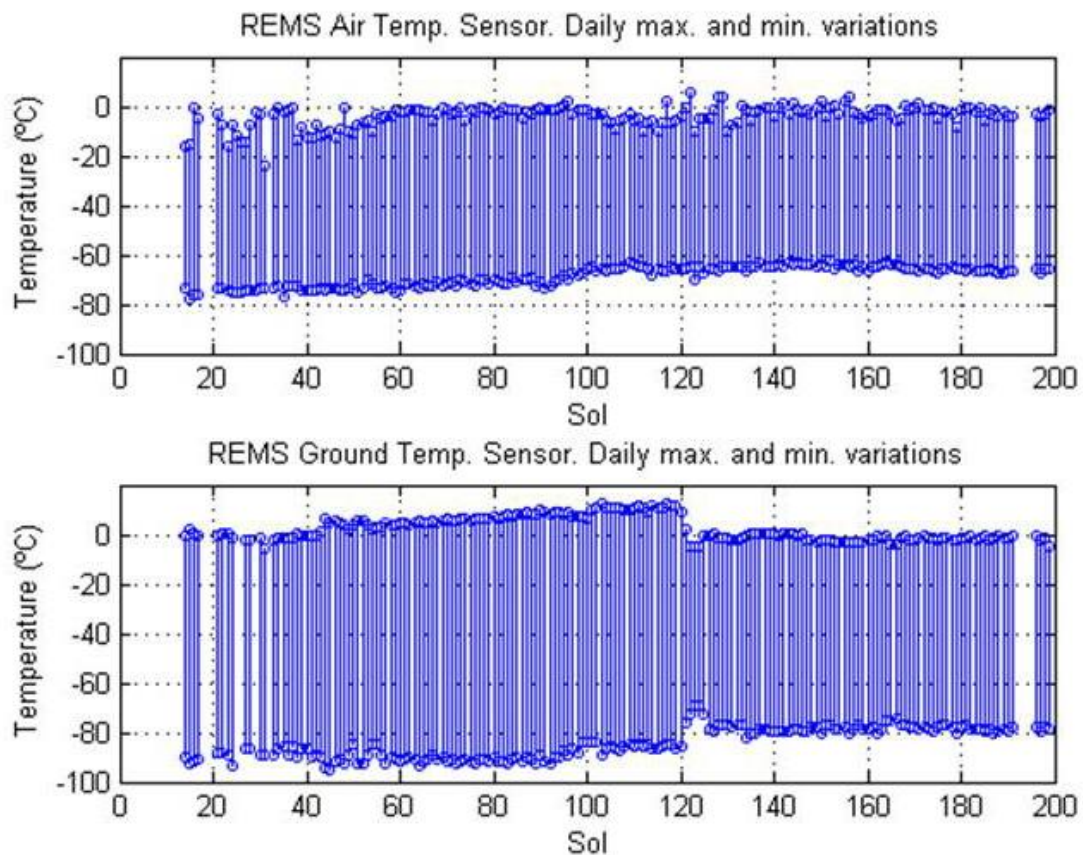
Fig. 1.3. Temperature measured by Curiosity rover from mid-August 2012 to late February 2013 at the Gale Crater.The upper graph shows the daily minimum and maximum of air temperature around the rover. The lower graph shows daily minimum and maximum of ground temperature measured byRover Environmental Monitoring Station (REMS). Image credit: NASA, http://photojournal.jpl.nasa.gov/catalog/PIA16913.

Curiosity measured temperatures above 0 °C on Mars. This is one of the conditions where liquid water could be present. Nevertheless, liquid water is not stable in the planet because the atmospheric pressure is below the water triple point: any liquid water would immediately sublime into vapour.

1.3 Age of Mars' surface

A common way to estimate the age of planetary surfaces is counting the number of craters. These craters have formed due to meteorite bombardments. When applied to Mars, this method resulted in the separation of the geologic history of the planet into three major periods: the Noachian, Hesperian and Amazonian (Tanaka, 1986; Scott and Tanaka, 1986; Tanaka et al., 1992). The Noachian is the oldest period of Mars history. It began at the origin of Mars and extended to ~3.9 Ga. The Noachian period was followed by the Hesperian, from ~3.9 to 3.0 Ga. The last period is the Amazonian, from ~3.0 Ga to the present. Figure 1.4 shows the map of the ages of the Martian surface.

Noachian: The name Noachian was chosen because of the high density of craters in the terrains of the Noachis Terra. This period is characterized by the highest density of meteorite impacts.

Hesperian: The Hesperian era is named after Hesperia Planum, a cratered highland region northeast of the Hellas Basin. This era is characterized by a lower density of craters but marked volcanic activity. It represents most of the lava plains in the northern hemisphere.

Amazonian: The most recent era, the Amazon, is named after Amazonis Planitia, which has a sparse crater density over a wide area. Such densities are representative of many Amazonian-aged surfaces. The Amazonian era is characterized by the lowest density of craters and corresponds mainly to the formation of the huge volcano Olympus Mons, the formation of landsides in the Valles Marineris, and the formation of the broad plains and sand dunes near the Martian poles.
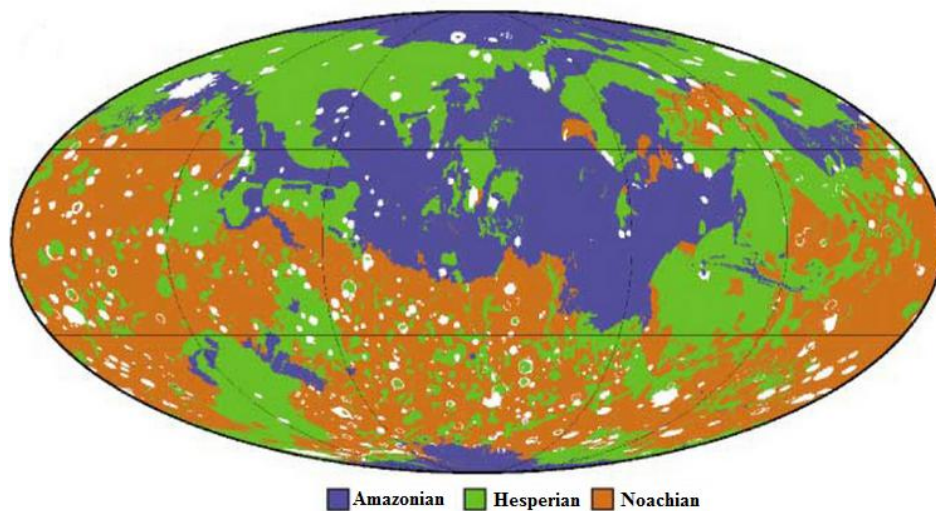
Figure 1.4. Map of the ages of the Martian surface, areas in white are impact craters and their ejecta deposits (Greeley and Guest, 1987; Scott and Tanaka, 1986).

Lunar studies have contributed to quantitative age estimations. The crater density on the Moon has been calibrated with absolute ages determined on samples returned by Apollo and Luna missions. For that study, the crater densities were measured at landing sites and radiometric ages were determined on returned samples. Therefore, the direct relationship between crater densities and absolute ages can be estimated. The lunar crater chronology provides rough measurements of absolute ages for the entire surface of the moon (Hartmann, 1970; Neukum and Ivanov, 1994; Neukum et al., 2001; Stöffler and Ryder, 2001). The lunar absolute chronology method has been transferred to Mars, taking into account the closeness of Mars to the main asteroid belt, the Martian gravity and the effect of the Martian atmosphere (Hartmann, 1999, 2005; Neukum et al., 2001; Ivanov, 2001; Hartmann and Neukum, 2001). In this manner absolute ages can also be estimated for Mars surfaces. Considering the margin of error in the age estimation, the boundary between the Noachian, the earliest period, and the Hesperian, is estimated to be between 3.5 Ga and 3.7 Ga. The

boundary between Hesperian and Amazonian is between 3 Ga and 2.9 Ga (Hartmann and Neukum, 2001; Ivanov, 2001; Werner, 2005).

1.4   Mars' composition and surface mineralogy

Although there are no samples directly returned from the Martian surface, there are Martian meteorites that provide data on the chemical composition of Mars. The composition of Mars was also inferred from the data collected from a number of successful missions. These data were collected from several instruments such as spectrometers on board of spacecrafts, remote sensing from orbit or *in situ* analyses on the Martian surface. The data confirmed the detection of not only magmatic minerals and rocks but also hydrated minerals, sedimentary and evaporite deposits (sulphates, carbonates). One of the objectives of this research is to determine if the RLS instrument is capable of identifying minerals which have been detected on Mars and if it is possible to determine compositional variations within individual mineral groups. Hence the major minerals that are found on Mars are summarized in this section. The accurate identification of these minerals by the RLS instrument can help to better understanding the geology history of Mars, its evolution and give clues about the present or past signs of life on Mars.

1.4.1   Magmatic rocks

1.4.1.1   Information from Martian meteorites

Martian meteorites were ejected from Mars by the impact of a comet or an asteroid and subsequently landed on Earth. There are currently around 120 meteorites that have been identified as Martian meteorites. The fact that they derive from Mars is based on elemental and isotopic compositions that are similar to rocks on Mars. They contained trapped gases (as bubbles) from which the composition is similar to the Martian atmosphere as measured by the Viking lander (Bogard and Garrison, 1999). Martian meteorites are classified into three main categories: Shergottites, Nahklites and Chassignites (SNC). They are mafic and ultramafic igneous rocks and have compositions close to terrestrial basalts, clinopyroxenites and dunites. The infamous meteorite called ALH84001 is also assumed to be from Mars but cannot be classified into one of these categories as it has a distinct composition and age. The classification of Martian meteorites is as follows:

a) Shergottites

Shergottites are named after the Shergotty meteorite, which fell at Sherghati, India in 1865. Shergottite consists mostly of olivine, pigeonite (a pyroxene mineral) and plagioclase feldspar, making it an basalt. Basaltic shergottites have volcanic effusive textures. They contain clinopyroxene and plagioclase. According to most authors these meteorites are considered young (younger than other meteorites, <500 Ma), while the Martian surface is generally very old (about 90% of the surface is > 3 Ga) and has only a few terrains that

belong to the Amazonian era (Hartmann and Neukum, 2001). The age of Shergottites is still a subject for discussion.

b) Nahklites

The Nakhla meteorites are named after a fall that occurred in El Nakhla, Egypt, in 1911. They are clinopyroxenites with a fine-grained texture. They consist primarily of green cumulate augite crystals with minor olivine in a very fine-grained mesostasis. These rocks were formed by slow cooling, possibly in the subsurface. They are estimated to have formed around 1.3 Ga (Bouvier et al., 2005).

c) Chassignites

This group is named for its only member, Chassigny, a meteorite that fell in France in 1815. Chassigny is a cumulate rock, resembling a terrestrial dunite. It consists of 91% iron-rich olivine, 5% clinopyroxene, 1.7% plagioclase, 1.4% chromite, 0.3% melt inclusions and other accessory minerals and phases (Nyquist et al., 2001; Bouvier et al., 2005). Its age is about 1.36 Ga and its compositional and elemental trends, indicate that Chassignites and Nakhlites may have been formed by similar magmatic processes.

d) ALH84001

The Antarctic meteorite Allan Hills 84001 was foundin late 1984. Orthopyroxenite ALH84001 has a crystalline structure and was estimated to have formed 4.09 Ga (Bouvier et al., 2009; Lapen et al., 2010). It contains carbonates that were initially reported to be Martian fossils (McKayet al., 1996) but further studies have brought this interpretation into question (Fig. 1.5) (Golden et al., 2001; Treiman and Essene, 2011).
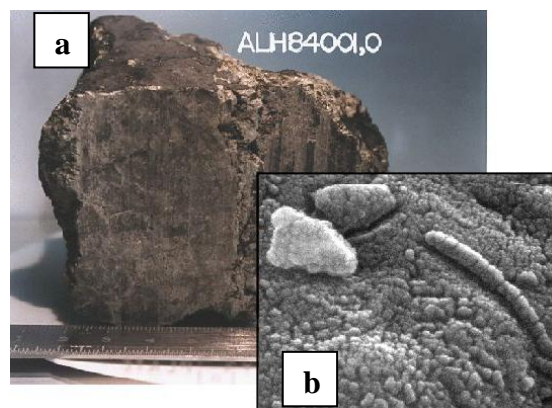
Figure 1.5. Images of a) the meteorite ALH84001 and b) electron microscope view. Nanoscale tubular structures were first interpreted as potential bacteria (McKay et al., 1996).

1.4.1.2 Information from space missions

Telescopic observations of the Martian surface have revealed the bright reddish areas covered by oxidized iron dust (hematite). The darker areas also contain minerals that are more difficult to oxidize (like pyroxene or olivine). These minerals are typical constituents of basalts on Earth.

Analyses from spacecrafts have provided additional information. Phobos 2 identified unoxidized volcanic pyroxenes in Mars dark regions, while hematite and even goethite were identified in brighter regions. Subsequently, thermal emission spectrometer (TES) aboard Mars Global Surveyor, confirmed the presence of pyroxene bearing rocks, which depending on the region, could be basalts or andesite. This instrument also detected some olivine rich regions.

The Sojourner micro-rover aboard the Pathfinder lander analysed volcanic rocks on the Martian surface. In addition to oxidized iron minerals and contrary to what one would expect from Martian meteorites, the detected volcanic rocks have a higher silicon content than basalt and are therefore classified as andesite. However, the instruments aboard the rover could only assess the global compositions of rocks and could not precisely identify minerals. These analyses were limited to the region of Chryse Planitia (26.7° N et 320° E) and does not exclude the presence of basalts in others Martian regions.

The Spirit and Opportunity rovers carried instruments that were able to identify minerals and analyse rock composition. The Spirit rover discovered unoxidized olivine and pyroxene bearing basaltic rocks in the Gusev Crater. It also identified ilmenite ($FeTiO_2$) in some areas. These oxidized minerals were also a major component of the dust covering those rocks. Similarly, the Opportunity rover landed in the dark region called Sinus Meridiani and discovered basaltic, olivine-rich dust, sand and cobbles. In this study, we will try to identify basaltic magmas such as olivine with the RLS instrument. Results are reported in chapter four of this thesis.

The presence of unaltered volcanic rocks on the Martian surface indicates that the Mars environment was quite dry and cold throughout the recent history of the planet. However, in addition to these magmatic rocks and minerals, coarse grained hematite, sulphates, hydrated minerals, sedimentary and evaporitic rocks have been identified. Their presence suggests that past aqueous activities occurred on the planet.

1.4.2   Minerals and rocks suggesting past aqueous activities at Mars' surface

The past aqueous activity can be detected from the composition of minerals such as carbonates, phyllosilicates and hydrated sulphates, which have been detected on Mars.

Carbonate is a weathering product of water and basalt in an atmosphere with CO_2 (Gooding, 1978; Catling, 1999). Carbonates are detected locally on the surface of Mars and within Martian meteorites (Bridges et al., 2001) and at less than 5% abundance in Martian dusts

(Pollack et al., 1990; Bandfield et al., 2003). During the Noachian era, water was assumed to have a neutral to alkaline pH. This suggestion is based on the presence of carbonates and clays. It also indicated that acidic weathering that is characteristic for the later Hesperian era did not dominate all aqueous environments, as it did not destroy all of these carbonates (Fairen et al., 2004).

The OMEGA visible and infrared mapping spectrometer has mapped almost the entire surface of Mars during the last 10 years. OMEGA has detected phyllosilicates and hydrated sulphates over large, but isolated, areas on the surface (Fig. 1.6). Phyllosilicates such as clay are alteration products of igneous minerals as a result of long-term contact with water (at alkaline pH). In contrast, hydrated sulphates are formed through rock interaction with acidic water. Phyllosilicates and sulphates are both a sign of the existence of water in active geochemical reactions. Compared to the presence of ferric oxide on the Martian surface today, the presence of phyllosilicates and sulphates in older landscapes suggests a transition from a wet to a dry climate over time (Bibring et al., 2006). The sulphates found on Mars come from the Hesperian era. Sulphates are not found in the Noachian era. This suggests that processes such as evaporation, crystallization and weathering were only present in the Hesperian era, probably as a result of volcanic activity and heating of the planet in general.
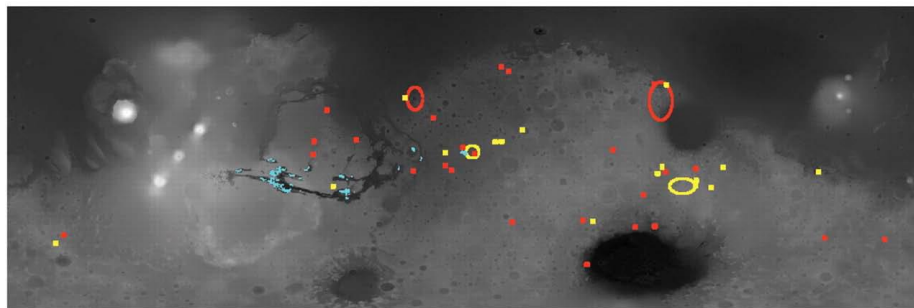
Figure 1.6. Detection of hydrated minerals by OMEGA, reported on a MOLA (Mars Orbiter Laser Altimeter)elevation map (black=low, white=high). Phyllosilicates are shown in red and sulphate is shown in blue. Other undetermined hydrated minerals are indicated in yellow (Bibring et al., 2006).

In addition the TES spectrometer of Mars Global Surveyor detected coarse-grained hematite. On Earth this kind of hematite is formed under the action of liquid water. The most hematite rich region is close to $0°$ longitude on Mars. This site was selected for landing the Opportunity rover. Confirming TES findings, Opportunity rover identified 2-5 mm sized hematite grains, probably eroded from layered sedimentary evaporates, containing also the hydrated ferric sulphate jarrosite. Aqueous activities have the possibility to have created an environment favourable for life on Mars. Therefore, in this study we tried to identify a group of hydrated minerals with the RLS instrument. Results are reported in chapter five of this thesis.

Currently the Mars Science Laboratory robot (Curiosity) is also collecting data from Mars planet. The data will be reviewed further in this chapter.

1.5   The Mars climate and its evolution

Figure 1.7 presents a summary of characteristic features associated with the three main Martian eras. During the Noachian era the following occurrences took place:

- Formation of valleys
- Formation of craters
- Formation of phyllosillicates
- Formation of oceans and lakes
- Heavy volcanic activity (in the late Noachian)

The end of the Noachian era, which coincides with the start of the formation of the Tharsis volcanic dome, marked a global climate change in which water gradually disappeared from the surface. The weathering and erosion by water is evidence of the presence of water in the Noachian era (Carr and Head, 2010). Valleys in the Noachian era gradually disappeared. Outflows channels with intense flows of water started to emerge in the Hesperian era (Baker, 1982). These channels existed for only brief periods in this era. The mineralogy recorded in sedimentary deposits that belong to the Hesperian era changed from containing phyllosilicates to sulphates.

For the Hesperian era the following occurrences took place:

- Decline of all the activities that are mentioned in the Noachian era
- Climate changed to become more dry and dusty
- Formation of lava plains
- Formation of sulphates (instead of phyllosillicates)

Liquid water and hydrated deposits disappeared quickly from the surface of Mars after the Hesperian era. This suggests that the planet was dry over the last ~3.0 Ga (throughout the Amazonian period).

For the Amazonian era, which is the latest era, the following occurrences took place:

- Climate changed to be more cold
- Formation of a lithosphere
- Formation of landslides in Valles Marineris
- Formation of broad plains
- Formation of sand dunes near Martian poles.
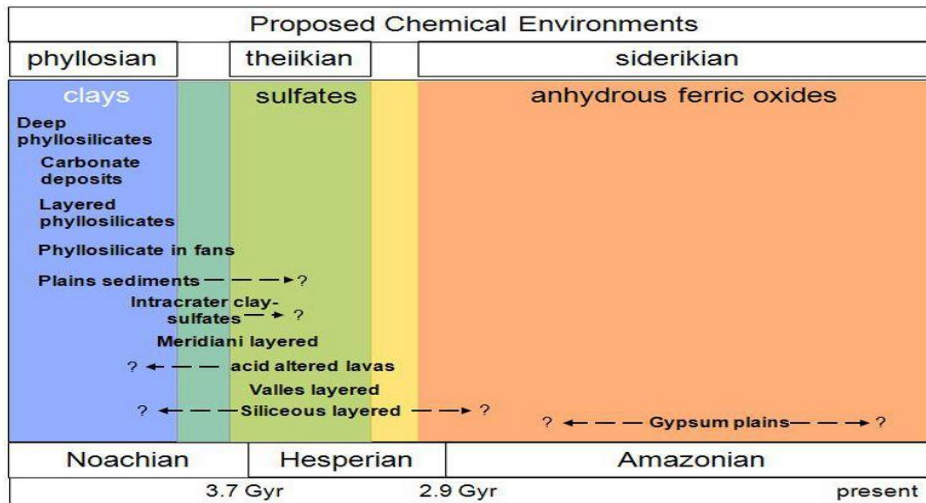
Figure 1.7. Diagram showing the evolution of the morphologies and weathering conditions that were observed at the surface of Mars over time. It also includes a mineralogical timeline that divides Mars into a phyllosian, theiikian and a siderikian period. These names are based on the minerals that are mostly found in each of these periods (Murchie et al., 2009).

The presumed existence of greenhouse conditions in the early Marian history made the Martian climate more hospitable in the past. The inferred denser atmosphere appears to have disappeared in the late Noachian era either through chemical reactions with the surface and / or gravitational escapes.

1.6   Search for life beyond Earth on Mars: Mars missions

Mars has been the subject of several missions since space exploration began. They can be briefly summarized as follows:

Currently active missions: Curiosity, Mars Reconnaissance Orbiter, Mars Exploration Rover Opportunity, Mars Exploration Rover Spirit, Mars Express, 2001 Mars Odyssey

Future missions: ExoMars, Maven, Mangalyaan

Past missions: Phobos, Grunt, Yinghuo-1, Phoenix, Mars Exploration Rover Spirit, Mars Polar Lander, Nozomi, Mars Climate Orbiter, Mars Pathfinder and Sojourner, Mars 96, Mars Global Surveyor, Mars Observer, Phobos 2, Phobos 1, Viking program, Mars 4, 5, 6 and 7, Mars 2 and 3, Mariner 9, Kosmos 419, Mariner 8, Mars 1969a and b, Mariner 6 and 7, Zond 2, Mariner 4, Mariner 3, Mars 1, Korabl 11 and 13, Korabl 4 and 5.

In total 50 missions were sent to Mars and only 21 of those missions made it to the planet. Table 1.3 shows an overview of the (relatively) successful missions that made it to Mars, their scientific goals and the result of these missions:

Launch Date	Name	Country	Type	Scientific goals	Result of the mission
1964	Mariner 4	US	Flyby	Making observations of Mars and transmit them back to Earth	First images of the Martian surface were taken
1969	Mariner 6 & 7 (dual mission)	US	Flyby	Analysing the atmosphere and the surface. (Equipped with an ultraviolet spectrometer)	Photographed about 20 percent of the planet's surface
1971	Mars 3 Orbiter/Lander	USSR	Landing	- Analyse the soil composition - Monitor solar radiation & wind - Monitor interplanetary and Martian magnetic fields	Transmission stopped after 14.5 seconds during its descent (5.7 km/s)
1971	Mariner 9	US	Orbit	Map over 70% of the Martian surface	- First spacecraft to orbit Mars - The 7329 images, covering about 80% of the planet - A lack of evidence for volcanic activity - Atmospheric pressures ranging from 2.8 to 10.3 mbar, measurements of atmospheric water vapour content - An ultraviolet spectrum of Phobos
1973	Mars 5	USSR	Orbit	- Orbiting the planet - Serving as a communication station for other Russian Martian explorers	Mission considered a failure. Only 22 loops around the planet were done
1973	Mars 6 Orbiter/Lander	USSR	Landing	-Performing a soft landing -To study proton and electron fluxes from the Sun	Lander smashed to the surface 5 minutes after entering Mars' atmosphere
1975	Viking 1 Orbiter/Lander	US	Landing	Researching the possibility of life on Mars	-First successful soft landing on the surface of Mars Measurements were made of : -The atmospheric composition -The surface elemental abundance -Temperature of the surface and meteorological conditions
1975	Viking 2 Orbiter/Lander	US	Landing	Further exploration of Mars as part of the Viking program	Discovery of river valleys
1996	Mars Global Surveyor	US	Orbit	Making observations of Mars at a height of 400 km	Discovery of landforms that were a result of weathering and winds
1996	Mars Pathfinder	US	Landing	- Making measurements of the atmosphere during its descent and sending these back to Earth - Conducting experiments to the soil with new equipment	Data showed that the central metallic core is between 1300 km and 2000 km in radius

Year	Mission	Agency	Type	Scientific goals	Results
2001	Mars Odyssey	US	Orbit	- Creating a map with chemical compounds of the surface of Mars - Trying to find water ice - Determining the radiation intensity in deeper layers	Retrieved data indicated the presence of water on Mars
2003	Mars Express Orbiter/Beagle 2 Lander	ESA	Landing	Studying interior, subsurface, surface and atmosphere, and environment of the planet Mars	- Discovery of water on the South Polar ice cap, consisting of carbon dioxide (85%) ice and water ice (15%) - Detection of methane and ammonia in the atmosphere
2003	Mars Exploration Rover – Spirit (MER A) Opportunity (MER B)	US	Lander	Further exploration of the geology of Mars, mainly looking for traces of water and characterising rocks and soils	- Found traces of water in the rocks of the Gusev Crater - Landing site turned out to be a place where a sea or a lake existed (Meridiani Planum)
2005	Mars Reconnaissance Orbiter	US	Orbit	- Identifying possible future landing sites - Identifying locations where liquid water existed (possible life forms) - Gain more knowledge of the climate on Mars	Found large amounts of lava traces (Cerberus Palus)
2007	Phoenix Mars Lander	US	Lander	Studying the Polar cap area of Vastitas Borealis to see if life existed in the past	Confirmation of the presence of water by Nasa
2011	Mars Science Laboratory	US	Lander	- Preparing a manned mission to mars - Studying the climate and geology - Determining if life could have been possible in the past	- Evidence for atmospheric loss - Evidence for ancient water - Evidence for ancient habitability

Table 1.3. The (relatively) successful missions and their scientific goals and results.

1.6.1 Mars Science Laboratory, Curiosity rover

Mars Science Laboratory (MSL) mission was launched in November 2011 and reached its destination in August 2012. The MSL rover, Curiosity, is about 6 times bigger than the Mars Exploration Rovers (MER) (Fig. 1.8). The MSL landed at the Gale Crater. The crater was chosen for study because of the presence of both clays and sulphate minerals, which are formed under different conditions in the presence of water. Water is a key ingredient of life as we know it and the history of water in the Gale Crater, based on rock material, will give Curiosity clues to a possible habitat for life.

Figure 1.8. Comparison of the Mars Exploration Rovers (MER) robot (Spirit and Opportunity left) with the robot Pathfinder (Sojourner, centre) and the Mars Science Laboratory robot (Curiosity, right) (Credit: Jet Propulsion Laboratory (JPL))

The Mars Science Laboratory rover was built to investigate the recent and ancient habitable environments (Grotzinger et al., 2012). Curiosity is designed to assess whether the Martian environment ever was/ is capable of supporting microbial life. The goal of the instruments onboard Curiosity is to characterize the geology, the atmosphere, the environmental conditions and to identify potential bio signatures. Curiosity will have a lifetime of at least one Mars year (~23 months), and has the capability to cross a distance of at least 20 km. The MSL science payload was reviewed in the work of Grotzinger et al., 2012 and includes:

- A laser induced breakdown spectrometer (LIBS) to analyse the chemical composition of minerals and rocks (ChemCam) (Meslin et al., 2013),
- An active neutron spectrometer to search for water in rocks/regolith (DAN)
- A weather station to assess modern-day environmental variables (REMS)
- A gas chromatograph-mass spectrometer and gas analyser that will search for organic carbon in rocks, regolith fines and the atmosphere (SAM) (Mahaffy, et al., 2012)
- An X-ray diffractometer that will verify mineralogical diversity (CheMin)(Bish et al., 2013)
- Focusable cameras that can image innatural colour (Mastcam, MAHLI)(Edgett, 2012)
- An alpha-particle x-ray spectrometer for *in situ* identification of rock and soil chemistry (APXS)
- A sensor designed for continuous detecting of background solar and cosmic radiation (RAD)

As the RLS instrument and the ChemCam instrument use a LIBS spectrometer, the ChemCam instrument will be briefly explained in this chapter but the principles of the LIBS technique are presented in more detail in chapter two. The ChemCam (Chemistry & Camera) instrument package consists of two remote sensing instruments:

a) The first planetary science Laser-Induced Breakdown Spectrometer (LIBS)
b) A remote Micro-Imager (RMI) (Wiens et al., 2013).

The LIBS provides elemental compositions, while the RMI places the LIBS analyses in their geomorphologic context. Both instruments will help determine which rock and soil material

are of sufficient interest to use the contact and analytical laboratory instruments for further characterization.

a) LIBS Instrument

The LIBS instrument uses a pulsed laser. The laser is focused onto a sample within 7 m of the rover. The LIBS instrument ablates atoms and ions in electronically excited states within a plasma from which they decay, producing light. The light is carried to three dispersive spectrometers that obtain spectra over a range of 240– 850 nm. The spectra consist of emission lines of elements present in samples.

b) Remote Micro-Imager (RMI)

The ChemCam instrument includes the highest resolution camera ever sent to the surface of Mars. The RMI can be used to look for physical alterations of a rock caused by the presence of water in the past (Fig. 1.9).
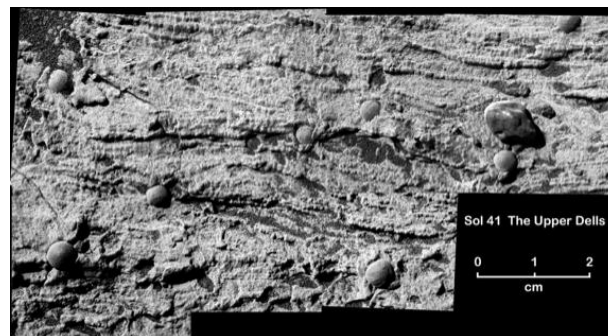
Figure 1.9. Microscopic Imager (MI) image on the Mars Exploration Rover (MER) of "festooning" on a Martian rock. Festooning is a trait of rock altered by water. Credit: NASA/JPL/Cornell/USGS

Several studies based on data obtained by the Curiosity rover from the Gale Crater were recently published. New data from ChemCam, were reported by Meslin et al., 2013. They explained the identification of two principal soil types. One main soil type is made of fine-grained particles, which carries a significant amount of hydrogen. This reflects the dust that covers the whole Martian surface. The other main soil type was coarse grained (up to 1 millimetre in size) and reflects the rocks that make up the Gale Crater. Meslin et al., (2013) have concluded that the ChemCam data did not reveal any significant exchange of water vapour between the regolith and the atmosphere.

Pathfinder, Spirit and Opportunity rovers had less sophisticated technology to analyse soil but their insights about the mineral composition of the Martian soil are similar to that reported by the Curiosity rover work. With ChemCam and Curiosity's other instruments, scientists are starting to obtain a deeper understanding of the composition and the geology history of the Martian soil.

1.6.2 ExoMars mission

Exobiologists have been studying data from past space missions in recent years trying to find any sign of present or past life on Mars. The discovery of some minerals such as clay and sulphates proves that there has been liquid water on the Martian surface during its early evolution. These discoveries make scientist more interested in studying the development of life forms and chemical reactions that could establish life. Hence, in 1999, a team of scientific advisors recommended to the European Space Agency (ESA) that it should pursue an exobiology mission using a rover that is able to access the subsurface in combination with the capability to perform experiments in an analytical laboratory. Therefore, ESA has established the ExoMars program to investigate the Martian environment and to demonstrate new technologies that pave the way for a Mars sample return mission in the future.

Currently the ExoMars concept has been modified in a way that two missions are expected within the ExoMars program: one consisting of an Orbiter plus an Entry, Descent and Landing Demonstrator Module, to be launched in 2016, and the other, featuring a rover, with a launch date in 2018 (Fig. 1.10) (Rull et al., 2011).

The initial design of the rover in (2006) had a weight of 240 kg and included 21 science instruments in addition to sample acquisition, preparation and handling systems. The scope of the science payload has been downsized several times and the rover mass was reduced to 150 kg with nine scientific instruments (Table 1.4). The rover will have the capability to travel on the Martian surface for a period of ~180 Martian sols. During this period it will cover a distance for several kilometres. This Pasteur package of instruments on the rover will carry out experiments to detect evidence of past and present life on samples from the surface and sub-surface. Mars is extremely cold and dry. It has a low atmospheric pressure (6-10 mbar) and all surface environments are subjected to very high levels of Ultra Violet (UV) and ionizing radiation. Consequently, the present surface of Mars is inhospitable for extant life as we know it and if life is still present on Mars, it would be in protective subsurface environments. Therefore, the rover will carry a drill to analyse the soil up to a depth of two metres below the Martian surface.

Figure 1.10. Elements of the ExoMars programme 2016-2018 Credit: ESA.

The initial design concept for a combined Raman and LIBS instrument for the ExoMars mission was first presented in 2006 at the International Conference on Space Optics. Since then, prototypes of the instrument were built, tested and developed (Ahlers et al., 2008). The main challenge was to combine the two techniques into a single instrument with the stringent mass, volume and the power requirements of the ExoMars mission. During the period from the initial design in 2006 until it was finished in 2009, ESA realised that the mission instrument such as the RLS instrument was too heavy and consumed too much power to be used for the mission. In an effort to reduce mass and costs, a new design had to be made that would include only the Raman spectroscopy instrument while the LIBS capability was left out of the ExoMars mission.

ESA has also confirmed that the mission would lose several of the initial planned instruments because of budget cuts. Instruments that were "de-scoped" from the ExoMars mission include:

- Mars X-Ray Diffractometer (Mars-XRD): This instrument retrieves information about the composition of crystalline minerals
- Miniaturised Mössbauer Spectrometer (MIMOS-II): This instrument provides the mineralogical composition of iron-bearing surface rocks, soils and sediments
- The Life Marker Chip: This instrument detects specific molecules associated with life
- Humboldt payload: This instrument was previously known as the GEP (Geophysical and Environmental) payload. It was designed to study atmospheric variations and the internal structure of the planet by monitoring Mars quakes (The ExoMars Newsletter, European Space Agency, 2012).

The remaining rover instruments for the ExoMars mission are listed in table 1.4.

PanCam	The Panoramic Camera: It will perform Digital Topographic Mappingof Mars.
WISDOM	Water Ice and Subsurface Deposit Observation On Mars, ground penetrating radar. WISDOM uses radar pulses, covering the frequency range from 500 MHz to 3 GHz, to map the subterranean.
CLUPI	Close - UP Imager: A camera system to obtain high-resolution colour close-up images.
Ma-MISS	Mars Multi-spectral Imager for Subsurface Studies: It will analyse the internal surface of the borehole generated by the ExoMars drill.
MicrOmega	A visible plus infrared imaging spectrometer: It will identify the mineralogical and the molecular composition of samples collected by the ExoMars drill.

Raman laser spectrometer	Raman spectrometer will determine the mineralogical composition of the soil and identify organic molecules.
MOMA	Mars Organic Molecule Analyser is a combined pyrolysis gas chromatograph mass spectrometer (GC-MS) and laser desorption mass spectrometer (LD-MS). It will study biomarkers to explain the potential origin, evolution and the distribution of life on Mars.
ISEM	Infrared Spectrometer for ExoMars: It will measure the mineralogical composition of a sample's surface. ISEM and PanCam contribute to the selection of suitable samples for further analysis by other instruments.
ADRON-RM	Adron is a neutron detector: It will search for hydrated minerals and subsurface water contributing to the search for suitable areas for drilling and sample collection.

Table 1.4. Onboard instruments for the ExoMars mission.

1.7   Conclusion

Mars has already revealed a great diversity of rocks at the surface. Recent missions such as Mars Express (ESA, 2003) and the Mars Reconnaissance Orbiters (NASA, 2005) have greatly extended our knowledge of the Martian surface through the discoveries of new minerals such as carbonates with the use of hyper spectral observations (Murchie et al., 2009). Morphological and mineralogical studies show that Mars could have experienced a major climate change in the past. It also revealed that the early conditions of Mars were warmer and wetter than today and could potentially have hosted life.

Each exploration mission focuses on more specific questions. Consequently, we can expect our understanding of the specific geologic environments and the evolution of Mars in general to continue to improve for the next decade. There is a need for more missions with new instruments such as a Raman spectrometer to better understand the changing geological environments and to analyse organic molecules. New missions such as the current Mars Curiosity rover and the planned ExoMars, will help to investigate the surface and subsurface of Mars and will provide a more accurate understanding of the (bio) geochemistry of the planetary surface. This PhD project will contribute in understanding the origin and evolution of geological environments on Mars in future missions such as the ExoMars mission. In these future missions, *in situ* measurements will help to detect carbonates and sulphates and the specific geological processes that led to their formation. The ExoMars mission is equipped

with a Raman spectrometer as an *in situ* instrument. This instrument is designed to provide more accurate *in situ* information compared to previous missions and the evaluation of the instrument undertaken in this thesis represents part of the large on-going work to bets interpret the data hopefully obtained on Mars in the near future.

1.8 References

Abell, P.A. et al., (2009), Scientific Exploration of Near-Earth Objects via the Orion Crew Exploration Vehicle, Meteoritics & Planetary Science 44, Nr 12, p. 1825-1836.

Ahlers, B., I. Hutchinson, R. Ingley and Raman LIBS EBB team, (2008), Combined Raman/LIBS Spectrometer Elegant Breadboard - Built and Tested - and Flight Model Spectrometer Unit, Proc. 7th Int. Conf. on Space Optics, pp. 8.

Baker, V. R. (1982), The channels of Mars, Research supported by NASA, NSF, and Australian-American Educational Foundation Austin, TX, University of Texas Press, pp. 198.

Bandfield, J. L. et al., (2003), Spectroscopic Identification of Carbonate Minerals in the Martian Dust, Science 301, p. 1084-1087.

Bibring, J. P. et al., (2006), Global mineralogical Aqueous Mars History Derived from OMEGA/Mars Express Data, Science, Vol. 312, p. 400-404.

Bish, D. L. et al., (2013), X-ray Diffraction Results from Mars Science Laboratory: Mineralogy of Rocknest at Gale Crater, doi: 10.1126/science.1238932.

Bogard, D. D. and D. H. Garrison, (1999), Argon-39-argon-40 "ages" and trapped argon in Martian shergottites, Chassigny, and Allan Hills 84001, Meteorit. Planet. Sci., Vol. 34, p. 451-473.

Bouvier, A., J. Blichert-Toft, and F. Albarède, (2009), Martian meteorite chronology and the evolution of the interior of Mars, Earth and Planetary Science Letters, Vol. 280, p. 285-295.

Bouvier, A., J. Blichert-Toft, J. D. Vervoort, and F. Albarède, (2005), The age of the SNC meteorites and the antiquity of the Martian surface, Earth and Planetary Science Letters, Vol. 240, p. 221-233.

Bridges, J. et al., (2001), Alteration assemblages in Martian meteorites: implications for near-surface processes. Space Sci. Rev. 96, p. 365-392.

Carr, M. H. and J. W. Head, (2010), Geologic history of Mars, Earth Planet. Earth and Planetary Science Letters 294, p.185–203.

Catling, D.C. (1999), A chemical model for evaporites on early Mars: Possible sedimentary tracers of the early climate and implications for exploration, Journal of Geophysical Research, Vol. 104, Issue E7, p. 16453-16470.

Chyba, C. F., and C. B. Phillips, (2002), Europa as an Abode of Life, Orig. Life Evol. Biosph, 32, p. 47-68.

Edgett, K. S. et al., Curiosity's Mars Hand Lens Imager (MAHLI) Investigation. Space Sci. Rev. 170, 259–317, (2012). doi: 10.1007/s11214-012-9910-4.

Ehlmann, et al., (2011), Subsurface water and clay mineral formation during the early history of Mars. Nature 79(7371), p. 53-60.

Fairen, A.G. et al., (2004), Inhibition of carbonate synthesis in acidic oceans on early Mars. Nature, Vol. 431, p. 423-426.

Golden, D. C. et al., (2001), A simple inorganic process for formation of carbonates, magnetite, and sulfides in Martian meteorite ALH84001. Am Min. 86, p. 370-375.

Gooding, J. L. (1978), Chemical Weathering on Mars Thermodynamic Stabilities of Primary Minerals (and Their Alteration Products) from Mafic Igneous Rock, Icarus, Vol. 33, p.483-513.

Grady, M. M. (2008), Astrobiology of the Terrestrial Planes, with Emphasis on Mars. In complete course in Astrobiology, eds Horneck, G. and P, Rettberg. (Wiley-VCH Verlag GmbH and Co. KGaA), p. 203-222.

Greeley, R., and J. E. Guest, (1987), Geologic Map of the Eastern Equatorial Region of Mars, USGS Misc. Inv. Ser. Map I-1802B.

Grotzinger, J. P. et al., (2012), Mars Science Laboratory Mission and Science, Investigation, Space Sci Rev 170: p. 5-56.

Hartmann, W. K. (1970), Lunar cratering chronology. Icarus 13, p. 299-301.

Hartmann, W. K. (1999), Martian cratering. VI. Crater count isochrons and evidence for recent volcanism from Mars Global Surveyor. Meteorit. Planet. Sci. 34, p. 167-177.

Hartmann, W. K. (2005), Martian cratering. 8. Isochron refinement and the chronology of Mars. Icarus 174, p. 294-320.

Hartmann, W. K. and G. Neukum, (2001), Cratering chronology and the evolution of Mars. Space Sci. Rev. 96, p. 165-194.

Hegde, S. and L. Kaltenegger, (2013), Colours of Extreme Exo-Earth Environments Astrobiology. 13(1). p. 47-56.

Houtkooper, J. M. and D. Schulze-Makuch, (2010), Do perchlorates have a role for Martian life? Journal of Cosmology 5, p. 930-939.

Ivanov, B.A. (2001), Mars/Moon cratering rate ratio estimates. Space Sci. Rev. 96, p. 87-104.

Kallenbach, J. G. and W.K. Hartmann, Editors, Chronology and Evolution of Mars, Kluwer, Dordrecht, p. 105-164.

Kieffer, H. H., B. M. Jakosky, C. W. Snyder and M. S. Matthews (1992), In: Mars, Tucson: University of Arizona Press. pp. 384–385.

Laan, E., W. Westrenen, A. Wielders, J. Heiligers, (2009), Moonshot: a combined Raman/LIBS instrument for lunar exploration, 40th Lunar and Planetary Science, doi:10.1117/12.825883.

Lapen, T. J. et al., (2010), A Younger Age for ALH84001 and Its Geochemical Link to Shergottite Sources in Mars; Science, Vol. 328, p. 347-351.

Levin, G. V., A. H. Heim, J. R. Clendenning and M. F. Thompson, (1962), "Gulliver" - A Quest for Life on Mars, Science 138, p. 114-121

Lipps, J. H. et al., (2004), Astrobiology of Jupiter's Icy Moons (PDF). Proc. SPIE 5555: 10.doi:10.1117/12.560356.

Mahaffy, P. R. et al., The Sample Analysis at Mars, Investigation and Instrument Suite. Space Sci. Rev. 170, 401–478 (2012). doi: 10.1007/s11214-012-9879-z.

Malin, M. C. and K. S. Edgett, (2000), Evidence for recent groundwater seepage and surface runoff on Mars. Science 288(5475), p. 2330-2335.

McKay, C. P. et al., (2008), The Possible Origin and Persistence of Life on Enceladus and Detection of Biomarkers in the Plume, Astrobiology, Vol. 8, No. 5.

McKay, C. P., H. D. Smith, (2005), Possibilities for methanogenic life in liquid methane on the surface of Titan, Icarus, Vol.178, Issue 1, p. 274-276.

McKay, D. S. et al., (1996), Search for past life on Mars: Possible relic biogenic activity in Martian meteorite ALH 84001, Science, Vol. 273, p. 924-930.

Meslin et al., (2013), Soil Diversity and Hydration as Observed by ChemCam at Gale Crater, Mars, doi: 10.1126/science.1238670.

Murchie, S. L. et al., (2009), A synthesis of Martian aqueous mineralogy after 1 Mars year of observations from the Mars Reconnaissance Orbiter, Journal of Geophys. doi: 10.1029/2009JE003342.

Neukum, G. and B.A. Ivanov, (1994), Crater size distribution and impact probabilities on Earth from lunar, terrestrial-planet, and asteroid cratering data.In: Hazards due to Comets and Asteroids, (T. Gehrels, Ed.) Univ. Arizona Press, pp. 359-416.

Neukum, G., B. A. Ivanov and W. K. Hartmann, (2001), Cratering records in the inner Solar System in relation to the lunar reference system. Space Sci. Rev. 96, p. 55-86.

Nyquist, L. E. et al., (2001), Ages and geologic histories of Martian meteorites, Vol. 96, Issue 1-4, pp 105-164.

Poulet, F. et al., (2005), Phyllosilicates on Mars and implications for early main climate. Nature 438(7068), p. 623-627.

Pollack, J. B., R. M. Haberle, J. Schaeffer and H. Lee, (1990), Simulations of the general circulation of the Martian atmsophere 1. Polar processes. Journal of Geophysical Research 95: doi: 10.1029/89JB01430. issn: 0148-0227.

Rull, F., (2011), ExoMars Raman laser spectrometer for Exomarsdoi:10.1117/12.896787.

Rull, F., S. Maurice, E. Diaz and the RLS Team, (2012), Raman spectroscopy for the 2018 ExoMars mission, EPSC Abstracts, Vol. 7, p. 740.

Reynolds, J., B. S. Weir and C. C. Cockerham, (1983), Estimation of the coancestry coefficient: Basis for a short-term genetic distance. Genetics 105: 767-779.

Schulze-Makuch, D. and L. N. Irwin, (2004), Life in the Universe: Expectations and Constraints, Springer-Verlag, Berlin, pp. 172.

Scott, D. H. and K. L. Tanaka, (1986), Geologic map of the western equatorial region of Mars, U.S. Geol. Surv. Misc. Invest., Map, I-1802-A.

Sheehan. W, (1996), The Planet Mars: A History of Observation and Discovery, Tucson: University of Arizona Press, pp.270.

Stöffler, D. and G. Ryder, (2001), Stratigraphy and isotope ages of the lunar geologic units: Chronological standard for the inner Solar System. Space Sci. Rev. 96, p. 9-54.

Tanaka, K. L. (1986), The stratigraphy of Mars, Journal of Geophys. Res., 91, p. 139-58.

Tanaka, K. L., D. H. Scott and R. Greeley, (1992), in Mars, Kieffer H. H., B.M. Jakosky, C.W. Synder, and M.S. Matthews (eds.), University of Arizona Press, Tucson, pp. 354–382.

Treiman, A. H. and E. J. Essene, (2011), Chemical composition of magnetite in Martian meteorite ALH 84001: Revised appraisal from thermochemistry of phases in Fe-Mg-C-O, Geochimica et Cosmochimica Acta 75, p. 5324-5335.

Werner, S. C. (2005), Major Aspects of the Chronostratigraphy and Geologic Evolutionary History of Mars. PhD thesis, Freie Universitaet Berlin, p. 160.

Wiens, R. C. et al., (2013), Pre-flight calibration and initial data processing for the ChemCam laser-induced breakdown spectroscopy instrument on the Mars Science Laboratory rover, Spectrochimica Acta Part B: Atomic Spectroscopy, doi:10.1016/j.

Chapter 2: Raman and Laser induced breakdown Spectrometer (RLS)

Contents

2.1 Introduction

The European space agency (ESA) instrument that was used during this PhD research study is a combined Raman and Laser-induced breakdown spectroscopy (LIBS) (RLS) instrument. It was initially designed by TNO (Nederlandse Organisatie voor Toegepast Natuurwetenschappelijk Onderzoek or Dutch Organization for Applied Scientific Research) as an elegant breadboard (EB) for the ExoMars mission. EB refers to equipment before it reaches the stage of engineering mode (EM). It is built using commercial grade components and a configuration close to that of the flight mode (FM).

At the beginning of the ExoMars mission program, this instrument had a high priority within the scientific community and had been chosen as one of the main instruments for ExoMars mission that would act as the first contact with Martian samples. However, due to the economic crisis, governments spent less money on space projects. ESA was affected and set new requirements such as less weight for the instruments aboard the ExoMars mission. The RLS instrument was therefore required to be lighter in order to fit within the mission budget. After extensive review, the LIBS capability was removed from the RLS instrument. Only a Raman spectrometer will be included in the scheduled ExoMars mission in 2018.

After initial testing at TNO, the RLS instrument was delivered to the instrument principal investigator (PI) in Spain. An agreement was made for subsequent delivery to the Vrije University Amsterdam. It arrived in 2011 after more than two years delay. One of its optical fibres was found damaged. The first step before assessing the capabilities of the RLS instrument was to repair the optical fibre of the spectrometer and to optimize its performance. The aim was to do this as quickly as possible and at the lowest cost possible.

Based on the changing size of the instrument and the changed goals of the ExoMars mission to a Raman only spectrometer, the focus of this PhD research was changed. The subject of the PhD was narrowed to the study of the performances of the Raman laser spectrometer only, including the influence of Mars' surface conditions on the Raman spectra of selected minerals. However, the design of the RLS instrument incorporates both Raman and LIBS capabilities. Consequently, in this chapter the basic theory of Raman and LIBS spectroscopy, the design of the instrument and its technical performance under Martian conditions are discussed.This chapter includes the development undertaken during this PhD to improve the instrument stability (for instance: laser stability, cooling of the spectrometer charge-coupled device (CCD)). Note that the LIBS technique and instrument design are briefly introduced because the performances of the Raman instrument are partly linked to the specific combined Raman-LIBS design. Finally, the results of the spectrometer calibration at different temperatures are presentedin the last section of this chapter.

2.2 Principles of Raman spectroscopy

In order to interpret the data collected by the Raman spectrometer one must firstunderstand the interactions between light and samples. The objective of this section is not to provide the full theory of Raman spectroscopy using quantum mechanics but to give the information

necessary for understanding and interpreting Raman data in space applications (for more information the reader can refer to the book "Raman spectroscopy applied to Earth science and culture heritage", edited by Dubessy et al., (2012).

The first section focuses on the classical theory of Raman spectroscopy. Subsequently, the intensity of Raman scattering is explained followed by the dynamics of molecules (described by harmonic oscillators). Then, an introduction to normal modes of vibration is provided. Finally, vibrational dynamics of molecules and solid crystalline materials are explained.

2.2.1   The Raman effect

In 1923, Adolf Smekal predicted the existence of inelastic scattering by quantum mechanical calculations (Smekal, 1923). Four years later, Krishnan and Raman provided the practical evidence of this inelastic scattering of light. This scattering was called the Raman effect (Raman, and Krishnan 1928).

Unlike Rayleigh scattering, which corresponds to an elastic scattering of light (Rayleigh. 1899), Raman scattering is inelastic scattering of light due to various elementary excitations where the energy is lost or gained during the scattering process. These excitations may be the internal vibration modes in:

  a) A molecule (vibrons or intermolecular vibration)
  b) Phononsin an ordered crystal structure (lattice vibrations or external vibrations). A phonon is an elementary vibrational motion in which a latticeof atoms or molecules uniformly oscillates at a single frequency
  c) Magnons in systems with magnetic-order transitions. Magnon or spin wave is a wave, propagatedthrough a crystal lattice as a result of changes in the spin angular momentum of electrons in the lattice

For Raman spectroscopy, a monochromatic laser beam (ν_o) is directed to a sample. The light interacts with the sample and is partly scattered. The scattered lights can be classified into two categories:

  a) Rayleigh scattering: Rayleigh elastic scattering is strong compared to Raman scattering (Raman scattering is about 0.001% of the incident beam) and has the same frequency as the incident beam (ν_o)
  b) Raman scattering: Raman scattering or inelastic scattering is very weak and has the frequencies $\nu_{o+}\nu_m$ or $\nu_{o-}\nu_m$, where ν_m is a vibrational frequency of a molecule. The $\nu_{o+}\nu_m$ and $\nu_{o-}\nu_m$ frequencies are referred to as the anti-Stokes and Stokes peaks respectively

      Raman shift is expressed as a wavenumber in units of inverse centimetres. The laser excitation light is used as a reference and therefore has a Raman shift of zero. Raman shift values are not specifically dependent on the laser excitation wavelength.

In order to convert from spectral wavelength to Raman shift (in wavenumber) in the Raman spectrum, the following equation is applied:

$$\Delta\omega \sim \left(\frac{1}{\lambda_0} - \frac{1}{\lambda_1} \right) \qquad (2.1)$$

where $\Delta\omega$ is the Raman shift in wavenumber, λ_0 is the excitation wavelength, and λ_1 is wavelength of the scattered light. Wavelength is usually expressed in nanometres (nm) and Raman shifts in cm^{-1}. Then:

$$\Delta\omega\left(cm^{-1}\right) = \left(\frac{1}{\lambda_0(nm)} - \frac{1}{\lambda_1(nm)} \right) \times 10^7 \qquad (2.2)$$

Figure 2.1 shows a Jablonski diagram for Raman scattering. The figure illustrates the electronic states of a molecule and the transitions between its electronic states. Most molecules are present in the ground electronic state (m state) at room temperature. When the laser interacts with the electrons in a molecular bond, virtual states, which are not the real states of the molecule, are created. Most photons scatter by a Rayleigh process. As light is reflected with the same energy, the Rayleigh process does not involve any energy change. In Stokes scattering, a molecule (in state m) absorbs energy and is excited to a higher energy vibrational state (n). However, depending on the ambient temperature, some molecules in the material will already exist in a higher energy excited vibrational state (n state) (Fig. 2.1). Scattering from these states to the ground state m is called anti-Stokes scattering. The population of molecules at state m is much larger than at state n. The relative intensities of the Stokes and anti-Stokes scattering depend on the population of the various states of the molecule. Therefore, anti-Stokes scattering is usually weaker than Stokes scattering in ambient conditions. As both processes give the same information about the characteristic energy levels within a molecule, it is more common to only measure the Stokes scattering.
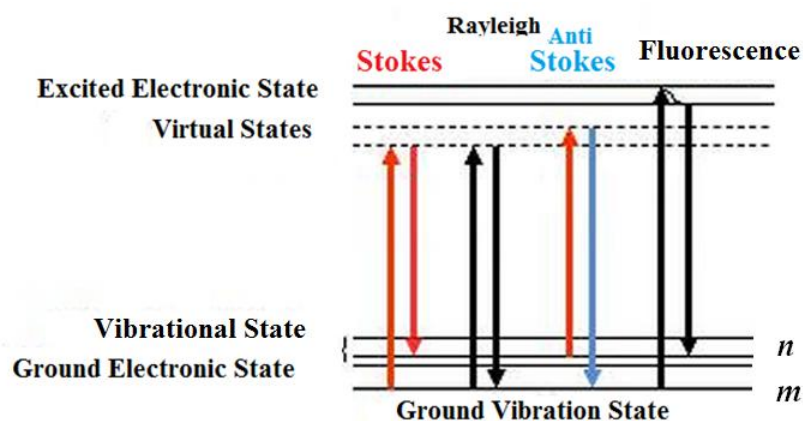

Figure. 2.1. Jablonski diagram showing the different processes and the states involved in different light molecule interaction: Stokes Raman scattering, Rayleigh scattering, Anti-Stokes Raman scatteringand fluorescence. Modified from http://biomed.tamu.edu/obsl/OBSL/Research%20Projects/SERS_biosensor.htm

The Raman and fluorescence process is shown in the Jablonski diagram (Fig. 2.1). In the fluorescence process, a molecule is first excited from its ground electronic state to one of the various vibrational states in the excited electronic state by absorbing a photon. Collisions

with other molecules cause the excited molecule to rapidly lose vibrational energy until it reaches the lowest vibrational state of the first excited electronic state. When the energy of the excitation wavelength (incident photons) is equal to the energy difference between ground energy state and one of the excited states of the molecule, Raman scattering sometimes overlaps with fluorescence. Fluorescence influences the overall quality of Raman spectra as it appears as a broad background.

Willes and Merlin (2000) and Lewis and Edwards (2001) explained the Raman scattering process in terms of the effect of an electric field on a molecule. When a molecule is affected by an electric field, the dipolar moment of the molecule μ is given by:

$$\mu = \mu_o + \alpha E \qquad (2.3)$$

where μ_o is the permanent dipole moment. The molecule has an electric dipole moment when it has a net separation of centres of positive and negative charges. A permanent electric dipole moment exists if the separation of charge is a characteristic of the molecule without the use of an external electric field.

αE is the induced dipolar moment: When a polarisable molecule (that did not have a permanent electric dipole moment) is subject to an electric field, the temporary distortion of the electron cloud around a certain molecular bond creates an induced electric dipole moment in the molecule.

When a molecule interacts with the electric field $E = E_o \cos\omega t$, the small vibrations of the molecule are given by $q_n(t)$, where $q_n(t) = q_{no} \cos(\omega t)$ (q_{no} is the amplitude and ω_n is the vibration frequency of the normal mode n). Therefore, based on the equation (2.3), the total dipolar moment is described as follows:

$$\mu = \mu_o + \alpha(0)E_o \cos(\omega t) + \Sigma_{n=1}^{0}(\frac{\partial \mu}{\partial q_n})_0 q_{n0} \cos(\omega_0 t)$$

$$+ \frac{1}{2} E_0 \Sigma_{n=1}^{0}(\frac{\partial \alpha}{\partial q_n})_0 q_{n0}[\cos(\omega + \omega_n)t + \cos(\omega - \omega_n)t]$$

(2.4)

Where a power series expansion of q_n, μ and α have been made and only the first terms are taken into account. The second and third terms in equation 2.4 correspond to the Rayleigh and the infrared processes (infrared spectrum is based on absorption spectroscopy and is beyond the scope of this study). The last term describes the Raman scattering (anti-Stokes and Stokes terms). Consequently, if $\frac{\partial \alpha}{\partial q}\Big|_{q=0}$ is zero, the molecular vibration is not Raman active. To be Raman active, the rate of change of polarizability α with vibration cannot be zero and in a Raman spectrum only those vibrations are detected that result in a change in polarizability. A more detailed explanation of the subject can be found in the book "Raman spectroscopy applied to Earth science and culture heritage", edited by Dubessy et al., (2012).

2.2.2 Raman intensity

A Raman spectrum is a plot of the intensity of Raman scattered radiation as a function of its frequency difference from the incident radiation (in units of wavenumbers, cm^{-1}). As mentioned before, this difference is called the Raman shift. Figure 2.2 shows the Raman spectrum of calcite as an example. The intensities of the different peaks depend in a complex way on the polarizability of the molecule, the intensity of the source and the concentration of the Raman active group in the sample structure (equation 2.5).
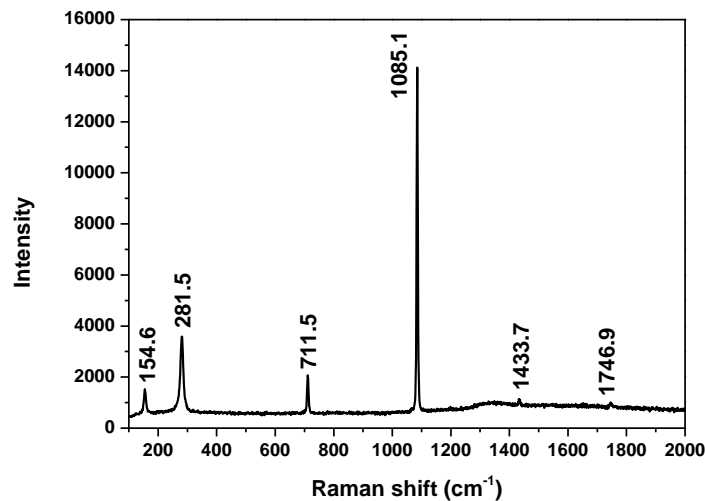

Figure 2.2. Calcite Raman spectrum taken with the Renishaw InVia Reflex confocal Raman spectrometer (for details information on calcite Raman spectrum see chapter five).

The intensity of *Stokes* Raman scattering is:

$$I(\omega_L - \omega_{fi}) = \frac{4\pi(\omega_L - \omega_{fi})^4}{3c^4} I_0(\omega_L) N \sum_{\rho\sigma} (\alpha'_{\rho\sigma})^2 \qquad (2.5)$$

where N is the number of scatters, $I_0(\omega_L)$ is the input laser power at frequency ω_L, ω_{fi} is the frequency of the vibrational transition from initial state i to final state f and $\alpha'_{\rho\sigma}$ is the $\rho\sigma$-component of the polarizability derivative. Normal Raman scattering occurs, when the frequency of the exciting radiation (incident photons) is much less than the frequency of an electronic transition. The normal scattering intensity is proportional to the furth power of scattered lightfrequency, $(\omega_L - \omega_{fi})^4$ and it is clear that using excitation sources of higher frequency increase the Raman intensity. Raman intensity increases significantly by movingfrom near infrared to visible or to ultraviolet exciting source radiations. More details about this subject can be found in the book by Smith and Dent(2005).

2.2.3   Number of normal modes of vibration

A molecular vibration occurs when atoms in a molecule are in a periodic motion. The molecule has a constant translational and rotational motion. The frequency of a periodic motion is known as the vibrational frequency. The number of normal modes of vibration of a molecule with N atoms is determined from the displacements of each atom in the x, y, and z direction. There are $3N$ such displacements, but 3 of these result in a translation of the whole molecule in the x, y, and z direction, and 3 result in molecular rotations. Thus the molecule has $3N-6$ normal modes of vibration. If molecule is linear there are $3N-5$ normal mode vibration, since there is no rotation possible around the molecular axis.

2.2.4   Vibrational dynamics of molecules and solid crystalline

In the simplest approach to calculate molecular vibration modes, a molecule is considered to be isolated. In other words, interactions between molecules and lattice vibrations are ignored. Therefore a normal vibration (no matter how complex) behaves like a harmonic oscillator. For example, a diatomic molecule will have only one normal mode ($3N-5=1$), the stretching mode. To keep the centre of gravity in a fixed position both atoms must move in opposite directions. The displacement is inversely proportional to the mass of the atoms.

The molecular vibration modes are described as a function of the force constant (spring coefficient) of the vibration or deformation and the mass of the participating atoms (Fig. 2.3). For this case of vibrating (diatomic species), the vibrational frequency is described by Hook's law:

$$\nu = \frac{1}{2\pi c}\sqrt{\frac{k_0}{\mu}} \qquad (2.6)$$

Here μ symbolises the reduced mass of participating atoms ($m_1 m_2 / (m_{1+}m_2)$). k_o is the force constant in Newton per metre. ν is the vibrational frequency in wave numbers. c is the speed of light in centimetres per second. In this model, the interatomic distance, hence the volume and the vibrational frequency are fixed. They do not vary with temperature.

For more complex molecules with more interatomic interaction, different stretching and bending force constants are required. Approximate equations of these force constants and the frequency vibrations for different polyatomic molecules were developed by Herzberg and Nakamoto (Herzberg, 1945; Nakamoto, 1986). They calculated the vibrational modes of different molecular bonds. In their method they measure the vibrational frequency of a complex molecule. However, these calculations were out of the scope of this PhD research project. The objective of this PhD project does not focus on the calculation of the vibrational frequency of different polyatomic molecules in Raman mineral analyses.

According to Hook's law, equation (2.6) the vibrational frequency of a bond is expected to increase with the increasing bond strength and it is expected to decrease with the increasing

mass of the atom involved. For instance, with respect to the bound strength, the stretching frequency increases in the $C - C < C = C < C \equiv C$ sequence (triple bonds are stronger than double bonds, which in turn are stronger than single bonds) and in relation to mass, the vibrational frequency decreases in the *H-F > H-Cl > H-I* sequence.

There are a number of factors that influence the precise frequency of a molecular vibration; these include:

- The mineral structure and the variety of different compositions in the mineral structure

These effects result in a combination of changes in the Raman peak positions, peak widths and peak intensities. Mineral crystal structures are determined by stoichiometric relationships, relative size of atoms and the nature of molecular bonds. In this PhD research project, Raman spectra are examined to see how frequency shifts when the composition of the mineral changes (see chapter four and five).

- The temperature and pressure factors

Temperature is known to have an influence on Raman scattering frequencies. Depending on the mineral structure, temperature potentially changes the Raman peak position, peak widths, peak intensities and new peaks may appear at lowtemperatures (~ -90 °C) (Sutherland, 1933; Lucazeau, 2003; Sobron and Wang, 2011).

If the change in temperature causes a change in the molecular structure of the mineral (such as association of simple molecules into more complex aggregates, or a change in the crystalline form of the mineral), then new peaks in the Raman spectrum are expected. Change in temperature could also result in a change of the Raman peak position. Equation 2.6 explains that when temperature decreases, the k_o (spring coefficient) increases. This also leads to an increase in the vibrational frequency (v) potentially causing the position of a Raman peak shift to a lower wavelength (v is correlated to *1/λ)*. In addition, the peak width refers to the thermal motion (the random motions) of atoms: peak width decreases when temperature decreases. More information on this matter is found in the research by Balkanski and colleagues (Balkanski et al., 1983; Sobron and Wang, 2011).

Pressure and temperature have an effect on a sample's volume and thereby could potentially cause Raman frequency variations. Temperature affects the population of the different vibrational levels (v = 0, 1, …) for each normal mode (Fig. 2.3). The difference between the different energy levels will not be equal and consequently the average position of the atoms will be changed by temperature changes. In both cases (pressure and temperature), the change in the lattice parameters is attributed to the anharmonicity of the potential energy of a molecule (Fig. 2.3). The effects of pressure and temperature on the mineral structures and consequently on the mineral Raman spectra have been discussed in previous studies (Lucazeau, 2003; Mammone and Sharma, 1979; Gillet et al, 1989, 1990, 1993a, 1993c, 1996a, 1997, 2000). However, rare studies exist about the magnitude of the variations of the

Raman shifts under Martian conditions. The study of the Raman shifts variations with temperature and pressure under Martian conditions is important in order to ensure the correct identification of minerals in future missions on Mars. Indeed temperature and pressure are expected to affect the frequency of Raman peaks of mineral on Mars, as temperature and pressure influences the structure of the minerals. However, peak frequencies also vary with mineral composition (such as olivine with different Fo values, see chapter five). Under such situations, then the effects of temperature and pressure have to be precisely quantified if we want to distinguish between the effect of Martian conditions and the effect of differentmineral compositions.
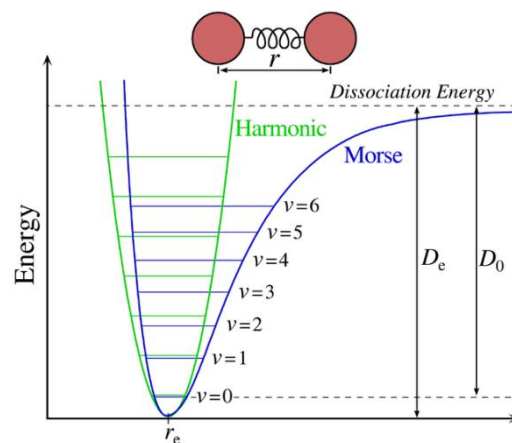

Figure 2.3. The harmonic (green colour) and Morse potential (blue colour) models for the interatomic potential for a diatomic molecule or bond. Morse potential is a model for the potential energy of a diatomic molecule. When describing vibration based on Hook's law, a harmonic oscillator potential is the model. Morse model is described as the deviation of a system from harmonic oscillation or an oscillator not oscillating in simple harmonic motion.r_e is the equilibrium inter nuclear distance (r is intermolecular separation) and D_e is the depth of the potential minimum. Unlike the energy levels of the harmonic oscillator potential (separated by $\hbar\omega$) the Morse potential level spacing decreases as the energy approaches the dissociation energy. The dissociation energy D_e is larger than the true energy needed for dissociation D_0 due to the zero point energy of the lowest ($v = 0$) vibrational level (modified from Reynard, et al., 2012).

2.2.5 Advantages and disadvantages of Raman Spectroscopy

The main benefits of Raman spectroscopy are:

- Non-destructive technique: Raman spectroscopy is a completely non-destructive and non-contact technique. It requires no sample preparation. Raman only involves illuminating a sample with a laser and collecting the scattered photons. Thus it is possible to analyse samples and retain the sample for additional analysis by other techniques such as LIBS if necessary.

- Raman is a technique that distinguishes sample's molecular structures.This technique produces a precise spectral fingerprint, unique to a molecule.

- Fast analytical technique: There is no need to dissolve solid materials, press pellets, dilute samples etc in Raman analysis. Therefore, this analytical technique leads to high quality data in a short period of time. It is potentially a great advantage for space missions.

- Raman is able to be coupled with optical fibre over long distances for remote analysis. Therefore, it is able to work in harsh conditions.

Raman spectroscopy also has certain disadvantages:

- The Raman effect is weak. High power excitation sources are needed to amplify the Raman effect and sensitive detectors are also potentially needed to detect the Raman effect.

- Samples could be destroyed. Raman is usually non-destructive, but if too much laser power is directed at a small point, it can be destructive and burn samples(depends on the selected sample and the laser wavelength). Lowering the laser power significantly reduces the risk of damaging a sample but results in lower signals.

- The interference of fluorescence in Raman spectra.Raman peaks are often swamped or obscured by the background due to fluorescence.Selecting the appropriate excitation wavelength can avoid the fluorescence problem. Choosing an excitation wavelength far from any electronic transitions avoidsfluorescence. If the Raman effect is stimulated in the near infrared (NIR) region at a wavelength of 1064 nm, many materials do not show fluorescence. However, the intensity of the Raman scattering depends on the fourth power of the excitation wavelength (see section 2.2.2 Raman intensity). It means that, to avoid the fluorescence effect, the wavelength of the laser excitation should be increased. The intensity of Raman peaks will be weak, however.

2.3   Laser induced breakdown spectroscopy (LIBS)

In this section the basic principle of laser induced breakdown spectroscopy (LIBS) and the advantages and disadvantages of this technique are briefly introduced. The application of this technique under Martian atmospheric conditions is not in the scope of this PhD research study. Nonetheless, studies of LIBS technique under Moon conditions are planned to be evaluated at the VU University in the Martian analogue chamber manufactured as part of this PhD (Colin et al., 2012).

2.3.1 History of LIBS spectroscopy

Laser induced breakdown spectroscopy (LIBS) was first developed as an analytical technique in the 1960's after lasers became commercially available. In the early 1980's there were a few groups working on LIBS. In the past decade the field has expanded greatly with many international groups now investigating and developing a method for a variety of applications. LIBS is also known as a laser-induced plasma spectroscopy (LIPS), laser ablation spectroscopy (LAS), and laser spark spectroscopy (LSS). These terms are rarely used because these abbreviations are often used in other contexts outside the field of optics/ spectroscopy. The abbreviation LIBS is the most well-known and is the terminology used in this research project.

LIBS is capable of analysing gases, liquids and solid state materials. It is able to work in harsh conditions (high/ low temperature and pressure). In addition, the simplicity and flexibility of the LIBS technique allows it to be applied to a wide variety of substances in material sciences and more recently, in planetary simulation laboratories.Several space missions to bodies in the solar system, such as asteroids, our moon and Jupiter's moon Europa,were equipped with the LIBS instrument. LIBS is capable of providing *in-situ* quantitative elemental analyses of all major and many minor trace elements of planetary surface material.

2.3.2 The basic principles of LIBS

In general terms, LIBS is based on the analysis of the spectral emission from laser-induced sparks or plasmas. Pulsed laser radiation is directed at a small spot (10-200 μm) of sample material. When power densities exceed hundreds of mW/cm^2, microplasma is formed. The temperature of this plasma is hot, about 10^4 to 10^7 °C. At such a temperature, any material is ablated and ionized (Sergey et al., 1999).

In the early stage of plasma thermalization, electrons interact and recombine with all types of ions so that energy will be released over a broad spectral range from soft X- rays to visible and near infrared (IR). This early plasma stage results in an intense continuous emission. Depending on the power of the laser pulse, the plasma cools down to the point where neutral atoms in excited states are formed, which takes about <0.1 second.

The most significant parameters for the generation of LIBS plasma are the laser irradiance on the sample and the environmental pressure. On Earth the laser irradiance necessary to generate plasma is above several 10 mW/mm^2. The plasma expansion is strongly affected by the ambient pressure. According to Knight work, the best pressure condition for LIBS plasma is between 5 and 150 mbar (Knight et al., 2000). This pressure range ensures a modest confinement of the expanding plasma and a moderate rate of ionic and atomic collisions resulting in non-radiative plasma relaxation. This is why the Martian atmosphere (between 6-10 mbar) is suitable for LIBS measurements (Knight et al., 2000; Salle´ et al., 2004; Lazic et al., 2007; Rauschenbach et al., 2010). One of the difficulties for interpretation of LIBS data is

that charged ions and molecules that form the plasma can absorb the characteristic wavelengths emitted by elements and the absorption and subsequent re-emission changes the spectral line profile, resulting in broadened lines and a marked increase in the background. This effect is called self-absorption. At very low atmospheric pressure the plasma expansion is fast and self-absorption is minimised. This leads to an advantage for LIBS applications on planetary bodies without or with a very thin atmosphere such as our Moon, Europa (moon of Jupiter) and asteroids (Harris et al., 2005; Pavlov et al., 2011; Lasue et al., 2012).

The spectrum of the plasma contains many peaks that correspond to the optical transitions between particular atomic levels. The LIBS spectrum yields qualitative information about the composition of sample elements. With the proper calibration, quantitative information on the concentration of elements in a sample can also be obtained (e.g., Rauschenbach et al., 2010). LIBS calibration will not be addressed further in this research project. Figure 2.4 presents the LIBS spectral analyses of the Martian basalt (shergottite).
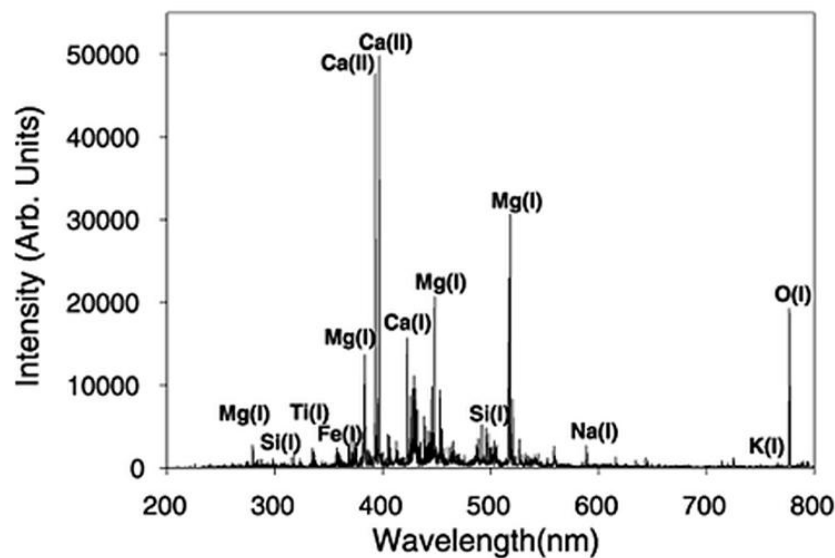

Figure 2.4. Major elemental emission peaks from Dar al Gani 476 (Martian basalt, Shergottite) are labelled in this LIBS spectrum. The Roman numbers in parentheses refer to the ionization state of an atom. (I) is an excited neutral atom; (II) is a singly-ionized atom (from Thompson et al, 2006).

LIBS captures the spectrum of photons emitted by the plasma over the entire 200– 965 nm range over which all elements have emission peaks. To obtain all elements, a large spectral range is essential. Wiens et al. (2005) explained the practical considerations in covering the whole spectral range for LIBS:

a) Apply a single fixed-grating spectrograph that covers the whole range.
b) Apply a moveable grating spectrograph, taking successive spectra to cover the whole range of spectral.
c) Split the light into several fixed-grating spectrographs that together cover the whole range of spectral.

For more details of the advantage and disadvantages of these strategies see Wiens et al. (2005).

2.3.3 Advantages and disadvantages of LIBS spectroscopy

- LIBS is able to analyse a sample directlywithout the need to prepare the samples beforehand. The LIBS laser radiation may be used for depth profiling and has the effect of cleaning any surface contamination-corrosion. The efficiency of the laser cleaning process depends upon the type of material being removed and the power of the laser.

- The LIBS technique detects all elements from high to low Z such as hydrogen to sodium, which are often not detected by other methodologies. However, LIBS is not applicable when high-sensitivity measurementsdown to sub-parts per trillion are required. Its field of application lies more in real-time remote sensing without contact with or preparation of the sample.

- In many cases, only one laser pulse is needed to analyse a material.This allows a large number of samples to be identified rapidly. When atomic peaks appear in a spectral region, the chemical composition of a sample is immediately recognized. Thus, it is real time spectroscopy.

- As LIBS is essentially an all-optical technique, only optical access to the material is required to carry out an analysis. This can be achieved by a direct line-of-sight method using a telescope instrument for distances of up to about 10 meters or alternatively with an optical-fibre probe instrument for distances of up to about 100 meters. These features make LIBS a particularly attractive solution for analysis of hazardous or high-temperature materials and for operation in hostile environments, such as space.For example ChemCam on the current Curiosity Rover can take spectra from a distance of about 7 meters(Sallé et al., 2006).

LIBS spectroscopy also has limitations such as:

- Non-reproducibility of the elemental composition detection from the same spot in a sample. Due to the ablation ofa sample area, LIBS technology is considered to be a practically non-reproducible technique.

2.4   The RLS instrument

The RLS instrument is composed of three basic parts:

- Two monochromatic laser sources, one each for Raman and for LIBS,
- An optical head (including focussing and collection optics, plus optical fibres),
- A spectrometer,

2.4.1 Laser sources

2.4.1.1   *Raman laser source*

Exciting radiation for Raman spectroscopy is always provided by lasers. An ideal laser Raman source should emit a stable monochromatic light (UV, Visible, NIR source), with sufficient energy (in general the power of Raman lasers are between a few mW to hundreds of mW) to produce a measurable amount of Ramanscattering. The first Raman laser selected for the RLS instrument (designed by Cosine Company with the assistance of Monochrom Company) was a diode laser that weighed less than 30 g, with a ~ 659 nm wavelength and an output power of 20 mW (Fig. 2.5). Using a large sample spot ~100 μm with a low laser power (20 mW) avoided the risk of sample damage (Escudero-Sanz et al., 2008). The Raman analyses presented in this PhD research were obtained with the diode laser with a ~ 659 nm wavelength. However, recently the RLS ExoMars team have decided that the diode laser with a wavelength of 659 nm will be replaced with the ~ 532 nm diode laser. Diode lasers have the advantage of being compatible with space missions requirements (small and light, low power, vacuum compatible) and they are now commercially available. The diode laser with 532 nm wavelength was chosen, as it is one of the most used wavelength for Raman spectroscopy.

The choice of the laser wavelength for the RLS instrument was a compromise between increasing the Raman efficiency and limiting the fluorescence. The key aspect when choosing the excitation wavelength is the Raman efficiency. Raman efficiency has an inverse relationship to λ^4 (Rull, 2012). The shorter the laser wavelength, the higher the intensity of the Raman peak will be. However, for short laser wavelengths the fluorescence increases and can obscure the Raman signalby reducing signal to noise, which makes detection of minor peaks more difficult (Harrigan and Goodacre; 2003). For the RLS instrument, the Raman laser excitation has to satisfy the objectives of the ExoMars research (Fig. 2.6). These objectives are:

a) Investigation of past and/ or present life based on the detection of organic compounds and the detection of minerals as indicators of biological activity.

b) The clarification of water-related processes through the detection of mineral phases produced by fluid-rock interactions.

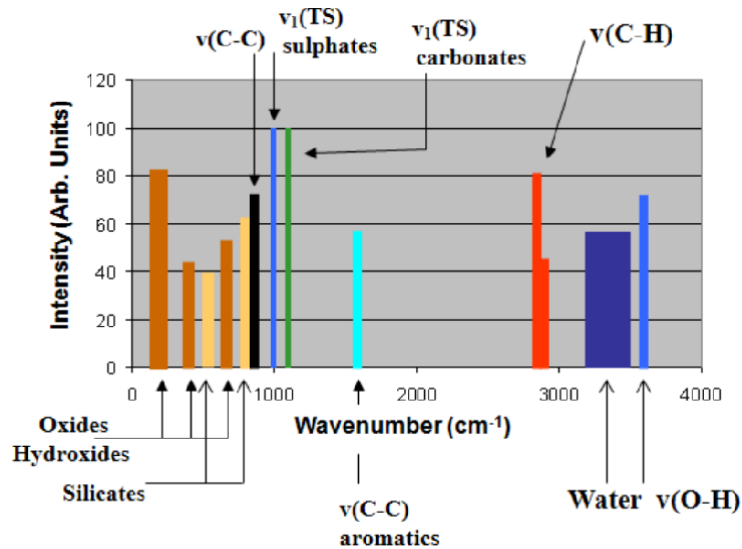
Figure 2.5. Diode laser, with a mass less than 30 g.

Figure 2.6. Raman spectral ranges for the ExoMars mission.

To produce high quality Raman spectra, the stability of the laser is important. Following delivery of a damaged system to the Vrije University Amsterdam, problems emerged while testing the performance of the 659 nm laser diode that was initially chosen for the RLS instrument. The laser wavelength was found to be unstable over time. This wavelength instability is a characteristic that is often found in diode lasers. The instability resulted in mode hopping, when temperatures changed (McCreery, 2000). To overcome this problem, the original Cosine design for Raman diode laser was coupled with a volume Bragg grating to increase the stability of the laser. However, even with this modification, instability of the Raman laser wavelength was still detected. Close examination of the instability of the laser wavelength showed that the Raman laser wavelength on the RLS instrumnet is without a doubt too unstable for practical use. Variations in the Raman excitation laser wavelength are shown in Fig. 2.7.
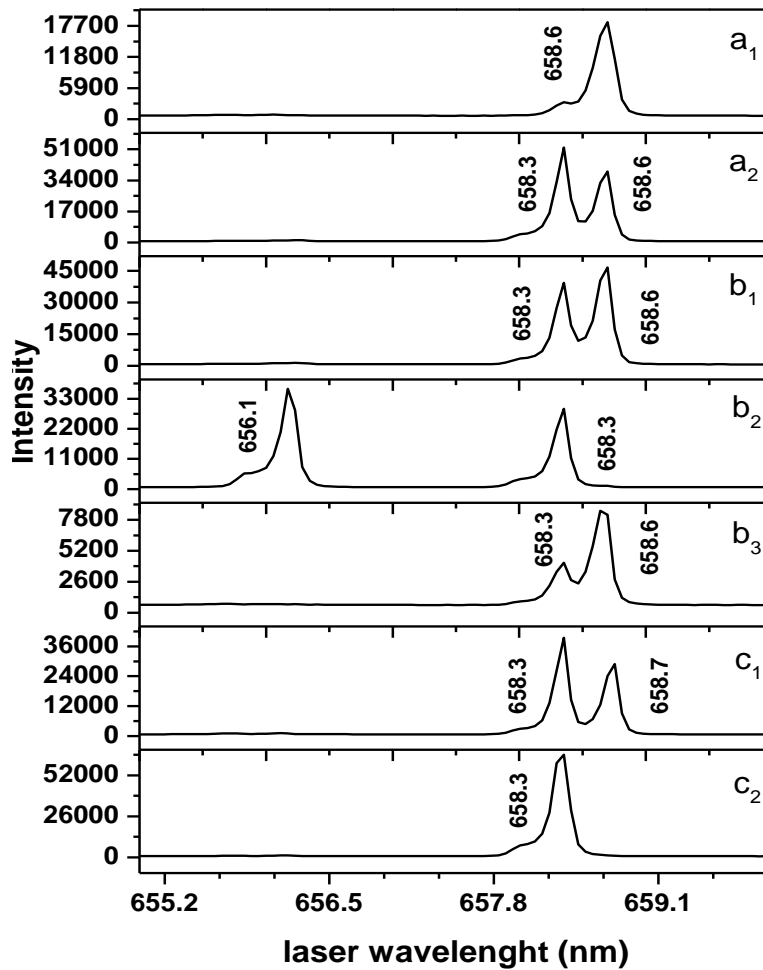
Figure 2.7. Variation in the Raman excitation laser wavelength with: temperatures a_1) 22 °C, a_2) 37 °C, direction of the Raman illumination optical fibre at different angles b_1) 0, b_2) 30, b_3) 45 degrees, c_1) applying stress (by hand) on the Raman illumination optical fibre, c_2) the Raman illumination optical fibre without stress.

Laser wavelength instability was shown to be not only related to temperature change but also with an exact path followed by the light in the Raman illumination optical fibre. The wavelength of Raman excitation laser was different between the edges and core of the optical fibre, (Fig. 2.10). Changes in laser wavelength were also caused by applying stress to the Raman illumination optical fibre. When the instability of the laser wavelength was proved, detailed step by step analyses of the causes of this instability were considered. The goal was to find practical solutions to overcome to the laser instability.

The following solutions were evaluated to minimise the effect of the ambient temperature:

i) lab temperature control

In an attempt to overcome some of the wavelength instability, a first approach was made to insulate the laser diode with thermoplastic elastomeric foam of 20 mm thickness in the

laminar flow cabin. Nevertheless, the laser wavelength remained unstable. The record of the ambient temperature in the lab and flow cabin where the laser was operated shows over 3.5 degree variations with ~ 4 hours intervals (Fig. 2.8, a). The air conditioning was designed to provide a temperature stability of ± 1 °C per hour. Examination of the design showed that the system was cooling too vigorously and it had a poor thermal regulation. After extensive testing and several consultations with the service company the implemented solution was to reduce the amount of water to the heat exchanger and to permanently activate the circulation fan that would then circulate on low power. This helped maintaining lab temperature to within ± 1 °C of the desired value. The optimal temperature range to provide a stable wavelength is between 16 and 24°C, based on studies by Cosine and Monocrom (Fig. 2.8, b). Temperatures higher than 24 °C are expected to cause laser instability and a significant change in laser wavelength. Therefore, lab temperature was fixed at 20 °C. All in all, the Raman laser wavelength was still unstable.
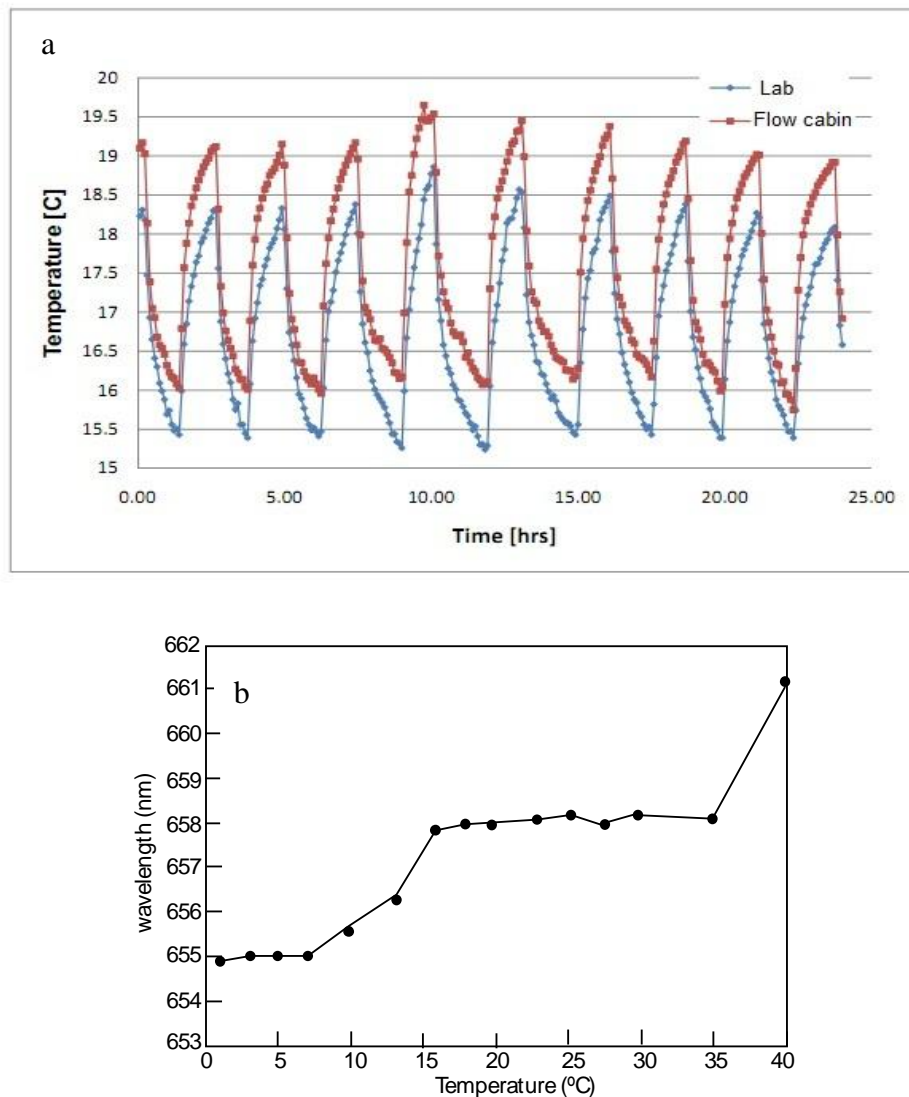
Figure 2.8. a) Temperature variation in the lab and flow cabin over one day prior to the renovation of the air conditioning system. Instability in temperature resulted in laser wavelength instability, b) Output wavelength of the Raman laser package as a function of temperature. The measurements were performed at the Monocrom Company in Spain.

ii) laser diode with heat sink

The ambient temperature around the Raman laser diode and the temperature of the laser diode were monitored with two handheld thermocouples. This showed a 5 degree difference between ambient temperature and local temperature of the Raman laser diode. The power of the Raman laser diode (20 mW) was sufficient to raise the local temperature in the device's environment. This could potentially lead to an unstable wavelength. To improve the cooling of the diode, an aluminium block was added to act as a thermal sink. This block had a size of 100 x 80 x 30 mm. The aluminium block was screwed to the gold-plated copper block at the base of the Raman laser diode (Fig. 2.9).
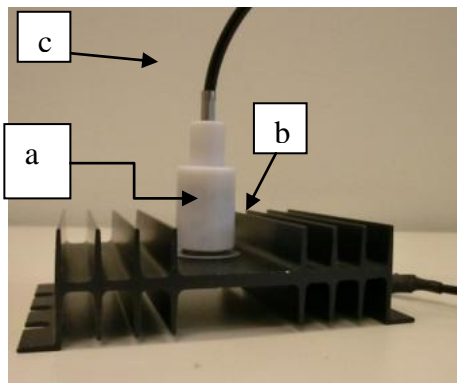
Figure 2.9. a) Raman laser diode attached from one side to b) aluminium heat sink and c) the Raman illumination optical fibre.

This aluminium thermal block was designed to have a large surface area (see Fig 2.9) and a consequently better thermal cooling capacity. As a result, the Raman laser diode could exchange heat more efficient with its environment and the Raman laser wavelength could be stable.

Finally to overcome the potential instability of the laser wavelength caused by changes in the stress on the optical fibre, the optical fibre was placed in a fixed position, carefully handled and protected to prevent the laser instability.
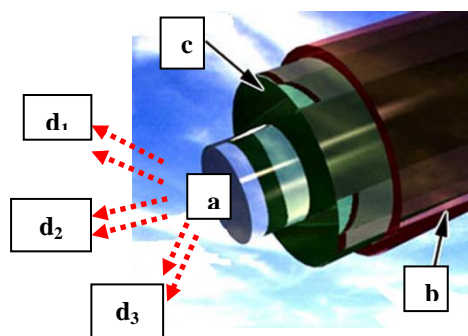

Figure 2.10. An optical fibre consists of: a) Core: The core of a conventional optical fibre is a cylinder of glass or plastic that runs along the fibre's length. b) Cladding: a medium with a lower index of refraction, which surrounds the core, c) Buffer: Protects cladding from moisture and physical damage. Raman laser excitation beam may have different wavelengths (d_1, d_2, d_3) in the centre and on the edges of the core in the Raman illumination optical fibre.

Raman spectra were only obtained when room temperature was around 20 °C, the Raman illumination optical fibre was fixed and there were no pressure on it. These actions improved the laser stability but the current design means that the RLS remains highly sensitive to very minor changes in the local environment and is impractical for use as a portable instrument.

2.4.1.2   LIBS laser source

The selected laser source for the LIBS system in the RLS instrument was a neodymium-doped yttrium aluminium garnet (Nd:YAG) solid state laser with 1064 nmwavelength. This laser is a reliable and convenient source for powerful pulse generation needed to produce a plasma under Martian conditions (Escudero-Sanz et al., 2008).

2.4.2 Optical head

As a final stage in the design of the RLS instrument a functional optical head was designed and manufactured by TNO. This optical head has a diameter of 300 mm and height of 300 mm (Fig. 2.11). The optical head included lenses (to parallelise and to focus light), parabolic metal mirrors to reflect light, optical fibres for light transfer and filters for Raman spectroscopy (a notch filter and a band-pass filter).

The first objective of the optical head was to direct laser light from either the Raman or LIBS laser to a sample to create Raman scattering or a plasma. The second objective was to catch Raman scattering or light from the plasma and direct it to the RLS spectrometer. Therefore, the optical head has effectively two sample illumination channels and two optical viewing channels linked to respectively the LIBS/ Raman lasers (Fig. 2.11). To obtain sensitive detection levels, efficient light transmission is required across a wide spectral range. The required transmission spectral ranges are given in Table 2.1.

Channel no.	Channel description	Spectral range (nm)
1	Raman viewing	669 to 840
2	Raman illumination	659
3	LIBS viewing	240 to 840
4	LIBS illumination	1064

Table 2.1. Spectral coverage required for the optical head.

When laser light is directed at the sample with an optical fibre, it is critical to remove the Raman peaks and fluorescence that are excited in the optical fibre by the laser. Band pass filters are designed to transmit light with a limited range of wavelengths, typically 1– 10 nm. This is an effective way to ensure that the lasers light is not contaminated by secondary

wavelengths inherited from optical fibres, mirrors, prisms etc. Notch filters are used in the opposite way to suppress the laser wavelength; i.e., Rayleigh scattered light derived from the laser light. The use of the notch filter is vital since the Raman effect is very weak (Escudero-Sanz et al., 2008).

In the sketch of the optical head, Fig. 2.11, the optical paths in red colour indicate the directionof the Raman excitation laser light to a sample and the direction of Raman emission from sample to the spectrometer (Fig. 2.11). In detailed the optical path is as follows:

a) The Raman laser light is first parallelised by a convex lens at the output of the Raman illumination optical fibre.
b) The Raman laser light is filtered by a band pass filter.
c) The parallel Raman laser light is reflected from a notch filter to a mirror.
d) The reflected Raman laser light is focussed onto a sample surface via a convex lens.
e) The Raman scattered light generated by the sample is parallelised by a convex lens.
f) The Raman emission light is reflected by a mirror to the notch filter where the Raman emission is transmitted through the notch filter while the elastically scattered light is blocked by the notch filter.
g) The light is focussed into an optical fibre via a convex lens and continues to the spectrometer.
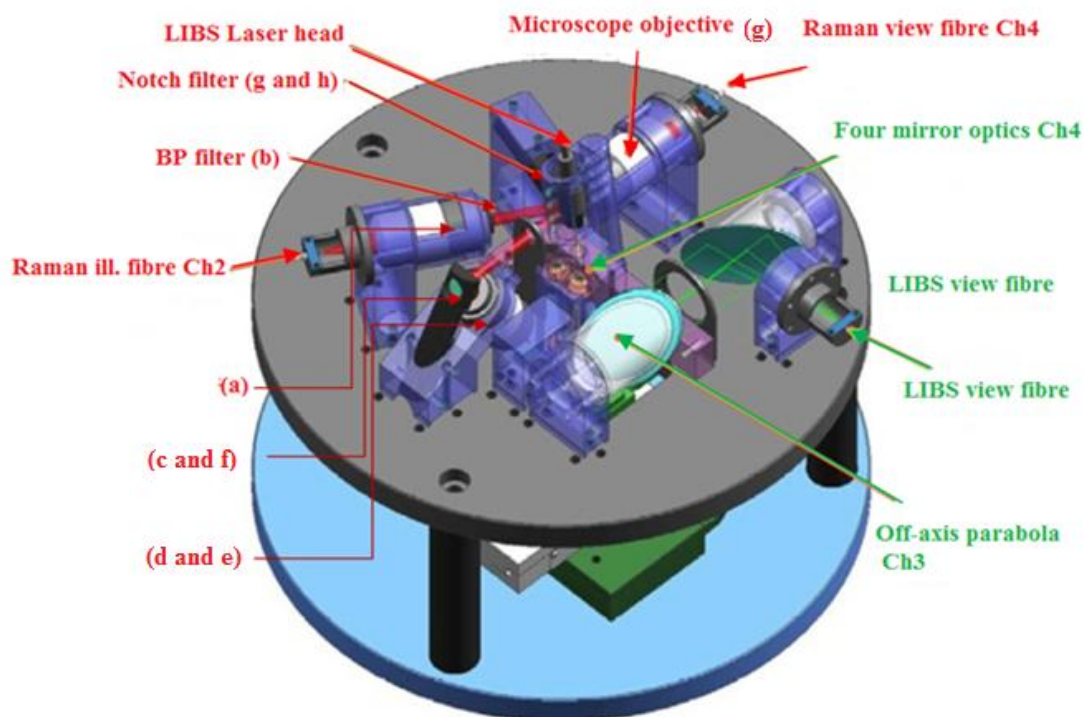
Figure 2.11. The mechanical design of the optical head. The optical head consists of four different optical channels/ pathways for illumination and detection. The optical head collects Raman scattered light (red optical paths) and light from the plasma (green optical path). There are two illumination and two detection channels for both Raman and LIBS techniques. (Abbreviation of "ill" refers to illumination).

In Fig 2.11 the paths in green colour indicate the direction of the LIBS laser light to a sample and the light of the plasma to the spectrometer. The LIBS laser light is first reflected from

several mirrors and then arrives at a sample. When the light from plasma is emitted in all directions, a concave lens focuses a portion of the light emitted from the plasma to a convex mirror. Finally, the light from plasma is reflected by several flat and convex mirrors to reach the LIBS viewing optical fibre and thereby on to the spectrometer.

Due to the LIBS technique producing a plasma, it is vital that the optics are protected from the deposition of ablated sample material. Therefore, the sample is maintained at a minimum distance of 50 mm from the optics to reduce as much as possible fouling of the optics.

2.4.3   Spectrometer

The most challenging requirement in the design of RLS instrument was maintaining a small volume and low mass that was robust enough to be capable of operating under Martian conditions (Fig. 2.12). The RLS spectrometer is compact (190 x 150 x 190 mm) and weighs less than 850 g (Courr`eges-Lacoste et al., 2007). It contains the prism, grating, lenses, mirrors and a CCD detector.
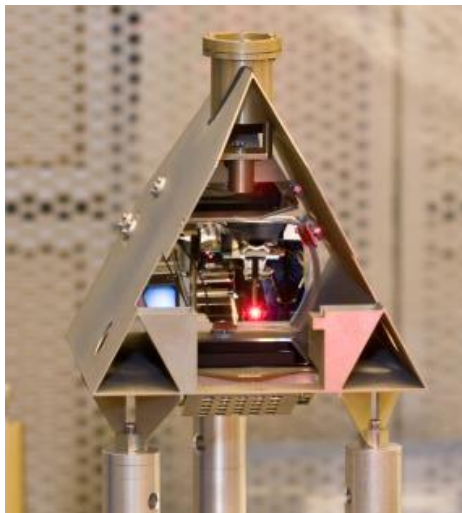
Figure 2.12. The RLS spectrometer is compact (190 x 150 x 190 mm).

The RLS spectrometer uses a prism to disperse the light.Dispersion is the phenomenon by which a spectrum of light is separated vertically by wavelengths. The dispersion of light reaches a grating where it diffracts light into several waves travelling in different directions. Figure 2.13 (a) shows the easiest method to explain the function of a reflection grating. This figure shows a light ray of wavelength λ incident at an angle α and diffracted by a grating (of groove spacing d) along angles β_m. These angles are measured relative to the "grating normal" (Fig. 2.13a), which is the plane perpendicular to the grating surface at its centre (dashed line in the figure). In a reflection grating, the angles $\alpha > 0$ and $\beta_1 > 0$ (as they are measured counterclockwise from the grating normal) whereas the angles $\beta_0 < 0$ and $\beta_{-1} < 0$ as they are measured clockwise from the grating normal (Fig 2.13a). Another figure of grating diffraction, using wavefronts (surfaces of constant phase), is shown in Fig. 2.13 (b). The geometrical path difference between light from adjacent grooves is $d \sin\alpha + d \sin\beta$. (Since $\beta <$

0, the latter term is actually negative). If this difference equals the wavelength λ of the light (or some multiple integral thereof), the light from adjacent grooves will be in phase (leading to constructive interference). At all other angles of β, there will be some measure of destructive interference between the wavelets originating from the groove surfaces. These relations are shown by the grating equation $m\lambda = d\,(\sin\alpha + \sin\beta)$. Here m is the diffraction order, which is an integer.
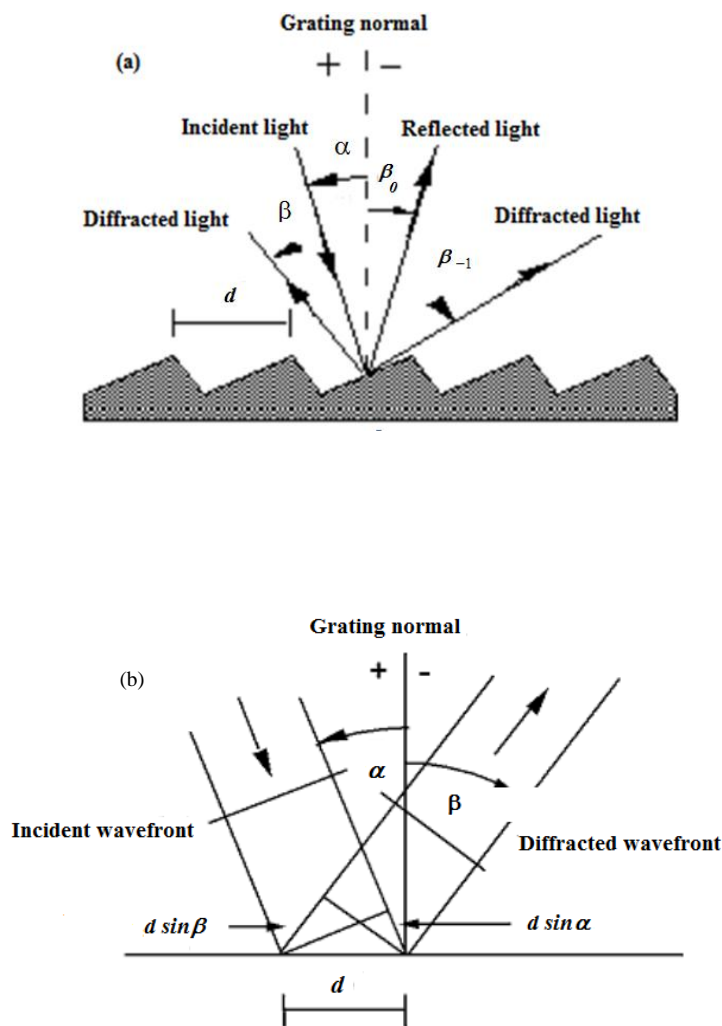
Figure 2.13. a) Diffraction by a plane grating. A beam of monochromatic light of wavelength λ is incident on a grating and diffracted along several discrete paths, b) Geometry of diffraction, for planar wavefronts (modified after http://gratings.newport.com/library/handbook/chapter2.asp).

In RLS instrument, Raman peaks appear in the third order, from 660 to 840 nm. The LIBS signals appear on the orders in the region from 240 to 630 nm. Table 2.2 shows the specific ranges of each order.

Diffraction order	Wavelength range on detector (nm)
1	1950 to 2520 (CCD not sensitive)
2	975 to 1260 (CCD sensitive to 1100, visibility of LIBS laser)
3	650 to 840 (Raman shift detection)
4	504 to 630
5	406 to 504
6	345 to 406
7	300 to 345
8	265 to 300
9	240 to 265
10	195 to 252
11	177 to 229

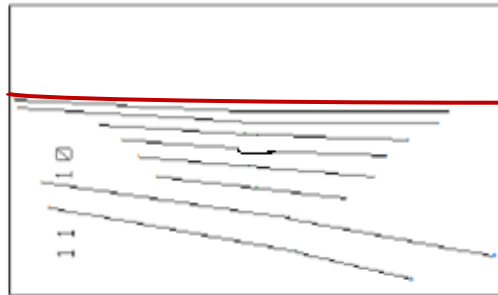Table 2.2. Wavelength ranges of diffraction orders as shown on the detector (the CCD is sensitive to order 9).

Figure 2.14. Diffraction orders imaged on the detector, the 3th order is shown in red colour and 10th and 11th are the last orders from bottom.

Detector

A charge-coupled device (CCD) is used to transform light (Raman scattered light or the light from the plasma) into an electrical signal. The selected CCD for RLS instrument is a back-illuminated device with 2048 x 2048 pixels that are 13.5 μm square (Fig. 2.15). The CCD has a UV coating in order to increase the quantum efficiency (QE) in UV region. The quantum efficiency is the percentage of photons hitting the CCD surface.
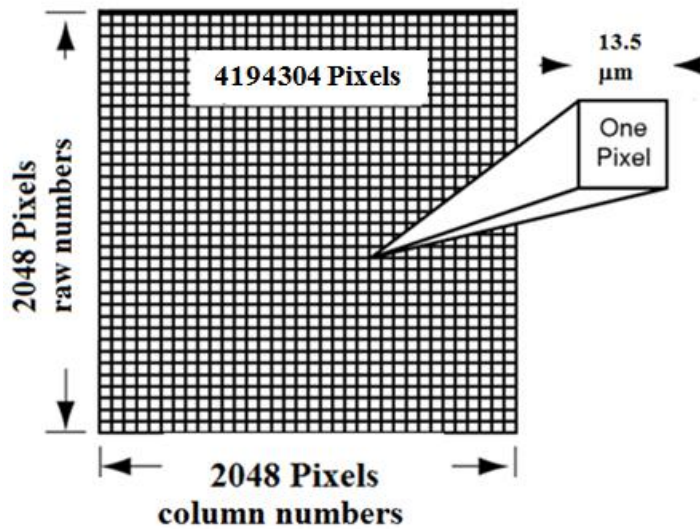
Figure 2.15. The basic design of a charge-coupled device (CCD) detector.

Minimisation of noise is one of the most important qualities required for a detector. Noise is an unwanted signal, either present in the relevant light signal or produced by the imaging process. It leads to inaccurate measurements of the light signal distribution (image). Noise usually comes from three main sources:

a) Photon or shot noise: The random arrival of photons on a CCD cause shot noise. Since each photon is an independent event, the arrival of any given photon cannot be accurately predicted. Instead the probability of its arrival in a given time period is described by a Poisson distribution. Shot noise can be reduced by obtaining spectra with longer acquisition times effectively averaging out the random noise or by combining multiple frames again averaging the background.

b) Thermal noise (dark noise): Additional electrons are generated within the CCD not by the absorption of photons (signal) but by physical processes within the CCD itself. The number of electrons generated per second by the CCD itself will depend on the operating temperature of the CCD. This noise is known as thermal noise (dark noise). The amount of dark noise decreases by a factor of two for every 7 or 8 $^{\circ}$C drop in temperature (Denson et al., 2007). CCDs are cooled by either Peltier systems down to -100 $^{\circ}$C (it is common to be -70 $^{\circ}$C) or by liquid nitrogen down to -140 $^{\circ}$C.

c) The CCD reads each pixel through an amplifier. Noise is also generated during the conversion of the electric charge into a voltage signal. This noise increases proportionally with the number of readings.

Consequently to obtain the best possible results the CCD temperature of the RLS instrument had to be as low as possible to reduce thermal noise. A cooling system was designed, developed and tested during this research process to help reduce thermal noise. Details of the water cooled Peltier system are discussed in chapter three.

The CCD was connected to an electronic box. The electronic box provided the bias voltages and timing signals required to operate the CCD. The raw CCD images were taken using

dedicated software written by colleagues from the University of Leicester (such as a raw image in Fig 2.18) and they were stored on a dedicated PC. The raw CCD images were then processed by in-house software (programmed by Dr. Aurelia Colin, Vrije University Amsterdam) to produce data such as Raman wavelength shifts and their intensities. Finally, Raman spectra were processed and spectra were obtained via the Origin program. The identification of the peak positions in the Origin program was done using Gaussian fitting, Fig. 2.16.
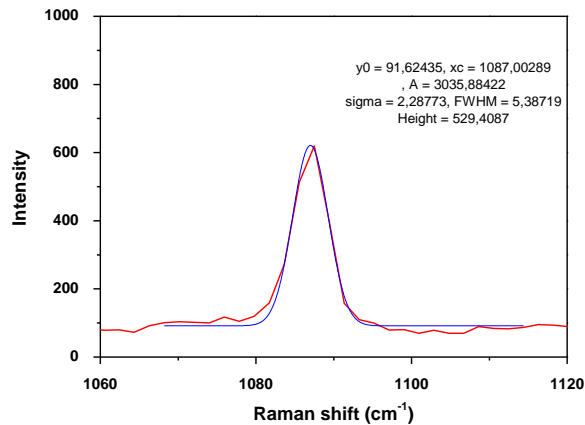
Figure 2.16. RLS calcite Raman spectrum, peak at 1087 cm^{-1} was determined using Gaussian fitting with Origin program.For each Gaussian peak, the parameter table shows y_0, x_c, A and w, which means: y_0 is base, x_c is the position of the centre of the peak, A is area andFWHM is full width at half maximum.

Figure 2.17 shows an example of a peak fitted with a Gaussian function:

$$y = y_0 + \frac{A e^{\frac{-4\ln(2)(x-x_c)^2}{w^2}}}{w\sqrt{\frac{\pi}{4\ln(2)}}} \qquad (2.7)$$
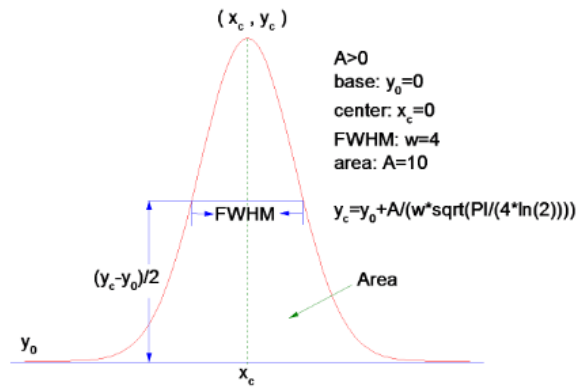
Figure 2.17. An example of a calculated peak using the Gaussian function. For each Gaussian peak, the parameter table shows y_0, x_c, A and w, where: y_0 is base, x_c is the position of the centre of the peak, A is area and w is FWHM.

2.5   Characteristics of the RLS instrument

As the RLS instrument is designed to operate under Martian conditions, the stability of the instrument needed to be validated at various temperatures. Consequently, a series of experiments were carried out at different temperatures to determine the performance of the RLS spectrometer.

2.5.1   Instrument resolution

One of the most important characteristic of a spectrometer is the spectral resolution. The spectral resolution of the spectrometer provides the ability to separate two peaks. It resolves two non-coherent radiations with the same intensity and full width at half maximum (FWHM), at λ and $\lambda + \Delta\lambda$ respectively, when the distance between their centres are equal or greater than their FWHM. The resolution of a spectrometer depends on the number of grooves in the gating, focal length of the spectrometer, size of the individual pixels in the CCD, size of the slit and the light wavelength. The spectral resolution is usually determined by measuring the FWHW of an emission line of a calibration lamp.

The spectral resolution of the RLS spectrometer was determined by measuring the FWHM of an emission peak of a mercury lamp. A mercury lamp was used to illuminate the spectrometer. One of the sharp peaks of the mercury spectrum was selected for calculating the FWHM.

The Origin program, which analyse the peaks of the RLS Raman spectra, was used to calculate the FWHM of the sharp peak of the mercury spectrum. The Gaussian function was selected in the Origin programme to fit a Gaussian curve to the intensive peak of mercury lamp and then calculate the FWHM of the fitted peak.

The spectral resolution was determined to be ~ 0.2 nm (~ 4 cm^{-1}). When the resolution of RLS instrument is 0.2 nm, it means that RLS instrument is capable of distinguishing adjacent Raman peaks separated by more than 0.2 nm.

2.5.2 Calibration of the CCD at different temperatures

To determine if the spectrometer will function under variable Martian conditions where daily temperatures may vary by several tens of degrees a major effort was spent in determining if Raman spectrum drifts with temperature. In this section the calibration procedure for the 3rd order is described in detail. This is where Raman Stockes vibration modes are detected with respect to the ~ 659 nm red excitation laser light. The calibration was performed in two steps:

- First the position of the different orders on the CCD is determined
- Second, for each order a correspondence between the column number of the pixels in the CCD image and the associated wavelength is determined.

2.5.2.1 White light to determine position of the third order

White light is the combination of all the colours of the visible light spectrum and includes the wavelength of the 3rd order (from 640 to 840 nm). Therefore, the RLS instrument was illuminated with white light in order to determine the position of the 3rd order in the CCD image. Figure 2.18 is an image of the CCD illuminated by white light. In the figures a series of light gray spots (pixels) create lines to form the different diffracted orders.
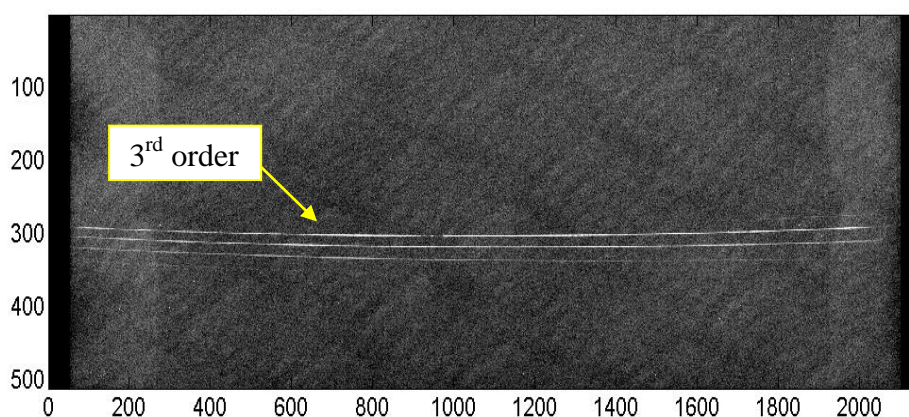

Figure 2.18. An image of the CCD, illuminated by white light. The almost complete orders that are visible in this image are the 3rd, 4th and the 5th orders with part of the second order visible on the right and sixth order on the left.

An in-house software programme was built to evaluate the CCD output (Dr. Aurelia Colin, Vrije University Amsterdam). This programme modelled the position of the orders and gave the user the ability to choose selected pixels on the CCD image to define a specific order.

The software records the position of these pixels (x is the column number of the CCD; y is the raw number of the CCD). In Fig. 2.19 the third order is shown. After the initial selection of pixels the software makes a polynomial regression fit to the data to define the 3rd order. At this stage the user zooms in on the image and refines the selected data points to optimise the curve fitting.

The software averages the light level of an individual pixels by including pixels above and below in the Y direction. Therefore, if there was a shift in the calibration in the Y direction of one pixel or less it would not affect the position of the final calibration spectrum. The user can check the accuracy of the fit and if required make manual adjustment to optimise the fit. The position of the line is reproducible to less than one pixel of difference over the period of the study at a specific temperature.
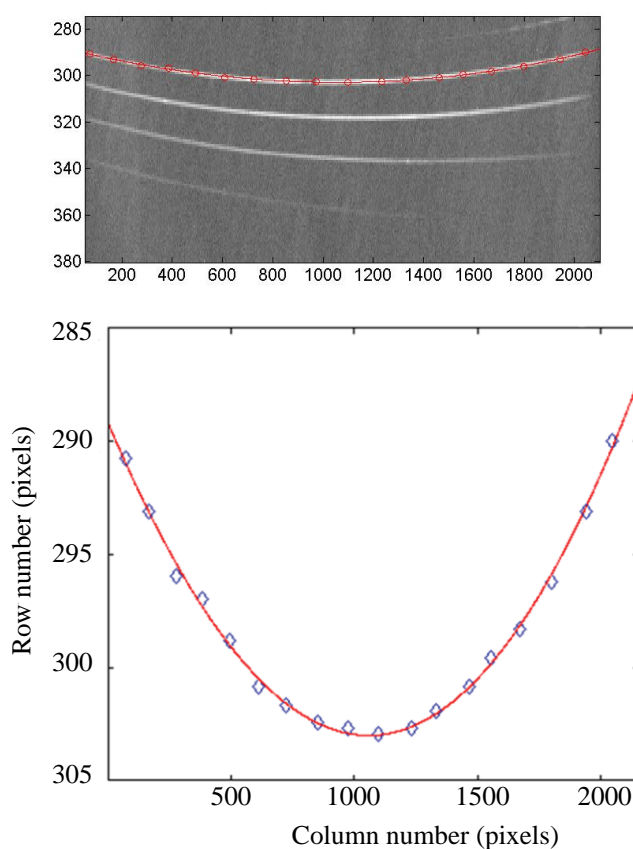
Figure 2.19. A 3rd order polynomial fit for the 3rd order of the spectrum over the wavelength 640 to 840 nm.

Figure 2.20 illustrates the position of the 3rd order on the CCD at 10, -5 and -20 °C. The position of these smoothed curves shifted along the vertical axes depending on the temperature of the RLS instrument. Significantly there was no resolvable variation of wavelength along the x axis. The total change in the Y axis was ~ 3 pixels (40 μm) over the 30 °C range. Note that the temperature of the CCD itself was kept between ~ -30 and -40 °C (depending on the temperature of the analytical chamber). Studies that involved varying the temperature of the CCD did not influence the position of the 3rd order. We therefore ascribe the shift in the Y axis in Fig. 2.20 to changing performance of the optics in the spectrometer,

most likely the prism, which diffracts the light in y-direction in the RLS spectrometer. The optical properties of the prism made of glass potentially depended on temperature. In addition, despite the design considerations and robust manufacture the position of the prism and its distance from CCD could change due to thermal contraction associated with lower temperatures. We recommend that the instrument designers (TNO) conduct a more thorough thermal analysis of the spectrometer to ascertain in detail the origin of the minor temperature induced spectral offsets so that designs of spectrometers for future missions that may be subjected to more extreme temperature conditions can be optimised. In conclusion, although the prism in the RLS instrument appears to cause minor variations in the position of the spectrum under varying thermal conditions, the offset is only in the Y direction and consequently does not affect calibrations of Raman spectra. As such the instrument is functional for the study of minerals under Martian conditions.
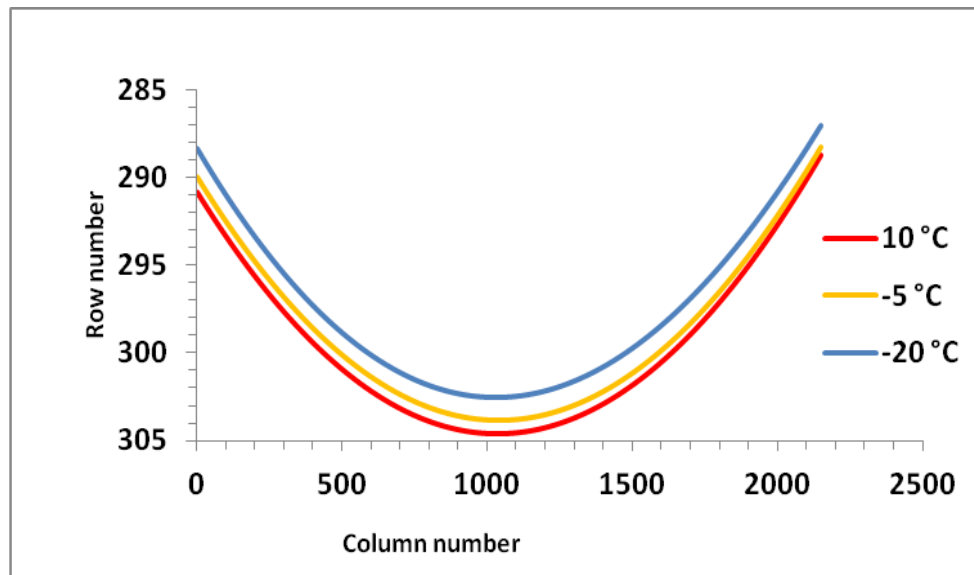
Figure 2.20. The position of the 3rd order on the CCD at 10, 5 and -20 °C.

2.5.2.2   *Calibration of the CCD column number to wavelength*

When the position of the 3rd order had been set for each temperature, the spectrum was calibrated for wavelength (x direction on the CCD). For this step, argon and neon lamps were used. These lamps produce narrow, intense peaks between 660 and 840 nm with known wavelengths.

Using the in-house software, the calibration peaks were identified and fitted individually using the Gaussian function, thereby determining the centre of the peak. The software allowed the user to ascribe the column number of the centre of the different peaks to

knownwavelengths from the literature. The software calculated a 3rd order polynomial adjustment to fit wavelength as a function of the column number. In case of mistakes in ascribing peaks, the user had the possibility to modify the calibration or to add more peaks with another lamp. An example of a calibration adjustment is shown Fig. 2.21. As discussed above the calibration procedure showed variation with temperature but only in the y-direction. Column numbers were always within error, irrespective of temperature (the difference between theoretical fit value and calibration lamp value) (Fig. 2.22). This means that the position of the peaks only shifts significantly in the y-direction. Figure 2.22b establishes that the differences between the calibrations at different temperatures are always less than 0.2 nm. However, on average there is a positive offset of ~ 0.1 nm for the -20 ^{o}C data. This difference is within our resolution capabilities but suggests that if the CCD is operated at even lower temperatures a specific calibration may be required.
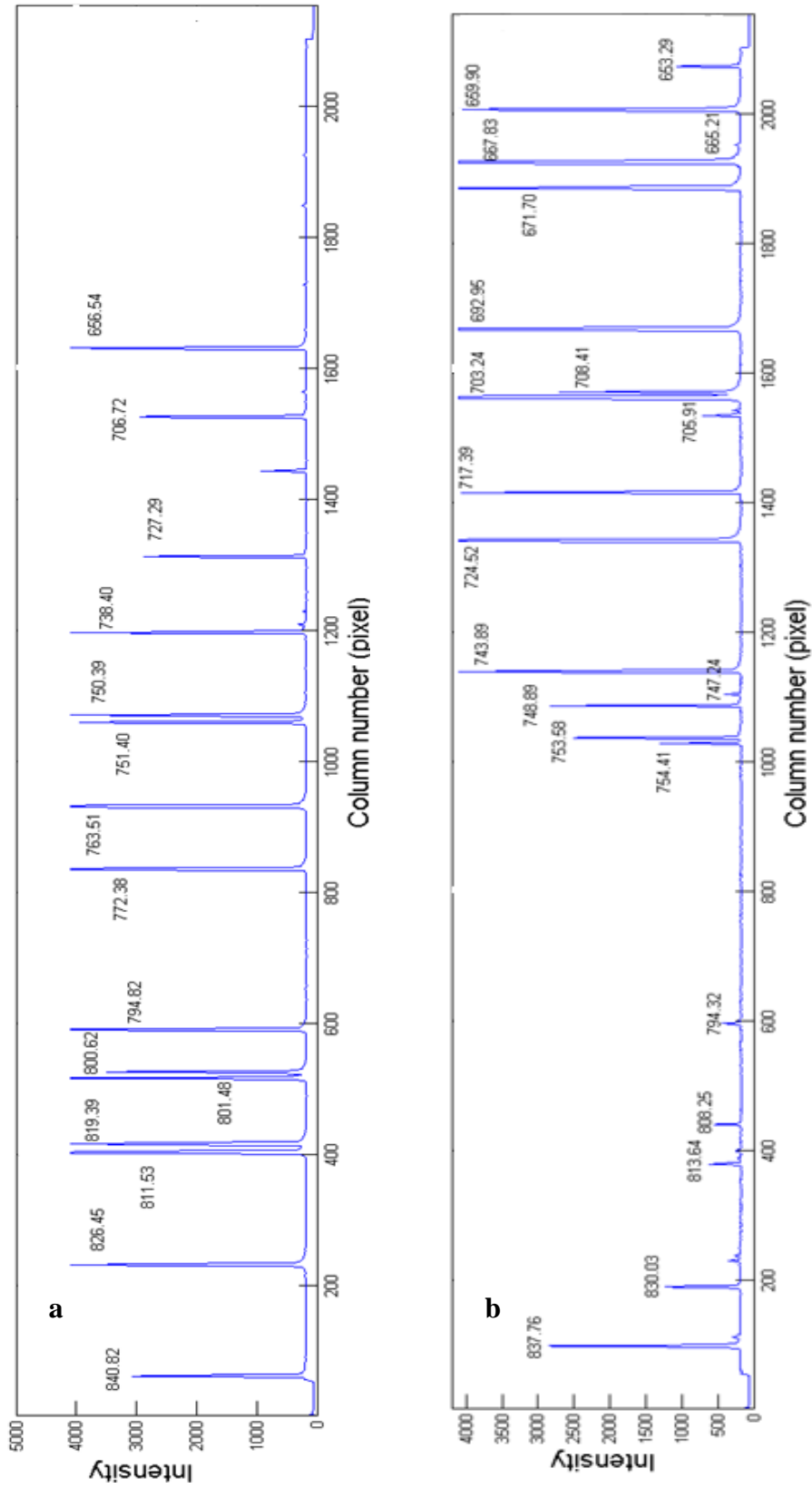
Figure 2.21. RLS spectra of a) argon, b) neon calibration lamps and peak wavelength of the identified peaks from the literature.
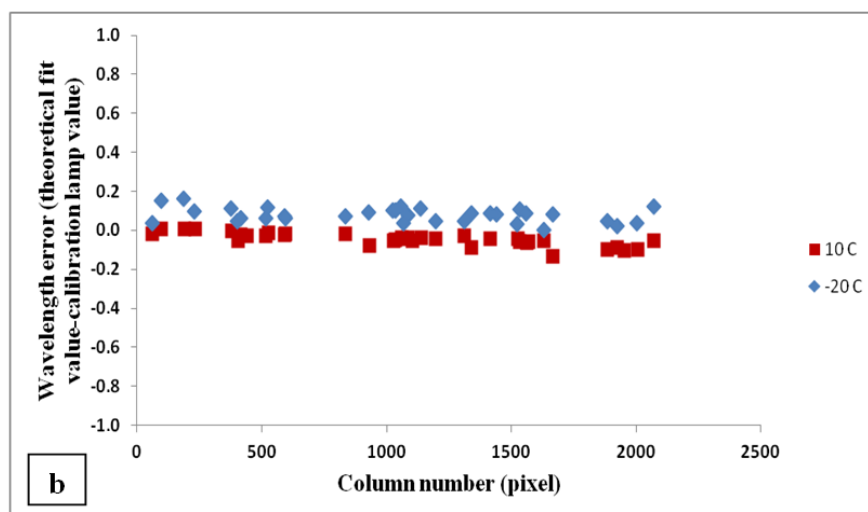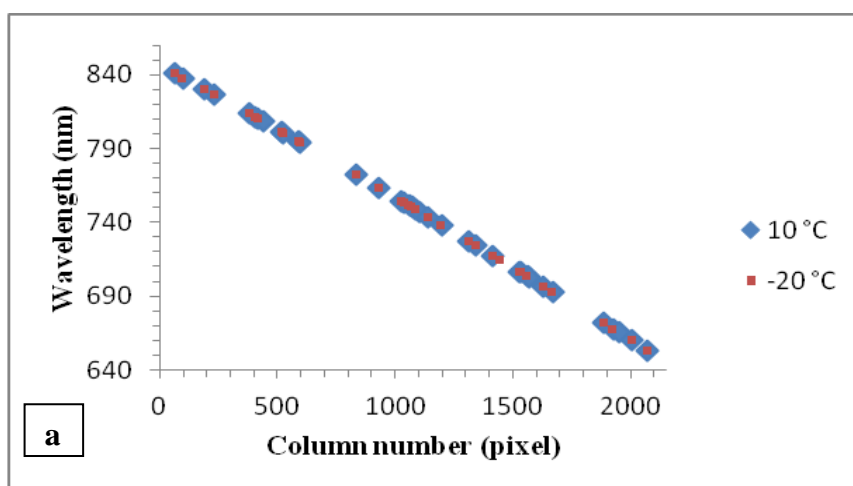
Figure 2.22. a) CCD column plotted against wavelength at 10 and -20 °C, note there is no significant change in the calibration with temperature, b) CCD column plotted against difference from theoretical fit of the curve. The difference between the calibrations is always less than 0.2 nm.

2.5.2.3 Accuracy of Raman shift values

The observed error of the CCD calibration is presented in Table 2.3.

The errors were calculated based on the difference between literature values (literature values after Newport company: http://www.newport.com/Pencil-Style-Calibration-Lamps/377846/1033/info.aspx) and the value calculated from the calibration. The root-mean-square error (RMSE) of the individual errors associated with the calibration lamp peaks was calculated. An error of ~ 0.02 nm or 0.4 cm^{-1} was obtained.

Wavelength literature (nm)	Wavelength calculated from calibration (nm)	Difference (nm)
840.82	840.81	-0.01
826.45	826.46	0.01
811.53	811.50	-0.03
810.37	810.37	0.00
801.48	801.48	0.00
800.62	800.63	0.01
794.82	794.82	0.00
772.38	772.40	0.02
763.51	763.47	-0.04
751.46	751.47	0.01
750.39	750.39	0.00
738.4	738.41	0.01
727.29	727.32	0.03
706.72	706.74	0.02
696.54	696.56	0.02
837.76	837.77	0.01
830.03	830.04	0.01
813.64	813.65	0.01
808.25	808.24	-0.01
794.32	794.33	0.01
754.41	754.40	-0.01
753.58	753.58	0.00
748.89	748.90	0.01
747.24	747.23	-0.01
743.89	743.90	0.01

724.52	724.49	-0.03
717.39	717.41	0.02
705.91	705.92	0.01
703.24	703.24	0.00
702.41	702.42	0.01
692.95	692.89	-0.06
671.7	671.68	-0.02
667.83	667.83	0.00
665.21	665.19	-0.02
659.9	659.89	-0.01
653.29	653.33	0.04
Root-mean-square error		**0.02 nm**

Table 2.3. The observed error of the CCD calibration procedure.

To assess the realistic level of error during Raman analysis multiple analyses were undertaken. This was initially carried out on a commercial Renishaw InVia Reflex confocal Raman microscope. This commercial spectroscope uses a 785 nm diode laser as excitation source. The spectral resolution of adjacent peaks in the system is ~ 3 cm^{-1} and the accuracy of the system is about 0.1 cm^{-1} (according to the specifications provided by Renishaw). Fig 2.2 is an example of a calcite Raman spectrum taken via Renishaw InVia Reflex confocal Raman microscope.

The Raman spectrum of a calcite sample was determined ten times over a period of a day to calculate the standard deviation in the Renishaw measurements, Table 2.4. Raman peak positions determined for the 1086 cm^{-1}, has a standard deviation of 0.04 cm^{-1} using the Origin program to fit the peaks (Gaussian).

Analysis number	Wavelength (cm^{-1})
Measurement 1	1086.29
Measurement 2	1086.25
Measurement 3	1086.24
Measurement 4	1086.25
Measurement 5	1086.29
Measurement 6	1086.37
Measurement 7	1086.34
Measurement 8	1086.33
Measurement 9	1086.34
Measurement 10	1086.29
Average	**1086.30**
2Sigma	**0.08**

Table 2.4. The Renishaw Raman calcite peak determined ten times on the same spot over a period of a day to calculate the error in the Renishaw measurements.

The same method was subsequently applied to a calcite sample using the RLS instrument. The measurements show that the software can fit the data within an error of ~ 0.02 nm or 0.5 cm^{-1}, Table 2.5. However, we consider this an unrepresentative experiment of the instrument capability due to the instability of the laser. The data in table 2.5 represents the best data from ~ 25 analyses that show the smallest variation in laser wavelength.

Analysis number	Wavelength (cm^{-1})
Measurement 1	1087.00
Measurement 2	1087.21
Measurement 3	1086.80
Measurement 4	1087.01
Measurement 5	1087.10
Measurement 6	1087.00
Measurement 7	1087.34
Measurement 8	1087.60
Average	**1087.14**
2Sigma	**0.48**

Table 2.5. The RLS Raman calcite peak (on a same spot) was determined eight times over a period of a day to calculate the error in the RLS measurements.

This accuracy is four times worse that the commercial Renishaw InVia Reflex confocal Raman microscope. However, based on the determination of the calibration lamps we are certain that with a stable laser the accuracy of the system would be better than 0.4 cm^{-1}. For the application of Mars missions this accuracy is suitable to achieve the main objectives we listed in chapter 1. For instance, it is enough to distinguish between calcite and aragonite v_4 asymmetric bending vibration mode at 711.5 and 703.5 cm^{-1} respectively.

2.5.3   CCD noise and the detection limit of Raman signals

In addition to the reproducibility of the instrument, an important aspect of the practical operation of the RLS instrument is the ability to detect and fit Raman peaks to the measured data. Above we examined the ability to fit large Raman peaks with reproducibility. An additional important question is the ability of the methodology to detect individual low amplitude Raman peaks. In this respect the signal to noise ratio is a key aspect.

Signal to noise ratio (SNR) is a measure of signal strength relative to background noise. Noise is the unwanted electrical or electromagnetic energy that is detected within the instrument and potentially degrades the quality of peaks. The signal to noise ratio will vary mainly dependent on the thermal design of the instrument and also the ambient thermal conditions. Commonly agreed threshold suggests that SNR lower than 3 makes Raman peaks hard to detect. Hence the operational temperature of the CCD is a key aspect of how well instrument functions.

$$\frac{S}{N} = \frac{\text{Mean}}{\text{Noise}} = \frac{\bar{x}}{\sigma} \qquad (2.8)$$

Under Martian conditions temperature fluctuations will affect the noise level in Raman spectra. Therefore noise (σ) was calculated at two different temperatures (-30 and -40 °C). σ is equal to the standard deviation of the baseline noise intensity in the random region divided by $\sqrt{2}$.

$$\sigma = \text{STDEV}/\sqrt{2} \qquad (2.9)$$

When operating the CCD at temperatures ~ -30 and -40 °C, noise values were ~ 5 and 3 respectively (Figs. 2.23 and 2.24). This means that, when the CCD is operated at ~ -40 °C, the peak detection limit is about two times better than the peak detection limit of CCD operated at -30 °C.

Due to the direct temperature dependency of CCD noise, the spectrometer does not operate at high efficiency when the CCD temperature is higher than -30 °C. With the presence of CO_2 at 8 and -8 °C inside the experimental chamber, the CCD could not reach -30 °C (respectively -17 and -25°C, cf. chapter 3). These conditions are a limitation to the study of the influence of Martian conditions on small peaks in individual Raman spectra. In the following chapters, under CO_2 atmosphere, only data obtained with the atmosphere at -20 °C are presented, i.e., when CCD temperature reaches -34°C.

Previous theoretical studies have emphasised that operating CCD at the lowest possible temperature improves signal to noise ratio (Chadwick and Cooper, 2012) and our practical experiences emphasises this conclusion. Given the outcome of measurements reported later in the thesis (Chapters four and five) stresses that it is not always possible to obtain strong Raman signals from minerals and that under the practical operational conditions on the

surface of Mars SNR optimisation will be important. Ensuring efficient insulation and cooling of the CCD in the RLS instrument on ExoMars mission is a vital design requirement.
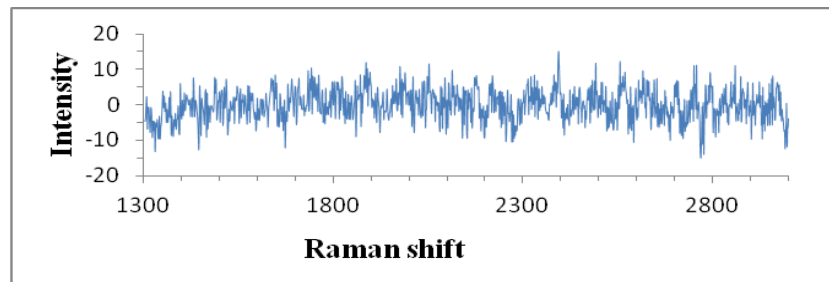

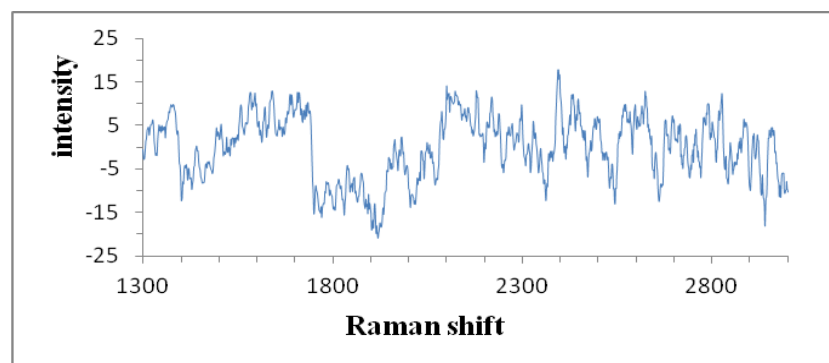Figure 2.23. When CCD was operated at ~ -40 °C, noise was about 3.

Figure 2.24. When CCD was operated at ~ -30 °C, noise was about 5.

2.6   Conclusion

In this chapter, the optical design of the RLS instrument (designed to work under Martian conditions) was compared to the design specifications from TNO. The instrument was intended to become the basis for realizing the instrument flight model for the ESA's ExoMars mission. The RLS instrument is shown to be capable of working under challenging environment conditions such as Mars conditions (8 mbar CO_2 and +10 to -20 °C). The instrument survived repeated cycling of the instrument between ambient terrestrial conditions and Martian conditions without long term changes in the calibration curves of the instrument.

Calibration of the CCD detector at different temperatures showed that the RLS instrument undergoes minor changes. Although, this effect did not change the horizontal position of Raman peaks (wavenumbers), it should be taken into account for the design of the RLS flight mode. Based on the design of the spectrometer we believe that the thermal characteristics of the prism or expansion-contraction of components that effectively change the position of the prism relative to other optical components.

It was established that the largest error in the determination of peak wavelengths during Raman analyses was 0.4 cm^{-1}. The SNR is a vital aspect of the instrument design and more efforts needs to be made in optimising the system. The ability to extract mineral structure information with the RLS instrument is highly correlated to the signal to noise ratio (SNR) of the CCD. The main contributor for the SNR is the temperature of the CCD. When the temperature goes up, the ability to extract mineral information goes down. This research cannot give a final conclusion as to the optimal temperature for the CCD as basic physics suggests that the lower the temperature the better the SNR. Clearly power usage of the cooling Peltier and the thermal environment of the RLS instrument within the instrument package will be a major issue in the overall design to the ExoMars Rover.

2.7   References

Balkanski, M., R. F. Wallis, E. Haro, (1983),Anharmonic effects in light scattering due to optical phonons in silicon, Phys. Rev. B 28, p. 1928–1934.

Bazalgette Courrèges-Lacoste, G., B. Ahlers, F. R. Pérez, (2007), Combined Raman spectrometer/laser-induced breakdown spectrometer for the next ESA mission to Mars, Spectrochimica Acta Part A 68, p. 1023–1028.

Colin A. et al., (2012), Exploring the feasibility of determining soil water contents on the Moon with a combined Raman/LIBS instrument, GeoRaman Xth Meeting, Nancy (France) – poster.

Denson, S. C., C. J. S. Pommier and M. B. Denton, (2007), The impact of array detectors on Raman spectroscopy. Journal of chemical education, Vol. 84, p. 67-74.

Escudero-Sanz , I., B. Ahlers, G. B. Courrèges-Lacoste, (2008), Optical design of a combined Raman–laserinduced-breakdown-spectroscopy instrument for the European Space Agency ExoMars Mission, Optical Engineering 47(3), 033001-1, 033001-11.

G. G. Harrigan, R. Goodacre, (2003), Metabolic Profiling: Its Role in Biomarker Discovery and Gene Function Analysis, Kluwer Academic Publisher, pp 337.

Gillet P. et al., (2000), A thermodynamic model for $MgSiO_3$ perovskite derived from pressure, temperature and volume dependence of the Raman mode frequencies, Physics of the Earth and Planetary Interiors, Vol. 117, Issue 1-4, p. 361-384.

Gillet, P. et al., (1993c), Phase changes and thermodynamic propperties of $CaTiO_3$. Spectroscopic data, vibrational modelling and some insights on the properties of $MgSiO_3$ perovskite. Physics and Chemistry of Minerals, Vol. 20, p. 159-170.

Gillet, P., A. Lecleach and M. Madon, (1990), High-temperature Raman spectroscopy of the SiO_3 and GeO_2 polymorphs: anharmonicity and thermodynamic properties at high-temperature. Journal of Geophysical Research- Solid Earth and Planets, Vol. 95, p. 21635-21655.

Gillet, P., C. Biellmann, B. Reynard and P. McMillan, (1993a), Raman spectroscopic studies of carbonates. Part I: High-pressure and high-temperature behaviour of calcite, magnesite, dolomite, aragonite. Physics and Chemistry of Minerals, Vol. 20, p. 1-18.

Gillet, P., F. Guyot and J.M. Malezieux, (1989), High-pressure and high-temperature Raman spectroscopy of Ca_2GeO_4: some insights on anharmonicity. Physics of the Earth and Planetary Interiors, Vol. 58, p. 141-154.

Gillet, P., F. Guyot and Y. B. Wang, (1996a), Microscopic anharmonicity and equation of sate of MgSiO perovskite. Geophysical Research Latters, Vol. 23, p. 3043-3046.

Gillet, P., I. Daniel and F. Guyot, (1997), Anharmonic properties of Mg_2SiO_4-forsiontc measured from the volume dependence of the Raman spectrum. European Journal of Minerafogy, Vol. 9, p. 255-262.

Harris, R. D., D. A. Cremers, C. Khoo, K. Benelli, (2005), LIBS-based detection of geological samples at low pressures (<0.0001 Torr) for Moon and asteroid exploration. LPSC XXXVI, 1796.

Herzberg, G. (1945), Molecular spectra and molecular structure: Infrared and Raman spectra of polyatomic Molecules, Van Nostrand Reinhold Company, pp. 650.

Knight, A. K., N. L. Scherbarth, D. A. Cremers, M. J. Ferris, (2000), Characterization of laser-induced breakdown spectroscopy (LIBS) for applications to space exploration. Applied Spectroscopy, Vol. 54, p. 331–340.

Lasue, J. et al., (2012), Remote laser induced breakdown spectroscopy (LIBS) for lunar exploration. Journal of Geophysical Research, Vol. 117, Issue E1, CiteID E01002.

Lazic, V. et al., (2007), Laser induced breakdown spectroscopy of soils, rocks and iceat sub-zero temperatures in simulated Martian conditions. Spectrochimica ActaB, Vol. 62, p. 1546-1556.

Lenain, B. et al., (2007), Raman Spectroscopy for Process Control in Chemical and Pharmaceutical Manufacturing, STP Pharma Techniques Pratiques Reglementations Vol. 17, p. 171-174.

Lewis, I. R. and H. Edwards, (2001), Handbook of Raman Spectroscopy: from the research Laboratory to the process Line. Practical Spectroscopy Series, Vol. 28, CRC Press.

Lucazeau, G. (2003), Effect of pressure and temperature on Raman spectra of solids: anharmonicity. Journal of Raman Spectrosc, Vol. 34, p. 478–496.

Mammone, J. F. and S. K. Sharma, (1979), Pressure and temperature dependence of the Raman spectra of rutile structure oxides. Carnegie institution yearbook, Vol. 78, p. 369-373.

McCreery, R. L. (2000), Raman spectroscopy for Chemical Analysis. In: A series of Monographs on Analytical Chemistry and its Applications (J.D. Winefordner, editor), 157. Wiley-Interscience, John Wiley & Sons. Inc.

Nakamoto, K. (1986), Infrared and Raman spectra of inorganic and coor-dination compounds.

Pavlov, S.G., et al,. (2011), Miniaturized laser induced plasma spectrometry for planetary in-situ analysis-the case for Jupiter's moon Europa. Advances in Space Research Vol. 48, p. 764-778.

Raman, C.V. and K.S. Krishnan, (1928), A new type of secondary radiation. Nature, Vol. 121, p. 501-502.

Rauschenbach, I., E. K. Jessberger, S. G. Pavlov, H. W. Hubers, (2010), Miniaturized LIBS for the in-situ analysis of the Martian surface: calibration and quantification. Spectrochimica, Acta B 65, p. 758–768.

Rayleigh, L. (1899), On the transmission of Light through an atmosphere containing small particles in susoension and on the origin of blue sky. Philosophical Magazine Series 5, Vol. 47, p. 375-384.

Reynard. B, G. Montagnac and H. Cardone, (2012), Raman spectroscopy at high pressure and temperature for the study of the Earth's mantle and planetary minerals, EMU Notes in Mineralogy, Vol. 12, chapter 10, p. 367-390.

Rull, F. (2012), The Raman effect and the vibrational dynamics of molecules and solids. In: application of Raman Spectroscopy to Earth Sciences and Cultural Heritage (J. Dubessy, M.-C. Caumon & F. Rull, editors). EMU Notes in Mineralogy, 12, European Mineralogical Union and the Mineralogical Society of Great Britain & Ireland, p. 1-60.

Sallé, B. et al., (2004), Laser-Induced Breakdown Spectroscopy for Mars surface analysis: capabilities at stand-off distances and detection of chlorine and sulphur elements, Spectrochimica Acta Part B: Atomic Spectroscopy 59(9), p. 1413-1422.

Sergey B. M. et al., (1999), A novel laser breakdown spectrometer for environmental monitoring, Proc. SPIE 3855, Air Monitoring and Detection of Chemical and Biological Agents II, 34, doi:10.1117/12.371277.

Smekal, A. (1923), Zur Quantentheorie der Dispersion. Naturwissenschafien, 11, p. 873-875.

Smith, E. and G. Dent, (2005), Modern Raman spectroscopy, a practical approach, John Wiley & Sons Inc, pp 224.

Sobron, P., A. Wang, (2012), A planetary environment and analysis chamber (PEACh) for coordinated Raman–LIBS–IR measurements under planetary surface environmental conditions, Vol. 43, Issue 2, p. 212–227.

Sutherland, G. B. B. M. (1933), Experiments on the Raman Effect at Very Low Temperatures, Proceedings of the Royal Society of London. Series A, Containing Papers of a Mathematical and Physical Character, Vol. 141, No. 845, p. 535-549.

Thompson, J. R., et al., (2006), Remote Laser-Induced Breakdown Spectroscopy Analyses of Dar al Gani 476 and Zagami Martian Meteorites. Journal of Geophysical Research, v. 111, doi: 1029/2005JE002578.

Wiens J. J., J. W. Fetzner, C. L. Parkinson, T. W. Reeder, (2005), Hylid frog phylogeny and sampling strategies for speciose clades. Syst. Biol. Vol. 54, p. 719–748.

Willes, W. and R. Merlin, (editors) (2000), Raman Scattering in Materials. Springer Series in Materials Science, Vol. 42. Springer-Verlag.

Chapter 3: Manufacture and design of a new Mars atmosphere simulation chamber

This chapter is the basis of a manuscript that will be submitted to the International Journal of Astrobiology

K. Motamedi, A. Colin, O. Postma, R. Lootens, D. Pruijser, R. Stoevelaar,G.R. Davies

Contents

3.1   Introduction

The fundamental aim of this PhD thesis is to rigorously evaluate the performance of an elegant breadboard RLS instrument under Mars analogue conditions. In order to evaluate the RLS instrument performance under Martian conditions an analogue chamber capable of reproducing the major features of the Martian atmosphere is required. A major component of this thesis has been the manufacture of such a chamber and this chapter will present a detailed discussion of the design, manufacture and testing of the capabilities of the MASC at the Department of Deep Earth and Planetary Science at the VU University.

Ambient Martian conditions include low atmospheric pressure (6-10 mbar) and an atmospheric composition that varies over the Martian seasons but is essentially 95% CO_2, 3% N_2, 1.5% Ar, 0.1% O_2, and 0.01% CO, with water vapour less than 0.03% (Jensen et al., 2008). The temperature on the planet is highly variable and varies seasonally. The average surface temperature is about -60 °C but during the Martian winter the temperature of the surface at the polar caps can drop to almost -140 °C while in the summer the warmest soil reaches near 20 °C at noon at the equator (Grady, 2008). The European Space Agency, to our knowledge, has yet to make a final decision on the exact operating temperature of the ExoMars rover. Previous work related to ExoMars Raman studies (Sobron and Wang, 2011) estimated the rover operation temperature range would be between -30 °C and +10 °Cduring the Raman measurements. Given that the Raman instrument will be housed within the Pasteur instrument package, we agree that this is a realistic operating situation and hence perform our experiments in a Mars Atmosphere Simulation Chamber (MASC) between +10 to -30 °C.

Given the climatic variations within the Martian atmosphere and on its surface, the control of temperature, humidity and pressure in Martian chambers are important for testing the performance of space instrumentation. Consequently, the experimental approach that needs to be followed is to test the performances of the RLS instrument over this temperature interval. This should involve a detailed calibration of the spectrometer to establish if spectra are reproducible for temperature range between +10 to -30 °C. Moreover the influence of the temperature on mineral Raman spectral features should be investigated over the same temperature range. Hence a key aspect of this thesis is to describe the influence of relatively low temperature on Raman spectra at Martian conditions as temperature variations may cause frequency shifts or changes in spectral peak widths. This subject was introduced and discussed in far greater details in chapter two.

This chapter describes the design and operation of MASC at the VU Amsterdam. This is followed in later chapters by a detailed assessment of the capability of the RLS instrument to obtain Raman spectra of minerals under Martian environmental conditions with a specific comparison made to terrestrial atmospheric conditions.

3.2 Current Mars Chambers

Worldwide there are a large number of atmospheric simulation chambers (>50) that are capable of mimicking Martian conditions to some extent. In the context of testing the RLS instrument, however, many are too small, or lack precise control of humidity and temperature. We first outline the characteristics of several existing chambers and then introduce the rationale behind the specific design characteristics of a new MASC. Discussion will include a focus on the control of the temperature and pressure required for simulating Martion conditions.MASC is constructed to be versatile to allow both testing of space instruments and the analysis of geological samples under Martian-like conditions. A secondary goal that was introduced during the early phase of this PhD study is the requirement to approach environmental conditions close to that of the lunar surface. This second aim will allow assessments to be made of how an RLS instrument would operate at the lower vacuum conditions present on the lunar surface and if the RLS instrument is viable for use on future lunar missions (Colin et al., 2012).

Some of the larger or most modern chambers and their major characteristics are briefly outlined below to provide the reader with an understanding of the diverse and sophisticated facilities that are currently available and also the rationale as to why a dedicated chamber was required to test the RLS instrument at the VU University:

- Planetary Simulation Chambers at the Centre for Astrobiology Research in Madrid: One of these chambers is a versatile environmental simulation chamber capable of reproducing atmospheric compositions and surface temperatures for most planetary objects. It has a length of 50 cm with a 40 cm diameter and was specifically developed to subjectsamples to *in situ* irradiation. The pressure in the chamber can be varied between 5 and 5×10^{-9} mbar. The required atmospheric composition is regulated using a residual gas analyser with ppm (parts per million) precision. Temperatures can be set from -269 to 52ºC. The sample under study can be irradiated with ion and electron sources using a deuterium ultraviolet (UV) lamp and a noble-gas discharge lamp. The chamber also has *in situ* analytical capabilities in the form of UV spectroscopy and infrared spectroscopy (IR). This chamber is especially suitable for following the chemical changes induced in a particular sample by irradiation in a controlled environment. Therefore, it can be used in different disciplines such as planetary geology, astrobiology, environmental chemistry and materials science as well as for instrumentation testing (Mateo-Martí et al., 2006).

- Planetary Simulation chambers at the German centre for air and space travel, the Deutsches Zentrum fur Luft-und Raumfahrt (DLR), in Germany:

There are two planetary simulation chambers in the Planetary Emissivity Laboratory at DLR. One is a vacuum chamber (approximately 40 x 30 x 30 cm) and simulates conditions on Venus and Mercury. Samples can reach 500 °C and beyond, while keeping the rest of the chamber relatively cold (Maturilli et al., 2010).The second chamber is a Mars Simulation Facility (MSF). The MSF lab consists of a cold chamber with a cooled volume of 80 x 60 x

50 cm. The effective operational experimental chamber, which is cooled within the cold chamber, is a cylinder with inner diameters of 20.1 x 32.4 cm. This chamber operates at 6 mbar CO_2 pressure at -75°C(Vera et al., 2010).

-Mars simulation facilities at the Open University, UK:

The Mars simulation facility consists of a large chamber (90 cm diameter x 180 cm length), providing pressure and temperature conditions representative of the surface conditions on Mars. This chamber is configured with the capability to incorporate large scale regolith experiments not usually possible within standard vacuum systems. Another chamber is a small Mars chamber (70 cm diameter x 100 cm length) provides a simulated Martian environment with a solar illumination facility designed for instrument qualification and astrobiology experiments. The facility is also configured to permit automated variation of the environment, such as thermal diurnal cycling (Patel et al., 2010).

- Martian simulation chamber at University of Toulouse, in France:

This chamber was developed to reproduce the Martian environment to test the first Laser Induced Breakdown Spectroscopy instrument sent into space as part of ChemCam on the Curiosity Rover (Cousin et al., 2011). The chamber has a volume of 70 l. The chamber is pumped to 10^{-3} mbar and then filled with 95.7% CO_2, 2.7% N_2 and 1.6% Ar to mimic the Martian atmosphere. In each experiment, five samples are placed in the chamber and the ChemCam instrument is installed 3 metres from the sample. The chamber is kept at room temperature, which is a difference compared to flight mode conditions, but it should be generally of no importance for LIBS analysis because of the high temperature of the plasma ~ 8000 ℃, (Cremers and Radziemski, 2006).

3.3 MASC chamber: Required performance

The essential requirements of a Mars simulation chamber ideal for the testing of spectroscopic instruments such as the RLS instrument are as follows:

- Variable Atmospheric Pressure: Atmospheric pressure inside a chamber potentially has a major influence on the performance of certain analytical instruments both in terms of measurement capabilities, LIBS for example (Andrew et al., 2010), as well as the actual functionality of the instrument. To fully assess the effects of low pressure on the instrumentation and instrument performance, it is desirable to create a chamber with flexibility to operate over a pressure range greater than that found on Mars. Therefore, an appropriate chamber should produce stable pressures from atmospheric conditions down to 4 x 10^{-5} mbar.

- Large Operational Volume: To test spectrometers and other instruments, as well as having the capability to examine Martian sample analogues, a suitably large chamber volume is required (~ 200 l). However, the larger the chamber volume, the greater the outgassing from chamber surfaces. There is also potential for outgassing of residual water from the components in the chamber as well as the samples and instruments

placed in the chamber. Many previous chambers have therefore had small dimensions to avoid potential problems with outgassing.

- Temperature Control: The control and monitoring of temperature (+10 °C to -30 °C) in all the previously discussed chambers proved to be technically challenging. A combined cooling and vacuum pumping system must create stable temperatures in the chamber. Previous research has sometimes adopted a pragmatic approach where temperature is only varied in the sample holders/trays in the Mars chambers (Sobron and Wang, 2011).Such an experimental approach will provide an indication of first order variations in analytical performance of instruments or analytical techniques but will not provide a true proxy of experiments performed under Martian conditions. Therefore, a far more rigorous chamber design approach is required.

- Flexible Functionality: A fully versatile Martian simulation chamber should also have the flexibility to support testing of specific instruments, many of which will include charge coupled device (CCD) as detectors (e.g., for ExoMars Cameras, XRD-XRF, RLS instrument). The optimal operation conditions of CCDs will vary from instrument to instrument but generally are operated at low temperature (< -10 °C) to reduce the sources of thermal noise. Consequently, if optimal results have to be obtained during the Mars simulation experiments, the CCD need to be kept at a constant and low temperature. For the ExoMars mission itself, it is proposed to keep the CCDs below -15 °C, irrespective of the ambient conditions on Mars and inside the ExoMars Rover.

- Safe Operational Conditions: The optical system of the RLS instrument is designed to be extremely robust and survive a Mars landing and subsequent variations in ambient Martian conditions. Repeated rapid changes in temperature will, however, subject the spectrometer optics to thermal stresses that may lead to damage of the instrument. It is therefore a requirement to design a chamber with capability of carefully controlling the heating and cooling rates at different parts of chamber. Hence, any potential damage to the RLS instrument will be avoided.

A summary of the required operational conditions of a new 200l MASC are given in Table 3.1.

Operating Pressure	5-10 mbar
Background vacuum	$<10^{-5}$ mbar
Leak tightness	$<10^{-9}$ std cc/sec
Atmospheric composition	Carbon dioxide ~100%
Water content	As low as possible < 0.05%
Temperature	+10 to -30 °C
Cool down / warm up time	16 hours

Table 3.1. Desired operational conditions MASC.

To the best of our knowledge, MASC is the first Martian/Moon simulation chamber that has enough room (200 l) and versatility for the study of different planetary instruments and materials under separately controlled environmental conditions. A note must be made that our Raman spectra were not obtained remotely through viewports mounted in chamber doors (with spectrometers outside the chambers). The design of the MASC allows *in situ* RLS measurements on the same set of samples under the same environmental conditions with the spectrometer inside the MASC and represents a true analogue of the expected operating conditions during a planetary mission.

3.4 Mars Atmosphere Simulation Chamber (MASC)

3.4.1 General design philosophy

Initially a vacuum chamber with a volume of 50 l (L = 70 cm; D = 50 cm) was chosen for the task of testing the RLS instrument. However, the final version of the RLS instrument did not conform to the original design, with some parts being more than a factor of 10 larger. Dimensions of the manufactured spectrometer were also changed due to a problem in obtaining a suitable space qualified and high precision diffraction grating. A delay in the final design of the spectrometer in turn led to a major delay (~ 1 year) in the manufacture of the optical head by the Netherlands Organisation for Applied Scientific Research, (TNO) science team. Ultimately, considering project deadlines, a less sophisticated optical head was manufactured that was a factor of ten times larger than originally planned (360 mm diameter, 326 mm height). The optical head that was delivered was intended to simply test the functionality of the overall design concept, i.e. that the RLS instrument would operate with a single spectrometer. This major change in the RLS instrument design required the manufacture of a new dedicated chamber and resulted in a total change in the focus of the PhD. Manufacture of the chamber became a major scientific-technology goal and the degree of Mars analogue experimentation had to be radically reduced.

The only practical solution to overcome the increased volume of the optical head was a new larger volume chamber. Hence, MASC with 200 l (1 m length and a diameter of 57.6 cm) was designed and built (Fig. 3.1). This new design included major contributions from Vrije University technical staff, most notably Onno Postma, Ron Lootens, Daniel Pruijser, Rob Stoevelaar and their colleagues. Without their input and guidance this project would never have reached completion.
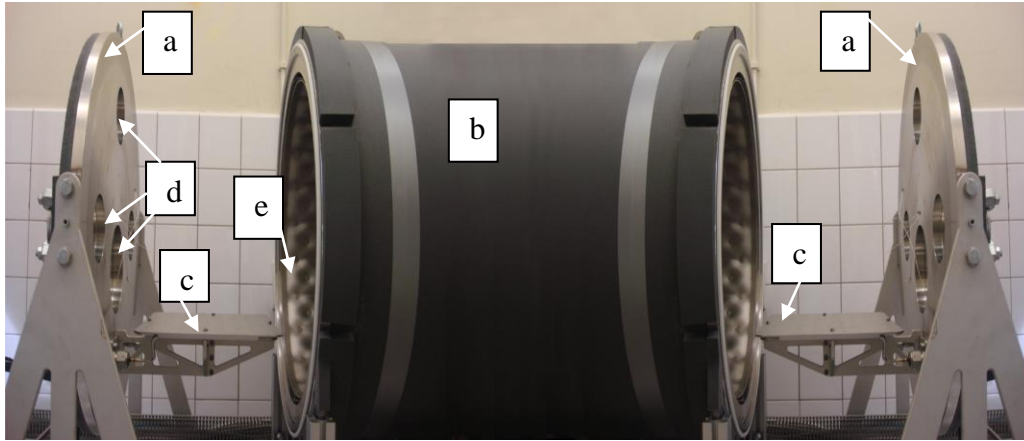
Figure 3.1. The outside view of the MASC presented as a mirror image to give an overall idea of the makeup of the chamber; a) main entrance doors, b) thermal insulation covers the chamber wall/doors, c) cooling/sample mounting plates, d) holes for electrical-thermal, optical feedthroughs and dedicated flanges are visible in the both doors, e) cooling pillow plate. See Fig 3.3 for further images of the chamber and Fig 3.10 for a schematic of the entire MASC.

3.4.2   Vacuum isolation

As it was explained in section (3.3), one of the challenging requirements in design of the planetary simulation chambers is creating stable temperatures within a considerable volume of the chamber. To allow operation with a stable internal temperature, MASC needs to be well insulated to avoid heat loss/gain from the ambient laboratory conditions outside the chamber. The design incorporates a double wall allowing production of an isolation vacuum over the full length of the chamber (Fig. 3.3). There is a 60 mm gap between the two walls. A vacuum in this volume was initially achieved using a portable pumping system that includes a turbo pump. This system generates an isolation vacuum in the order 10^{-5} to 10^{-6} mbar, which is sufficient to minimize heat conduction from ambient laboratory conditions into the inner tank wall. The isolation volume can be closed off so that it is not required to be continually pumped. Despite careful manufacturing specifications, our practical experience was that initially the isolation volume underwent significant outgassing. Consequently the isolation volume was baked and outgassed several times before it was possible to achieve a stable vacuum of $<2 \times 10^{-6}$ mbar.

The vacuum isolation alone is not sufficient to achieve stable temperatures within the chamber. It was therefore essential to further improve the thermal insulation as the large surface area of MASC causes elevated heat conduction (from both the doors and chamber walls). Hence, MASC is covered with a flexible 20 mm thick insulation layer made of Thermoplastic elastomeric foam (TPE). This material is designed to provide effective insulation over a temperature range between -80 and +95 °C. The highly flexible nature of TPE made it possible to cover the outer wall and two main flanges of the chamber (Fig. 3.1).

3.4.3   Cooling screen

The cooling/heating power of MASC is provided via a cooling screen (pillow plate) that is inserted inside the chamber. The pillow plate is made of 2 stainless steal plates that are partially welded together with a pattern that forms inter-connected channels. In order to create a pillow like shape, the 2 welded plates are deformed by putting them under a pressure of between 40 and 60 bar. This way the plates will locally "puff up" like a balloon. As shown in Fig. 3.2, there are six welds (concentric circles) in the design of the cooling plate to create the cylindrical tube. The outer dimension of the pillow plate before creating the cylindrical tube was 75 x 171.85 cm.
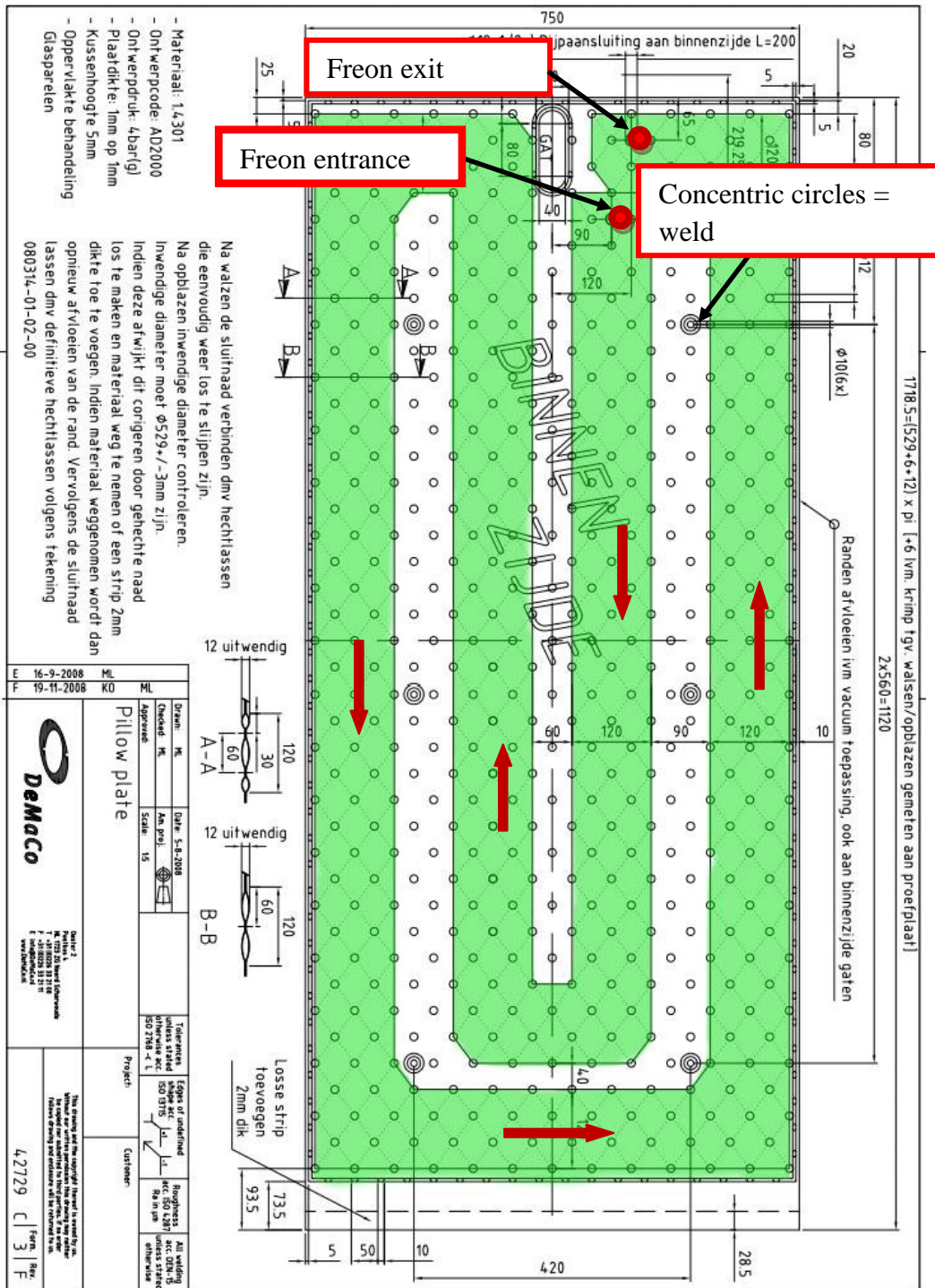
Figure 3.2. The initial design (in Dutch) and the dimension of the cooling plate. Freon enters from the red entrance hole and passes along the green path inside the cooling plate. Circles connect the two plates of cooling plate together but allow Freon to flow between the welds (area in green). There are six welds (concentric circles) plus one large oval weld in the cooling plate that fix the plates together and prevent Freon circulation; white areas.

The entrance and exit of the cooling plate are located in the middle of the screen so that connecting tubing to a cooling machine can be made as short as possible ensuring minimum thermal loss (Fig. 3.3).
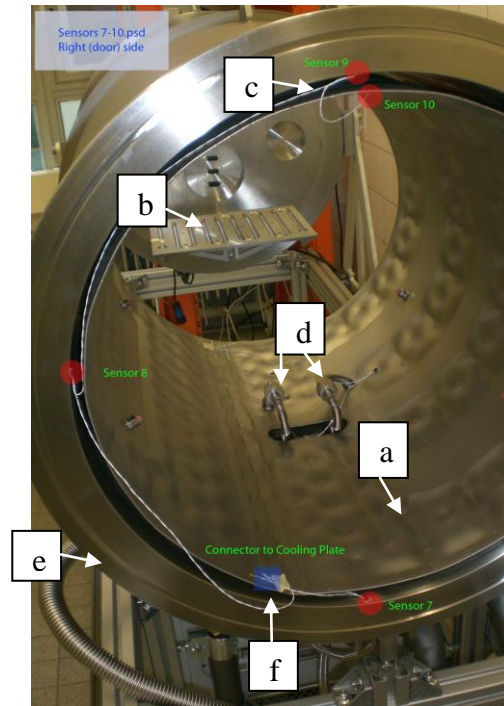
Figure 3.3. The internal view of MASC: a) the cooling screen (pillow plate), b) available space for mounting Raman/LIBS components and 3D linear stages on the cooling plate, c) temperature sensors, d) the entrance and exit of Freon to the cooling screen, e) chamber double wall, f) temperature sensors of cooling plates are connected to the rest of sensors in chamber via a single wire system.

3.4.4   Design of door/flanges and mounting plates

The design goal of the end flanges is to ensure high versatility of the chamber, i.e. compatibility for use with a variety of different analytical instruments and to perform a wide variety of analyses on different analogue materials. To allow ease of access, the entire ends of the chamber are designed as flanges/doors. The doors specifically allow for the incorporation of multiple electrical and optical feedthroughs, which provides the MASC with great flexibility. Instruments cannot be directly attached to the chamber walls due to the presence of the cooling screen. Therefore the two main doors must be designed to fulfil several roles. First they must provide support for platforms that hold samples for analysis and instruments that will be tested under Martian conditions or perform measurements under these conditions. Most instruments that will be tested inside the chamber operate in a horizontal plane. So it was necessary to create a horizontal platform that can hold the instruments. To mimic Martian conditions for both samples and instruments, it is also necessary that any mounting plates have cooling-heating capacity. Consequently for extra cooling capacity, a cooling

channel is integrated within the horizontal platforms and these platforms are called mounting plates (Fig. 3.3).

The doors also have internal cooling channels and are directly connected to the cooling system. Practical experiments have shown that condensation appears on the surface of small flanges/feedthroughs at temperature near or below 17 °C, potentially leading to problems for electronic and optical components. Therefore, it is required to maintain flanges/feedthroughs above 20 °C. Depending on thenumber, size and other mechanical properties of the feedthroughs, flanges on each door can be independently heated to 20 °C. The heaters on the flanges are power resistors. They have a low resistance (1-2 Ohms) and can handle up to 30 Watts. A Call9300 temperature controller is used to set the temperature. Therefore, each door can be set to a desired temperature, such as 20 °C (Fig. 3.4).
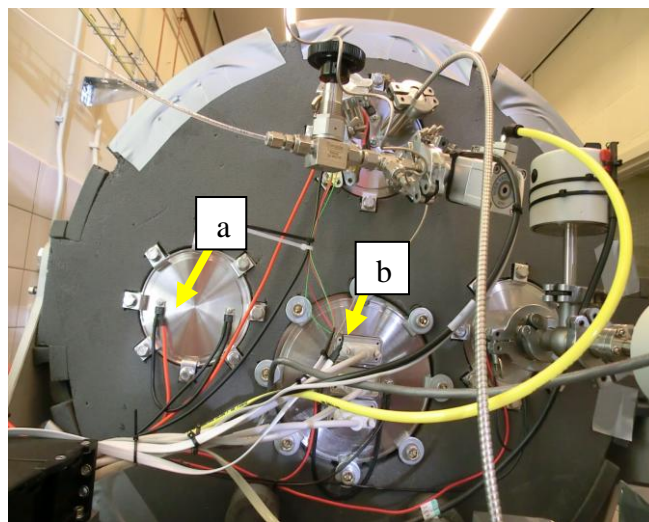
Figure 3.4. The view of one of the main MASC doors with a) local heater and b) a flange that can be fitted with optical or electrical feedthroughs as seen on the flange to the right.

3.5   Control and operation of the vacuum system

3.5.1   Design of the vacuum system

Maintaining and accurately controlling internal pressure of the chamber is another design requirement. The system must operate at a pressure typical of ambient Martian conditions (6–10 mbar). Significantly, however, the Martian atmosphere only contains ~ 0.03% water. The large surface area of the doors and chamber and the multiple electrical and optical feedthroughs could lead to extensive outgassing. Therefore, the vacuum system needs to be designed to keep water levels at a minimum and hence has the capability to reach ~ 10^{-5} mbar levels to ensure that water vapour contents do not exceed Martian values. To reach a basic vacuum in the approximately 200 l chamber volume, an oil free dry-compression diaphragm pump (Pfeiffer PKT01300) is used as the backing pump to a turbo pump. In the MASC experimental setup, the diaphragm pump controls the vacuum in the 4 to 12 mbar pressure

range and an oil free turbo molecular pump, (Pfeiffer TMH 071P) is used to reach an initial vacuum of ~ 10^{-5} mbar. Table 3.2 reports measured pressure inside the MASC as a function of time following initial pump down after a sample change; i.e., the chamber contained spectrometer, optical head, samples and all optical fibres and electrical cables. Pump down time is rapid and H_2O is quickly and effectively removed from the system without the need for an additional cold finger (Table 3.2).

Time (min)	pressure (mbar)
0	1010
15	24.8
30	4.2
45	0.1
60	4×10^{-3}
90	4×10^{-4}
120	4×10^{-5}

Table 3.2. Measured pressure inside the MASC as a function of time.

3.5.2   Selecting a suitable vacuum seal

To maintain stable Martian or lunar conditions, the MASC needs to be leak tight. However, MASC has two large entrance doors (57.6 cm diameter), so ensuring a good vacuum seal potentially presents a major practical problem. One possible solution is to use a metal gasket (e.g., annealed Cu) and a knife edge. However, the use of multiple metal gaskets associated with numerous sample changes is not viable as it would prove expensive. Therefore, the use of Viton O-rings is the preferred solution for both ease of use and expense. However, there are potential problems with rubber products when used over a large temperature range; thermal expansivity, brittle at low temperature and high outgassing rates. To assess these three problems, a series of elastomer O-rings were evaluated. The O-rings are held in place with a 6.5 mm thick aluminium O-ring holder. Although this practical experimentation is not an academically challenging exercise, a detailed discussion is given to provide the reader with an idea of the technical and practical challenges faced when seeking solutions for even apparently minor technical problems and the compromises that need to be made in choosing components. Such technical problems were frequently encountered during the manufacture of MASC.

The first aspect to consider is the effective operational temperature of the O-rings. The operational temperature range of common elastomeric materials is given in Fig. 3.5. Most rubber-based compounds such as High Temperature Nitrile butadiene rubber (NBR), polyacrylate (ACM) and Tetrafluoroethylene/Propylene Rubber (FEPM) have a limited low temperature resistance (from near -33, -12 and 0 °C respectively) and hence are not recommended for use at sub-zero conditions. Ethylene-Proylene-Diene elastomer (EPDM) is the first choice for low temperature O-ring sealing because of its proven behaviour down to -

50 °C. An alternative is Viton FKM (Fluorocarbon rubber). Although other candidates for low temperature application exist (e.g. silicone rubbers (VMQ), styrene butadiene rubber (SBR)), the possible application of these other rubber types is not recommended due to their large permeability for atmospheric gases and their high volume change with temperature and in some cases high cost.
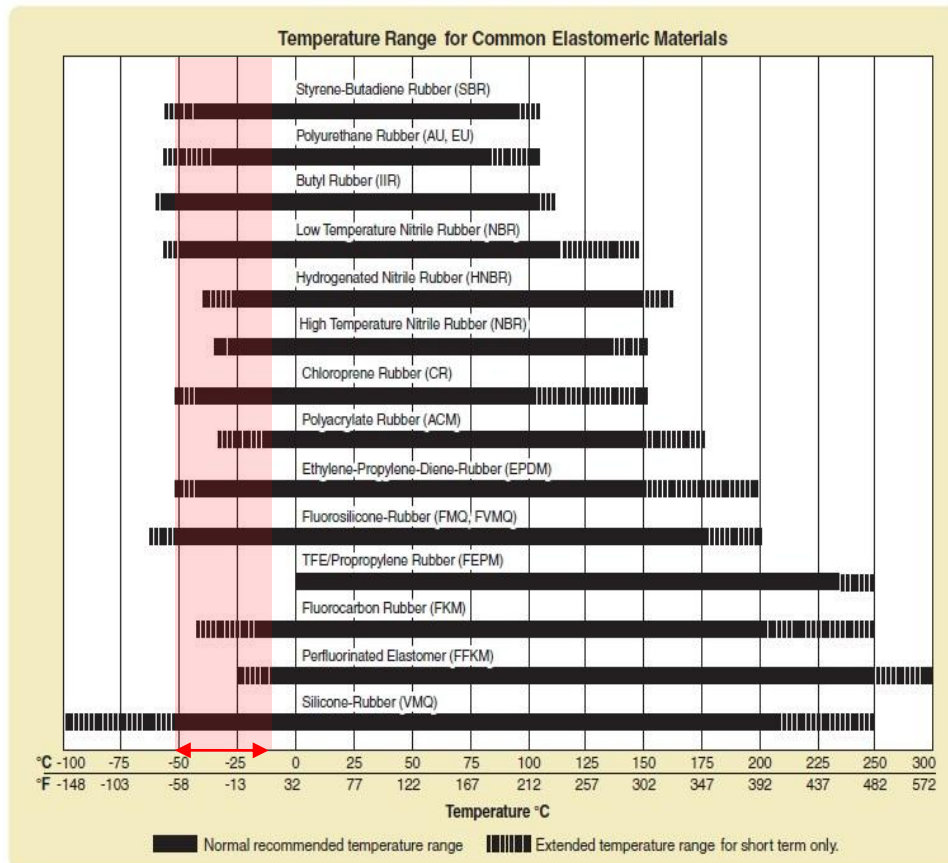
Figure 3.5. Temperature range of use of common elastomeric materials after Hannifin (2001). The lowest and highest operating temperature of MASC indicated in red at -30 and +10 °C.

The second design consideration for O-rings is the effect of decreasing temperature on the hardness of elastomeric compounds. Figure 3.6 summarises the hardness of several rubber-based compounds. As temperature decreases, the hardness of rubber based compounds increases. In order to maintain a seal when there is a large pressure difference, a material must maintain a low rigidity and hence easily deform when compressed between flange surfaces. The recommended temperatures for use of elastomers are in generally higher than the temperature when a maximum hardness is attained. In Fig. 3.6, the vertical scale is Shore durometer, which is one of several measures of the indentation resistance of materials based on the depth of penetration of a conical indenter. Shore durometer is typically used as a measure of hardness in polymers, elastomers and rubbers. The two most common scales are type A and D. The A scale is used for softer plastics as is required in our case. In Fig. 3.6, the vertical scale shows the hardness, 50 to 100 Shore A scale between -57 °C to 27 °C. EPDM, FKM and NBR have the highest shore hardness. EPDM records substantial variation: from 75 at room temperature to 90 at -40 °C. For FKM a hardness of 97 Shore is reached

94

atapproximately -40 °C. Although FKM has a high hardness of 97 at -40 °C (Fig. 3.6), the manufacturers recommend its use at temperatures higher than -15°C (Fig. 3.5). Therefore FKM is not suitable for experiments below 15 °C with MASC. In addition, we should keep in mind that, normal FKM fluorocarbon (viton) has a glass point near 0 °C (below the glass transition temperature, the polymer becomes hard and brittle, like glass). However, other types of polymers with a very low glass point can only be acquired by special commissions and are therefore expensive (€1000's per commission).
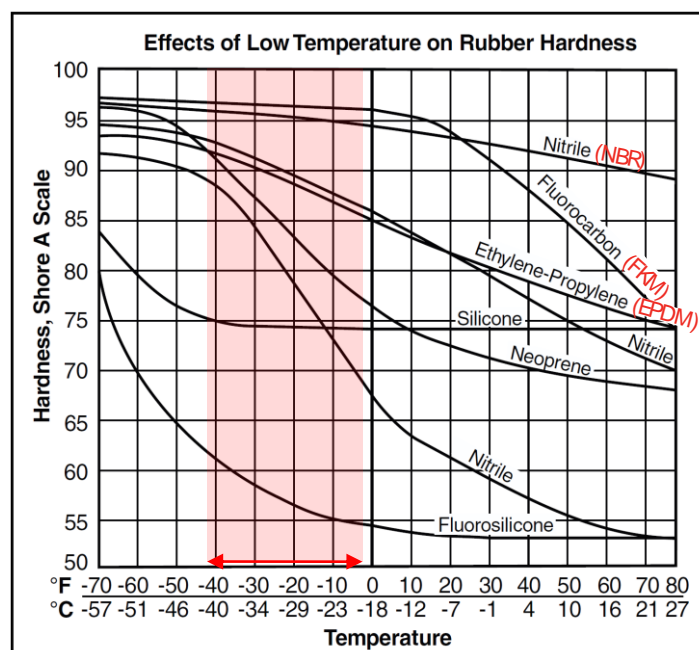
Figure 3.6. Effect of temperature on rubber hardness after Hannifin (2001). The operational temperature range of the MASC is -30 to +10 °C.

Another important property of elastomeric materials is thermal expansion. Most rubber-based compounds have significant thermal expansionthat results in expansion/contraction upon heating or cooling leading to a poor vacuum seal. According to the suppliers, length changes for an O-ring elastomer with a length of 1.5 m and a seal diameter D=0.5 m are in the order of several millimetres between the proposed different operating temperatures. This order of magnitude length change is insufficient to cause significant problems to the vacuum provided that the length change is uniformly distributed along the entire O-ring. The O-ring is therefore held in place with an aluminium holder to ensure uniform distribution of strain.

The final character of elastomeric material to be considered is outgassing. Any outgassing from the O-ring and other installed materials within MASC must be limited to ensure that no coatings are adsorbed onto any optical components inside the chamber and water levels are maintained at or below Martian levels. Any contamination in the MASC and particularly on spectrometer optics would compromise performance and make the development of a technique to the search for organic molecules in the presence of complex hydrocarbons almost impossible. In the Table 3.3, the weight loss of elastomers compounds under vacuum conditions (1.33 x 10^{-6} mbar) at room temperature for the period of two weeks are presented (Hannifin, 2001). EPDM seems to be in the middle of the weight loss range: between 0.39and

0.92%, while, FKM with high vacuum applications has the lowest weight loss: 0.07 to 0.09% (Table 3.3). Hence, for high vacuum applications in the temperature range from 20 up to 200 °C, FKM is often used. However, normal FKM grades have a limited low temperature resistance and are therefore not applicable as door seals for use in the MASC.

Weight loss of compounds in vacuum		
Test samples: Approximately. 075" thick Vacuum Level: ~ 13 mbar Time: 336 hours (two weeks) Room temperature		
Compound Number	Polymer	weight loss percentage
B0612-70	Butyl	0.18
C0873-70	Neoprene	0.13
E0515-80	Ethylene Propylene	0.39
E0529-60	Ethylene Propylene	0.92
E0692-75	Ethylene Propylene	0.76
L0449-65	Fluorosilicone	0.28
L0677-70	Fluorosilicone	0.25
N0406-60	Nitrile	3.45
N0674-70	Nitrile	1.06
P0648-90	Polyurethane	1.29
S0455-70	Silicone	0.03
S0604-70	Silicone	0.31
V0747-75	Fluorocarbon	0.09
V0884-75	Fluorocarbon	0.07
V0894-90	Fluorocarbon	0.07

Table 3.3. Weight loss of compounds in vacuum after Hannifin (2001).

To test the functionality of O-rings, a helium leak detector (quadrupole mass spectrometer) was used. At first, helium was flushed onto flanges, connectors, and valves on the outside of the MASC. The performance of O-rings was tested when MASC was at different temperatures. The current of helium ions produced in the leak detector is proportional to the partial pressure of helium in the installation, i.e., the leak rate.

Leak tests were performed on the EPDM and FKM O-rings under vacuum conditions (~ 10^{-5} mbar) at different temperatures. FKM O-rings, which are commonly used as high vacuum seals, showed leaks between T= 0 °C and -40 °C. The leaking was so marked that the pressure gauge increased by several orders of magnitude and the door clamps were found to be completely loose after cooling to -40 °C. Subsequent testing established that, as predicted, FKM is not suitable for low temperature sealing applications and therefore EPDM was the

best solution. However, the potential drawback in using EPDM rings, as discussed above, may lie in the amount of outgassing. EPDM rings are typically sulphur cured, i.e. they are cross linked using sulphur. The presence of this element is not compatible with the cleanliness levels required for the MASC. An alternative type of EPDM (Hydrogen peroxide, H_2O_2) is produced for ultraclean conditions demanded by the pharmaceutical/food industry.Therefore, this type of the EPDM O-rings was chosen for the MASC because of their resistance to low temperature (down to -40 °C) in combination with their compatibility towards clean application in pharmaceutical/food industry.

3.6   The design, layout and operation of the cooling and heating system

The thermal control of the different sections of MASC involves a combination of methods that are unique in chamber design.Here we explain the three separate cooling/heating circuits that provide thermal control to: 1) Flanges, 2) Cooling screen and mounting plates, 3) The cooling circuits for instrumentation, which in the case of the RLS instrument includes a cooling circuit dedicated to the CCD.

When designing the heating-cooling systems we had to take the following fundamental factors into consideration:

a) In each heating/cooling circuit, the correct selection of the cooling/heating transfer medium is of crucial importance for the safe and reliable operation of different parts of MASC. In addition to having an adverse effect on the vacuum, any fluid leak inside the MASC could potentially cause catastrophic damage to the components/instruments inside the chamber. Consequently the cooling medium with potential access to the inside of the chamber must be inert.
b) Different parts of the chamber and the analytical instrumentation have different requirements for heating/cooling rate. One crucial aspect to consider is that the RLS instrument and optical fibres must not be damaged by high thermal stresses, hence well controlled temperature changes are required.

3.6.1   Cooling / heating of the flanges

To cool/ heat the flanges, a Lauda XT-150 cooling machine is used. This is considered a simple, safe and reliable machine, with an accuracy of ± 0.05 °C (Fig. 3.7). The power outputs of the Lauda at 20 and -40 °C are 1.50 and 0.06 kW respectively, which are sufficient for the heating/cooling of MASC when operated between -30 and +10°C.
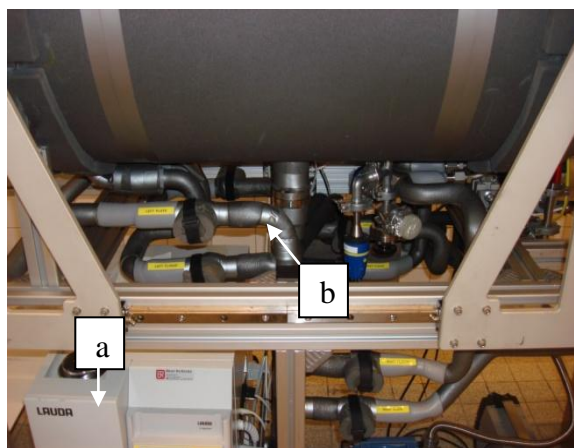
Figure 3.7. View of the bottom of MASC, connected to; a) Lauda cooling machine, via b) relevant channels and pipes.

The Lauda cooling machine uses silicone oil as the cooling medium for low temperature applications. Silicone oil (polydimethylsiloxane) has the chemical formula $(C_2H_6OSi)_n$.

The most important properties of silicone oil that led us to its choice as the cooling medium are listed in Table 3.4 and shown in Figs 3.8 and 3.9.

Colour		Colourless
Viscosity, kinematic	at 20 °C	3 mm²/s
Density	at 20 °C	894 kg/m³
Flash point		> 62 °C
Fire point		> 110 °C
Boiling point		≥ 200 °C
Water solubility		insoluble
Solvent		Petrol, Acetone, Alcohols

Table 3.4. Important properties of silicone oil.

The changes in density (~ 18%), viscosity (~ factor 10), volume (~ 18%) and specific heat capacity (~ 15%) of silicone with temperature are such that effective heat transfer is accomplished between -60 to 80 °C (Figs. 3.7 and 3.8).
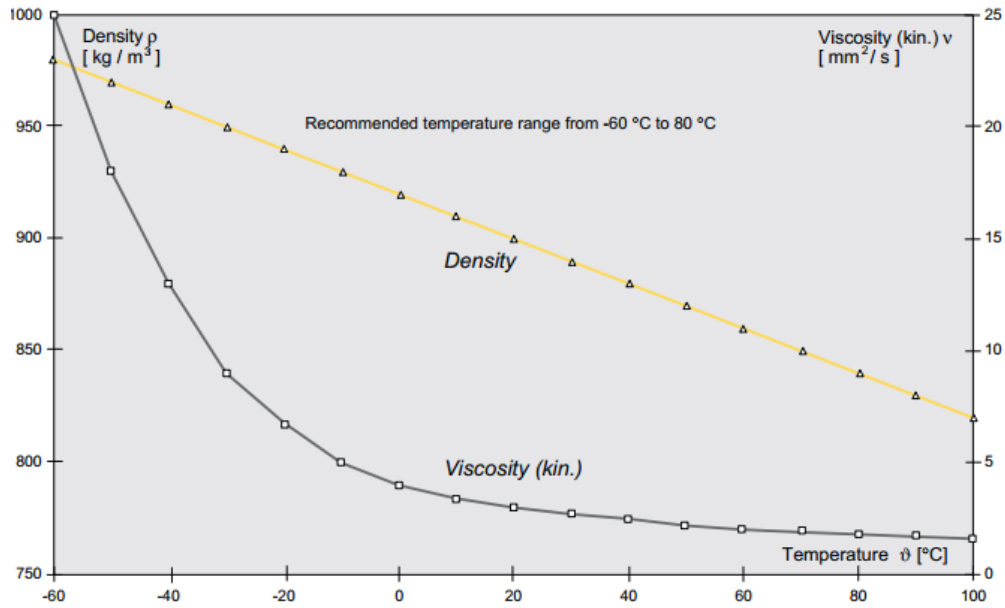
Figure 3.8. Variation of the density and viscosity of silicone oil over the temperature range -60 to +100 °C. See online Lauda manual for details.
http://www.lauda.de/hosting/lauda/website_de.nsf/urlnames/kryo60_produkte
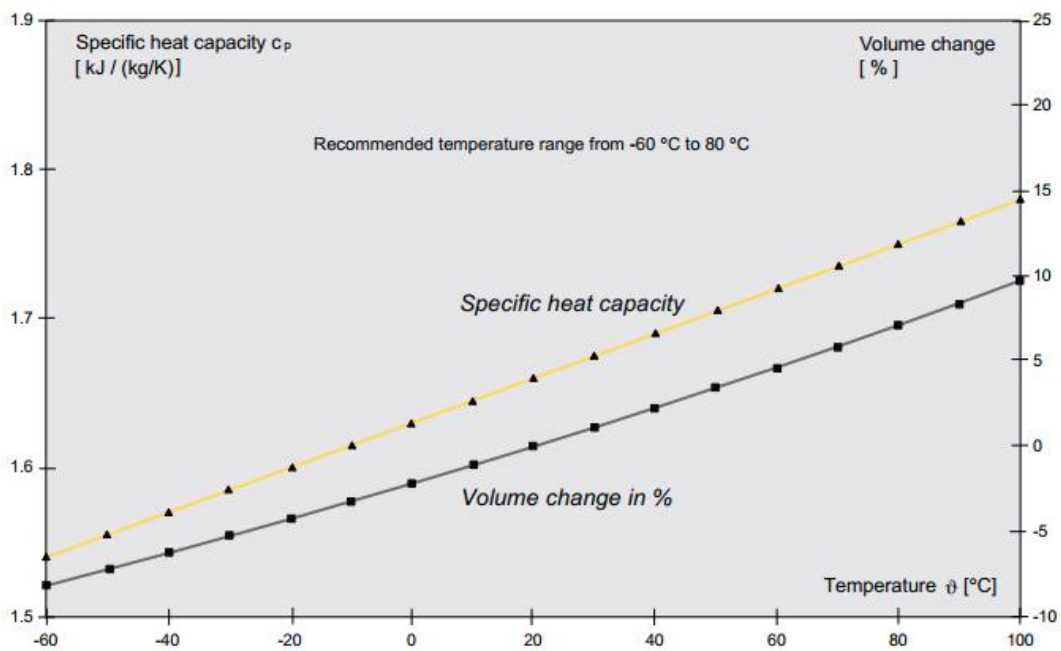
Figure 3.9. Variation of the heat capacity and volume change of silicone oil between temperatures -60 to 100 °C. See online Lauda manual for details.
http://www.lauda.de/hosting/lauda/website_de.nsf/urlnames/kryo60_produkte.

In the MASC, temperature regulated silicone is pumped from the Lauda via cooling channels to the two main flanges and runs back to the cooling machine where the cycle restarts (Fig. 3.10). Silicone oil is used directly as a cooling medium only inside the flanges because the flanges are considered leak-proof. The system can only leak to the outside of

the chamber at the entrance and the exit of channels. Hence silicone oil can never leak into the chamber and cause contamination.
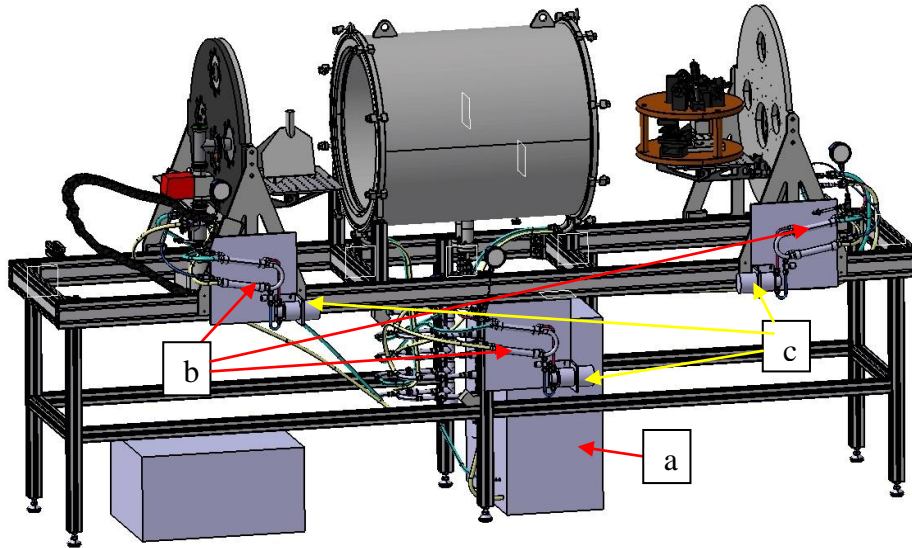
Figure 3.10. Sketch of the Mars atmosphere simulation chamber (MASC) a) Lauda cooling machine, b) heat exchanger type HE, c) pump used to circulate Freon.

3.6.2 Cooling / heating of the cooling screen and mounting plate

The cooling screen (pillow plate) and mounting plates, upon which experiments are performed or instruments tested, need to be temperature controlled between +10 and -30 °C. Due to their position inside the MASC it is possible that these parts of the cooling system could leak, resulting in the cooling medium entering the chamber interior. This would cause catastrophic contamination of the chamber interior and any instrumentation within, particularly devastating for RLS instrument optics. Hence, an innovative cooling design was needed that allowed use of an inert cooling medium within the cooling screen (pillow plate) and mounting plates inside the chamber.

The basic principle adopted was to use a cooling medium in a secondary closed system in thermal contact through heat exchanges with the primary silicone cooling system driven by the Lauda. For practical operation and to achieve the greatest flexibility, three secondary circuits where manufactured each with a dedicated pump and heat exchanger.

The choice of the secondary cooling fluid is a vital part of the performance of MASC. The fluid must have a working temperature between -40 and +20 °C and have good cooling properties; i.e.,high specific heat capacity and thermal conductivity. Initially ethanol, with high a specific heat capacity (2.460 J/kg.K) was considered as a good cooling medium (e.g., Atkins, 2010). However, ethanol is highly flammable and considered too dangerous for operation in a system where heating experiments and lasers are in routine use. An ethanol-

water solution that contains between 10% and 96% (alcohol by volume) will catch fire if heated to about 49 and 17 °C respectively. Therefore, we selected cooling medium 134a, Freon, which is nontoxic and inflammable.

Temperature (°C)	Density (kg/m3)	Specific heat capacity (103 J/kg.K)	Thermal conductivity (W/mK)
-40	1519	0.885	0.069
-30	1490	0.896	0.069
-20	1461	0.907	0.071
-10	1429	0.920	0.073
0	1397	0.935	0.073
10	1364	0.950	0.073

Table 3.5. The variation of density, heat capacity and thermal conductivity of Freon with temperature.

The chemical composition of Freon is $C_2Cl_3F_3$. The physical properties of Freon, the variations of density, heat capacity and thermal conductivity with temperature can be found in Table 3.5. Freon comprises several different chlorofluorocarbons (CFCs), which are a group of aliphatic organic compounds containing the elements carbon and fluorine and in many cases other halogens (especially chlorine) and hydrogen.

The thermodynamic and physical properties of Freon coupled with its low toxicity make it an efficient and safe cooling medium. In our new design Freon, as a liquid phase (under ~ 6 bars at room temperature) moves through the cooling pipes, two mounting plates and cooling screen. The system is filled to 90% of the volume to withstand the expansion of the fluid when the temperature is raised. Based on the different volume of the cooling systems, 120.47 and 114.24 g of Freon were added to the two mounting plates and 433.3 g of Freon to the cooling screen.

Heat exchangers transfer heat from one substance to another. Usually, but not always, the two substances are separated by a wall. In our design, the selected heat-exchanger (type HE 0.5 from Danffos) consists of a large outer tube with a small inner tube. Heat is transferred by a counter flow principle. Heat exchangers can function with fluid/fluid, fluid/gas or gas/gas systems. Our design is fluid/fluid. The silicone oil flows through the outerwall and the 134a cooling liquid flows though the inner tube of the heat changer. We utilised the smallest available heat exchanger (HE 0.5), which is 178 mm in length and weighs 0.3 kg. The cooling capacity of the HE 0.5 type is ~ 0.33 and 4 kW at -40 and +20 °C respectively. The heat exchanger has a working range between -60 and +120 °C and is designed to withstand a maximum pressure of 28 bars, well above our operational requirements. This type of heat exchanger is safe, cheap and based on the mentioned technical data is an appropriate component for our design.

In total three pumps from the Micro Pump company are utilised to control the flow of Freon in the separate cooling circuits. They are adapted for the use of Freon over the temperature range of -46 to +177 °C. Two pumps with flow capacities of up to 380 ml/min circulate Freon from heat exchangers to mounting plates. As the cooling screen has the largest volume and is mounted at the highest level, a pump with a higher capacity (930 ml/min) was selected to control the cooling screen.

3.6.3 Cooling the CCD of the RLS instrument

As discussed in detail in chapter two, the background noise of a CCD chip can be highly temperature dependant (Denson et al., 2007). To maintain the best possible signal/noise ratio, the CCD should be operated below room temperature and effectively at as low temperature as possible (<-30 °C). Due to the operational requirements of MASC (+10 and -30 °C) the chamber needed to be above room temperature for certain experiments. Hence, it proved impractical to integrate a CCD cooling system into the main MASC cooling system. Consequently, any instrument that incorporates a CCD chip and is to be tested in MASC requires a separate cooling circuit. A water cooling machine is insufficient to decrease the CCD temperature to -30 °C. Therefore, to keep the CCD cooled during Raman and LIBS experiments performed at variable temperatures (+10 to -30°C), a Peltier was mounted onto the CCD, which in turn is cooled by an Etscheid water cooler (Fig. 3.11).
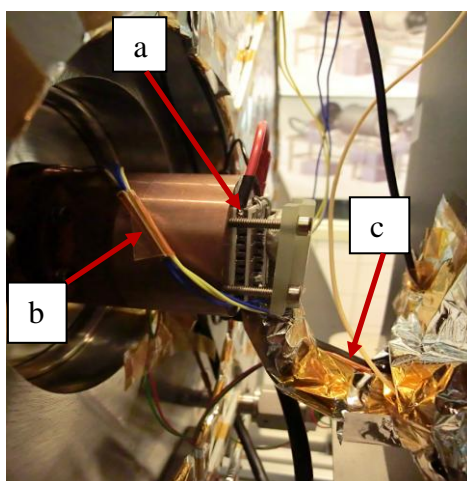
Figure 3.11. The view of the inside of a door showing the CCD cooling system: a) the Peltier, b) the copper cooling block, c) flexible copper braid thermal strap connected to CCD.

A braided Cu thermal strap (approximately 25 mm wide and ~ 5 mm thick) connects the Peltier to a copper cooling block (Fig. 3.11). In MASC, the hollow cooling block is mounted to one of the small flanges on the chamber's door and thereby connected to an Etscheid water cooler with the cooling capacity of 750 kcal/h at 15 °C. At lower temperatures the cooling capacity is about 3% per °C. This cooler is located directly under the chamber to make the cooling pipes as short as possible to avoid unnecessary heat exchange.

Designing and maintaining efficient thermal contacts proved to be a major challenge in producing effective cooling of the CCD. Initial designs resulted in significant thermal

gradients across connections and flanges. Thermal contacts were improved by making better physical contacts and the application of thermal paste. In addition, the cooling strap was insulated with stretched polyethylene terephthalate (PET) foil. However, we established that heat radiation and conduction tothe cooling strap and CCD derived from an ambient N_2 atmosphereintroduces so much energy that, even with the Peltier in operation, a minimum temperature of only 0 °C could be achieved. Further experimentation was performed under vacuum conditions. N_2 was initially flushed through the MASC to remove water vapour and then the system evacuated. After initial cooling of the CCD with the Etscheid water cooler (set at 5 °C), with the Peltier, the CCD temperature reached -30 °C within 1 hour.

Tests were performed to assess the minimum operational temperature of the CCD, under vacuum condition ($4x10^{-5}$ mbar) and 8 mbar of CO_2. When MASC temperatures were +8, -8 and -35 °C, the minimum CCD temperatures achieved under vacuum condition, were -31.4, -35.7 and -41.2°C respectively. In contrast, in the presence of CO_2, the minimum CCD temperatures were -17.4, -25.1 and -34.3 °C. The temperature of the CCD as a function of time, when MASC was operated at different temperatures, is reported in Table 3.6. Irrespective of the MASC operating temperature, the CCD always reaches a temperature below -30 °C under vacuum conditions. In contrast, under CO_2 condition with the MASC operation temperature at +8 and -8 °C, the CCD reached temperatures of -17.4 and -25.1 °Crespectively. The increased thermal noiseassociated with the increased temperature may potentially obscure some weak peaks in Raman spectra. We will discuss the effect of temperature on the CCD performance in chapters four, five and six. Clearly on the longer term the CCD cooling design needs to be improved further to achieve efficient cooling in the presence of an atmosphere.

| Time (min) | CCD temperature | | | | | |
| | MASC T: 8 °C | | MASC T: -8 °C | | MASC T: -35 °C | |
	pressure $4x10^{-5}$ mbar	pressure 8 mbar CO_2	pressure $4x10^{-5}$ mbar	pressure 8 mbar CO_2	pressure $4x10^{-5}$ mbar	pressure 8 mbar CO_2
0	13.6	13.6	8.1	1.3	-3.1	-8.2
15	0.5	5.7	-3.1	-4.3	-14.2	-16.1
30	-09.5	-0.41	-14.8	-12.1	-21.8	-21.6
45	-20.4	-06.7	-22.1	-16.2	-29.8	-27.1
60	-25.7	-08.7	-29.1	-21.0	-35.8	-31.0
75	-28.9	-13.0	-32.3	-23.5	-39.8	-32.6
90	-30.4	-15.6	-34.7	-24.8	-40.7	-34.0
105	-31.0	-16.3	-35.7	-25.1	-41.2	-34.2
120	-31.4	-17.4	-35.7	-25.1	-41.2	-34.3

Table 3.6. Temperature of the CCD as a function of time at $4x10^{-5}$ (vacuum) and 8 mbar CO_2 pressure, when MASC was operated at 8, -8 and -35 °C.

3.7   Control of the carbon dioxide (CO_2) in MASC

Simulated Martian conditions (100% CO_2) are achieved with an atmosphere gas control system. This system is designed to operate in two modes: static or continuous flow. In static mode the atmospheric conditions are simulated by a single gas filling of the chamber. In this mode we considered that outgassing of the chamber and samples limits the functional time period over which Martian conditions can be maintained to about 1 hour, after which the Mars atmospheric water content 0.03% is exceeded. In contrast under continuous flow conditions, CO_2 continually flows into the chamber and there is minimalbuild-up of degassed species during the experiments (<0.01%). Due to the variable pumping speed capabilities of the diaphragm pump, it can serve as a CO_2 pressure regulator during operation of the chamber in continuous flow mode (DP 1 in Fig. 3.12). In the pressure range 4-12 mbar the accuracy of the pump is typically $\pm$ 0.02 mbar.

A summary of the process design chosen to simulate Mars condition in MASC is presented in Fig. 3.12. In this scheme, the CO_2 gas is delivered from a bottle (quality 2.7 and purity 99.7%). A major design requirement is to maintain low levels of H_2O and two approaches are used. First, a parallel arrangement of Nafion tubes cleans the CO_2 gas of water (DRY-CO_2). This method of water removal uses a dry helium flow around the permeable Nafion tube to flush away the water that is transported across the membrane wall. Second, water can be flushed from the CO_2 and He supply lines prior to start up with He or N_2 using valve V6. A particle filter of 0.5 µmmesh is mounted in the CO_2 feeding line to prevent deposition of solid particles in the tank volume. A needle valve controls the required CO_2 refreshment rate between 10 and 200 ml/min (V-Meter). Flow is measured using a floating ball flow meter (FLOW-CO_2). Pressure measurements are performed with a Penning gauge (P2; $10^{-7}< p < 10^{-3}$ mbar) and a Pirani gauge (P3; $10^{-3}< p < 10^3$ mbar). Air pressurized valves V1, V2 and V3 are used for switching between CO_2 flow and vacuum operation. Valve V4 can be used for connection of a helium leak tester to the chamber to allow leak testing of the system (Fig. 3.12). It is important to mention that our design is capable of handling any gas mixing so that any planetary atmosphere can be mimicked. Equally should it be considered, a true Martian atmosphere can be established by mixing gases before they enter the chamber, e.g., 1.6 % Ar, 2.7% N_2, 0.13% O_2.
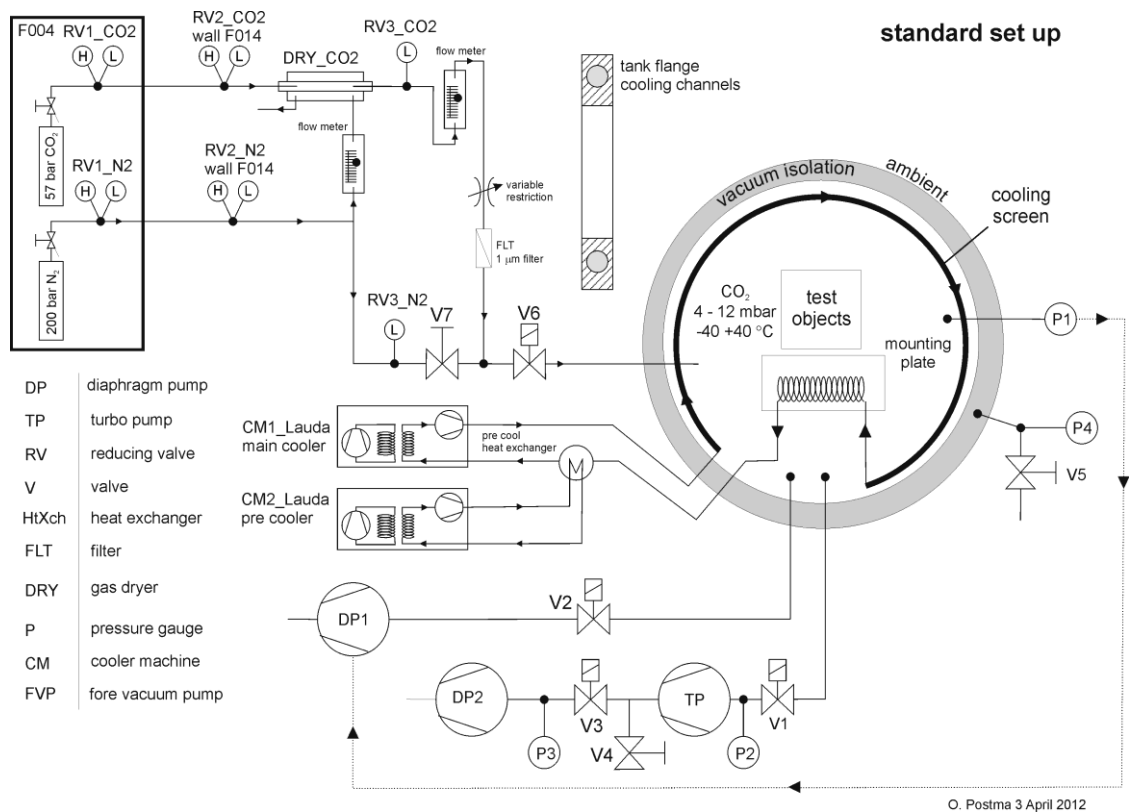
Figure 3.12. Process scheme of the vacuum system of MASC.

3.8 Temperature monitoring in the MASC

Dallas temperature sensors (type DS18B20) are used to monitor the temperature behaviour as a function of time within the chamber (Fig. 3.3). The main reason to use this type of sensor is that it is based on a 1-wire protocol (Dallas Semiconductor). Two pins on a vacuum connector are needed. Sensors (22 in total) are mounted in a chain and have a unique serial address. With a small electronic interface that connects the sensors to a computer, it is simple to collect temperature data throughout the chamber.

The temperature sensors are mounted in good thermal contact with the system components.Epoxy glue (Loktite, type: Hysol C1), which is vacuum compatible, is used to connect the sensors to stainless steel surfaces. Sensors are located throughout the chamber, the flanges, the sample holder and instrument support structure in order to have a detailed overview of the temperature throughout the MASC. It should be consider that the atmosphere in the chamber is dilute, so thermal coupling of the sensor to the CO_2 gas by conduction and convection is weak. Furthermore, radiation from the walls, flanges and cooling plate can also potentially affect the CO_2 gas temperature sensor and it could be a major problem with the measuring of CO_2 temperature. Future development work is needed to install a gas temperature sensor dedicated to measuring the ambient CO_2 temperature in the chamber.

3.9   Temperature validation inside the MASC

To determine the temperature response of samples as a function of time, a series of cooling experiments was performed in the MASC. A representative low temperature experiment under Mars atmospheric conditions inside MASC consists of five stages: (1) reshaping samples as tablets and placing them in the sample tray, (2) producing appropriate vacuum inside the MASC ($4x10^{-5}$ mbar), (3) pumping 8 mbar of CO_2 into the MASC, (4) setting the Lauda cooling machine to -35°C (5) recording the temperature data from the temperature sensors. Setting the Lauda cooling machine to temperature lower than -35 °C does not decrease further the temperature of the chamber, due to the limited cooling capacity of the system and to heat loss in different areas of the cooling system.

The starting temperature was typically 20 °C. Consequently, the Lauda temperature controller was programmed first to cool down MASC and consequently the RLS instrument and samples to 0 °C at a rate of 0.2 °C/min. This slow rate of cooling is needed to avoid unnecessary thermal stress on the spectrometer and optical fibres. For the next stage the Lauda was set to -35 °C. To protect the RLS instrument from thermal shocks, the cooling rate is set at 0.1°C/min. The results of the above cooling process are reported in Fig. 3.13. A stable temperature distribution is reached after about 27 hours.
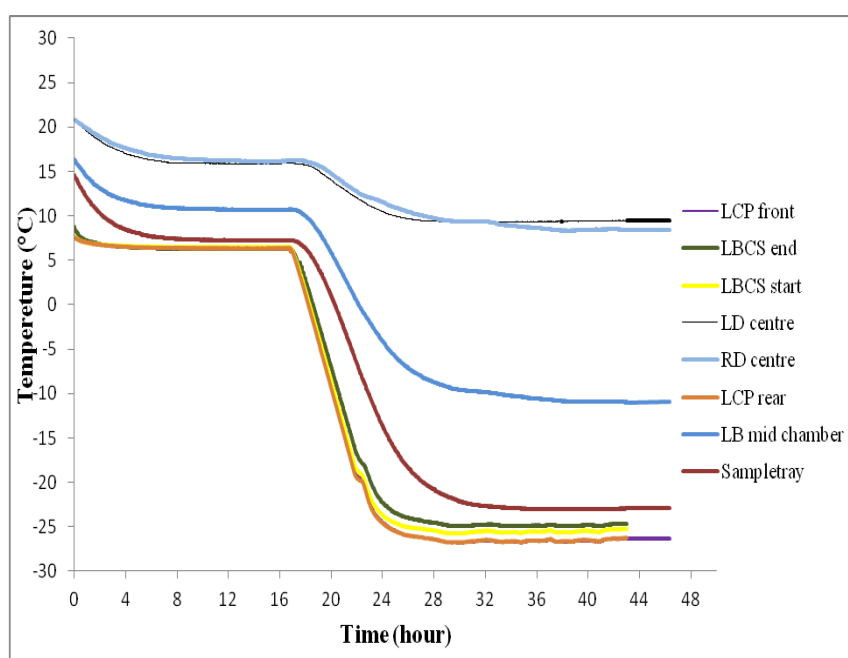
Figure 3.13. The temperature profiles inside MASC over a 44-hour period. Lauda set point was at -35 °C, while the actual Lauda temperature only achieved -30 °C. Temperature sensors are named after their position within the chamber. (L= left, R= right, B= bottom position, CS= Cooling Screen, CP= Cooling Plate, D= Door). Sensors are installed on the LBCS where the cooling fluid enters (start), and exits (end), LB of mid chamber, LCP front, LCP rear, RD centre, LD centre and sample tray.

The rear LCP sensor is directly cooled by the Freon cooling pipe and consequently records the lowest temperature ~ -27 °C inside the MASC. However, due to the open structure of the 3D liner stages, there is weak thermal conductivity between the cooling plate and sampletray.

106

Additional thermal straps were added to the initial design but currently thermal conduction is insufficient to reduce the sample tray to below ~ -23 °C. The end doors/flanges are not insulated from ambient conditions. Therefore, the two temperature sensors installed on the two main MASC doors (RD and LD) do not reach negative temperatures; +12 and 10 °C respectively. LB mid-chamber sensor (Fig. 3.3, sensor number 7) is located outside the cooling screen and is only indirectly cooled by the cooling screen. The position of this sensor is also close to the left door which is why the LB mid-chamber sensor cannot reach temperatures lower than -10 °C.

The data summarised in Fig. 3.13 clearly demonstrate the temperature difference between the entrance and exit of the cooling liquid to the cooling screen is ~ one degree difference. Moreover, the chamber reaches thermal equilibrium within ~ 27 hours since we started to decrease the temperature and hence is a practical system in which to undertake experiments. A weak point in the current design is that the sample tray does not reach a temperature lower than ~ -23 °C. As a consequence, in the next chapters, the effect of temperature on the structure of minerals and their Raman spectra will be studied in the range ~ -20 to +10 °C, although the temperature inside the ExoMars rover could be potentially as low as -30 °C. Further assessment of ways to improve the thermal conduction to the sample tray is required or the addition of greater cooling power (>0.06 kW).

3.10   Design of a sample holder with 3D linear stages

Once the manufacturing of the MASC was completed and the vacuum and temperature control systems calibrated, analyses could be performed under Martian conditions. To ensure efficient use of the system, multiple samples should be placed in the chamber to avoid breaking vacuum between analyses. An automatic sample transport system was therefore designed (Fig. 3.14). This requires an XYZ sample translation stage that operates at low vacuum and variable temperature. An XYZ stage was manufactured from three linear stages obtained from the Physik Instrument (PI), Karlsruhe Germany. Three different components were combined: M-403 (maximum travel range of 100 mm), M111 (maximum travel range of 15 mm) and M112 (max. travel range 25 mm). These 3 linear positioning stages can carry up to 20 kg and push/pull up to 50 N. They have an accuracy of about ±0.1 mm. For our experiments, a sample tray is mechanically connected to the upper linear stages.
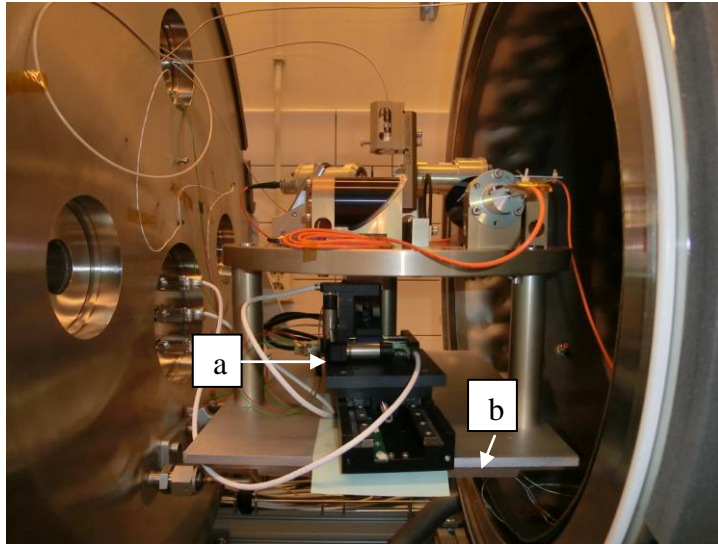
Figure 3.14. Picture of the optical head and a) the XYZ sample translation stage, installed on b) the cooling/ mounting plate inside the chamber.

The sample tray carries 10 samples of 10 mm diameter that are maintained 3 mm apart to prevent potential cross sample contamination from LIBS plasma (Fig. 3.15). The sample tray is made of aluminium with a black anodized coating to reduce potential light reflections. Anodizing is an electrolytic process that increases the thickness of the natural oxide layer on the surface of their metal parts. Anodizing also decreases chemical reactions with the metal's surroundings and so reduces potential outgassing after exposure to air.
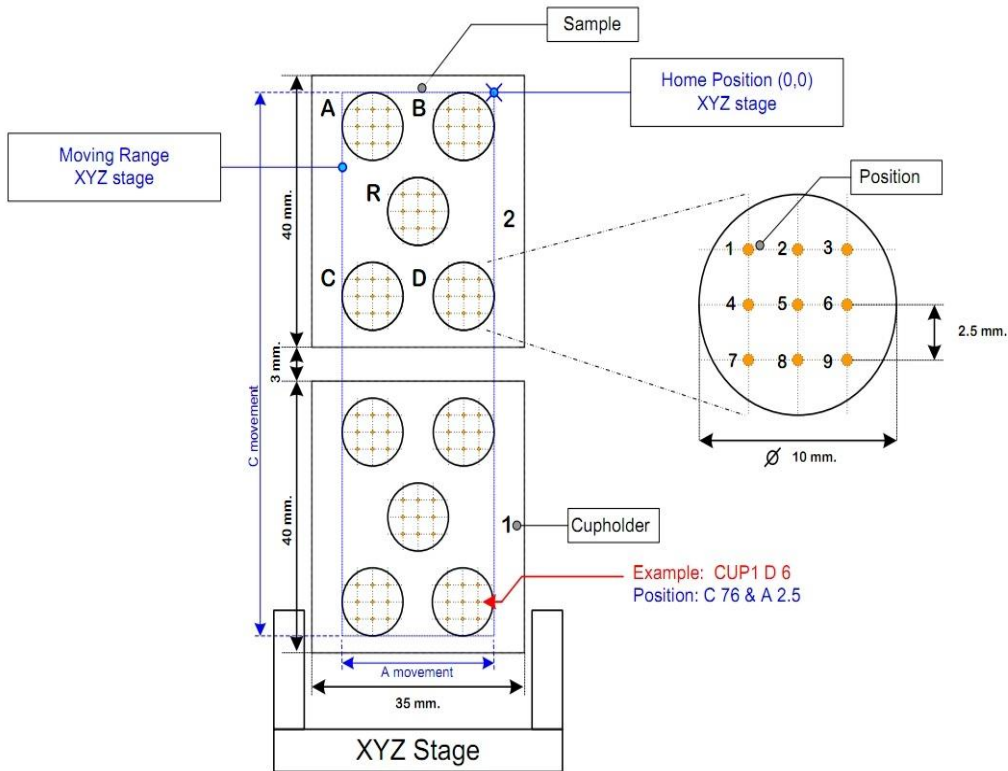
Figure 3.15. The design of the sample tray that carries 10 samples.

The computer controlled transport system can operate in two modes. First, it is possible to enter absolute positions manually for each of the 3 stages. However, for ease of use a second option is used where macros have been defined in the software with pre-defined positions. A series of macros have been programmed that make it possible to organize position and timing in a set of commands. For example the macro 'Go home' moves the samples try to a defined zero position (0, 0). The centre positions of the samples have also been configured. It is also possible to define a number of positions within the area of each specific sample. The initial version of this program is able to move to 5 positions on each sample.

The Physik Instrument linear stages were only guaranteed to operate at their highest precision at temperatures down to 0 °C. Consequently a series of tests were carried out to evaluate the minimum temperature under which the XYZ stage would function in the MASC. To follow realistic experimental conditions, the 10 sample cups were filled with different types of mineral and placed on top of XYZ sample translation stage. All three linear stages were shown to function at 0, -5 and -20 °C. However, at the sub zero temperatures the stages do not reach normal operation velocities (1.5mm/s). This is probably due to thermal contraction of the components of the stages at low temperature. However, following a series of detailed experiments we established that the system would function at lower velocities even at ~ -30 °C by using lower motor velocities. We found that 0.5 mm/s produced optimal results at low temperature and now is the default setting for all experimental runs.

3.11   Conclusion and future applications

The recently developed MASC at Vrije University in Amsterdam reaches most of our initial design goals. Specifically, it produces low pressure and low temperature that can simulate Martian environmental conditions. The operational temperature range inside the MASC is 10 to -30 °C and the pressure range is from atmospheric pressure to 10^{-5} mbar and practically any gas mixture can be used to simulate planetary atmospheric composition. The unique design of MASC, large volume (200 l) and separate cooling circuit with stable low temperature, allows detailed *in situ* characterization of space instruments and samples under simulated planetary atmospheres. For the specific goals of this thesis, we are planning to obtain a set of Raman spectra from minerals under Martian conditions. At sample level, the temperature can be varied between ~ +10 to -22 °C. Operation at lower temperature is viable but needs increasing cooling power. Colleagues will use the system to study LIBS under similar conditions.

It should be stressed that the rationale of the control and operation of MASC (including the vacuum system, O-rings vacuum compatible, cooling-pumping system, CO_2 gas supply, and sample holder with XYZ stages) is designed for operation of the RLS instrument and other space instruments.Moreover, the MASC is not restricted to simulations of the Martian environment but can be used for a whole range of experiments that require a controlled atmospheric composition and temperature.

3.12 References

Andrew, J., J. R. Effenberger, R. S. Jill, (2010), Effect of Atmospheric Conditions on LIBS Spectra. Sensors, 10(5), 4907-4925. Atkins, P. (2010), Atkins' Physical Chemistry. Oxford University Press. pp. 913–947.

Colin, A. et al., (2012), Exploring the feasibility of determining lunar soil water contents with a combined Raman/LIBS instrument. European Lunar Symposium, DLR, Berlin (Germany) – poster.

Cousin, A. et al., (2011), Laser induced breakdown spectroscopy library for the Martian environment, Spectrochimica Acta, in press. doi:10.1016/j.sab.2011.10.004.

Cremers, D. and L. Radziemski, (2006), Hystory and Fundamentals of LIBS, in: Laser Induced Breakdown Spectroscopy: Fundamentals and Applications, Cambridge University Press, pp. 9–16, Chapter 1.

Denson, S.C., C. J. S. Pommier and M. B. Denton, (2007), The impact of array detectors on Raman spectroscopy. Journal of Chemical Education, 84, p. 67-74.

Gallori, E. (2011), Astrochemistry and the origine of genetic material. Rendiconti Lincei-Scienze. Fisiche E Naturali 22 (2:113-118).

Hannifin, P. (2001), O-Ring Handbook. Parker Hannifin Corporation. http://www.parker.com/o-ring.

Jensen, L.L. et al., (2008), A Facility for Long-Term Mars Simulation Experiments: The Mars Environmental Simulation Chamber (MESCH). Astrobiology, Vol. 8, Number 3.

Mateo-Martí, E., O. Prieto-Ballesteros, J. M. Sobrado, J. Gómez-Elvira and J. A. Martín-Gago, (2006), A chamber for studying planetary environments and its applications to astrobiology, Institute of physics publishing, Meas, doi:10.1088/0957-0233/17/8/03.

Maturilli, A., J. Helbert, and M. D'Amore, (2010), Dehydration of phyllosilicates under low tempeatues: an application to Mars, 41st Lunar and Planetary Science Conference, LPI Contribution No. 1533, p.1299.

Patel, M. R., K. Miljkovic, T.J. Ringrose, and M. R. Leese, (2010), The Hypervelocity Impact Facility and Environmental Simulation at the Open University. European Planetary Science Congress, Vol. 5, EPSC, p. 655.

Sobron, P. and A. Wang, (2011), A planetary environment and analysis chamber for combined in-situ spectroscopic measurements on selected materials under planetary relevant environments, Raman Spectroscopy, doi: 10.1002/jrs.3017.

Vera, et al., (2010), Survival Potential and Photosynthetic Activity of Lichens Under Mars-Like Conditions: A Laboratory Study. Astrobiology Vol. 10(2), p. 215-27.

Chapter 4: The effect of ambient temperature and composition on the Raman study of olivine: implications for the stoichiometric changes

This chapter is the basis of a manuscript that will be submitted to the journal of Raman spectroscopy.

K. Motamedi, A. Colin, J.H. Hooijschuur, G.R. Davies.

Contents

4.1 Introduction

To better determinethe mineralogy of other planets we need to fully understand the crystal structure of all minerals so as to predict the signatures obtained by spectroscopic instruments utilised on space missions. Olivine is the common name for a suite of iron-magnesium silicate minerals, which vary in composition from Mg_2SiO_4 (forsterite) to Fe_2SiO_4 (fayalite). On Earth, olivine makes up a large proportion of the upper mantle and is known to crystallize first from many types of basaltic magmas. Hence its detection at the surface of a planet can potentially provide important constraints on the evolution of the planetary interior. For example, the internal differentiation of most planetary bodies leads to the formation of a metal core and potentially the differentiation of the mantle, sometimes associated with the development of a magma ocean (Zerr et al., 1998; Hofmann, 1997; Labrosse, 2007). The processes that cause planetary differentiation lead to a major re-distribution of Fe within planetary bodies, for example the formation of a Fe-rich metallic core. Hence knowledge of parameters such as the Mg/Fe ratio of olivine at the surface of a planet can potentially place useful constraints on the nature and extent of differentiation of a planetary interior. During melting of the silicate portion of a planetary body, Fe is preferentially partitioned into the melt phase (Walter and Tronnes, 2004). Consequently, discovery of high Mg/Fe ratios in olivine at the surface implies a silicate mantle with low Fe content and by implication we can infer the presence of a metallic core.

Another important characteristic of olivine is that it readily alters in the presence of water into clays or iron oxides (Hoefen et al., 2003). As olivine is a mineral particularly influenced by breakdown under wet conditions, the detection of olivine on the surface of the Earth and other planets can also help us assess how long it has been at the surface and provide constraints about the climate history. For instance, the extensive detection of olivine from Mars orbit on post-Noachian surfaces indicates persistently low chemical weathering rates throughout much of Mars' history (Bandfield et al., 2000; Hoefen et al., 2003; Bibring et al., 2006).

The crystal structure of a mineral such as olivine is controlled by stoichiometric relationships, relative size of atoms (ions and cations) and the nature of molecular bonds. These characteristics can be determined by different spectroscopic techniques such as Raman spectroscopy. Raman spectroscopy is selected as a method for structural and compositional characterization of minerals in ESA's first mission of the Aurora programme, ExoMars.

In this chapter we first review the structure of olivine and then analyze how the mineral structure is affected by different chemical compositions. We then assess how these variations will influence Raman spectra and if it is viable to detect such variations using the combined Raman and Laser induced breakdown Spectrometer (RLS)instrument. In addition, a fundamental goal of this thesis is to assess if the RLS instrument is a viable instrument for operation in planetary missions, therefore experiments are carried out in our Mars atmosphere simulation chamber (MASC). Olivine spectra are taken withthe RLS instrument and compared with Raman spectra determined by using a Renishaw InVia Reflex confocal

Raman microscope. Our approach is to determine olivine compositions, classify its structure using the RLS instrument based on olivine Raman vibrational modes and then examine if there are any changes when measured under Martian conditions. In addition, we will compare our Raman data to lunar and Martian samples reported by Kueble et al. (2006). This work reports olivine compositions comparable to those from Martian meteoritesand the Moon. We will investigate if comparable Raman spectra are obtained and examine the relationship between Raman peak positions and the Mg value (Table 4.1) of olivines under both terrestrial and Martian conditions.

The structure of olivine

Figure 4.1 shows the general structure of olivine. Individual SiO_4 tetrahedra are linked by mainly Mg and Fe atoms, in general M atoms. Each M atom has six oxygen neighbours. Oxygen atoms are placed in sheets parallel to the (100) plane and are positioned in approximately hexagonal arrays. The orthorhombic symmetry means that Si– O tetrahedra point in alternate directions along the z and y axes (Fig. 4.1). Half of the available octahedral voids are occupied by M atoms and one-eighth of the available tetrahedral voids by Si atoms. The M atoms do not occupy a single set of equivalent lattice positions: half are placed at centres of symmetry, M1, and half on mirror planes, M2. Therefore, there are two types of octahedra in the olivine structure. The distribution of Mg^{2+} and Fe^{2+} in M1 and M2 sites records variable ordering with the larger Fe^{2+} cation commonly showing a small preference for the smaller M1 site. M1 octahedra have a shorter average M–O bond length; 2.094 and 2.161Å for forsterite and fayalite respectively (Smyth and Bish, 1988).

To quantitatively describe the tetrahedra and octahedra, we use the terms quadratic elongation and angle variance, which are both measures of lattice deformation (Fleet, 1976). Quadratic elongation is described as a unitless measure of distortion and is based on the actual bond length compared to a theoretically undistorted octahedron. Angle variance is a measure of the variance of the central angle of tetrahedra/ octahedra compared to 90° and has units of degrees squared (Smyth and Bish, 1988).

The degree of SiO_4 tetrahedral distortion is higher in forsterite (Quadratic Elongation 1.0122, Angle Variance 49.4) than in fayalite (Quadratic Elongation 1.0085, Angle Variance 36.7), which is also reflected in the length differences of the Si–O bonds in the SiO_4 tetrahedra: from 1.6139 to 1.6549 Å (difference: 0.0410) in forsterite and from 1.6248 to 1.6533 Å (difference: 0.0285) in fayalite (Smyth and Bish, 1988). As the ionic radius of Fe^{2+} (0.86Å, high spin state, Whittaker and Muntus, 1970) is bigger than that of Mg^{2+} (0.80Å), the M1 and M2 octahedra of fayalite are more comparable than those of forsterite; the volume difference between the two octahedra in fayalite is only half that of forsterite (Smyth and Bish, 1988).
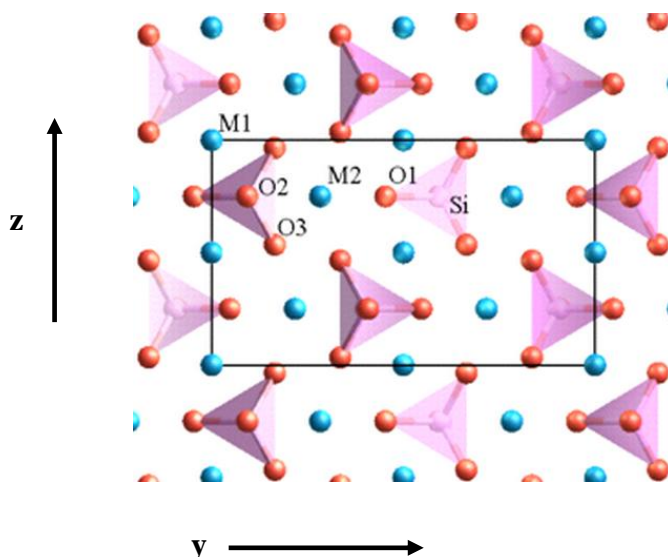
Figure 4.1. The atomic structure of olivine along the x axis is shown. Oxygen is in red, silicon in pink and magnesium/iron in blue colours. The unit cell is described by the black rectangle.

We can predict the effect of the presence of different metallic ions (Fe, Mg) on the SiO_4 tetrahedra in the olivine structure. The structural differences cause a shift of the major Raman peaks related to the stronger covalent groups in SiO_4. Here, we focus on a doublet of peaks between 815– 825 cm^{-1} (peak (a)) and 838– 857 cm^{-1} (peak (b)) and study the changes in Raman shift of the doublet based on different olivine compositions. We will examine the effect of composition on the doublet peak positions as well as relative peak heights. We also aim to assess if it is possible to determine the effect of parameters such as temperature and crystallographic orientation on the peak intensity ratio.

As mentioned above, metallic ions are bonded to oxygen. However, silicon is also in oxygen tetrahedral sites. Hence, the difference in atomic masses and bonds between Fe, Mg and oxygen affect the vibration frequencies of the strong Si– O bonds resulting in shifts in Raman peaks. Potentially, peak shifts such as peak (a) and peak (b) can be used to calculate the ratios of the cations involved. Naturally occurring olivines also have minor amounts of MnO, NiO and CaO but at generally less than 0.5 wt %. Therefore in most naturally occurring olivine, these elements are expected to have minimal effect on Raman spectra.

4.2   Sample selection

Olivine detected on Mars records a compositional range of Fo_{60} to Fo_{70} in the southwest region of Nili Fossae and Fo_{40} to Fo_{60} in the northeast region of Nili Fossae (Hoefen et al., 2003;Fo is the molar ratio and is equal to Mg/(Mg+Fe) reported in mol%). We have selected natural olivine samples with comparable compositions (olivine 1, olivine 2, olivine 3 and olivine 4) and also made use of a synthesised fayalite. Table 4.1 lists the compositions of two selected samples determined by electron microprobe analysis (EMPA) labelled olivine 1 and 2 with Fo value of 64 and 93 respectively.

Two additional olivine samples, olivine 3 and olivine 4, were also studied by EMPA. Olivine 3 and olivine 4 where obtained by mineral separation from basaltic lavas. Unfortunately, despite initial thin section studies that suggested a single olivine population both samples contained olivine with a large range of compositions and individual grains with marked zonation on a 20 μm scale. In total, Fo varied between 69 and 85. Consequently it is not viable to measure these samples with the RLS instrument as it is impractical with the current set up to analyse specific regions of an individual grain with the required spatial resolution to ensure a specific composition is measured. These samples did not provide useful information for the main goal of the study, i.e. assessing the capabilities of the RLS instrument to identify different olivine compositions under Martian conditions.

The final sample used was a pure fayalite synthesised by Dr Jellie de Vries as part of her PhD research. Table 4.2 shows the compositions of the synthesised fayalite.

Due to the small grain size (less than 15 μm) that usually characterises high pressure-temperature experimental products, we were unable to find and focus on the grains and obtain good quality Raman spectra using the RLS instrument. In contrast, the more user friendly design of the Renishaw associated with a smaller spot size (2 μm) allowed us to obtain a Raman spectrum (Fig.4.5). EMPA determined the composition of the olivine to be Fo_{01}.

4.3   Analytical methods and data handing

Our analyses were performed with three instruments, which are described in the following sections.

4.3.1   Electron microprobe analyser

Electron microprobe analysis (EMPA) is an almost non-destructive method to determine the chemical composition of solid materials. EMPA uses a high-energy focused beam of electrons to generate X-rays that are characteristic of the elements within an unknown sample. Chemical compositions are determined by comparing the intensity of X-rays signals with those derived from standards of known composition and correcting for the effects of absorption and fluorescence in the sample. The EMPA of major element data will be compared with Raman analyses to understand how different compositions lead to different stoichiometry and how this results in changes in Raman spectra. This methodology allows the determination of the relationship between chemical composition from EPMA and spectral peak position from Raman spectra. The EMPA were collected on a JEOL JXA-8800M Superprobe with four wavelength dispersive spectrometers (WDS) at the VU University Amsterdam. Spot analyses were performed by a focused beam where the smallest practical beam diameter was used for surface analysis, in this case 1-3 μm.

	Olivine1, Fo$_{64}$			Olivine 2, Fo$_{93}$		
	Weight%	STDEV	2 σ	Weight%	STDEV	2 σ
MgO	31.79	0.44	0.23	51.27	0.18	0.10
SiO$_2$	37.27	0.37	0.20	40.75	0.28	0.15
FeO	31.34	0.47	0.25	6.36	0.09	0.05
CaO	0.01	0.01	0.00	0.01	0.00	0.00
Al$_2$O$_3$	0.01	0.01	0.00	0.00	0.01	0.00
MnO	0.41	0.02	0.01	0.08	0.01	0.01
TiO$_2$	0.01	0.01	0.01	0.01	0.01	0.00
NiO	0.14	0.01	0.01	0.35	0.01	0.01
Cr$_2$O$_3$	0.00	0.00	0.00	0.03	0.01	0.00
Total	100.98	0.40	0.21	98.86	0.33	0.18

Table 4.1. Average compositions of the olivine 1 and olivine 2 determined by EMPA.

The EMPA operating conditions were an acceleration voltage of 15 kV and the nominal beam current is about 25 nA. The counting times for the measurement of each element were 25 seconds on the peak and 12.5 seconds on the background for all oxides measured except FeO where 36 seconds were measured on the peak and 18 seconds on the background. In general minor elements are measured with longer counting times than major elements. Measurements are calibrated and standardized against well-characterized standards. In this case CaO and SiO$_2$ were measured in diopside. MgO in olivine, FeO in fayalite, TiO$_2$ in ilmenite, NiO in synthetic NiO, MnO in tephrite and Al$_2$O$_3$ in corundum.

Standard deviation (*STDEV*) and standard error (σ):

(2σ) are reported for 14, 24 and 6 analyses in samples olivine 1, olivine 2 and fayalite respectively. The true standard error of the sample mean is defined by:

$$\sigma = 2(\frac{STDEV}{\sqrt{n}}) \qquad (4.1)$$

Where *STDEV* is the standard deviation of analyses and *n* is the number of analyses of a sample.We have calculated 2σ to show the maximum error.σ (standard error) is an estimate of how close to the population mean our sample mean is likely to be, whereas standard deviation is the degree to which individuals within the sample differ from the sample mean (Gurland and Tripathi, 1971; Sokal and Rohlf, 1981).

Fayalite, Fo_{01}			
	Weight%	*STDEV*	2σ
SiO_2	30.44	0.19	0.15
Al_2O_3	0.02	0.02	0.02
FeO	70.62	0.27	0.21
CaO	0.00	0.00	0.00
MgO	0.01	0.00	0.00
Total	101.09	0.21	0.10

Table 4.2. Average compositions of the fayalite sample determined by EMPA (De Vries, 2012).

4.3.2   Micro-Raman spectrometer

A commercial Renishaw InVia Reflex confocal Raman microscopewas used for initial Raman characterisation. This commercial Raman microscope uses a 300 mW 785 nm diode laser asan excitation sourcein combination with a 1200 lines per mm (l/mm) grating. It has multiple optic options with 5, 20 and 50 times magnification objectives, which produce spot sizes of 20, 5 and 2 μm respectively. The spectral resolution of adjacent peaks in the system is ~ 3 cm^{-1} and accuracy of the system is about 0.1 cm^{-1}. The charge coupled detector (CCD) is cooled to -70 °C to ensure ultra-low dark noise.

4.3.3   The combined Raman and Laser induced breakdown Spectrometer (RLS) instrument

The RLS instrument uses a laser with an excitation wavelength of ~ 659 nm for Raman analysis. It weighs less than 30 g and has an output of 20 mW (For more details see chapter two). The spectralresolution is ~ 4 cm^{-1}.The RLS instrument was used to obtain Raman spectra from different olivine compositions under Martian conditions within the MASC. These experiments were also effectively a test of the ability of the RLS instrument to act as a field instrument for planetary missions. Such data are required in order to establish if the RLS instrument will be able to provide information about the processes that formed specific geological environments and hence help unravel the history of a planet in general.

4.4   Raman study of olivine

To better investigate the Raman spectra of the selected olivine samples, we first consider the vibrations of an isolated silicate tetrahedron. The isolated silicate tetrahedronis characterised by symmetric and asymmetric stretching and bending vibrations (Fig. 4.2). The symmetric stretch of the tetrahedron depends on the strength of the Si$-$O bond. The symmetric bending vibration, however, is controlled principally by the O$-$Si$-$O angle bending force constant. For silicate tetrahedron, peaks in the Raman spectral region between 800 and 950 cm^{-1} are formed by the vibrational modes of symmetric stretch (v_1). The Raman peaks in the spectral region 300$-$500 cm^{-1} are attributed mostly to symmetric bending vibrations (v_2). The vibrational modes of asymmetric stretch (v_3) produce weak Raman peaks in the spectral region 850$-$1200 cm^{-1}. Finally peaks at 400$-$600 cm^{-1} are attributed to asymmetric bending vibrational modes (v_4) (Figs. 4.2 and 4.3). We expect that the effect of low temperature on the symmetric and asymmetric stretching vibration might be clearly observed as the bonds of the molecule usually become shorter at lower temperature.
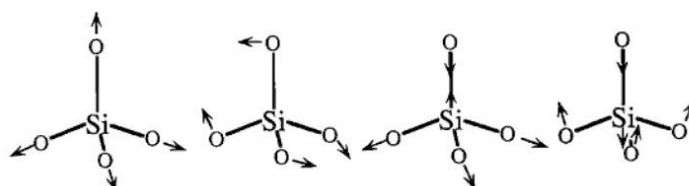
$v_1v_2v_3v_4$

Figure 4.2.The vibration mode of an isolated silicate tetrahedron, v_1: symmetric stretch, v_2: symmetric bend, v_3: asymmetric stretch, v_4: asymmetric bend (modified from Silverstein, et al., 1981).

As mentioned previously, individual SiO_4 tetrahedra in the olivine mineral structure are connected by Mg and Fe atoms and each Mg and Fe atom has six oxygen neighbours. The olivine group forms a complete solid solution series between forsterite (Mg_2SiO_4) and fayalite (Fe_2SiO_4). The four internal SiO_4 vibration modes are supposed to be retained in the spectra but are slightly changed by the olivine crystal composition. Previous workers have demonstrated that the Raman spectrum of olivine can be practically divided into three spectral areas: < 400 cm^{-1}, 400$-$700 cm^{-1} and 700$-$1100 cm^{-1}(Fig 4.3; Ishii, 1978; Kuebler, et al., 2006; Chopelas, 1991).
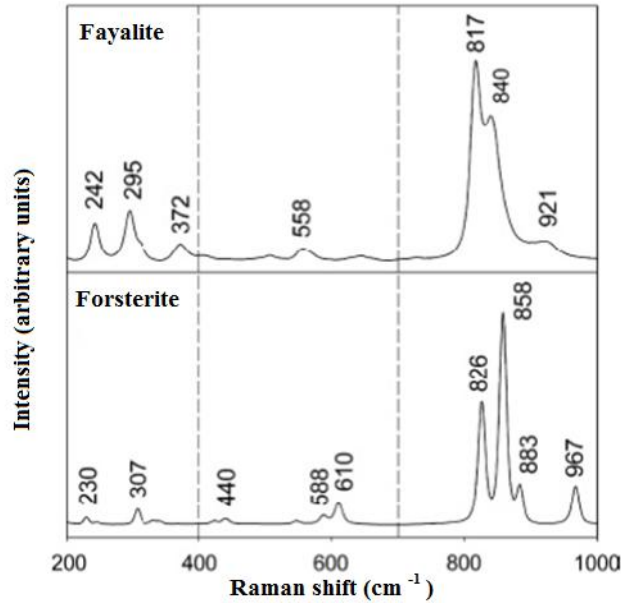
Figure 4.3. Spectra of the olivine end members: fayalite and forsterite. The three distinct areas of the spectra are divided by the dashed lines (Kuebler, et al., 2006;Note that the exact mineral compositions are not provided in the publication).

In general, peaks below 400 cm^{-1} are formed by lattice modes. Lattice modes are caused by the movements of groups of atoms in the crystalline lattice. In the olivine crystal structure, rotational and translational motions of SiO$_4$ tetrahedra and translational motions of octahedral cations (Mg^{2+}, Fe^{2+}) in the crystal lattice create the lattice modes (Chopelas, 1991). Peaks in the 400–700 cm^{-1} spectral region are derived from internal bending vibrational modes of the SiO$_4$ ionic groups, Fig. 4.3. The peaks lower than 400 cm^{-1} and peaks in the 400–700 cm^{-1} spectral area are usually much weaker than those in the 700–1100 cm^{-1} region (Wang et al., 1995; 2004b). Peaks in the area of 700–1100 cm^{-1} are attributed to the internal symmetric and asymmetric stretching modes of the SiO$_4$ tetrahedra. The main feature within this area is a doublet of peaks between 815–825 cm^{-1} (peak (a)) and 838–857 cm^{-1} (peak (b)). The positionsof the doublet depend on the chemical bonds that have a higher degree of covalence. Nevertheless, because the metallic ions within olivine share an O atom with the silicate tetrahedral, the attractive force between the different ions (Fe and Mg) and difference in atomic mass can affect the vibrational frequencies of the Si– O bonds. These effects cause the shifting of the doublet peak positions when composition varies between fayalite and forsterite. They are the main reason responsible of controlling the Raman spectra of olivine in the spectrum between 700 and 1100 cm^{-1}. From Hook's law (equation 4.2), it is clear that the vibration modes are a function of the force constant of the vibration and the mass of the participating atoms:

$$\nu = \frac{1}{2\pi c}\sqrt{\frac{k_0}{\mu}} \qquad (4.2)$$

where μ is reduced mass of participating atoms (see section 2.2.4), k_o is force constant, V is vibrational frequency in wavenumber, c is speed of light. Consequently, changes in mass associated with compositional variations of olivine will produce different vibration frequencies. We should also keep in mind that at low temperature, bonds of the molecule usually become shorter. Therefore, the value of k would increase and cause possible changes in Raman peak positions.

The relationship between the Mg number (Mg/Mg+Fe) and the Raman frequency shifts of olivine hasbeen discussed by Guyot et al., 1986; Wang et al., 1995, 2004b Kuebler et al., 2006. These studiespropose correlations between the positions of the two peaks occurring between 815– 825 cm^{-1} and 838– 857 cm^{-1} in Raman spectra and the Mg value of Mg– Fe olivine. In our study we review the results of pervious work and asses the ability of the RLS instrument to identify different olivine mineral compositions under Martian conditions. We may expect an effect of temperature on strong vibration modes such as symmetric stretching vibration. Other vibration modes are weak and consequently we expect it will be hard to assess if there are small differences between terrestrial and Martian conditions.

4.5 Renishaw and RLS data of selected olivine samples

In this section, we present olivine Raman spectra obtained with: a) Renishaw Raman microscope under laboratory condition, b) RLS instrument under vacuum condition at 10 and -20 °C, c) olivine RLS spectra under CO_2 condition at -20 °C.

The Raman spectra of olivine 1 (Fo_{64}) and olivine 2 (Fo_{93}) taken with the Renishaw InVia Reflex confocal Raman microscope are presented in Fig. 4.4.
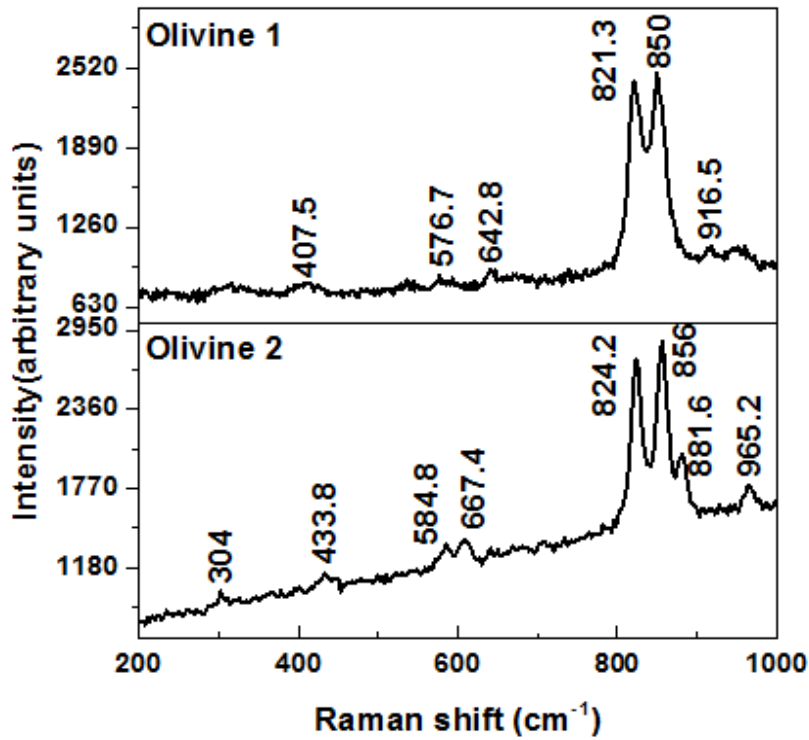
Figure 4.4. The Raman spectra of olivine 1 (Fo_{64}) and olivine 2 (Fo_{93}) taken with the Renishaw InVia Reflex confocal Raman microscope for the 200-1000 cm^{-1} region.

A Raman spectrum of fayalite (Fo_{01}) taken with the Renishaw InVia Reflex confocal Raman microscope is presented in Fig. 4.5.
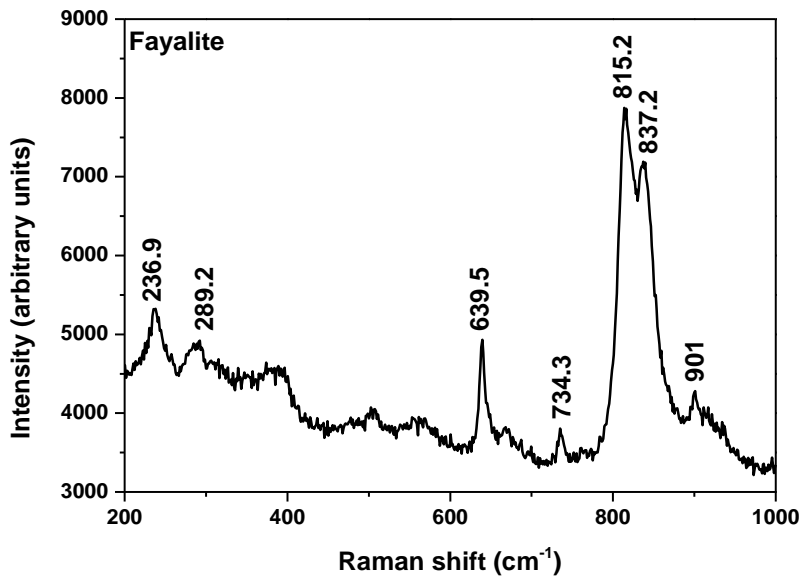
Figure 4.5. The Raman spectra of fayalite (Fo_{01}) taken with the Renishaw InVia Reflex confocal Raman microscope for the 200-1000 cm^{-1} region.

The Raman spectra obtained from 10 random grains of olivine 3 and 4 are shown in Figs. 4.6 and 4.7 respectively.
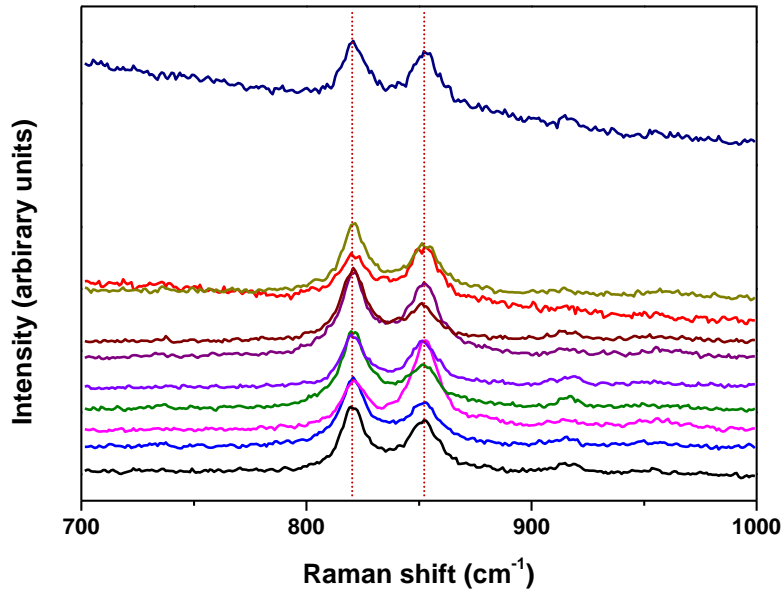
Figure 4.6. The Raman spectra obtained from 10 random grains of olivine 3 taken with the Renishaw InVia Reflex confocal Raman microscope for the 700-1000 cm^{-1} region. Spectra are vertically offset for legibility.
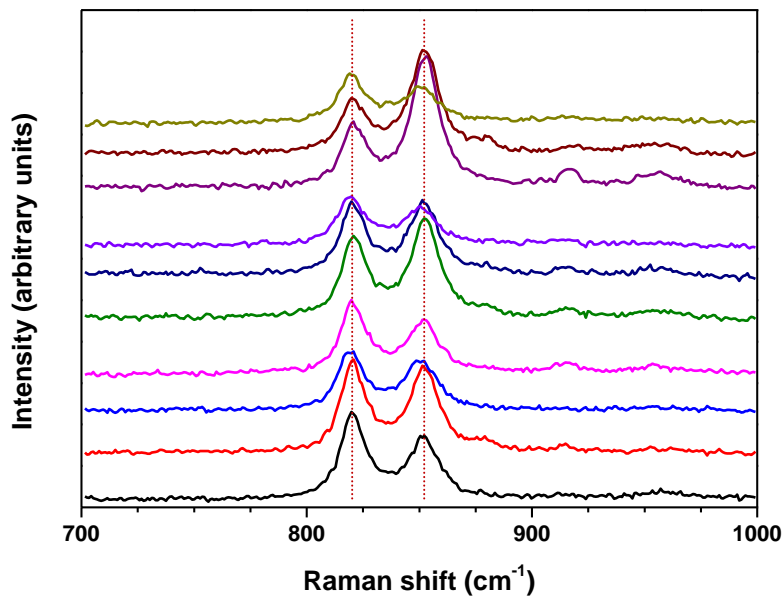
Figure 4.7. The Raman spectra obtained from 10 random grains of the olivine 4 taken with the Renishaw InVia Reflex confocal Raman microscope for the 700-1000 cm^{-1} region. Spectra are vertically offset for legibility.

The RLS Raman spectra of olivine 1 and olivine 2 are presented at Fig. 4.8. These spectra obtain under vacuum condition at 10 °C.
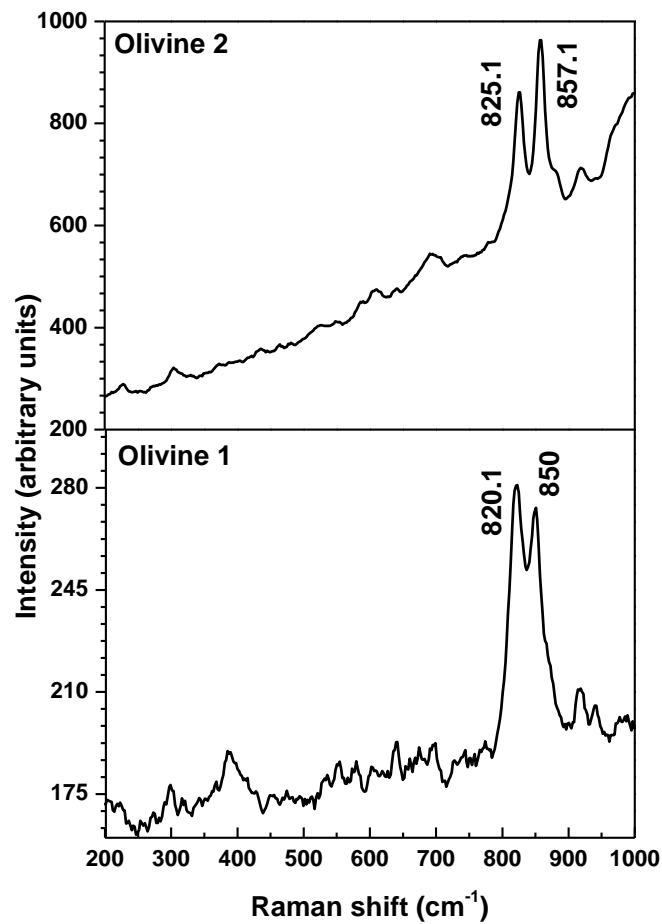
Figure4.8. The RLS Raman spectra of olivine 1 and olivine 2 obtain under vacuum condition at 10 °C.

Raman spectra of olivine 1 and olivine 2 obtained using the RLS instrument under vacuum condition at +10 and -20 °C are present at Figs. 4.9 and 4.10.
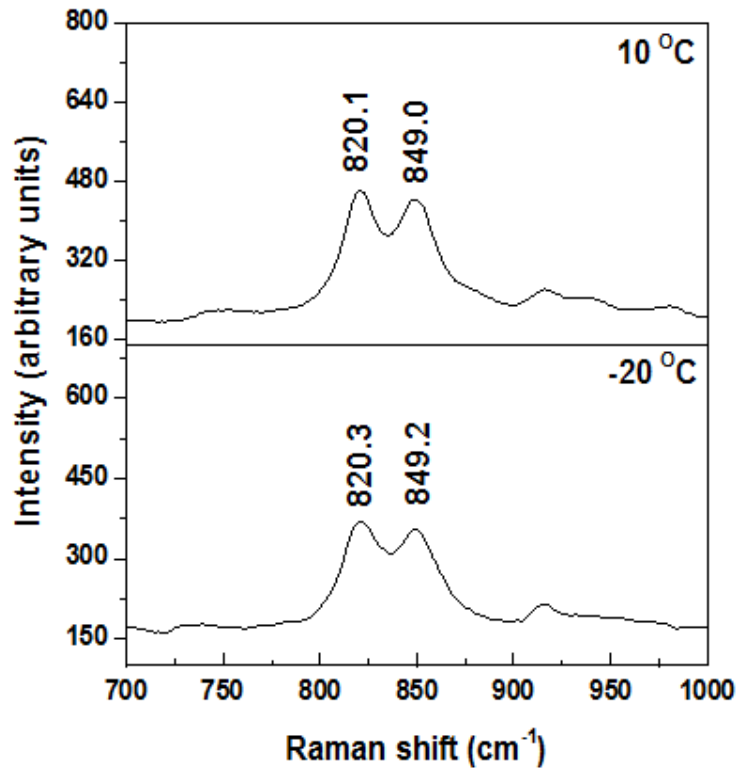
Figure 4.9. RLS Raman spectra of olivine 1 in the range 700– 1000 cm^{-1}, the measurement conditions are under vacuum condition at +10 and -20 °C.
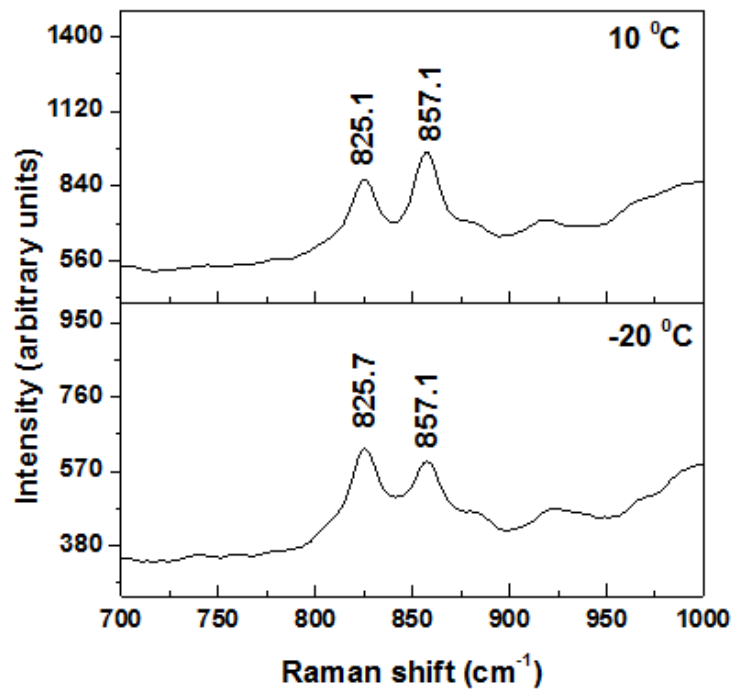
Figure 4.10. RLS Raman spectra of olivine 2 in the range 70– 1000 cm^{-1}, the measurement conditions are under vacuum condition at +10 and -20 °C.

In Figs. 4.11 and 4.12, Raman spectra of olivine 2 and olivine 1 obtained under 8 mbar CO_2 pressure at -20 °C are presented.
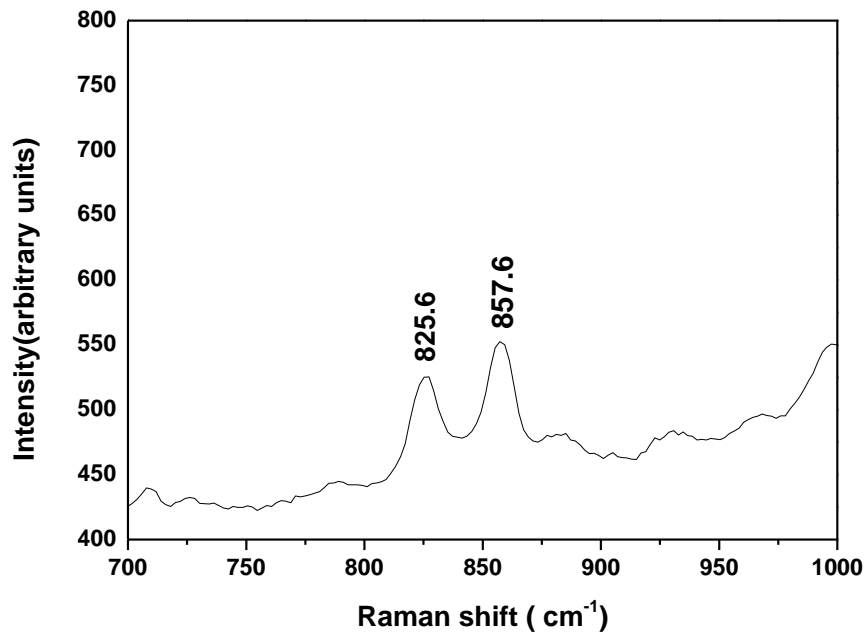
Figure 4.11. RLS Raman spectra of olivine 2 in the range 700– 1000 cm^{-1}, the measurement condition is CO_2 atmosphere with -20 °C.
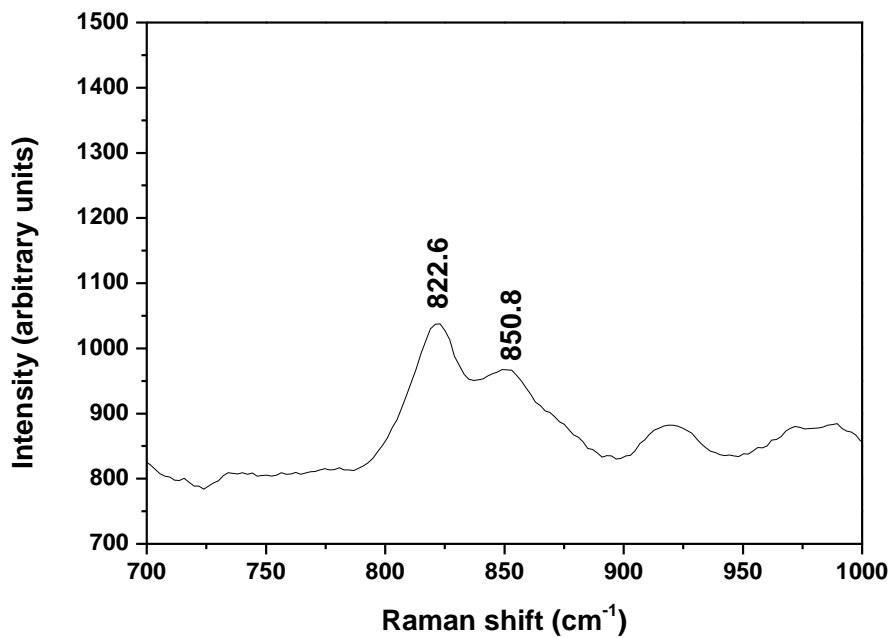
Figure 4.12. RLS Raman spectra of olivine 1 in the range 700– 1000 cm^{-1}, the measurement condition is CO_2 atmosphere with -20 °C.

4.5.1 Discussion of the Renishaw olivine data

Figure 4.4 presents the Raman spectra of olivine 1 and olivine 2 obtain with the Renishaw Raman microscope. As expected, peaks below 400 cm^{-1} and in the 400–700 cm^{-1} spectral region are weak. These weak peaks are not often determined in multi-phase spectra from mixtures such as igneous materials (Kuebler et al., 2006). Moreover the small peak size will make effective detection under planetary conditions particularly difficult. Therefore, we focus on the 700–1100 cm^{-1} region with stronger peak intensities, attributed to the internal symmetric and asymmetric stretching vibration modes of the SiO_4 tetrahedron. These vibration modes could be affected by temperature variations.

As we explained in the section of the Raman study of olivine, olivines with different Fo values have different Raman vibrational frequencies of Si– O bonds. According to the EMPD analyses, olivine 1 and olivine 2 have Fo value of 64 and 93. These variations are clearly resolved in the Renishaw Raman spectra with shifts in peaks (a) and peak (b) related to the change of olivine composition. The different Fo value is the major reason responsible for controlling the Raman spectra of olivine in the spectra between 700 and 1100 cm^{-1} (Fig 4.4 and Table 4.3). The observed peaks in the Raman spectrum of olivine 2 (Fo$_{93}$) are comparable to peaks of fosterite with Fo of 91 and 100 reported by Kuebler et al (2006).

	Fo ranging	Peak (a) cm^{-1}	Peak (b) cm^{-1}
Olivine 1	Fo$_{64}$	821.3	850.0
Olivine 2	Fo$_{93}$	824.2	856.0
Synthesised fayalite	Fo$_{01}$	815.2	837.2

Table 4.3. The Renishaw Raman peak positions of olivines with different Mg / (Mg + Fe) compositions.

In the Raman spectrum of the fayalite sample of Keubler et al., 2006 peak (b) appears as a shoulder of peak (a), Fig. 4.3. We establish a similar relationship in the Renishaw analysis.As an example, Raman spectrum of the synthesised fayalite, Fig. 4.5 shows peak (b) at 837.2 cm^{-1}as a shoulder of the peak (a) at 815.2 cm^{-1}. Two peaks at 639.5 and 734.3 cm^{-1} are also resolved in Renishaw Raman spectra.We considered the detection of these peaks is due to the presence of contamination (the epoxy resin) in the fayalite sample as theses peaks were not observed at pure fayalite Raman spectrum by Kuebler**.**

The variations in Raman spectra based on different Fo values for olivine 3 and 4 are shown in Figs. 4.6 and 4.7 respectively. The variations in Raman peak positions are about 2 cm^{-1} for olivine 3 and 3.5 cm^{-1} for olivine 4. These variations are significantly greater than the peak position error (~ 0.4 cm^{-1}) of the RLS instrument. Hence we can expect to detect these variations using the RLS instrument. However, due to the limitation of optical view of the sample within the MASC we could not perform measurement of specific individual grains. We encountered the same problem with the fine grained fayalite sample, which proved to be impossible to measure using the RLS instrument.

We conclude that using the Renishaw Raman microscope under laboratory condition, we could clearly resolve the different peak positions for selected olivine samples, fayalite, olivine 1 and olivine 2.Therefore, we used samples olivine 1 and 2 to assess the RLS instrument performance inside MASC under variable temperatures and atmospheric pressure.

4.5.2 Discussion of the RLS olivine data

4.5.2.1   Effect of the vacuum condition and low temperature on RLS olivine Raman spectra

In the next step of our experimental protocol samples and the RLS instrument were placed inside the MASC. Martian environmental conditions (low pressure and temperature) were applied to both the sample tray and RLS instrument. Such a study is important for further understanding how the fine structure and properties of minerals vary with physical conditions; for example possible changes in the length of atomic bonds. These data are required to assess how great is the need to characterise mineralogy under Martian conditions before the launch of ExoMars. To our knowledge only little work has yet been reported on the effect of temperature on the Raman spectra of olivine (Weber et al., 2012; Kolesov and Geiger, 2004; Chopelas, 1991) and in previous work samples were locally cooled via their sample tray or holder. In addition, there have been no specific studies based on the effect of the environment condition on the olivine spectra. Hence, we developed such studies with the RLS instrument within MASC to evaluate any possible pressure/temperature dependency of olivine Raman spectrum.

In the RLS Raman spectra of both olivine 1 and olivine 2, peaks below 700 cm^{-1} were not resolved from the background noise due to low laser power and relatively high background noise levels. In addition, these peaks are not regularly determined in mulit-phase spectra from mixtures samples (Kuebler et al., 2006). The application of the current design of the RLS instrument to planetary missions means that determination of the weak Raman peaks below 400 cm^{-1} is impractical. Peaks below 700 cm^{-1} were not the main focus of our study and we concentrated on the 700–1100 cm^{-1} region. The most characteristic olivine peaks with the strongest intensity appear in this spectral region.

In Fig. 4.8, we present RLS Raman spectra of olivine 1 and olivine 2 obtained under vacuum (10^{-5} mbar) at 10 °C. The reported RLS spectra focus on the positions of the olivine doublet peak in the 700–1000 cm^{-1} region. Compositional variations in the olivine 1 and olivine 2 (Fo_{64} and Fo_{93}) result in clear shifts in the wavelengths of the doublet peaks between the two olivine samples. The RLS Raman spectrum of olivine 2 (Fo_{93})has distinct peaks at 825.1 cm^{-1} and 857.1 cm^{-1}. The maximum intensity occurred at the second of these two peaks. In the RLS Raman spectra of olivine 1 (Fo_{64}), the doublet is less well resolved than of olivine 2 (Fo_{93}) and the peak near 850.0 cm^{-1} appears as a shoulder of the peak near 820.1 cm^{-1}.

In general, the double peaks in fayalite Raman spectra are closer together (lower resolution) due to the less distorted SiO_4tetrahedra and this leads to a less complex Raman spectra (Kuebler et al., 2006).The lesser separation of the doublet peaks in olivine 1 is because of

theless distorted SiO_4 tetrahedra and greater similarity of the M1 and M2 octahedra in the olivine 1 mineral structure compared to olivine 2 structure.

As a test that the samples chosen for study were representative of potential lunar and Martian samples, we compare the RLS Raman data with the Raman data of Martian meteorite EETA 79001.530 and Twin Sister (eight lunar, Martian and terrestrial olivine samples from Kueble et al., (2006)). Olivine 1 from this study has Fo value (64) close to EETA 79001.530 (Fo_{62}) and olivine 2 has Fo value (93) as Twin Sister (Fo_{92}). We confirmed that we obtain comparable Raman peak positions for olivine 2 and EETA 79001.530 and olivine 1 and the Twin Sister samples (Table 4.4).

sample	Fo	Peak (a) (cm^{-1})	Peak (b) (cm^{-1})
Olivine 2/ Twin Sister	Fo_{93}/ Fo_{91}	825/823	857/855
Olivine 1/ EETA 79001.530	Fo_{64}/ Fo_{62}	820/820	850/849

Table 4.4. Comparison between Raman peaks from Kueble et al., 2006 and RLS Raman peaks form olivine 1 and olivine 2 under vacuum (10^{-5} mbar) at 10 °C.

In the next part of our study we examine the influence of temperature on RLS Raman spectra under conditions expected to be used for the ExoMars mission. Our study is a practical approach designed not to resolve potential marked variations in Raman spectra at extreme temperatures but as a test of the effects likely to be encountered by Raman analysis by the ExoMars rover. ExoMars experiments are expected to be performed inside the rover at temperatures in the range 10 to -30 °C.

The data obtained in our experiments at temperatures between 10 and to -20 °C are presented in Table 4.5 and Figs 4.9 and 4.10. The position of peak (a) near 825 and 820 cm^{-1} in olivine 2 and olivine 1 and peak (b) near 857 and 849 cm^{-1} in olivine 2 and olivine 1 show no resolvable change with temperature; i.e. within the ~0.4 cm^{-1} error of the RLS instrument. The work of Kolesov (2004), similarly reported that there is no shift in the two peaks of the fayalite sample at temperatures between -40 to -268 °C.

In chapter two (section 2.2.2), it was discussed that the intensities of specific peaks depends on the polarizability of the molecule in the mineral, the intensity of the laser excitation source and the concentration of the Raman active group in the mineral structure. Therefore, we initially considered undertaking a rigorous assessment if it was possible to use intensity ratios of the different Raman peaks to establish if such parameters also proved to be a characteristic feature of Raman spectra of olivine in terms of composition, crystallographic orientation and temperature.

Most minerals have different optical properties depending on the cyrstallographic orientation. Previous work by Ishii (1978) and Chopelas (1991) established that this is the case for the orthorhombic olivine mineral group. Consequently the intensity of Raman peaks is known to change depending on the crystallographic orientation of the mineral.

Kolesov (2004) also reported a change of the relative intensity of fayalite Raman peaks at low temperature (-40 to -268 °C). The change of intensity might be a result from Fe in olivine, by which magnetic interactions can take place. In our measurements we also observe the effect of the Fe in the structure of olivine 1 at lower temperature with a decrease the intensity of the peak at 857.1 cm^{-1} in olivine 2. For example, in olivine 2, the intensity ratio of peak (a)/peak (b) under vacuum at 10 °C is 0.89. However, this intensity ratio at -20 °C is about 1.02.

The data presented above establishes that there are distinct variations in the intensity ratios between Raman peaks. Unfortunately, initial work with the RLS instrument immediately proved that it is impractical to determine the crystallographic orientation of each mineral under study in a context that mimics field conditions i.e., as the RLS instrument would be used upon Mars. More importantly in respect of the planned experimentation, the laser excitation wavelength in the RLS instrument (and the power output 20 mW) was unstable making it impossible to consistently produce repeatable data. Hence, we were unable to make a quantitative assessment of if we could use the intensity ratio of Raman peaks to study, for example, olivine composition or crystallographic orientation. The latter is probably of limited use in most geological environments but the ability, for example, to determine if minerals have a preferred orientation could provide valuable information about geological or bio-geochemical processes.

From this work we are only able to conclude that the intensity of Raman peaks in natural minerals is variable as is the intensity ratio between peaks. Further work will be required with a stable instrument to assess if peak intensity ratios can be used to help distinguish different olivine compositions and/or crystallographic orientation.

We conclude that for olivine there is no resolvable change (based on the temperature) in peak positions under the analytical conditions operable inside the ExoMars Rover. Hence, these data establish that the potential temperature induced variation in peak position discussed previously is not relevant over the range studied in this work (+10 to -20 °C). Moreover, the study of Raman peak couplet is a viable technique for determining olivine composition on Mars using the RLS instrument.

	Olivine 2		Olivine 1	
Vibration modes (cm^{-1})	10 °C	-20°C	10 °C	-20°C
Peak (a)	825.1	825.7	820.1	820.3
Peak (b)	857.1	857.1	849.0	849.2

Table 4.5. RLS Raman peaks of olivine 1 and olivine 2 at 10 and -20 °C.

4.5.2.2 Effect of 8 mbar CO$_2$ pressure at low temperature on olivine Raman spectra

In Figs. 4.11 and 4.12, the Raman spectra are reported for olivine 1 and olivine 2 obtained at -20 °C in an atmosphere of 8 mbar CO$_2$. The identification of peak (a) and peak (b) in the olivine Raman spectra were possible (Table 4.6). In olivine 2 peak (a) and peak (b) are recorded with the Raman shifts of 825.6 and 857.6 cm^{-1}. For olivine 1 Raman shifts are 822.6 and 850.8 cm^{-1}. The positions of the peaks reported in Table 4.6 for olivine 2 and olivine 1 under CO$_2$ atmosphere conditions are within ~ 0.5 and 2 cm^{-1} those obtained under vacuum conditions. Since the peaks were not well resolved the exact peak position could not be determined.

We estimate that the error in peak identification for olivine 1 (~2 cm^{-1}) under Martian conditions was due to none-resolved peaks. Hence we cannot confidently detect any shift in wavenumber in the olivine 1 spectra. The intensity ratios of the Raman spectra are comparable to spectra obtained under vacuum conditions.

Vibration modes (cm^{-1})	Olivine 2		Olivine 1	
	10^{-5} mbar Vacuum condition	8 mbar CO$_2$ pressure	10^{-5} mbar Vacuum condition	8 mbar CO$_2$ pressure
Peak (a)	825.7	825.6	820.3	822.6
Peak (b)	857.1	857.6	849.2	850.8

Table 4.6. RLS Raman peaks for olivine 1 and 2 under vacuum (10^{-5} mbar) and at 8 mbar CO$_2$ condition; at -20 °C in both cases.

4.6   Conclusion

With the RLS instrument under vacuum /CO$_2$ condition at 10 and -20 °C, the doublet peaks in the 820 to 860 cm^{-1} range were identifiable and the intensity of these peaks mean that olivine identification under Martian conditions is clearly possible. However, in the context of application of the RLS instrument under planetary conditions it must be noted that the determination of some lattice vibration modes that produce weak Raman peaks was not possible. To detect weak peaks, we need to increase the laser power and/or operate the CCD at lower temperature (-70°C) to increase the signal to noise ratio.

Olivine produces Raman modes in the 200 to 1000 cm^{-1} range. Comparison of the frequencies of the various mode categories indicates that the doublet peak in the 820 to 860 cm^{-1} range is most sensitive to compositional variation. These data are similar to those found for the Raman spectra reported in the work of Kuebler, et al., (2006). These data suggest that not only can accurate spectral data yield good estimates of determining different type of olivine

but the opposite may also be true, i.e., that accurate Fo calculation can be used to estimate spectral properties.

We should keep in mind that the identification of the doublet peaks depends on the resolution of the RLS instrument (4 cm^{-1}). Further study is needed with numerous (>10) olivine compositions (Fo$_{01}$– Fo$_{100}$) to fully determine the resolution that can be achieved by the RLS instrument.

Further study at the lower temperature is needed to evaluate any effect of low temperature on the peak (a) and peak (b) in olivine Raman spectrum that may be required for the application of Raman studies on atmosphere free planetary bodies where temperatures will be significantly lower than on Mars or in the case of Mercury potentially higher than on Mars. In general, the effect of very low temperatures on mineral structure (lower that -95 °C) is expected to result in changes of Raman peak position, peak widths, peak intensities and appearance of new peaks (Sobron and Wang, 2011).

4.7   References

Bandfield, J. L., V. E. Hamilton and P. R. Christensen, (2000), A global view of Martian surface compositions from MGS-TES: Science, Vol. 287, p.1626-1630.

Bibring et al., (2006), Global Mineralogical and Aqueous Mars History Derived from OMEGA/Mars Express Data, Science 312 (5772), p. 400–404.

De Vries, J. (2012), Lunar Evolution; a combined numerical modelling and HPT experimental study, PhD thesis, Utrecht University, Netherlands.

Chopelas, A. (1991), Single crystal Raman spectra of forsterite, fayalite, and monticellite. Am Mineral Vol. 76, p. 1101–1109.

Fleet, M. E., (1976), Distortion parameters for coordination polyhedra: Mineralog. Mag., U 40, p. 531-533.

Gurland, J, R. C. Tripathi, (1971), A simple approximation for unbiased estimation of the standard deviation". American Statistician (American Statistical Association) 25 (4), p. 30–32.doi:10.2307/2682923. JSTOR 2682923.

Guyot, F. et al., (1986), Comparison of the Raman microprobe spectra of $(Mg,Fe)_2SiO_4$ and Mg_2GeO_4 with olivine and spinel structures. Phys. Chem. Mineral. Vol. 13,p. 91–95.

Hoefen, T. M. et al., (2003), Discovery of olivine in the Nili Fossae region of Mars. Science. Vol. 302, p. 627-630.

Hofmann, A. W. (1997), Chemical differentiation of the Earth: The relationship between mantle, continental crust and oceanic crust. Earth Planet. Sci. Lett. 90, p. 297-314.

Ishii. K., (1978), Lattice dynamics of forsterite. Am. Mineral. 63, p. 1198–1208.

Kolesov, B. A., C. A. Geiger, (2004), A temperature-dependent single-crystal Raman spectroscopic study of fayalite: evidence for phono-magnetic excitation coupling, vol. 31, pp. 155-161.

Kuebler, K. E. et al., (2006), Extracting olivine (Fo–Fa) compositions from Raman spectral peak positions. Geochimica et Cosmochimica Acta. Vol. 70, p. 6201-6222.

Labrosse, S., J. W. Hernlund and N. Coltice, (2007), A crystallizing dense magma ocean at the base of the Earth's mantle. Nature 450, p. 866-890.

Smyth, J. R. and D. L. Bish, (1988), Crystal structures and cation sites ofthe rock-forming minerals, Allen and Unwin, Boston, Massachusetts, pp. 332.

Sobron P., A. Wang, (2011), A planetary environment and analysis chamber for combined in-situ spectroscopic measurements on selected materials under planetary relevantenvironments, J. Raman Spectroscopy, doi:10.1002/jrs.3017.

Sokal, R. R. and F. J. Rohlf, (1981), Biometry: Principles and Practice of Statistics in Biological Research, 2nd ed. ISBN 0-7167-1254-7 , p. 53.

Silverstein, R. M., G. C. Bassler, T. C. Morrill, (1981), Spectrometric Identification of Organic Compounds. 7th ed., John Wiley & Sons Inc., USA, p. 95-98.

Walter, M. J., R. G. Tronnes, (2004), Early Earth differentiationEarth and Planetary Science Letters, 225, p. 253–269.

Wang, A., B. L. Jolliff, L. A. Haskin, (1995), Raman spectroscopy as a method for mineral identification on lunar robotic exploration missions. Journal of Geophys, Res. Vol. 100, p. 21189–21199.

Wang, A., K. Kuebler, B. L. Jolliff, L. A. Haskin, (2004b), Mineralogy of aMartian meteorite as determined by Raman spectroscopy. J. Raman Spectrosc. Vol, 35, p. 504–514.

Whittaker, E. J. W and R. Muntus, (1970), Ionic radii for use in geochemistry Geothim Cosmochim Acta, Vol. 45, p. 945-956.

Weber, I. et al., (2012), Raman spectra of olivine measured in different planetary Environments, European Planetary Science Congress (EPSC), Vol. 7, p. 156.

Zerr, A., A. Diegeler and R. Boehler, (1998), Solidus of Earth's deep mantle. Science Vol. 281, p. 243-246.

Chapter 5: Raman study of hydrated sulphates and carbonates under Martian conditions with the RLS instrument

This chapter is the basis of a manuscript that will be submitted to the journal of Raman spectroscopy.
K. Motamedi, A. Colin, J.H. Hooijschuur, G.R. Davies.

Contents

5.1 Introduction

One of the main scientific objectives of the forthcoming ExoMars mission is the search for definitive signs of past or present life. A key goal of the mission will be to obtain more information about the current and past distribution of water on Mars. Evidence of the past liquid water activity has been found in multiple areas such as the MeridianiPlanum region explored by the Opportunity rover. Observation of the layered sedimentary rocks show that these rocks contain high (30%–40%) abundances of sulphates (mostly jarosite) (Christensen et al., 2004) likely formed by the evaporation of sulphur-rich water (Squyres et al., 2004). Sulphates were also observed from orbit instruments in the layered deposits of VallesMarineris as well as in more local locations such as crater interiors (Langevin et al., 2005).

Carbonates are expected weathering products of water and basalt in a CO_2 rich atmosphere (Gooding, 1978; Catling, 1999). The presence of carbonates as well as accompanying clays on Mars suggest that water was neutral to alkaline at the time during the Noachian era (Fairen et al., 2004). According to the recent data, carbonates exist locally on Martian surface and in veins within Martian meteorites (Bridges et al., 2001) and possibly at <5% abundance in Mars dust (Bandfield et al., 2003).

Laboratory studies demonstrate that the Martian meteorites contain sulphur and water bearing minerals such as amphiboles. The discovery of hydrated minerals in meteorites was the first unambiguous evidence of a hydrous history of Mars. The discovery of sulphur determines that the abundant sulphur on the surface of Mars is due largely to chemical reactions in the Martian atmosphere that are similar to those that occur in Earth atmosphere. Therefore in order to understand the history of water on Mars current and future missions aim to identify carbonate and hydrated minerals and determine the geologic environments and processes responsible for their formation. Consequently, analysis of carbonate and hydrated minerals is a fundamental goal of the ExoMars mission to enable assessment of the geological and climatic history and possible past and present 'habitability' of Mars. Therefore it is vital that a full assessment is made as to the potential of the RLS instrument to detect carbonate and hydrated minerals under Martian conditions. This chapter examines the capability of the RLS instrument to detect and distinguish between different hydrated sulphates and carbonates.

Our analyses were carried out with the RLS instrument. Raman spectroscopy is potentially a powerful method for structural and compositional characterization of minerals. To simulate Martian conditions our experiments were carried out in the Mars atmosphere simulation chamber (MASC). Our approach was initially to assess if the RLS instrument can provide Raman spectra on a series of natural carbonates and hydrated sulphates before assessing the effect of Martian condition (low pressure, 8 CO_2 mbar, temperatures at +10 and -20 °C) on the Raman peaks. As in previous chapters, key questions are therefore if Raman spectra are potentially influenced by a CO_2 atmosphere and low temperatures, down to -20 °C.

5.2 Analytical procedure

RLS instrument uses a laser with a ~659 nm laser with 20 mW output energy. The spectral resolution is ~ 4 cm^{-1} and the spectral range between ~ 187 and 3293 cm^{-1}. The data acquisition are performed for a single integration of 40 s. The Raman spectra are obtained with the RLS instrument at +10 and -20 °C. In most cases the minerals are also analysed using a commercial Renishaw InVia Raman microscope under laboratory conditions to provide high quality Raman spectra for comparison. The spectra resolution of Renishaw is ~ 3 cm^{-1}. We recorded data between 125 and 4000 cm^{-1} range with acquisition time of 10 s. This commercial spectrometer uses near infrared laser excitation at 785 nm. To ensure high quality data, the charge coupled detector (CCD) is cooled to -70 °C.

5.2.1 Sample compositions

The compositions of the selected minerals are presented in Table 5.1.The EMPA data were collected on a JEOL JXA-8800M Superprobe at the VU University Amsterdam, the details information based on Electron microprobe analyser (EMPA) was presented in chapter four, section4.3.1.

	Barite			Gypsum			Aragonite			Calcite		
	Weight%	STDEV	2σ	Weight%	STDEV	2σ	Weight%	STDEV	2σ	Weight%	STDEV	2σ
Na$_2$O	0.14	0.02	0.00	0.02	0.00	0.00	0.00	0.00	0.00	0.00	0.00	0.00
BaO	62.63	0.23	0.19	0.01	0.02	0.01	0.01	0.01	0.01	0.00	0.01	0.01
CaO	0.00	0.00	0.00	34.65	0.36	0.30	51.77	0.26	0.21	51.72	0.22	0.18
K$_2$O	0.00	0.01	0.00	0.01	0.01	0.01	0.00	0.00	0.00	0.00	0.00	0.00
SrO	0.01	0.02	0.02	0.02	0.02	0.01	0.33	0.16	0.13	0.00	0.00	0.00
SO$_3$	34.56	0.16	0.13	53.40	0.27	0.22	0.01	0.01	0.01	0.01	0.01	0.01
MnO	0.00	0.00	0.00	0.00	0.01	0.01	0.00	0.00	0.00	0.05	0.01	0.01
MgO	0.00	0.00	0.00	0.00	0.00	0.00	0.00	0.00	0.00	0.00	0.00	0.00
Total	97.35	0.26	0.21	88.11	0.30	0.24	52.13	0.23	0.19	51.79	0.23	0.18

Table 5. 1. Average compositions of barite, gypsum, calcite, aragonite by EMPA.

5.2.2 Raman analyses of hydrated sulphates: gypsum, barite and anglesite

On Earth sulphur (S) occurs as the pure element as well as in the sulphate (SO_4^{2-}) and sulphide (S^{2-}) form, producing minerals such as barite ($BaSO_4$) and pyrite (Fe_2S). Sulphur is one of the most reactive elements and can form covalent chemical bonds both with itself and with other elements. Sulphur easily enters solution where it forms sulphate complexes, which may ultimately precipitate as sulphates. On Earth, sulphates represent a large group of minerals that occur in different environments. For example, sulphates can appear as products of marine sediment formation. They are also common at Mid Ocean Ridges, which are the major cooling environments on Earth. Here anhydrite ($CaSO_4$) is precipitated from Ca rich

hydrothermal fluids when they mix with seawater (Haymon, 1983; Tivey and McDuff, 1990). Over time the physical conditions of a hydrothermal system evolve and anhydrite can be altered to gypsum ($CaSO_4 \cdot 2H_2O$), or dissolved as the temperature drops below 130°C. Barite ($BaSO_4$) can also be found as a minor component of hydrothermal systems (Haymon and Kastner, 1981; Hannington and Scott, 1988).

The sulphate ion with a formula of SO_4^{2-} consists of a central sulphur atom surrounded by four equivalent oxygen atoms in a tetrahedral arrangement. The sulphur atom is in the 6+ oxidation state whereas the four oxygen atoms are each in the 2- state and therefore, sulphates create strong Raman signals (Griffith, 1970). The vibrations of the sulphate ion ($SO4^{2-}$) are v_1 symmetric stretching, v_2 symmetric bending, v_3 asymmetric stretching and v_4 asymmetric bending and these vibration modes are Raman active (Fig. 5.1). The stretching modes are usually monitored in the 950–1200 cm^{-1} area, and the bending modes occur between 400 and 650 cm^{-1} area (Ramakrishnan et al., 1985). In a crystal structure the molecular vibration of SO_4^{2-} are under other influences from the cations, for instance Ba or Ca.
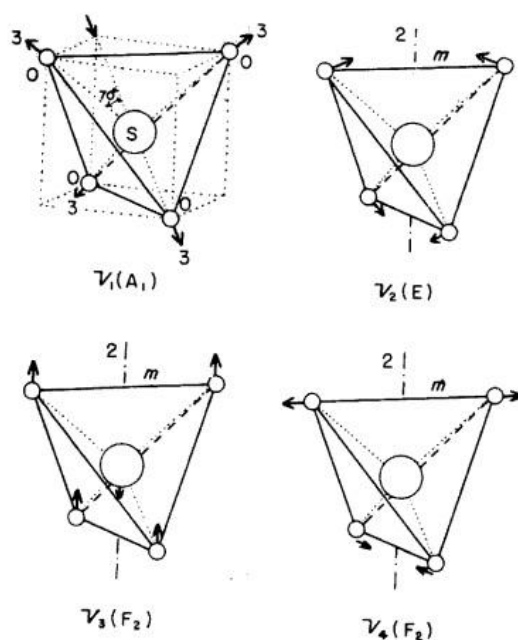
Figure 5. 1. The four vibration modes of sulphate ion SO_4^{2-} (Mitra and Gielisse, 1964).

For this study we have selected two of the most common sulphates that have relatively simple chemical compositions and mineral structures; barite and gypsum. In addition, sulphates that are geologically less common (e.g. anglesite) and phases that are more complex and more hydrated such as jarosite where also studied. We also examined polyhalite, epsomite, glauberite and coelestine. However, we could not obtain high quality RLS Raman spectra of these minerals as spectra show strong noise without any resolvable peaks. As explained in detail in chapter six, the current set up of the RLS instrument does not allow us to detect Raman peaks of OH vibration modes. Consequently, we focus on the Raman spectral region of

i) Fundamental vibrational modes of $(SO_4)^{2-}$
ii) Vibration modes of cation– O bonds from the interactions between the cation and O of either H_2O or SO_4^{2-} (Nakamoto, 2009)

5.2.3 Raman analyses of carbonates: calcite and aragonite

Based on the importance of detection of carbonate minerals on Mars (section 5.1), we have selected calcite and aragonite to analyse their RLS Raman spectra in MASC under Martian conditions. Calcite is one of the most common minerals on Earth, comprising about 4% by weight of the Earth's crust and it is formed in many different geological environments; sedimentary, igneous, and metamorphic rocks. The other selected sample, aragonite is formed by biological and physical processes, including precipitation from marine and freshwater environments (Brian et al., 1989). Aragonite is a polymorph of calcite, both having the chemical composition $CaCO_3$ but with a different molecular structure. Aragonite forms orthorhombic crystals, whereas calcite forms trigonal crystals. Raman spectroscopy is also capable of identifying polymorphs as the technique is based on distinguishing differences in molecular bonds. It should be kept in mind that Raman spectra mostly provide information on covalent bonds and that the Raman effect is very weak for ionic bonds. Importantly, the covalent bonding environment is influenced by cation substitution in a carbonate mineral structure and this enables different carbonates to be distinguished using the Raman spectroscopy.

The structure of the carbonate ion has two (long) single bonds that link carbon to negatively charged oxygen atoms, and one short double bond to a neutral oxygen (Fig. 5.2).
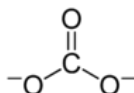
Figure 5.2. The structure of the carbonate ion
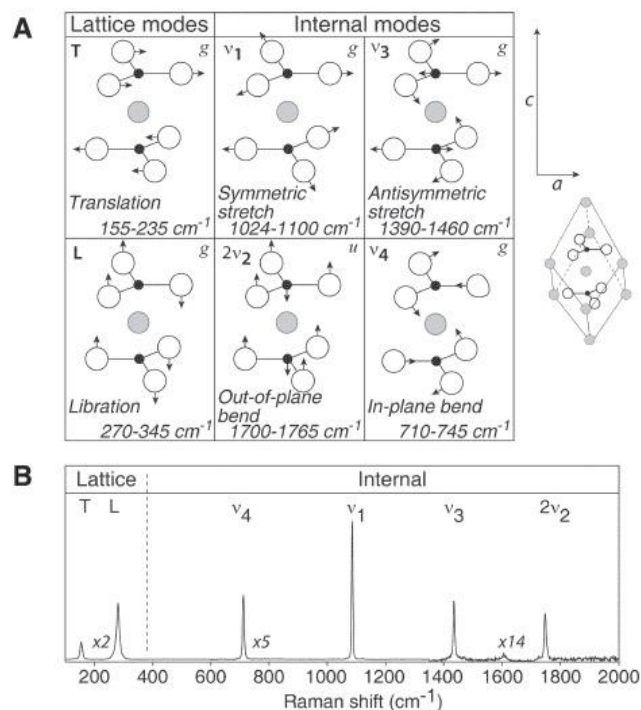
Figure 5.3. Raman peaks of the basic carbonate unit cell produced by lattice and internal modes (Buzgar and Apopei, 2009).

Raman spectra of the carbonate ion can be divided into two parts: lattice and internal modes (Fig. 5.3). Carbonate lattice vibration modes include translational and librational modes, which generate peaks with Raman shifts between 50 and 360 cm^{-1}. Internal vibration modes of the carbonate ion produce more intense Raman peaks. ν_1 is the most intense peak (at 1087 cm^{-1}) of the calcite spectrum and results from the symmetric stretching of CO$_3$ group. The ν_2 asymmetric bending vibration mode is not active in Raman. However, the peak $2\nu_2$ is an overtone of the first order ν_2 and detected between 1700 and 1765 cm^{-1}. ν_3 is related to the asymmetric stretching mode, 1437 cm^{-1} and ν_4 is attributed to a symmetric bending mode at 715 cm^{-1}. A weak peak detected at 1749 cm^{-1} is considered as a combination peak ($\nu_1 + \nu_4$) (Gunasekaran et al., 2006).

5.3   Renishaw data of hydrated sulphates and carbonates

In order to obtain Raman spectra under laboratory condition, selected minerals were placed on the polished stainless steel surface on the stage of the Renishaw microscope. We obtained Raman spectra with 20 X microscope objective. Raman spectra (obtain with the Renishaw InVia Reflex confocal Raman microscope) of gypsum, barite and anglesite (as representative sulphate samples) and calcite and aragonite (as representative carbonate samples) are presented in the following Figures. The data are presented in this section and discussed in details in the following sections.
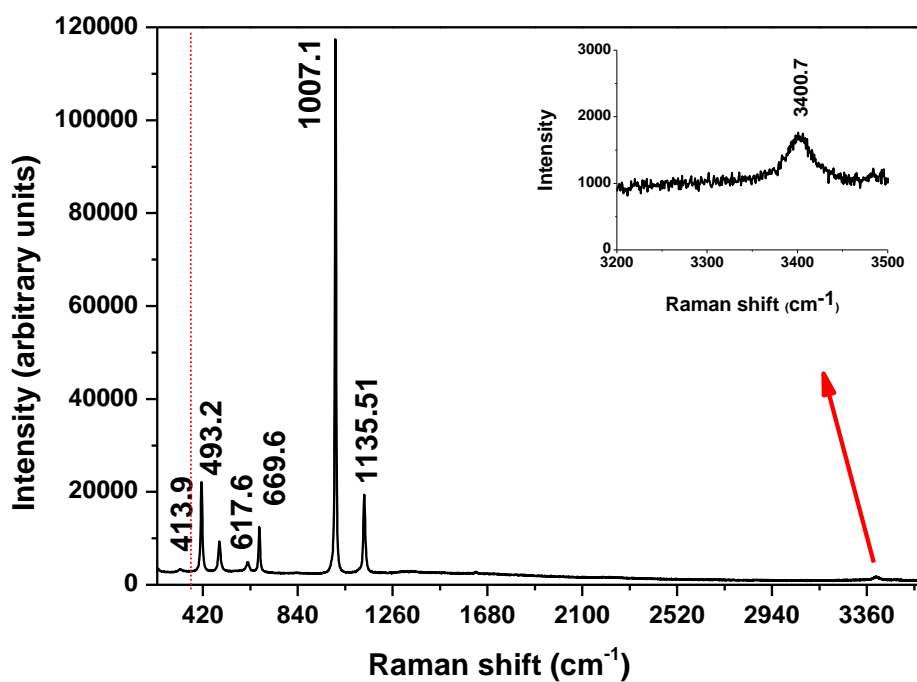
Figure 5.4. Gypsum Raman spectrum taken with the Renishaw InVia Reflex confocal Raman microscope. The peak at 3400.7 cm^{-1} is attributed to O−H vibration mode of water in the gypsum structure. The Raman spectrum of gypsum is separated into two parts, external vibrations (<400 cm^{-1}) and internal vibrations (400−1200 cm^{-1}) of the sulphate groups.
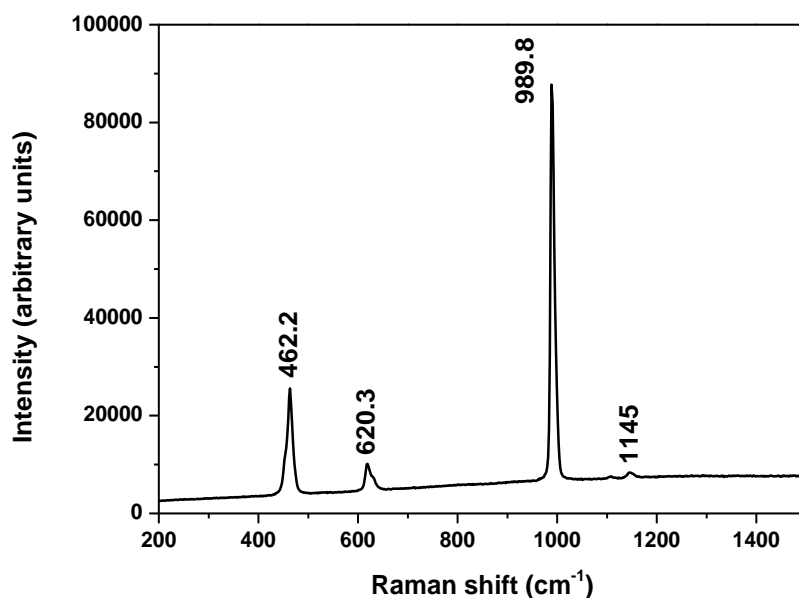
Figure 5.5. Barite Raman spectrum taken with the Renishaw InVia Reflex confocal Raman microscope.
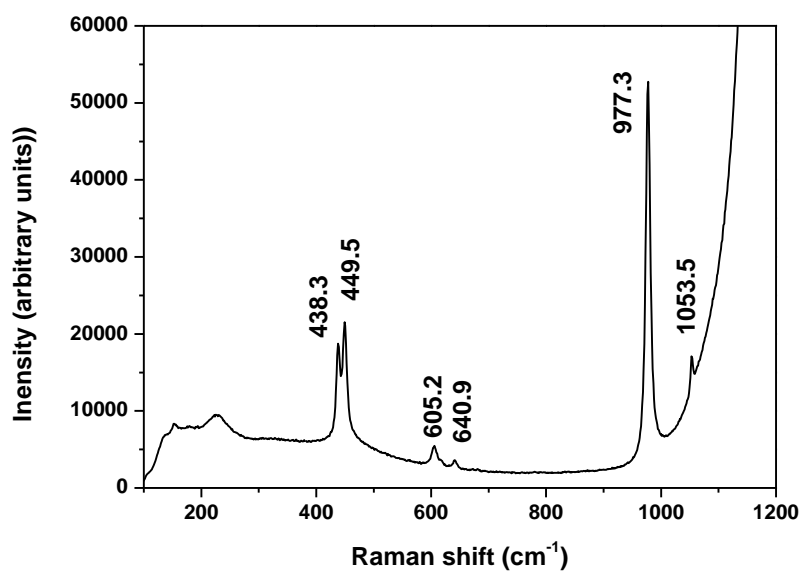
Figure 5.6. Anglesite Raman spectrum taken with the Renishaw InVia Reflex confocal Raman microscope.
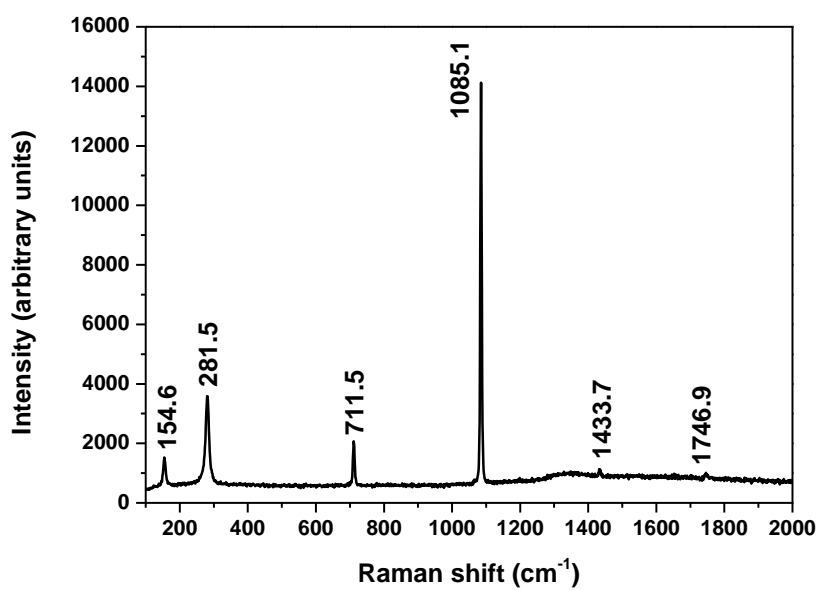
Figure 5.7. Calcite Raman spectrum taken with the Renishaw InVia Reflex confocal Raman microscope.
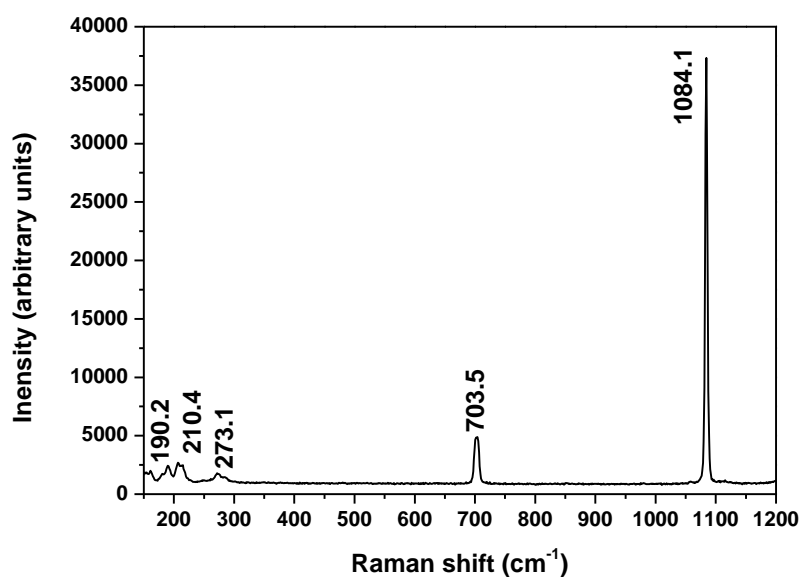
Figure 5.8. Aragonite Raman spectrum taken with the Renishaw InVia Reflex confocal Raman microscope.

5.4 RLS data of hydrated sulphates and carbonates samples

We acquired RLS Raman spectra of selected samples while MASC was under vacuum condition and sample temperatures were between 10 °C and -20 °C. In the next step, we obtained Raman spectra at -20 °C, while MASC was at 8 mbar CO_2. The RLS Raman spectra of gypsum, barite and anglesite (representing hydrated sulphate samples) and calcite and aragonite (representing carbonate samples) are presented in the following Figures:
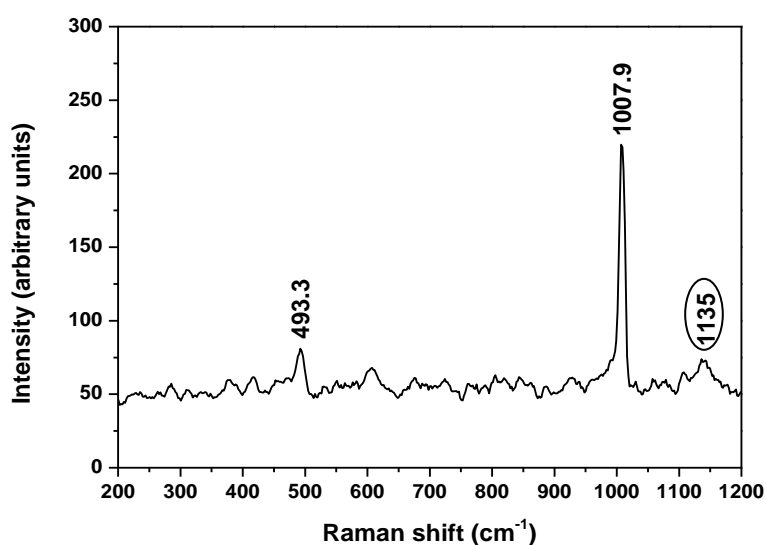
Figure 5.9. Gypsum RLS Raman spectrum under vacuum at 10 °C. The peak at ~ 1135 cm^{-1} is poorly resolved from the background noise.
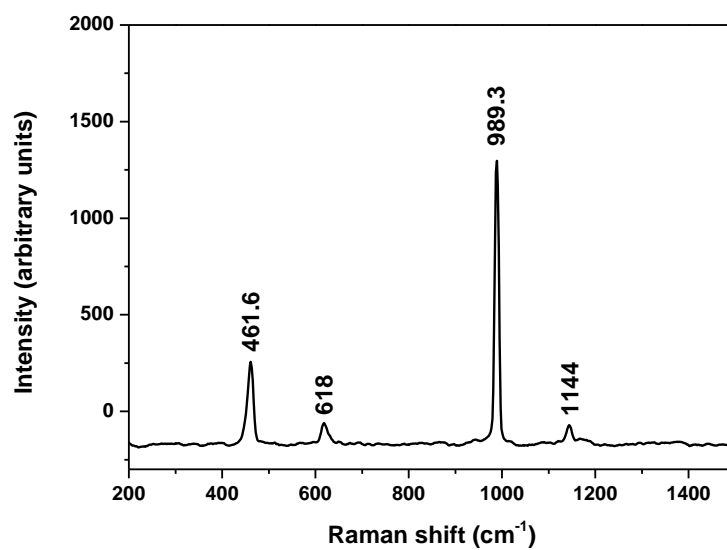
Figure 5.10. RLS Barite Raman spectrum under vacuum at 10 °C.
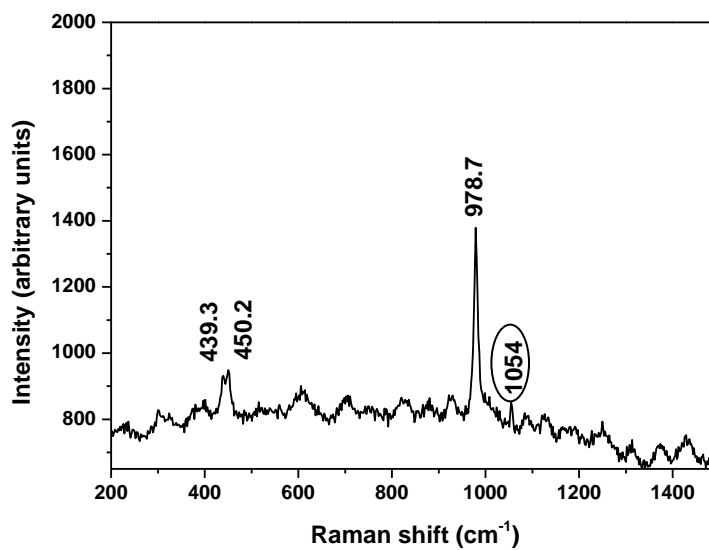
Figure 5.11. RLS anglesite Raman spectrum under vacuum at 10 °C. The possible peak at 1054 cm^{-1} was poorly resolved from the background at 10 °C.
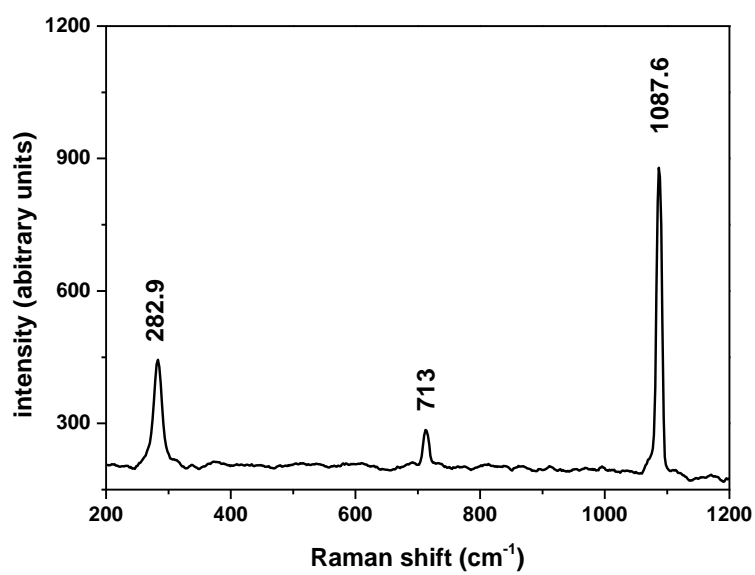
Figure 5.12. RLS calcite spectrum under vacuum at 10 °C.
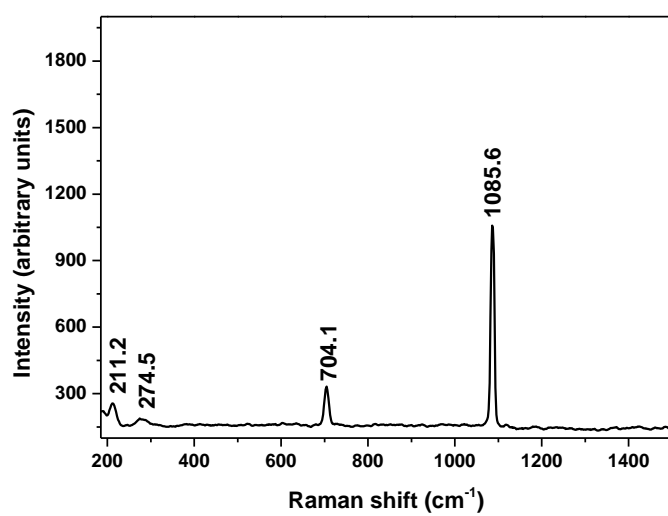
Figure 5.13. RLS aragonite Raman spectrum under vacuum at 10 °C.
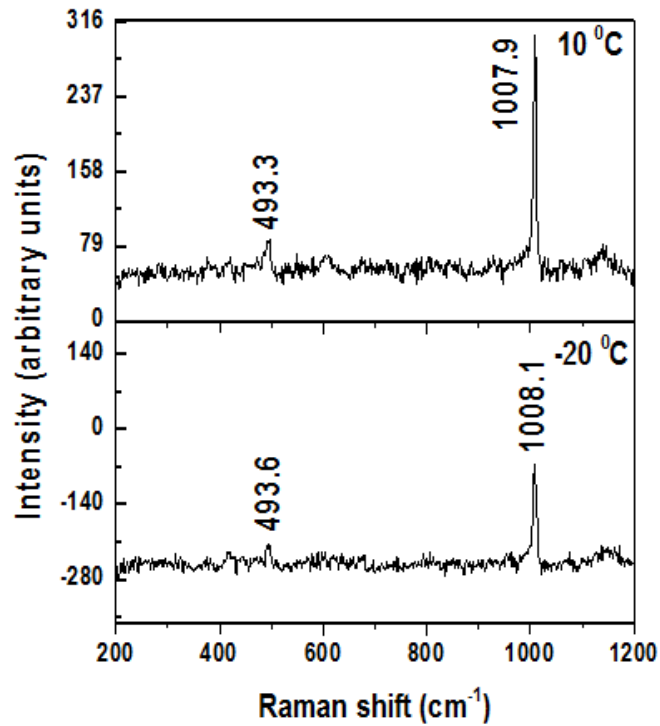
Figure 5.14. RLS Raman spectra of gypsum in the range 200– 12000 cm^{-1}, the measurement conditions are vacuum at +10 and -20 °C (the negative values are the result of temporal variation in the performance of the CCD. Backgrounds were determined for each specific analytical condition; e.g. +10 °C or -20 °C. In this specific case an unknown thermal perturbation of the CCD caused an over correction of the baseline during measurement at -20 °C).
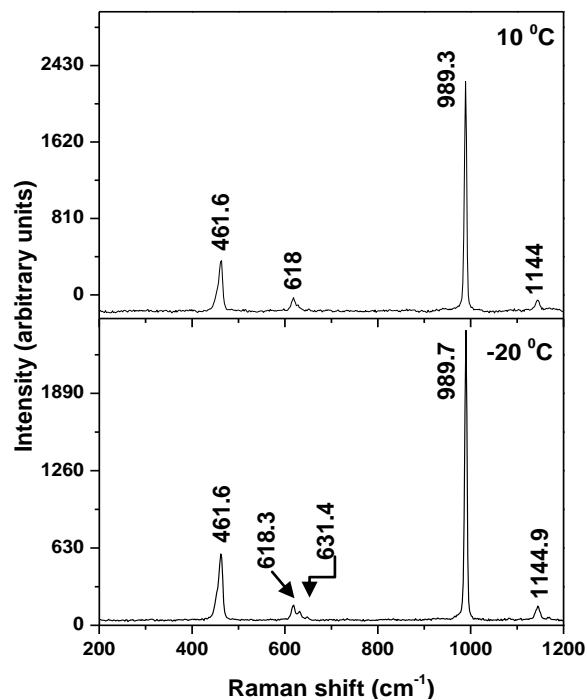
Figure 5.15. RLS Raman spectra of barite in the range 200– 12000 cm^{-1}, the measurement conditions are vacuum at +10 and -20 °C.
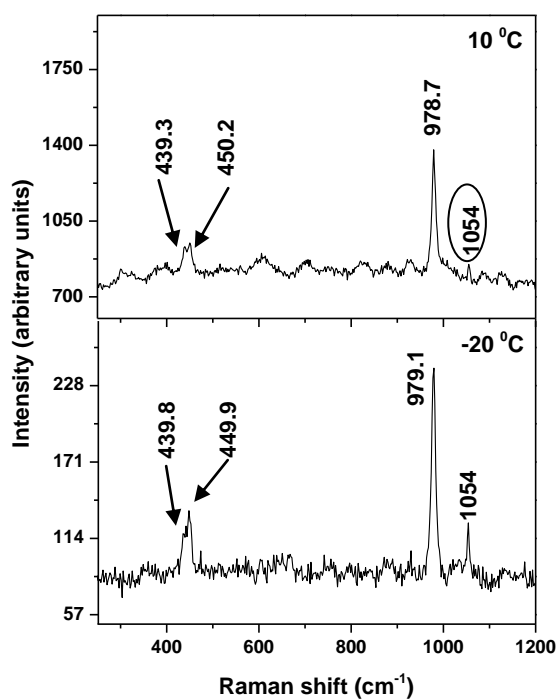
Figure 5.16. RLS Raman spectra of anglesite in the range 200– 12000 cm^{-1}, the measurement conditions are vacuum at +10 and -20 °C. The possible peak at 1054 cm^{-1} was poorly resolved from the background at 10 °C.
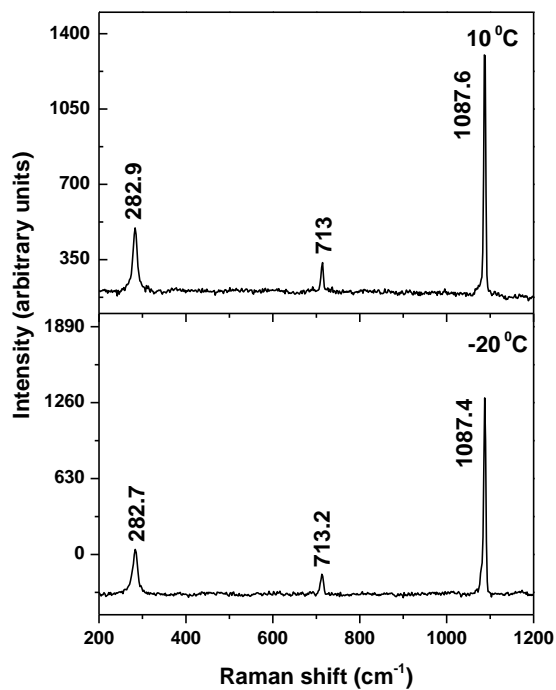
Figure 5.17. Raman spectra of calcite in the range 200– 12000 cm^{-1}, the measurement conditions are vacuum at +10 and -20 °C.

147
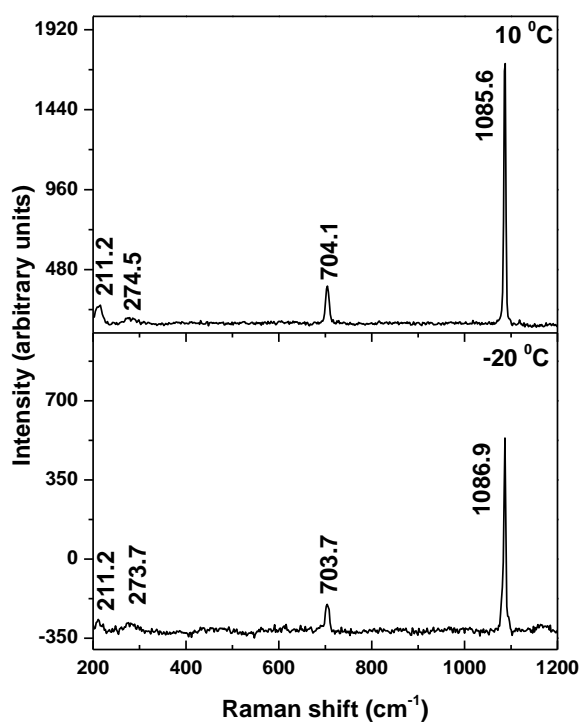
Figure 5.18. Raman spectra of aragonite in the range 200– 12000 cm^{-1}, the measurement conditions are vacuum at +10 and -20 °C.
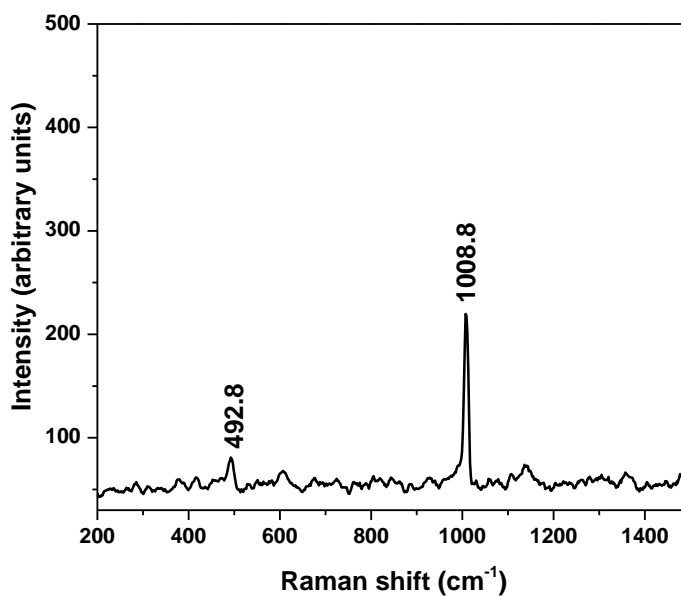
Figure 5.19. RLS gypsum Raman spectrum under 8 mbar CO_2 atmosphere at -20 °C.
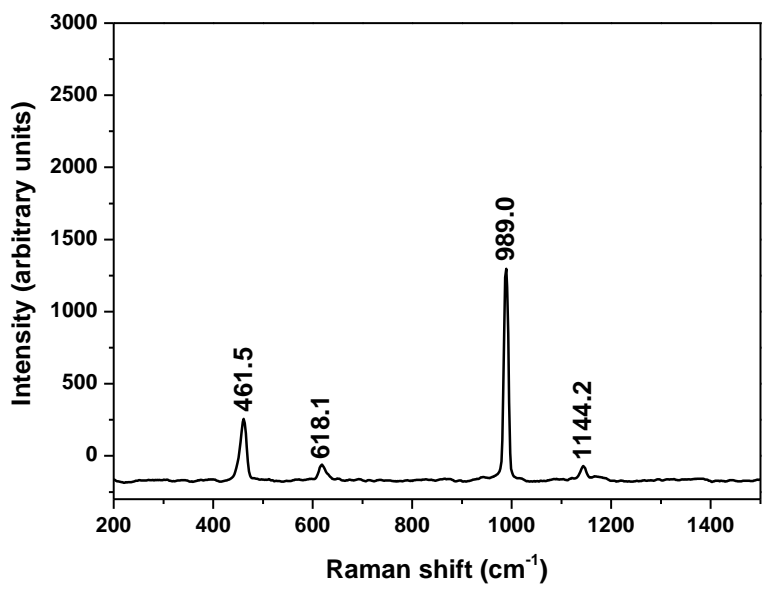
Figure 5.20. RLS barite Raman spectrum under 8 mbar CO_2 atmosphere at -20 °C.
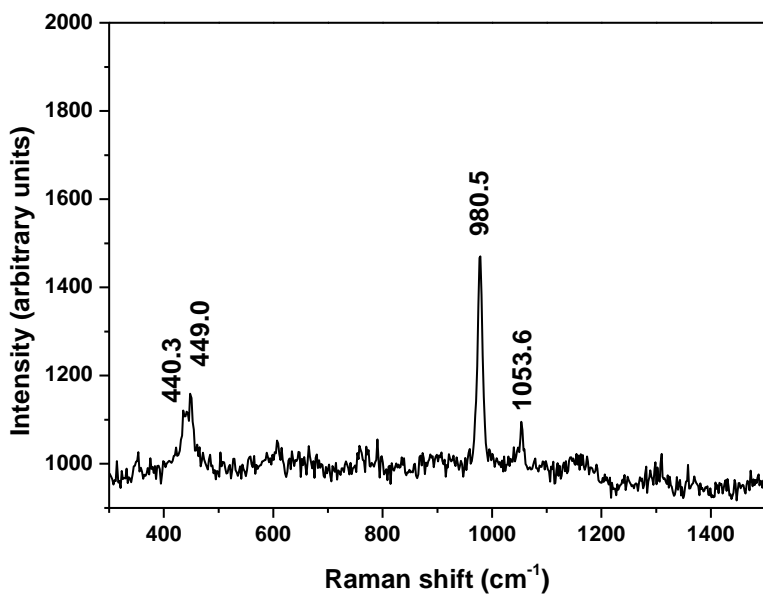
Figure 5.21. RLS anglesite Raman spectrum under 8 mbar CO_2 atmosphere at -20 °C.
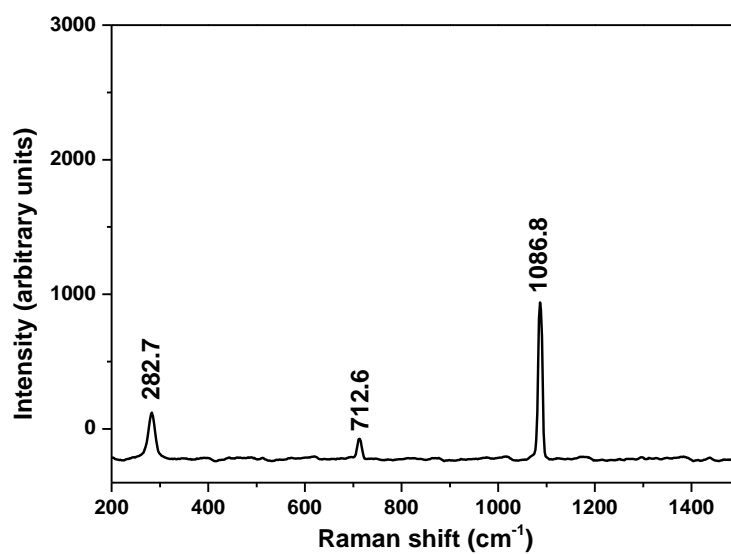
Figure 5.22. RLS calcite Raman spectrum at -20 °C under 8 mbar CO_2 atmosphere.
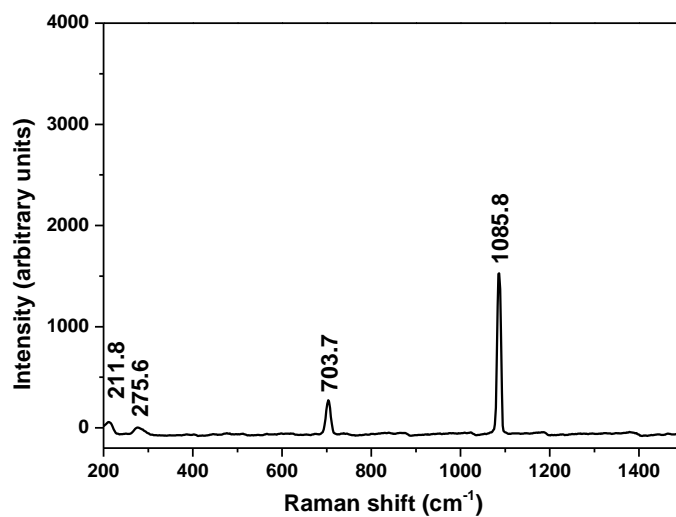
Figure 5.23. RLS aragonite Raman spectrum at -20 °C under 8 mbar CO_2 atmosphere.
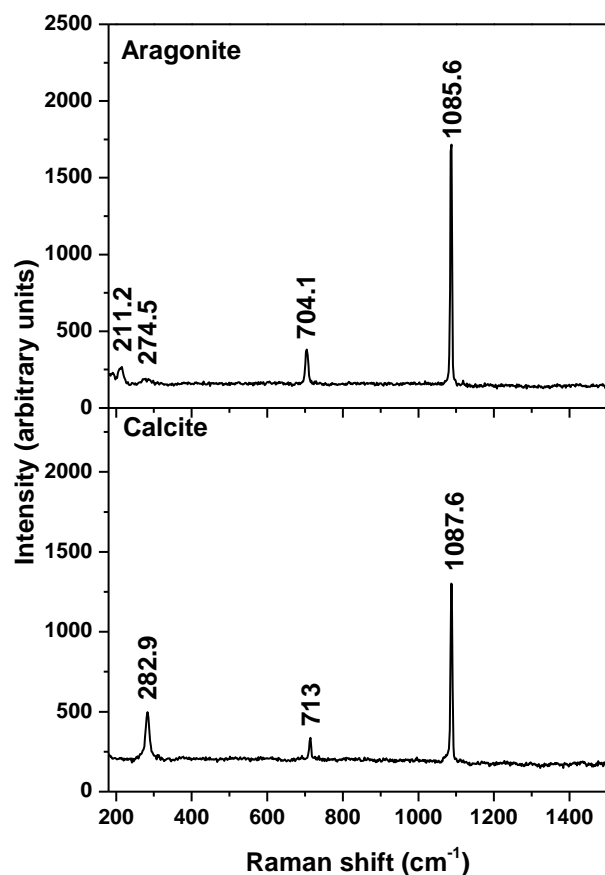
Figure 5.24. RLS Raman spectra of aragonite and calcite under vacuum at 10 °C in order to classify their mineral structure.

5.5 Raman data of selected hydrated sulphates and carbonates

5.5.1 Discussion on the Renishaw data of hydrated sulphates and carbonates

5.5.1.1   Renishaw Raman spectrum of gypsum (CaSO$_4$·2H$_2$O)

Gypsum (calcium sulphate, CaSO$_4$·2H$_2$O) has a layered structure. The atomic arrangement in the crystal structure comprises two sheets of sulphate ions that are closely bonded together by calcium ions (Ca^{2+}) to form strong double sheets in a repetitive mode. These sheets are held together by water molecules that share the two oxygen atoms with calcium in an octahedral structure. The water molecules hold the sheets together with hydrogen bonds.

The Raman spectrum of gypsum can be separated into two parts, which is shown in the Renishaw Raman spectrum in Fig. 5.4. The Raman spectrum of gypsum at frequency modes, <400 cm^{-1}, caused by the external vibrations from both translator and rotator modes from sulphate, water groups and calcium. The vibrations of these bonds are between the Ca and the oxygen atoms of the sulphate ion and the bond between Ca and the oxygen of the water

molecules. Previous workers have proposed that the peak near 316 cm^{-1} is attributed to lattice vibration mode (Sarma et al., 1998).The weak Raman peaks caused by external vibrations were not detected in the Renishaw spectrum (Fig. 5.4).

Raman peaks in the region 400– 1200 cm^{-1} are attributed to internal vibrations of the sulphate groups. Previous studies indicate that these internal vibrations of the sulphate molecule are detected at frequencies above ~ 416 cm^{-1} with the last peak detected at ~ 1143 cm^{-1} (Sarma et al., 1998; Berenblut et al., 1971). Gypsum Raman spectrum obtained using the Renishaw (Fig. 5.4), yields the strongest Raman peak at 1007.1 cm^{-1}. This peak belongs to the v_1 symmetric stretch vibration mode of the SO_4 tetrahedra. The peak at 1135.5 cm^{-1} corresponds to the v_3 asymmetric stretch vibration mode. The v_4 asymmetric bending vibration mode was detected as very weak peaks at 617.6 cm^{-1} and 669.6 cm^{-1}. The vibration modes at 413.9 cm^{-1} and 493.4 cm^{-1} show a pair of peaks related to v_2 symmetric bending in the Renishaw Raman spectrum.

In gypsum Raman spectra, peaks in the spectral region> 3000 cm^{-1} describe the internal water group vibrations. The v_1 and v_3 vibration modes correspond to the symmetric and asymmetric stretching of the O–H bond and are present in Raman spectra in the 3300 to 3500 cm^{-1} region (Brotton and Kaiser, 2013). The Gypsum Renishaw spectrum showed peak at 3400.7 cm^{-1} for v_1 as the signature of O–H vibration modes in our selected gypsum sample.

5.5.1.2 *Renishaw Raman spectrum of barite (BaSO$_4$)*

Renishaw spectrum of barite acquired under laboratory condition is presented in Fig. 5.5. The dominant intense peak, v_1 symmetric stretching of SO_4 tetrahedra is detected at 989.8 cm^{-1}. The v_3 asymmetric stretching vibration mode generates a peak at 1145 cm^{-1} and the peak at 462.2 cm^{-1} is attributed to the v_2 bending vibration mode. The v_4 asymmetric bending vibration mode generates a peak at 620.3 cm^{-1} in Renishaw barite spectrum.

5.5.1.3 *Renishaw Raman spectrum of anglesite (PbSO$_4$)*

The vibration modes of anglesite detected in the Renishaw spectrum are shown in Fig. 5.6. Renishaw spectrum demonstrates v_1 symmetric stretching mode at 977.3 cm^{-1}. v_2 bending vibration mode is characterise as a doublet peak at 438.3 and 449.5 cm^{-1}. A weak peak at 1053.5 cm^{-1}, is attributed to v_3 vibration mode. Peaks at 605.2 and 640.9 cm^{-1} are attributed to the v_4 asymmetric bending vibration mode.

5.5.1.4 *Renishaw Raman spectrum of calcite (CaCO$_3$)*

A calcite Raman spectrum determined by the Renishaw Raman microscope is shown in Figure 5.7. The calcite structure is well characterised with the dominant intensev_1 symmetric stretching vibration mode of CO_3 group occurs at 1085.1 cm^{-1} and v_4 at 711.5 cm^{-1}. Lattice vibration modes at 154.6 and 281.5 cm^{-1} are also distinguishable in this spectrum. The two

weak peaks at 1433.7 and 1746.9 correspond to the ν_3, asymmetric stretching mode and $2\nu_2$ vibration modes.

5.5.1.5 *Renishaw Raman spectrum of aragonite (CaCO₃)*

The Raman spectrum of aragonite obtained with the Renishaw Raman microscope is shown in Fig. 5.8. The characteristic Raman peak due to the ν_1 symmetric stretching mode of carbonate group at 1084.1 cm^{-1} is easily distinguished. The ν_4 mode of CO_3 has values at 703.5 cm^{-1}. The $2\nu_2$ vibration mode and ν_3 vibration mode, which appear in higher wavenumbers (> 1400 cm^{-1}), were not observed in the Renishaw spectrum. The peaks due to the external vibration modes of carbonate group are at 190.2, 210.4 and 273.1 cm^{-1}.
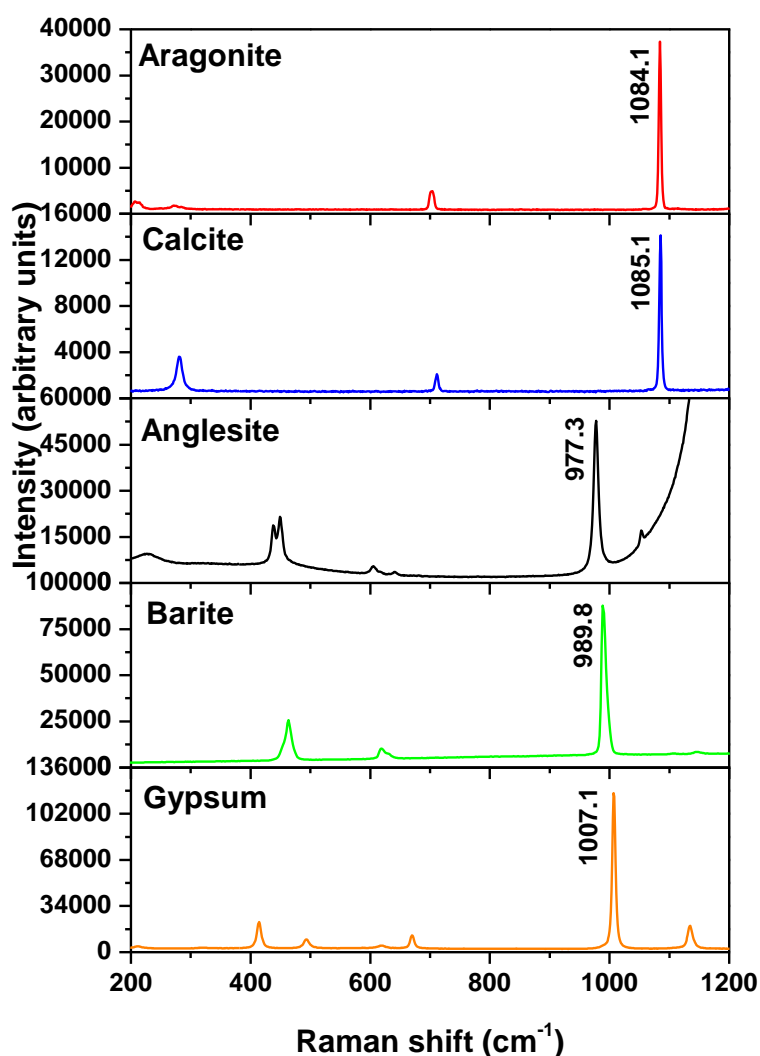
Figure 5.25.The Raman spectra of selected minerals taken with the Renishaw InVia Reflex confocal Raman microscope.

When the temperature of a sample is decreased, the bonds of the molecule usually become shorter. This means that, according to the Hook's law (see section 5.5.2.4) k (spring coefficient) increases. Consequently, Raman peaks might be affected by the temperature variations. Therefore, the peaks attributed to the symmetric stretching and asymmetric stretching vibration modes might have the most variation due to changes in the temperature. We might expect the peaks caused by stretching vibration modes as intensive and distinguishable peaks at 1084.1, 1085.1, 977.3, 989.8 and 1007.1 cm^{-1} in Raman spectra of aragonite, calcite, anglesite, barite and gypsum to be affected by the temperature variations (Fig. 5.25). Other peaks are so weak that we expect it will be hard to assess if there are small variations caused by lower temperature. We will study possible variations in Raman spectra due to the change in temperatures with the RLS instrument in the following section.

5.5.2 Discussion on the RLS data of hydrated sulphates and carbonates

5.5.2.1 RLS Raman spectrum of gypsum (CaSO$_4$·2H$_2$O)

The RLS Raman spectrum of gypsum is presented in Fig. 5.9. RLS instrument detected two Raman peaks of gypsum (noise were appeared in shape of possible peaks in some part of this spectrum. However, they are not match to the peaks reported in the references). The strongest Raman peak at 1007.9 cm^{-1} is attributed to the ν_1 symmetric stretch vibration mode of the SO$_4$ tetrahedra. The peak at 493.3 cm^{-1} is related to ν_2 symmetric bending vibration mode. The detected peaks have a maximum error of ~0.8 cm^{-1} compared to the data reported in the Renishaw section. ν_4 and ν_3 were obscured in the strong background noise. Among of seven peaks detected via the Renishaw InVia Reflex confocal Raman microscope, RLS instrument detected the two strongest peaks (ν_1 and ν_2). RLS instrument was unable to fully focus on a grain of the selected gypsum sample. Our selected gypsum has grains in different optical orientations, which causes reflection of laser light in different directions. Therefore, the collection of the Raman emission was very week and we were unable to obtain a full Raman spectrum using RLS instrument. The RLS instrument cannot detect peaks in the spectral region > 3000 cm^{-1}. In order to detect the water molecular vibration, the effective operational range of the CCD detector must be re-scaled by either changing the angle of the grating or using a shorter wavelength laser source.

5.5.2.2 RLS Raman spectrum of barite (BaSO$_4$)

The RLS spectrum of barite is presented in Fig. 5.10. The main intense peak, ν_1 symmetric stretching vibration mode of SO$_4$ tetrahedra, occurs at 989.3 cm^{-1}. The peak at 461.6 cm^{-1} is attributed to the ν_2 bending vibration mode. The ν_3 asymmetric stretching vibration and ν_4 asymmetric bending vibration modes create peaks at 1144 cm^{-1} and 618 cm^{-1}. In the RLS Raman spectra, the four vibration modes of SO$_4$ correspond within error (~ 2 cm^{-1} to data reported above from the the Renishaw InVia Reflex confocal Raman microscope).

The vibration modes of anglesite detected with RLS instrument are shown in Fig. 5.11. RLS spectrum shows v_1 symmetric stretching mode at 978.7 cm^{-1}. v_2 bending vibration mode is determined as a doublet peak at 439.3 and 450.2 cm^{-1}. The RLS anglesite spectrum does not have well developed peaks with a flat base line. Multiple reflections from the sample surface made weak Raman peaks with low intensity (see section 6.2). v_3 and v_4 vibration modes were not detected in the RLS spectrum. In the Renishaw spectrum, these peaks were observed at a frequency of 1053.5 cm^{-1} (attributed to v_3 vibration mode) and 605.2 and 640.9 cm^{-1} (attributed to the v_4 vibration mode). The detected RLS Raman peaks match within an error of ~ 1.5 cm^{-1} with the data reported in Renishaw section.

5.5.2.4   A comparison of the internal vibrations of sulphate groups in anglesite and barite

In the mineral structure of sulphates, the size of the unit cell changes with composition. Replacements of cations with different mass, ionic radius and even different valency affect bond lengths and bond angle. These changes in the unit cell cause shifts in the frequencies of Raman peaks. Therefore the sulphate groups in barite and anglesite are expected to generate slightly different Raman peaks (Figs. 5.10 and 5.11). Table 5.2 shows that the RLS instrument is able to characterise these differences. In addition, the values of the four vibration modes of SO₄ match with data found in previous studies (Buzgar and Apopei, 2009; Beny, 1991; Dimova et al., 2006).

	Barite			Anglesite		
Vibration modes	RLS study	Buzgar et al., 2009	Dimova et, al., 2006	RLS study	Buzgar et al., 2009	Beny, 1991
v_2 SO₄	461.6	461	453, 462	439.3, 450.2	450, 553	437, 449
v_4 SO₄	618	619, 648	618, 647	ND*	611, 646	617, 640, 643
v_1 SO₄	**989.3**	**989**	**988**	**978.7**	**978**	**977**
v_3 SO₄	1144	1085,1143,1167	1140, 1167	ND*	1058, 1157	1051,1140, 1155

Table 5.2. Raman vibration peaks for barite and anglesite (cm^{-1}, * not detected).

As mentioned in chapter two, the molecular vibration modes are described as a function of the force constant of the vibration and the mass of the participating atoms. For a diatomic molecule, the vibrational frequency is described as Hook's law:

$$v = \frac{1}{2\pi c}\sqrt{\frac{k_0}{\mu}} \quad (5.1)$$

μ is reduced mass of participating atoms ($m_1 m_2 / (m_1 + m_2)$), k_o is force constant in Newton per metre. ν is vibrational frequency in wave numbers. c is speed of light in centimetres per second. Therefore, according to Fadini and Schnepel (1989) the different sulphate vibration modes in barite and anglesite minerals are determined by differences in:

- Bond strength
- Atomic masses

In sulphates, ν_1 vibration mode depends on the S–O stretching force constant. The ν_1 vibration mode increases with an increase in the force constant. According to the study of Miyake et al. (1978), the stretching force constants for barite and anglesite are $k=6.27$ and $k= 5.98$ md/A (md= millidyne, one dyne (1 dyn=1 g·cm/s²) is defined as force F that accelerates an object with a mass of one gram one centimetre per second per second, Å angstrom, 1 Å=0.1 nm).From equation 5.1, it is expected that the wavenumber decreases with an increase of the atomic mass of the cations. Table 5.3 presents ν_1 RLS Raman peak values for barite and anglesite, where the atomic masses of Ba and Pb are 137.32 and 207.2 u respectively. A comparison of the Raman spectra of barite and anglesite illustrates that the value of ν_1 decreases with an increase of the atomic mass of the major metal ion in the lattice. Data from RLS study therefore agrees with the predictive model of Fadini and Schnepel (1989) discussed above. Given the diverse nature of sulphate mineralogy reported from Mars we expect that this model will be useful in classifying the structure of sulphates with different atomic masses on Mars. However, it should be kept in mind that, the variation in peak positions could potentially be caused by temperature changes. Hence, this matter is investigated in the following sections.

5.5.2.5   Raman spectra of gypsum, barite and anglesite at low temperature under 8 mbar CO$_2$ pressure and vacuum conditions.

The mineral structure of gypsum, barite and anglesite were studied with the RLS instrument at -20 °C under two different conditions: i) 4×10^{-5} mbar vacuum condition, ii) 8 mbar CO$_2$ pressure.

i) 4×10^{-5} mbar vacuum condition: RLS Raman spectra obtained at -20 °C were compared to RLS Raman spectra obtained at 10 °C (Figs. 5.14, 5.15 and 5.16).

The wavenumbers of the resolved peaks for vibration modes of each mineral are summarised in Table 5.3. Their Raman spectra obtained at -20 °C under vacuum condition, are all within ~ 0.3 wavenumber of those acquired at 10 °C under vacuum condition. Therefore we conclude that we are unable to detect any significant change in Raman spectra related to temperature change. However, we should keep in mind that depending on mineral symmetry, shifts in Raman spectra of specific minerals have been reported at much lower temperatures (-253 °C ; Weber et al., 2012). Hence for the unambiguous detection of carbonates and sulphate minerals on planetary bodies without an atmosphere and under more extreme temperature conditions extensive further experimentation is required.

	Barite		Gypsum		Anglesite	
Vibration modes	-20°C	10 °C	-20°C	10 °C	-20 °C	10 °C
ν_2 SO$_4$	461.6	461.6	493.6	493.3	439.8, 449.9	439.3, 450.2
ν_4 SO$_4$	618.3, 631.4	618	ND*	ND*	ND*	ND*
ν_1 SO$_4$	989.7	989.3	1008.1	1007.9	979.1	978.7
ν_3 SO$_4$	1144.9	1144	ND*	ND*	1054	ND*

Table 5.3. RLS Raman peaks for barite, gypsum and anglesite at -20 and 10 °C under vacuum, * not detected.

As explained in section 3.6.3, the inefficient cooling of the CCD in the RLS instrument means that the minimum temperature reached by the CCD depends on the atmospheric conditions in the MASC. CCD reached its lowest temperature (~ -41.2 °C) when we obtained RLS Raman spectra under vacuum condition at -20 °C. Therefore, the CCD thermal background noise was lower and allowed resolution of some weak peaks. For example in the barite RLS Raman spectrum acquired at -20 °C, one of the weak peaks, which is attributed to ν_4 vibration mode of the sulphate group, was detected at 631.4 cm^{-1}. However, this peak was not observed in the barite RLS Raman spectra obtained at 10 °C when the CCD temperature was -31.4 °C. Similarly, different peaks are resolved in the RLS Raman spectra of anglesite at -20 and 10 °C under vacuum condition. At -20 °C, a weak peak at 1054 cm^{-1}, which is attributed to ν_3 vibration mode of the sulphate group, is resolved. This peak is not detected at 10 °C. Noise levels varied from 3 to 5 when the CCD was operating at temperatures of ~ -30 and -40 °C respectively.

ii) 8 mbar CO$_2$ pressure (Martian conditions): Raman spectra obtain at -20 °C under 8 mbar CO$_2$ pressure were compared to RLS Raman spectra obtain at -20 °C under 4x10^{-5} mbar vacuum conditions (Figs. 5.19, 5. 20 and 5. 21).

Data presented in table 5.4, establishes that the Raman peaks obtained under Martian conditions are all within ~1 wavenumber of those obtained under vacuum condition and consequently we can conclude that we are unable to detect any significant change in Raman spectra related to temperature and pressure changes applicable to the operational conditions.

	Barite		Gypsum		Anglesite	
Vibration modes	4x10^{-5} mbar	8 mbar CO$_2$	4x10^{-5} mbar	8 mbar CO$_2$	4x10^{-5} mbar	8 mbar CO$_2$
ν_2 SO$_4$	461.6	461.5	493.6	492.8	439.8, 449.9	440.3, 449
ν_4 SO$_4$	618.3, 631.4	618.1	ND*	ND*	ND*	ND*
ν_1 SO$_4$	989.7	989.0	1008.1	1008.8	979.1	980.5
ν_3 SO$_4$	1144.9	1144.2	ND*	ND*	1054	1053.6

Table 5.4. RLS Raman peaks for barite, gypsum and anglesite at -20 °C under vacuum and at 8mbar CO$_2$, * not detected.

5.5.2.6 *RLS Raman spectrum of calcite (CaCO$_3$)*

The RLS calcite spectrum is presented in Fig. 5.12. The Raman spectra of calcite is characterised by the most intensive v_1 symmetric stretching of CO$_3$ group at 1087.6 cm^{-1}, v_4 symmetric bending mode is shown at 713 cm^{-1} and one lattice vibration mode at 282.9 cm^{-1}. These peaks are within ~ 2 cm^{-1} of the data reported in the Renishaw section. The possible $2v_2$ and v_3 peaks, which were detected with the Renishaw Raman microscope, were not detected with the RLS instrument. These weak peaks appear to have been obscured within the background noise.

5.5.2.7 *RLS Raman spectrum of aragonite (CaCO$_3$)*

Figure 5.13 shows the RLS aragonite spectrum. The spectrum has well-formed peaks with a flat base line. The observed peaks in this spectrum are as follow: v_1 as the very strong Raman peak at 1085.6 cm^{-1}, v_4 vibration mode with the value of 704.1 cm^{-1} and two weak lattice vibration modes at 211.2 and 274.5 cm^{-1}. The resolved peaks have the same value within ~ 2 cm^{-1} of the data presented in Renishaw section. In RLS Raman study, the $2v_2$ and v_3 vibration modes were not observed. The detection of the $2v_2$ vibration mode and v_3 vibration mode (> 1400 cm^{-1}) of aragonite was also impossible with the Renishaw InVia Raman microscope.

5.5.2.8 *A comparison between calcite and aragonite RLS Raman spectra*

A comprehensive study of the calcite and aragonite spectra is reported by Couture 1947; Krishnamurti 1956, 1957; Porto et al., 1966; Griffith 1969; Rutt and Nicola 1974; White 1974; Frech et al., 1980; Bischoff et al., 1985. The principal Raman peak of both calcite and aragonite is produced by the internal vibrations of the carbonate ion, which is an essential component of both calcite and aragonite. It is therefore expected that the v_1 vibration mode of CO$_3$ group may be indistinguishable between the two minerals. We present the RLS Raman spectra of aragonite and calcite in Figure 5.24. v_1 vibration modes occurred at 1087.6 cm^{-1} and 1085.6 cm^{-1} in calcite and aragonite RLS Raman spectra respectively. As the two minerals are not pure end-member compositions but contain additional elements such as Mg, Mn and Sr, it is impossible to establish if the small (~ 2 cm^{-1}) differences between v_1 vibration modes of calcite and aragonite are caused by compositional variations of minor elements or the minerals themselves. Further work on pure endmember compositions are required to resolve this question.

The shorter wavenumber peaks, however, are significantly different in the RLS Raman spectra of calcite and aragonite (Table 5.6). The lower wavenumber peaks are attributed to the vibrations of the ionic arrangement within the crystals. These peaks present the characteristic differences in Raman spectra of the two minerals (White, 1974). In our work, we can clearly observe the predicted differences between lattice vibration modes at 282.9 and 274.5 cm^{-1} in calcite and aragonite (Figure 5.24). The difference is ~ 8.4 cm^{-1}. v_4 modes at 713 cm^{-1} in the calcite RLS spectrum and 704.1 cm^{-1} in aragonite RLS spectrum have a difference of ~ 8.9 cm^{-1}. Therefore, we can conclude that with the RLS instrument, we have identified the similarities and differences in the RLS Raman spectra of aragonite and calcite.

5.5.2.9   RLS Raman spectra of calcite and aragonite at low temperature under 8 mbar CO_2 pressure and vacuum condition.

In this section, we study the mineral structure of calcite and aragonite with the RLS instrument at -20 and 10 °C under vacuum condition. Our goal is to identify any possible structural changes in the mineral lattice of calcite and aragonite at low temperature by identifying Raman shifts. In subsequent experiments, we have analysed the mineral structure of calcite and aragonite under 8 mbar CO_2 pressure and vacuum condition at -20 °C. Our goal is to monitor the possible effect of Martian conditions on RLS Raman spectra of calcite and aragonite.

Peaks in the Raman spectra of calcite and aragonite under vacuum condition at -20 °C (are respectively) within $\sim$ 0.5 and 1 cm^{-1} of spectra obtained under vacuum condition at 10 °C (Figs 5.17 and 5.18). We conclude that there are no detectable shifts due to the low temperature. As we discussed in section 5.5.2.5, for the clear detection of carbonates and sulphate minerals on planetary bodies without an atmosphere further low temperature experimentation is needed.

Table 5.5 demonstrates that peaks resolved in the Raman spectra obtained under Martian conditions are within $\sim$ 1 cm^{-1} of those obtained under vacuum condition. As a result, we can again conclude that there are no resolvable differences in Raman spectra related to pressure changes.

Vibration modes	Calcite		Aragonite	
	4×10^{-5} mbar	8 mbar CO_2	4×10^{-5} mbar	8 mbar CO_2
ν_1	1087.4	1086.8	1086.9	1085.8
ν_4	713.2	712.6	703.7	703.7
Lattice vibration mode	282.7	282.7	211.2, 273.7	211.8, 275.6

Table 5.5. RLS Raman peaks for calcite and aragonite (cm^{-1}) under vacuum (10^{-5} mbar) and at 8 mbar CO_2 at -20 °C.

5.6   Conclusion

This study describes the successful application of the RLS instrument to detect sulphate and carbonate minerals under Marian conditions. We investigated if the temperature affects some of the vibration modes in selected mineral structure.

The Raman peaks obtained with the RLS instrument under vacuum conditions at -20 °C inside MASC chamber are indistinguishable to those obtain with Renishaw InVia Reflex confocal Raman microscope and data reported in the literature. These data indicated the accurate performance and calibration of the RLS instrument at lower temperatures. Moreover, Raman spectra obtained under Martian conditions (8 mbar CO_2 pressure and -20 °C) are indistinguishable to those obtained under vacuum conditions at temperature of -20

°C. These data establish that there is no significant shift in Raman peaks of carbonates and sulphates under Martian conditions. Significantly, this means that Raman spectra of these minerals obtained in the ExoMars rover will be indistinguishable from terrestrial spectra and for carbonates a standard terrestrial derived database can be used for the identification of carbonate minerals.

RLS Raman spectra for barite, anglesite and gypsum have clear differences that can be related to the different mineral structures. In all spectra, there were variations in peak positions and peak splitting due to the influences of the different metal cations. In the case of barite and anglesite, the wavenumber of the vibrational modes of SO_4 tetrahedra, decreases with an increase of the atomic mass of the metal cations. In addition, Raman peaks shift to higher wavenumbers with an increase of the stretching force constant of S–O bonds.

The water vibration mode is detected in the Renishaw Raman gypsum spectrum. However, we could not identify any water vibration mode in RLS Raman gypsum spectrum. Therefore, we can conclude that the design of the RLS instrument is not optimal. To detect the vital component of hydrated minerals we suggest a redesign of the RLS instrument. To detect this molecular vibration, the range of the CCD detector must be re-scoped by either changing the angle of the grating or applying a shorter wavelength laser source (see chapter six for more discussion).

The purpose of the study of calcite and aragonite with the RLS instrument was to highlight the possibility for the analysis of polymorph minerals with the RLS instrument. We have shown that the RLS instrument is a useful device for the determination of polymorphs under Martian conditions.

5.7 References

Bandfield, J. L. et al., (2003), Spectroscopic Identification of Carbonate Minerals in the Martian Dust.Science, Vol. 301, p.1084.

Beny, C. (1991), Société Française de Minéralogie et de Cristallographie - Base de données de spectres Raman. Anglesite. (http://wwwobs.univ-bpclermont.fr /sfmc/ramandb2/fpdf/ANGLE11.pdf).

Berenblut B. J., P. Dawson and B. R. Wilkinson, (1971), The Raman spectrum of gypsum. Spectrochimica, Acta A., 27(9), p. 1849-1863.

Bischoff W. D., S. K. Sharma, F. T. Mackenzie, (1985), Carbonate ion disorder in synthetic and biogenic magnesian calcites: a Raman spectral study. Am Mineral 70, p. 581-589.

Bridges, J. C. et al., (2001), Alteration assemblages in Martian meteorites: implications for near-surface processes. Space Sci. Rev. 96, p. 365–392.

Brotton S. J. and R. I. Kaiser, (2013), In Situ Raman Spectroscopic Study of Gypsum (CaSO4&middot2H2O) and Epsomite (MgSO4&middot7H2O) Dehydration Utilizing an Ultrasonic Levitator .JPCL, 4, p. 669-673.

Buzgar, N., A. I. Apopei, (2009), The Raman study on certain carbonates. Iasi, Tome 55, issue 2, p. 97-112.

Catling, D.C. (1999), A chemical model for evaporites on early Mars: Possible sedimentary tracers of the early climate and implications for exploration, Journal of Geophys. Res., 104, 16,453-16,470.

Christensen, P. R. et al., (2004), Mineralogy at Meridiani Planum from the Mini-TES experiment on the Opportunity rover, Science, Vol. 306, p. 1733–1739.

Couture, L. (1947) Etude des spectres de vibrations de monocristaux ioniques. Annales de Physique, 2(12), 5-94.

Dimova, M., G. Panczer, M. Gaft, (2006), Spectroscopic study of barite from the Kremikovtsi deposit (Bulgaria) with implication for its origin. Annales Géologiques de la Péninsule Balkanique, Vol. 67, p. 101-108.

Fairen, A. G. et al., (2004), Inhibition of carbonate synthesis in acidic oceans on early Mars, Nature 431, p. 423.

Frech R, E. C. Wang, J. B. Bates, (1980), The IR and Raman spectra of CaCO3 (aragonite). Spectrochim Acta 36A, p. 915-919.

Gooding, J. L. (1978), Chemical weathering on Mars thermodynamic stabilities of primary minerals (and their alteration products) from mafic igneous rocks. Vol. 33, Issue 3, p. 483–513.

Griffith W. P. (1969), Raman spectroscopy of minerals. Nature 224, p. 264-266.

Griffith W. P. (1970), Raman studies on rock-forming minerals. II. Minerals containing MO3, MO4 and MO6 groups. Journal of Chem. Soc. A(2), 286-91.

Gunasekaran. S, G. Anbalagan, S. Pandi, (2006), Raman and infrared spectra of carbonates of calcite structure. Journal of Raman Spectroscopy, Vol. 37, p. 892-899.

Hannington, M. D. and D. Steven, (1988) Scott Mineralogy and geochemistry of a hydrothermal silica-sulfide-sulfate spire in the caldera of Axial Seamount, Juan De Fuca RidgeCan Mineral, Vol. 26, p. 603-625.

Haymon, R. M., (1983), Growth history of hydrothermal black smoker chimneys, Nature 301, 695 - 698; DOI:10.1038/301695a0.

Krishnamurti, D. (1956), Raman spectrum of magnesite. Proc Indian Ac Sci A43:210-212.

Krishnamurti, D. (1957), The Raman spectrum of calcite and its interpretation. Proc Indian Ac Sci A46, p. 183 202.

Langevin, Y., F. Poulet, J. P. Bibring, B. Gondet, (2005), Sulphates in the North Polar Region of Mars Detected by OMEGA/Mars Express. Science, Vol. 307, no. 5715, p. 1584-1586.

Mitra S. S. and P. J. Gielisse, (1964), Progress in Infrared Spectroscopy (Plenum Press, Inc., New York,), Vol. 2, pp. 47-125.

Nakamoto, K. (2009), Infrared and Raman Spectra of Inorganic and Coordination Compounds Part A: Theory and Applications in Inorganic Chemistry (Sixth edition). John Wiley and Sons, New Jersey.

Porto S. P. S, J. A. Giordmaine, T. C. Damen, (1966), Depolarization of Raman scattering in calcite. Phys Rev 147, p. 608-611.

Rachel M. Haymon and M. Kastner, (1981), Hot spring deposits on the East Pacific Rise at 21°N: preliminary description of mineralogy and genesis, Earth and Planetary Science Letters, Vol. 53, Issue 3, p. 363–381.

Ramakrishnan, V., V. U. Nayar, G. Aruldhas, (1985), Vibrational spectra of LiRbSO4 Infrared Phys. 25 (4), p. 607–610.

Rutt, H. N., J. H. Nicola, (1974), Raman spectra of carbonates of calcite structure. Journal of Phys C 7, p. 4522-4528.

Sarma, L. P., P. S. R. Prasad, N. Ravikumar, (1998). Raman Spectroscopic Study of Phase Transitions in Natural Gypsum. Journal of Raman Spectroscopy, Vol. 29, p. 851-856.

Skinner, B. J., S. C. Porter, (1989), The dynamic earth: an introduction to physical geology, pp. 540.

Squyres, S.W. et al., (2004), The Opportunity Rover's Athena Science Investigation at Meridiani Planum, Mars. Science 306, 1698. Vol. 306, no. 5702, pp. 1698-1703.

Tivey M. K., R. E. McDuff, (1990), Mineral precipitation in the walls of black smoker chimneys: a quantitative model of transport and chemical reaction. Journal of Geophys. Res., Vol. 95, p. 12617-12637.

Weber, I. et al., (2012), Raman spectroscopy of Mars relevant and minerals for planetary exploration, 43rd Lunar and Planetary Science Conference, 1793.

White, W. B. (1974), The carbonate minerals. In V. C. Farmer, Ed., The Infrared Spectra of Minerals, Mineralogical Society Monograph 4, p. 227-284.

Chapter 6: RLS capabilities under Martian conditions; current and future perspectives

Content

6.1   Performance of the RLS instrument under Martian conditions

The first objective of this PhD research was to design, manufacture and test a simulation chamber (MASC) to reproduce the atmospheric conditions of Mars. The MASC is a temperature and atmosphere controlled chamber (200 l). In order to reproduce Mars' atmosphere and temperature inside the MASC, an innovative heating-cooling system was coupled to a vacuum and gas control system (more details about the MASC chamber are found in chapter three). The MASC chamber can simulate planetary atmospheres and by doing so we are able to:

- Perform *in situ* sample analysis
- Test the performance of space instruments.

The second objective of this PhD research was to validate the performance of the RLS instrument within the MASC under Martian conditions, specifically assessing the capability to determine Raman spectra on minerals thought to be present on the Martian surface. Therefore, the RLS instrument was installed inside the MASC and the performance of the RLS instrument was evaluated and discussed in previous chapters.

This chapter reviews the performance of the RLS instrument under practical conditions and based on the performance makes recommendations for potential improvements for future mission instruments. A major observation of this work is that the RLS instrument is far less effective at producing and detecting Raman signals than the commercially available Renishaw InVia Raman microscope that we used for comparison studies. We evaluate key aspects of performance of the RLS EB instrument and make a series of suggestions for improvements for RLS instruments for future planetary missions.

Basic RLS instrument calibration: The performance was initially assessed based on the calibrations of the spectrometer at different temperatures. Visible light (~400–800 nm) was directed at the RLS instrument to localise the position of the orders on the CCD (for this research, the 3rd order (660–800 nm) was used for Raman analyses). The positions of the orders on the CCD were influenced by the temperature of the spectrometer. The result of the calibrations suggested that the prism of the RLS instrument was significantly affected by thermal changes.

Consequently a discussion of the role of the prism and grating in the RLS instrumentation design is warranted to understand how the prism and grating may influence RLS data obtained under Martian conditions. The prism in the RLS instrument was used to separate Raman emission light into its constituent spectral colours with their different range of wavelengths. Therefore, the spectrum of light is separated vertically by wavelengths. Then, the light with different ranges of wavelengths reaches a grating in the RLS instrument. Light with different wavelengths disperses from grating in different directions and creates diffraction orders (see section 2.4.3 for more information). Gradually lowering the temperature of the RLS instrument from 10 to -20 °C led to a vertical shift in the position of

the orders on the CCD of the spectrometer (~ 3 pixels or 40 μm). The most probable causes of the change in position on the CCD are:

- (Unwanted) movement of the prism
- (Unwanted) change(s) in the properties of the prism due to the thermal expansion

A key observation is that the makeup of the individual orders did not change and that all the wavelengths in each order remained the same. In addition, the orders did not shift horizontally on the CCD so that wavelength calibrations were not affected. From these observations we conclude that the grating was not affected by temperature. The CO_2 pressure (~8 mbar) had no effect on Raman spectra of this study (see chapter four and five). Consequently, we conclude that the RLS instrument can be operated under Martian atmospheric conditions where temperature can vary in the range +10 to -20 °C. The effect of temperature variation on the RLS instrument performance is fully characterised in chapter two, section 2.5.2.

The final objective of this PhD research was to assess the effectiveness of the RLS instrument in obtaining Raman spectra from different minerals under Martian conditions. Chapters four and five described that there was no influence of temperature and pressure on mineral Raman spectra at Martian conditions. Different composition in mineral structure caused frequency shifts.

6.2   Detection of minerals with the RLS instrument

A variety of different mineral compositions were successfully identified with the RLS instrument under Martian conditions. A list of analysed minerals isreported in table 6.1. These minerals were selected because they are already known or suspected to exist on Mars and identification of these minerals will help in understanding the evolution of planet Mars (see chapter one for more information). The minerals are classified in three groups, depending on the ability of the RLS instrument to detect them and the reason for the success or otherwise in detecting the minerals are discussed:

Group *A*: Minerals that were successfully identified
Group *B*: Minerals that were more difficult to detect
Group *C*: Minerals that were not identified

Minerals in group A and B	
	Sulphates: - Barite ($BaSO_4$) - Anglesite ($PbSO_4$) - Gypsum ($CaSO_4 \cdot 2H_2O$) (hydrated sulphate)
A	**Carbonates:** - Calcite ($CaCO_3$) - Aragonite ($CaCO_3$)

	Silicates: $(Mg, Fe)_2SiO_4$ - Olivine 1 (Fo_{64}) - Olivine 2 (Fo_{93})
B	**Phosphates:** - Apatite ($Ca_5(PO_4)_3(F, Cl, OH)$) **Silicates:** - Quartz (SiO_2) (sample of Rose Quartz)
C	**Sulphates:** - Polyhalite (hydrated sulphate), $K_2Ca_2Mg(SO_4)_4 \cdot 2(H_2O)$ - Epsomite (hydrous magnesium sulphate mineral) $MgSO_4 \cdot 7H_2O$ - Glauberite (sodium calcium sulphate) $Na_2Ca(SO_4)_2$

C	**Silicates:** • <u>Phyllosilicates</u> *<u>Micas</u>, the mica group of sheet silicate (phyllosilicate) ($X_2Y_{4-6}Z_8O_{20}(OH,F)_4$ in which X is K, Na, or Ca or less commonly Ba, Rb, or Cs; Y is Al, Mg, or Fe or less commonly Mn, Cr, Ti, Li, etc.; Z is mainly Si or Al, but also may include Fe^{3+} or Ti) - Phlogopite (magnesium mica), $KMg_3AlSi_3O_{10}(F,OH)_2$ - Biotite,phyllosilicate mineral within the mica group, $K(Mg,Fe)_3AlSi_3O_{10}(F,OH)_2$ *<u>Chlorite</u>, the chlorites are a group of phyllosilicate minerals, $(Mg, Fe)_3(Si, Al)_4O_{10}(OH)_2 \cdot (Mg, Fe)_3(OH)_6$ • <u>Pyroxenes</u>**:** $XY(Si, Al)_2O_6$, where X represents Ca, Na, Fe^{2+} and Mg and more rarely Zn, Mn and li and Y represents ions of smaller size, such as Cr, Al, Fe^{3+}, Mg, Mn, Ti, V and even Fe^{2+} - Augite $(Ca, Na)(Mg, Fe, Al, Ti)(Si, Al)_2O_6$ - Diopside $MgCaSi_2O_6$ - Wollastonite $CaSiO_3$ - Hypersthene $(Mg, Fe)SiO_3$ - Hedenbergite (iron pyroxene end-member), $CaFeSi_2O_6$, - Enstatite, (magnesium endmemberof the pyroxene silicate mineral, $MgSiO_3$) - Bronzite(orthopyroxene) $(Mg, Fe)SiO_3$ • <u>Amphiboles:</u> ($A_{0-1}B_2C_5T_8O_{22}(OH, F, Cl)_2$ where **A** represents Na, K**;** B represents Na, Zn, Li, Ca, Mn, Fe^{2+}, Mg; **C** represents Mg, Fe^{2+}, Mn, Al, Fe^{3+}, Ti, Zn, Cr; and T represents Si, Al, Ti) - Hornblende, $Ca_2(Mg, Fe, Al)_5(Al, Si)_8O_{22}(OH)_2$ - Actinolite, amphibole silicate mineral, $Ca_2(Mg, Fe)_5Si_8O_{22}(OH)_2$ - Anthophyllite, an amphibole mineral, $(Mg, Fe)_7Si_8O_{22}(OH)_2$, magnesium iron inosilicate hydroxide • <u>Olivine:</u>Olivine 3, Olivine 4 ($(Mg, Fe)_2SiO_4$), Synthetic fayalite,Fe_2SiO_4

Table 6.1. List of samples that were a) identified by the RLS instrument, b) were more difficult to detect by the RLS instrument, c) that could not be identified by the RLS instrument. For ease of the reader all the well resolved spectra are repeated in the appendix at the end of this chapter.

In the following paragraphs we will discuss some of the parameters that led to Raman peaks in group *A* and *B*minerals being hard to detect and why minerals in group *C* could not be detected. Subsequently some recommendations will be given of how to improve the RLS

instrument for future space missions. Detections (or the lack of) are based on the following condition/parameters:

- The RLS instrument obtained Raman spectra only between ~ 200 and 3200 cm^{-1}.

This wavenumber range is limited by the specific design of the RLS instrument, notch filter and the use of Raman laser with a ~ 659 nm wavelength. The RLS instrument includes a notch filter that transmits the Raman emission, while filtering the laser excitation wavelength. This filter blocks Raman peaks with wavenumbers shorter than ~200 cm^{-1}.

Above 3200 cm^{-1}, the Raman emission is not detected on the RLS CCD detector. Based on the wavelength of the Raman laser excitation source (~ 659 nm), Raman emission is detected in the 3rd diffraction order. This order covers the wavelength range 650–840 nm, i.e. Raman shift between~200 and 3200 cm^{-1}. Because of the design of the grating, the 2nd diffraction order with the wavelength ranging only between 975 and 1256 nm reaches the CCD. So there is a gap between 840 and 975 nm on the CCD and Raman shifts higher than 3200 cm^{-1} cannot be analysed (see chapter two, section 2.4.3). As an example of this limited detection: O–H vibration modes in the spectrum of gypsum were not detected because they give Raman shifts in the 3300 to 3500 cm^{-1} region. A solution could be to change/rotate the position of the grating inside spectrometer to be able to detect the wavelength between 840 and 975 nm on the 3rd order or the 2nd order. Another solution is to change the laser wavelength so that the Raman shift above 3200 cm^{-1} have wavelength within the CCD range (see section 6.3.2).

- Grain size control

As discussed shortly in chapter 2 section 2.2.1, Raman emission can be created from the emissions by oscillating dipoles in molecules. These molecules are located within the small volume of the sample, which is illuminated by the Raman laser beam. The intensity of the Raman emission depends on the number of molecules in the volume illuminated by the Raman laser (see section 2.2.2). Therefore, the intensity of the Raman emission is dependnt on the number of the molecules involved in the emission. As a result, the reduction of the illuminated volume decreases the number of excited molecules and thus the intensity of the Raman peaks (e.g., Wang, et al., 1999). A fine-grained sample will generally have a lower volume to surface ratio than a larger crystal.

Previous researchers have shown that the most important factor that reduces the collecting efficiency of Raman emission is multiple reflections at various surfaces within and near the excitation volume (Wang, et al., 1999). As examples of the work presented here were RLS Raman spectra of gypsum and anglesite. These spectra contained strong background noise (see section 5.4). The effective power of the Raman laser beam was reduced by multiple reflections at the sample surfaces and at internal boundaries within the samples. In addition, due to all the reflections a proportion of the Raman emission photons would be outside of the collecting angle of the RLS instrument, (see part b in section 6.3). As a result the SNR is effectively reduced and this leads to problems in detecting weak Raman peaks.

The analyses performed on rose quartz provide an example of this sort of problem. Only one peak at 465 cm^{-1} was resolved in the Raman spectrum. This is the largest Raman peak resolved in quartz spectra but other peaks were completely obscured in the background noise, Fig 6.1. The Raman spectrum of quartz obtained by the Renishaw InVia Raman microscope is presented in Fig 6.2. Quartz was identified through a high peak near 464 cm^{-1} and weaker peaks at 263, 354, 393, 401, 508, 694, 806, 1080 and 1158 cm^{-1}. The reason for poor data from the rose quartz was twofold; the Raman laser could not be focused properly on the sample surface due to the amorphous nature of the sample and the extensive internal reflection of the laser light due to the fine grained nature of the sample. The advantage of the Renishaw InVia Raman microscope is that using the highest optical magnification (x 50) it was possible to adjust the focus of the laser to the desired spot on the sample surface and optimise the Raman signal. This example emphasises the need for a high quality optical system in any planetary RLS instrument with an automatic focus possibility to ensure that the optimal focal point can be achieved. The optical head on the RLS instrument was not versatile enough to allow fine tuning to achieve optimal Raman signals.
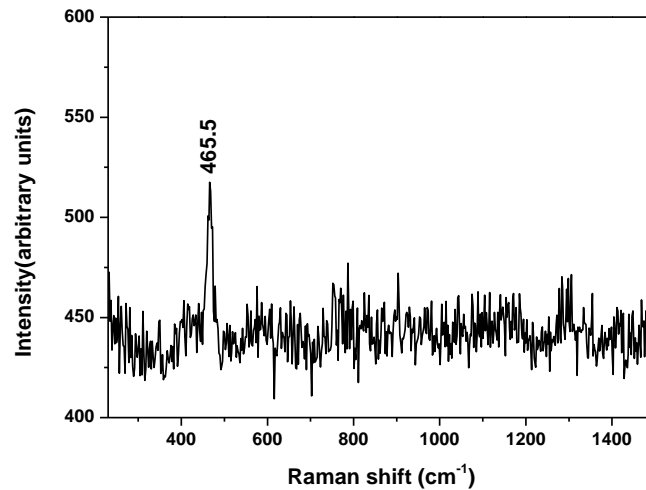
Figure 6.1. RLS Raman spectra of rose quartz.
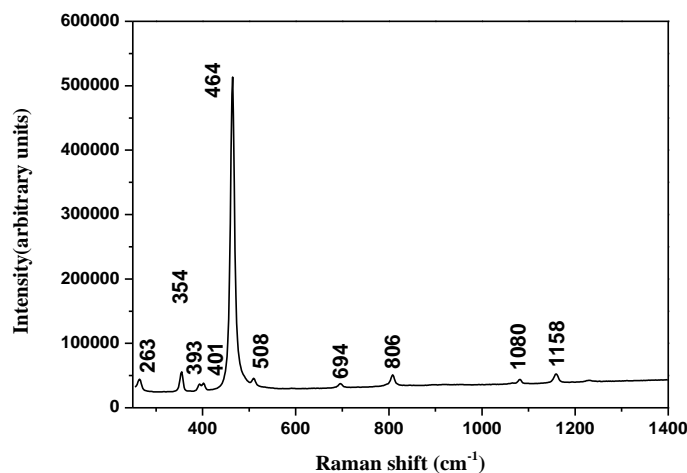
Figure 6.2. Renishaw Raman spectrum of rose quartz.

6.3   Suggestions for improving the RLS instrument

In this section, some suggestions for the improvement in the design of the RLS instrument are made. These suggestions are designed to provide feasible solutions to detect minerals that were hard to detect (or impossible to be detected) by the RLS instrument. These solutions are divided into two. First, solutions will be presented to increase the Raman peak intensity (increasing SNR). Second, suggestions are made to improve the spectral range of the RLS instrument above 3000 cm^{-1}. This suggestion will help to detect water vibration modes in hydrated minerals. We consider the detection of the water vibration modes in hydrated minerals vital for the study of the mineralogy of Mars to help understand the evolution of the planet.

6.3.1   Improving the Raman peak detection

An assessment of the Raman spectra obtained from minerals that were difficult to identify led to the following suggestions for the possible re-design or different measurement strategies to detect minerals:

  a) Increase the laser power
  b) Improvement of the Raman signal collection and transmission efficiency
  c) Improvement of the SNR

6.3.1.1   *Increase the laser power*

One possibility to improve the Raman peak intensities is to increase the power of the Raman laser (chapter two, section 2.2.2). Based on the use of a second RLS instrument manufactured by TNO it was established that Raman intensity can be increased by use of a laser higher power that the 20 mW.

Increasing the Raman laser power, however, can cause destruction of some samples. The laser energy absorbed by the sample is correlated to different parameters such as the absorption coefficient of the sample and the mean irradiance at the laser focal point. The mean irradiance at the focal point of the laser depends on the laser power. If power increases, the irradiance at the focused point also increases (Delhaye et al., 1996). In a sample with a high absorption coefficient, laser light is absorbed. The absorption coefficient determines how far a particular wavelength can penetrate into a material light before it is absorbed. The greater power of the TNO laser caused damage to most hydrated and dark minerals. Therefore although increased laser power appears an attractive option there is limited benefit from increased power as minerals are damaged and it will no longer be possible to study hydrated minerals nor allow subsequent LIBS analysis. Therefore, when increasing the laser power, the properties of samples such as absorption coefficient and the wavelength of Raman laser should be reviewed. Based on the worked performed at the Vrije University

Amsterdamand TNO company we recommend an upper power limit of 200 mW but ideally any future planetary RLS instrument should have the potential to use variable power so that highly absorbent dark minerals and hydrated minerals can be analysed with lower laser power if needed.

6.3.1.2   Improvement of the Raman signal collection

- Decrease the RLS instrument spot size to analyse minerals with fine grain size

The RLS Raman laser has a spot size of 100 μm and it could not be focused on the fine grained mineral size samples such as the selected fayalite sample; ≤15 μm grain size. When analysing fine grained crystals, the main part of the Raman excitation light is diffracted in all directions or absorbed at the crystal grain interfaces, resulting in decrease of the Raman peak intensity. This was the reason that the detection of fayalite was impossible with the RLS instrument and the peaks obtained on rose quartz were poorly resolved. On Mars the ExoMars mission can expect to encounter numerous fine grained minerals in environments that will be selected for detailed analysis; areas of past active water-rock interaction and sulphate formation. Reduction of the laser spot size is therefore recommended. The down side of such an approach is that far more analyses will be needed to characterize the mineralogical variation in individual rocks. Reduction of the spot size from 100 to 10 μm for example will result in the analysis of a factor of 100 less material. Although this approach will lead to better resolution of individual minerals the decreasing the spot size will result in the increase in the amount of energy per volume and potentially destroy the sample. Therefore, the recommendation for variable power output is again emphasised. An ideal compromise would be to have variable magnification options on the optical head of the RLS instrument. Without such flexibility many minerals will not be identified (large spot size) or potentially destroyed (high laser power and small spot size). More detailed research needs to be conducted on rocks considered representative of Martian surface environments to have a better understanding of the potential trade-offs required between laser spot size and power. Such work particularly needs to take into account that most Martian surfaces are not flat, even at the 100 μm scale. Methodologies are needed to optimise analyses of true samples as opposed to the laboratory samples measured in this study. Time constraints related to the manufacture of the MASC prevented this PhD research from conducting such work, which was part of the original research plan. We are totally aware that the recommendations made above for variable laser power and magnification will have major repercussions for the overall power usages, mass and size of any future instrumentation. However, the practical experience of using the RLS instrument make it clear that performance is far below that of a research instrument and any Flight Model needs greater flexibility than the current EB instrument.

- Improvement in the RLS instrument design

TNO, the designers and manufacturers of the RLS instrument, undertook a detailed analysis of the optical efficiency of the RLS instrument. A power meter was used:

- To measure the amount of Raman laser light energy from Raman laser excitation source to the sample surface, Table 6.2.
- To measure Raman emission energy from the sample surface to the spectrometer and CCD, Fig 6.3.

Light loss in the instrument is expected to be caused by absorption of the different optical components (such as fibres, mirrors and filters), optical misalignment and inefficient coupling between components. The contribution of different components in the loss of Raman laser excitation light (before reaching the sample) is presented in table 6.2. At the laser output, 6.62×10^{16} photons per second are emitted but at the sample surface only 1.6×10^{16} photons per second are measured.These data emphasise that optimal alignment of the fibres and connectors is essential to avoid the loss of the Raman laser excitation light in the RLS instrument design.

Source laser	6.62×10^{16} photons/s
Optical interface Fibre	85%
FC optical fibre connectors (use in high-vibration environments)	90%
Fibre coupling connector	80%
	55%
Overall transmission	24.25%

Table 6.2. Percentage of Raman laser light transmitted by the different optical components from the Raman laser excitation source to the sample surface.

In addition, Raman emission was also lost in different parts of the RLS instrument from the sample surface to the spectrometer. First, Raman emission is emitted in all directions from the sample surface and the RLS instrument collects the Raman emission within a cone with a half angle of 12.7 degrees. Therefore, the Raman emission, which was emitted in different directions outside this cone, was lost: only ~1% of the light is indeed collected (half angle of 12.7 degrees corresponds to a solid angle of 0.15 steradian, which is 1% of the solid angle of a full sphere).Additional Raman emission was lost inside the optical head, at optical interfaces and finally inside the spectrometer. Therefore, only approximately one Raman photon in 10000 produced at the sample was detected by the CCD. A graph summarising the loss of Raman emission from the sample surface to the CCD is shown in Table 6.3. This graph demonstrates that Raman emission was mostly lost at the collection angle. Then there are successive losses at optical interfaces. Almost half of the Raman emission was lost significantly in the spectrometer. Consequently,re-design of the collection angle and spectrometer can be a potential option to avoid the Raman emission loss.
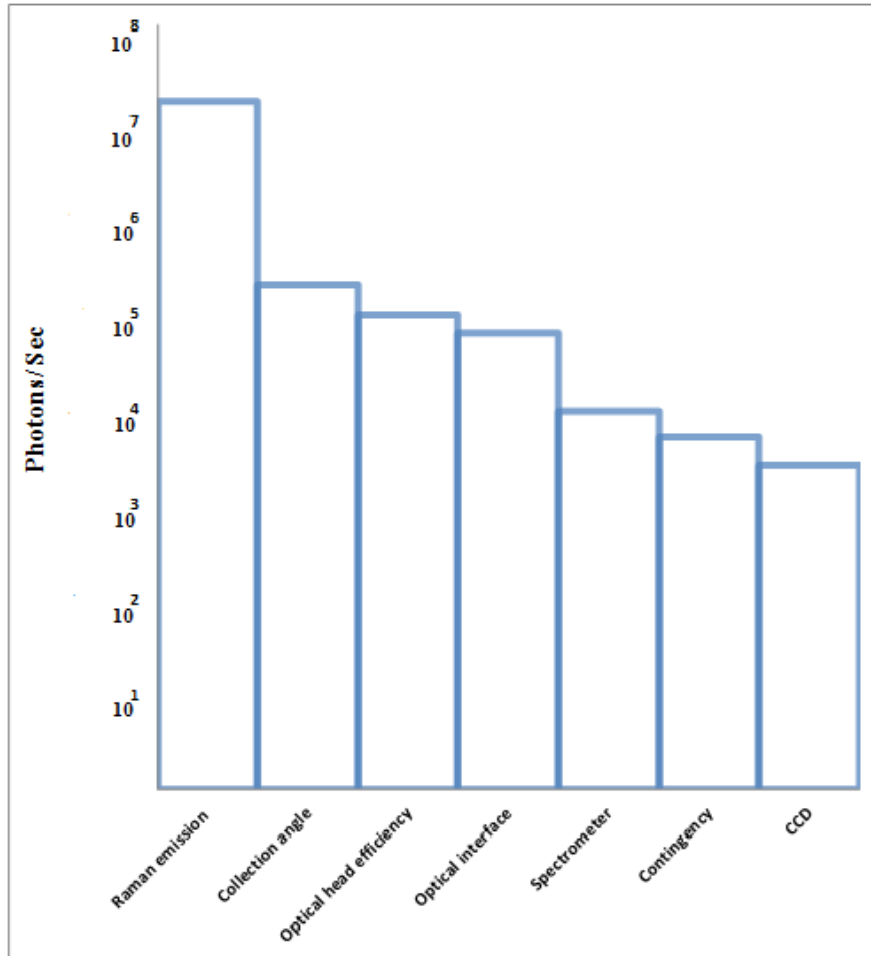
Table 6.3. Graphs of Raman emission loss from the sample surface to the CCD. Note the graph has a logarithmic scale (TNO document-ESA-RLS-RP-2008).

6.3.1.3   *Improvement in the SNR*

Given the relatively inefficient production of Raman signals in the RLS instrument compared to laboratory instrument (such as the Renishaw InVia Raman microscope that we used for comparison studies), improvement in SNR of the RLS instrument is potentially of great benefit. Noise sources can be classified into two types: temporal and spatial. Examples of temporal noise were shortly discussed in section 2.4.3.1 and are:

- Shot noise,
- Output amplifier noise,
- Dark noise,

Spatial noise sources contain dark current non-uniformity and photo response non-uniformity. Some spatial noise can be removed for example by applying frame subtraction or gain/offset correction techniques to the data obtained from the CCD.

Temporal noise varies with time and can be decreased by increasing the integration time. Integrating for longer time on the CCD or stacking the Raman spectra will improve the SNR.These two solutions will be treated in the following sections to find the more relevant technique to improve the SNR in the RLS instrument.

- Increase the acquisition time to decrease shot noise

To assess the best way to improve the SNR a series of simple experiments were performed with different acquisition times where a straightforward spectrum such as calcitewas examined. Raman spectra of calcite were obtained with the acquisition time of 9, 30, 40, 90 and 100 s. The SNR of the weak peak at ~1087 cm^{-1} at the same spot of a calcite sample was 70.3, 80, 180, 196.4 and 140 counts for acquisition times of 9, 30, 40, 90 and 100 s respectively, Table (6.4). Unfortunately, SNR of the peak at the acquisition time of 100 decreases, because the lower laser was unstable and produced multiple wavelengths (Fig. 6.3).Further experimentationestablished that the laser wavelength is definitely unstable with an acquisition time longer than 40 s irrespective of the numerous remedial measures applied. Therefore, in this PhD research an acquisition time of 40 s was selected to avoid the instability of the laser excitation light and for the detection of weak peaks for all measurements. Clearly it is unviable to manufacture the RLS instrument that contains an unstable laser and this point is not discussed in any further detail in this work.

The integration time required to obtain a useful spectrum also depends on the selected samples. Raman spectra of group B and C (Table 6.1) were obtained with longer integration times, but even for long acquisition time such as 100, 120 s and 160 s Raman peaks for minerals in group *C* were not detected.
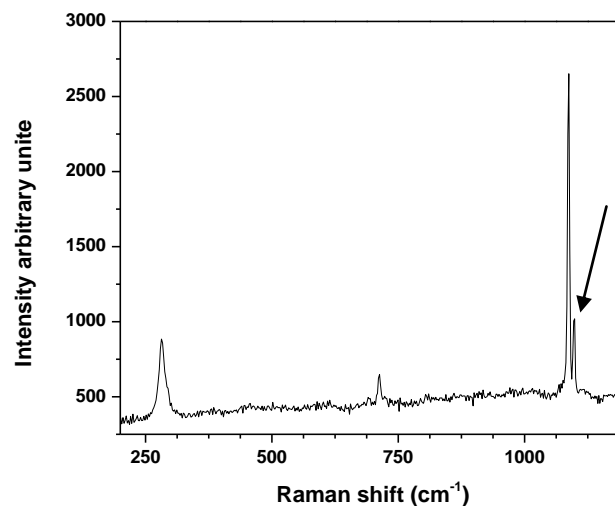
Figure 6.3. RLS Raman spectrum of calcite with acquisition time of 100 seconds. Laser excitation wavelength was unstable at 100 s acquisition time leading to a "ghost peak" at 1087 cm^{-1}; marked with the arrow.

Acquisition time	Noise	S	S/N
9	8	562.5	70.3
30	9	720	80
40	12	2160	180
90	14	2750	196.4
100	15	2100	140

Table (6.4). The SNR of the weak calcite peak at ~1087 cm^{-1} for acquisition times of 9, 30, 40, 90 and 100 s.

- Improvement in the SNR by stacking Raman spectra

Stacking a series plots is expected to show benefit as some of the random noise will be cancelled out thereby producing better SNR. The stack Raman spectrum is presented in Fig 6.4. Eight Raman spectra of a calcite sample were collected to determine if the SNR increases. However, as already mentioned, the laser excitation source was unstable and "ghost peaks" were presentin the calcite Raman peaks spectrum. Therefore, experiments performed with the RLS instrument at the VU did not find this method useful. However, in using the Renishaw InVia Raman microscope, we successfully adopted this approach and it is therefore recommended that the operational software of the RLS has the flexibility to vary both integration time and stack spectra.
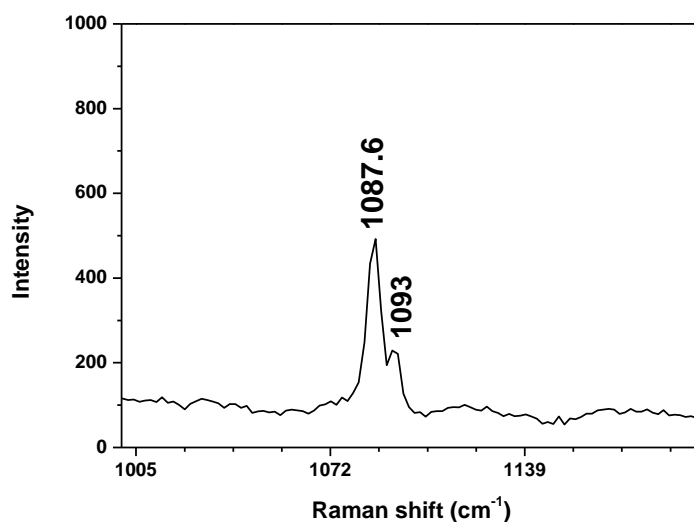
Figure 6.4. Stack plots of eight Raman spectra of a calcite sample (with 40 s acquisition time) from 1000 to 1200 cm^{-1}. The integrated spectrum shows that the laser excitation wavelength was unstable as there were two ν_1 intense peaks results from the symmetric stretching of CO_3 group at 1087.6 and 1093 cm^{-1}.

In the next generation of the RLS instrument, we do not expect problems with laser stability. Therefore, we recommend that the software that controls integration times of the CCD can be varied dependent upon an initial analysis. RLS instrument operates on Mars, it needs to have a very flexible analytical protocol. For instance, measuring carbonate is relatively easy and

the problem will be that large peaks may over saturate the CCD. Long integration times for all analyses are therefore not possible. A complementary solution would be to stack multiple integrations. But this will require additional processing power and could be limited by processing power within the Rover. As well, according to section 2.4.3 the combination of the multiple integration times may instead increase read-out noise. Increasing the acquisition time is then a better solution. So we recommend to first increase the acquisition time as much as possible, then to stack different spectra if still necessary.

6.3.1.4   Decrease thermal noise in the CCD cooling system

As discussed at section 2.4.3.1 electrons not related to the absorption of photons are generated within the CCD by physical processes within the CCD itself. The number of these electrons generated mainly depends on the operating temperature of the CCD. Based on the Raman spectra of some potentially key minerals in respect of Martian exploration that were studied in this thesis (e.a., gypsum, barite and anglesite at low temperature), it was not always possible to detect all their weak peaks, even when the CCD was at its lowest temperature (~ -40 °C). Given the expected sampling methodology of ExoMars, analyses of multiple minerals will be a common event and so it will be vital to detect as many Raman peaks as possible so as to be able to recognise all the minerals that contribute to a single Raman spectra; the more Raman peaks recognised the easier it will be to recognise multiple minerals. Our experimentation established that reduced dark noise from the CCD when operated at ~ -40 °C, makes peak detection limit about two times better than at -30 °C. Clearly further improvement in peak detection will provide benefits in the identification of weak Raman peaks. Two recommendations are therefore made. First, to replace the current CCD with the better and more modern CCD that is more sensitive and has lower dark noise. Such instrumentation is already available (Holland et al., 2004). Second, re-design of the CCD cooling circuit is required to reduce the operating temperature of the CCD to below -40 °C. The latter recommendations has a potentially significant implication for the power usageof the ExoMars rover, however, given the generally low temperatures encountered on the Martian surface, especially at night, it should be possible to accommodate a more efficient CCD cooling system with low weight and power consumption.

6.3.2   Improve the spectral range of RLS instrument above 3000 cm^{-1}

A major conclusion of this thesis is that the spectral range of the RLS spectrometer is too limited; as explained in section 6.2. Most crucial is the lack of capability to detect peaks associated with water vibration modes in minerals above 3000cm^{-1}. This is a fundamental design limitation of the RLS instrument and is a reason why the Raman only instrument now being prepared for ExoMars will have a different spectrometer design and a larger spectral range.

In principle it is possible to re-align the optics of the RLS spectrometer to allow the detection of O–H Raman vibration modes in the 3300 to 3500 cm^{-1} region. However, as the RLS

instrument is the property of ESA and it was not possible to make major modifications to the spectrometer; e.g., re-alignment of the grating. Our research has established that it is possible to detect Raman peaks > 3000 cm^{-1} when the position of the grating or the wavelength of the excitation laser light is changed. Work led by Dr A. Collin resulted in the introduction of a new laser system and replacement of the laser optical system. Several laser excitation sources were reviewed to select a suitable wavelength for detection of the O–H vibration mode of water. Figure 6.5 shows the Raman spectra of an amphibole sample with different laser excitation sources. The O–H vibration mode of water is identified with 473 and 532 nm Raman lasers. According to the data shown in chapter two (section 2.4.3) Raman laser with a 532 nm wavelength did not completely fit in the RLS CCD range. Based on the wavelength of the Raman laser excitation source (532 nm) Raman emission is detected in the 4rd diffraction order that covers the wavelength range 504–630 nm, i.e. Raman shift until 2900 cm^{-1}. Because of the design of the grating, the 3rd diffraction order with the wavelength ranging between 650 and 840 nm reaches the CCD. So there is a gap between 650 and 630 nm on the CCD and Raman shift between 2900 and 3400 cm^{-1} cannot be analysed (see chapter two, section 2.4.3). In contrast the range of the Raman spectrumobtained by a 473 nm wavelength laser, was found to fit in the fourth and fifth diffraction orders in the CCD detector (200 to ~5300 cm^{-1}). In addition, this laser is small (~ 10 cm x 6 cm) and commercial Raman filters were available. Therefore, this commercial laser with band filter and ultrasteep edge filter was selected for identification of the O–H vibration mode of water with the RLS instrument.
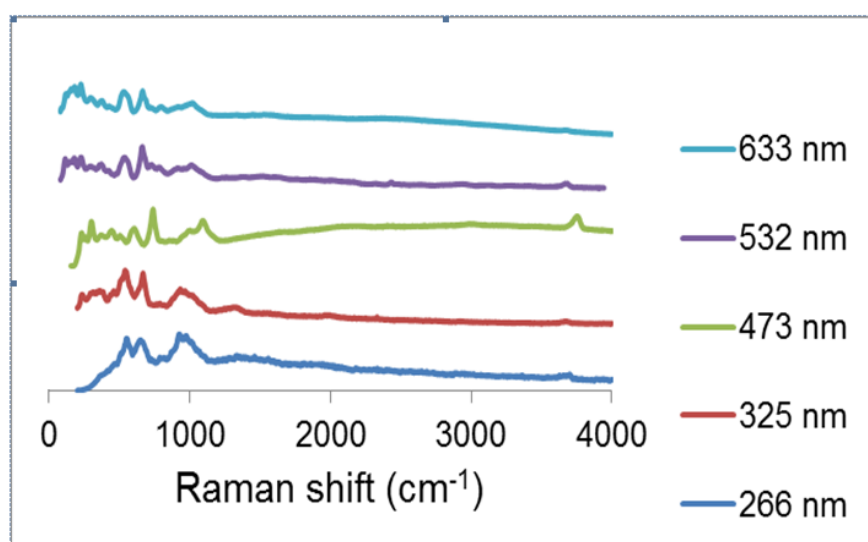
Figure 6.5. Influence of the laser wavelength on the water signal in amphibole, taken from the commercial Raman instrument in Lille, France. The Y axis is arbitrary units and all spectra are normalised to their highest peak and vertically offset for legibility. Water peak is observed with laser with 473 nm wavelength.

By installing the ~473 nm laser on the RLS instrument, detection of O– H vibration modes of gypsum were possible as shown in Fig 6.6. In the gypsum Raman spectrum, the peak around 3300 and 3500 cm^{-1} are generated by symmetric stretching (v_1) and antisymmetric (v_3) stretching vibration modesof water respectively. v_2 bending vibration mode of water as a

weak mode (at ~ 1880 cm^{-1})was not detected. This approach emphasises that a redesign of the RLS instrument would allow better identification of minerals by Raman spectroscopy while maintaining a comprehensive coverage of the LIBS spectrum.
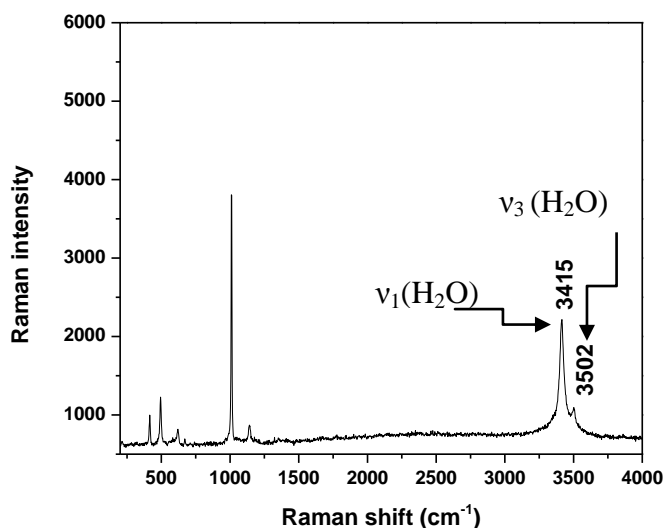
Figure 6.6. RLS Raman spectrum of gypsum, with 473 nm excitation laser.

6.4   Conclusion

The fundamental conclusion is that the RLS instrument was able to analyze a group of selected minerals under Martian conditions inside the MASC validating the basic principle that a combined Raman/LIBS instrument is applicable for planetary missions. A second major conclusion is that no significant variations in Raman spectra were determined due to changes in environmental conditions pertinent to Mars. Importantly it has been shown that it is possible to use changes in Raman spectra to determine the composition of olivine with the RLS instrument by monitoring variations of a doublet peak in the 700–900 cm^{-1} range. Moreover, recognition of carbonates and different sulphate minerals was also possible. RLS Raman spectra for barite, anglesite and gypsum have clear differences that can be related to the different mineral structures. In all spectra, there were variations in peak positions and splitting, due to the influences of the different metal cations. In the case of barite and anglesite, the wavenumber of the vibrational modes of SO$_4$tetrahedra, decreases with an increase of the atomic mass of the metal cations. In addition, Raman peaks shift to higher wavenumbers with an increase of the stretching force constant of S–O bonds.

The use of the RLS instrument inside the MASC chamber has raised a series of practical aspects of Raman analysis that need to be addressed before a RLS instrument is sent on a planetary mission. These mostly concern the analysis of typical surfaces on Mars. The RLS instrument was unable to detect Raman signals from several mineral samples that were

identified by the commercial Renishaw InVia Raman microscope, even though all the samples were prepared as flat surfaces. The fact that fine grained samples (< 15 μm) were difficult to analyse emphasises that on the non flat surfaces that will be encountered on Mars it will be even more difficult to obtain high quality Raman spectra. We recommend extensive further testing of the RLS EB instrument and the newly designed Raman-only instrument for ExoMars on samples that will be more typical of Martian surfaces. The work carried out to date, although under Martian conditions, was essentially under laboratory conditions. More rigorous assessments of the effects of variable grain size and surface morphology are needed, as the intensity of the Raman peak is determined not only by instrument optics, but by the sample properties. The influence of the crystals properties (such as grain size, surface relief, colour and absorption coefficient) on the peaks intensity needs to be studied.

We identified several aspects of the RLS instrument that were sub-optimal and a series of recommendations were made of how to improve instrument performance. These are summarised below.

Recommendation	Goal
- Select a suitable stable Raman laser source	- Accurate and reproducible Raman spectra
- Increase the laser power	- Improving the detection limits of minerals
- Decrease the RLS instrument spot size	- Ability to identify minerals of small grain size
Improving the RLS optical design - Re-design spectrometer - Shorter optical fibres - Use less connectors	- To increase SNR and optical transmission
- Improve the CCD cooling system	- Increasing SNR (decrease thermal noise)
- Change the angle of the grating or apply a shorter wavelength laser source	- To expand the Raman spectral range to above 3000 cm^{-1} to include water

Table 6.5. Recommendations for improving the RLS instrument.

The current RLS instrument has been shown to be viable as a Raman instrument and initial work with LIBS has also produced valuable data (Colin et al., 2012). Coupled with the proposed improvements above we are confident that the use of a combined Raman-LIB spectrometer will be a valuable addition to the contact instrument package of future planetary missions.

6.5   References

Delhaye, M. et al., (1996), Chap 3: Instrumentation. in: Turrell G and Corset J (eds) Raman Microscopy. Developments and Applications. Academic Press, London.

Colin, A. et al., (2012), Sensitivity study of lunar soil water content measurements using a combined Raman/LIBS instrument. ESA/ESTEC conference: Scientific Preparations for Lunar Exploration, ESA/ESTEC- Noordwijk (The Netherlands) – poster.

Holland A. D. et al., (2004), CCDs for the rotational velocity spectrometer on GAIA doi:10.1117/12.517151.

Wang, A., (1644),Some Grain Size Effects on Raman Scattering Intensity for In Situ Measurements on Rocks and Soils Experimental Tests and Modeling, Lunar and Planetary Science XXX, 1644.

Appendix
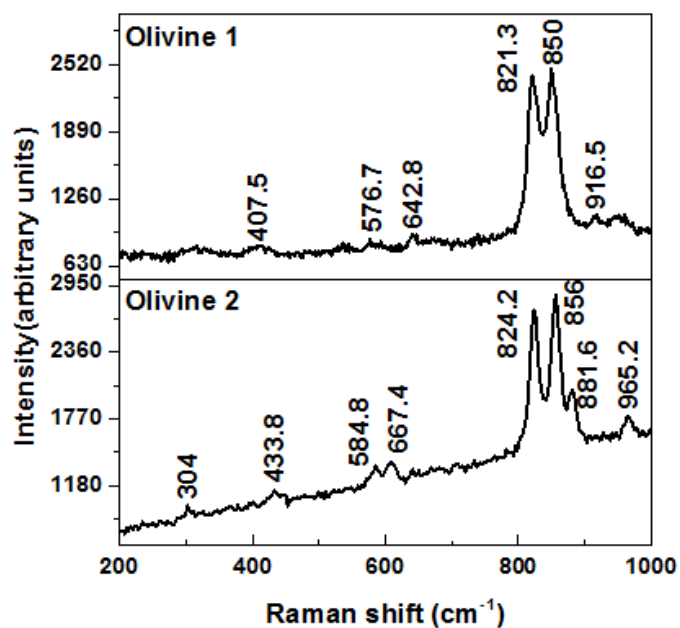
Figure 1. The Raman spectra of olivine 1 (Fo_{64}) and olivine 2 (Fo_{93}) taken with the Renishaw InVia Reflex confocal Raman microscope for the 200-1000 cm^{-1} region.
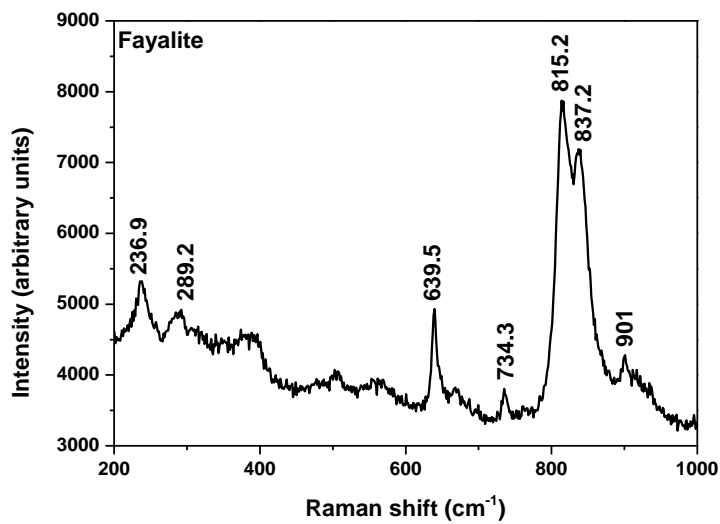
Figure 2. The Raman spectra of fayalite (Fo_{01}) taken with the Renishaw InVia Reflex confocal Raman microscope for the 200-1000 cm^{-1} region.
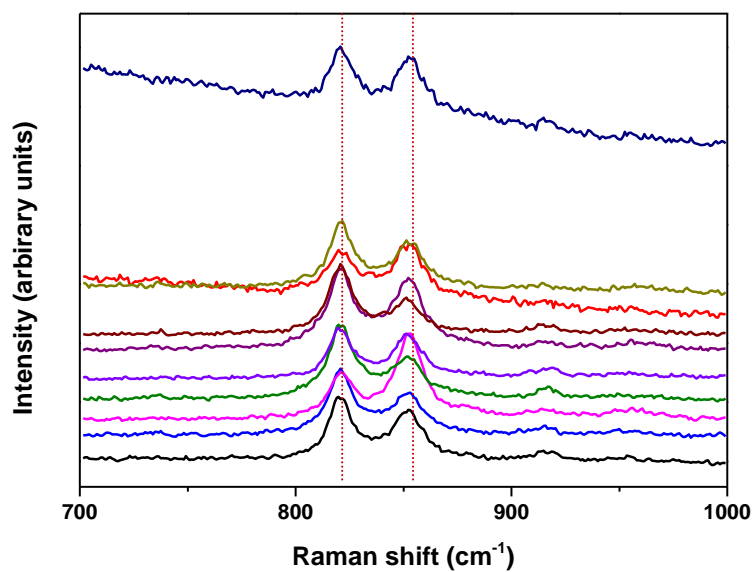
Figure 3. The Raman spectra obtained from 10 random grains of olivine 3 taken with the Renishaw InVia Reflex confocal Raman microscope for the 700-1000 cm⁻¹ region. Spectra are vertically offset for legibility.
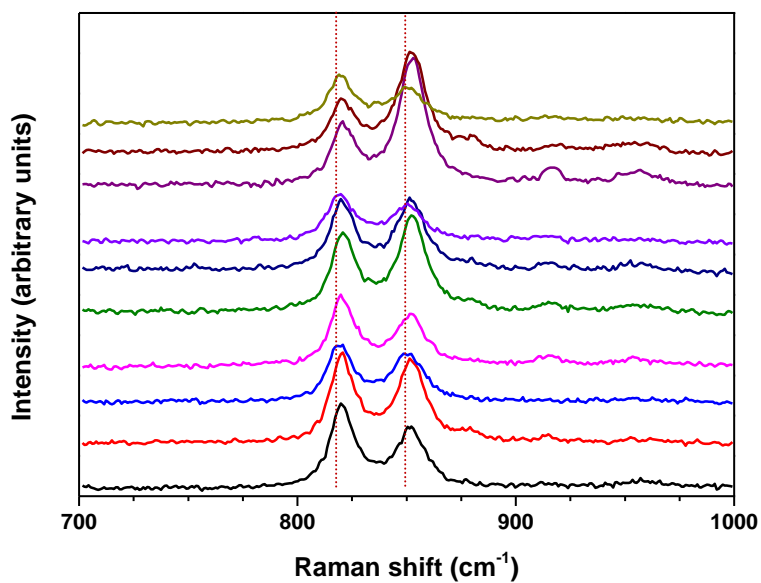
Figure 4. The Raman spectra obtained from 10 random grains of the olivine 4 taken with the Renishaw InVia Reflex confocal Raman microscope for the 700-1000 cm⁻¹ region. Spectra are vertically offset for legibility.
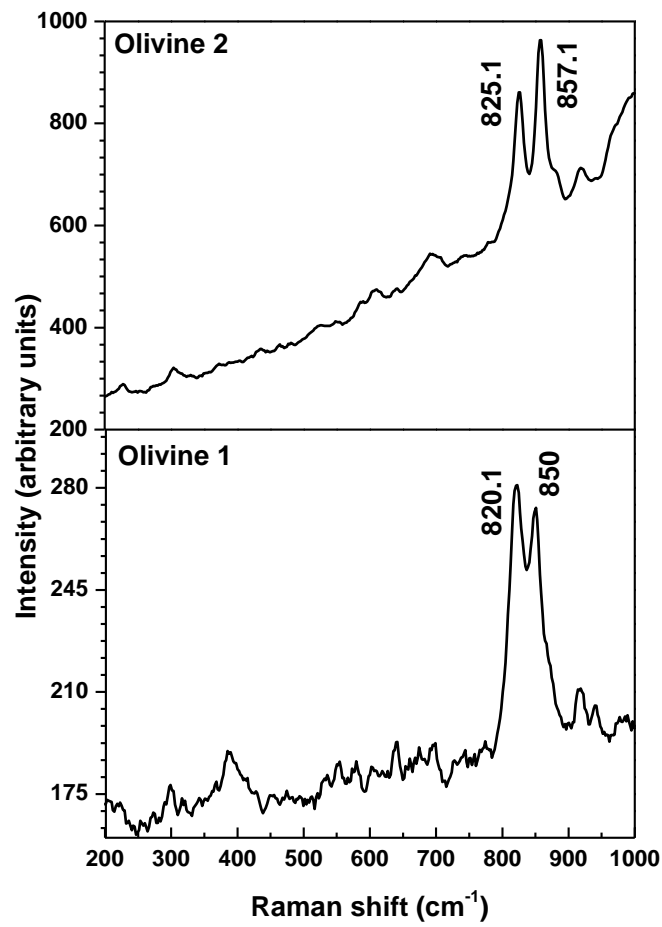
Figure5. The RLS Raman spectra of olivine 1 and olivine 2 obtain under vacuum condition at 10 °C.
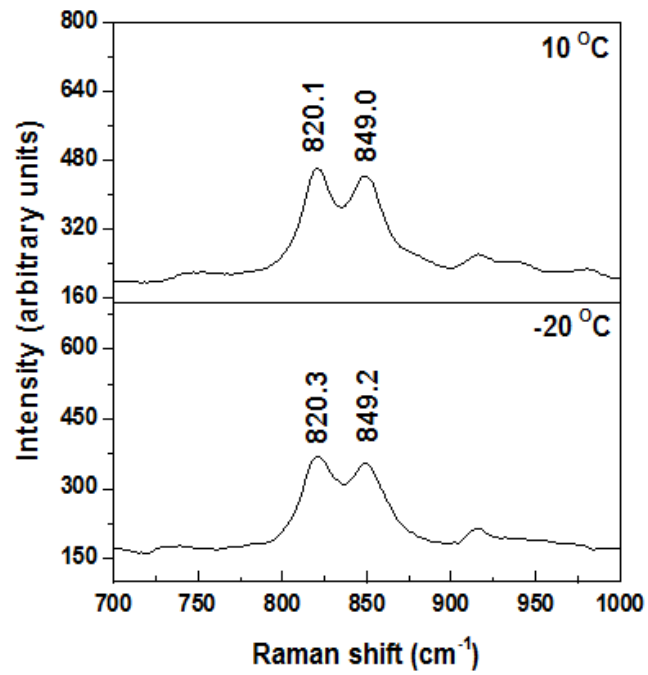
Figure 6. RLS Raman spectra of olivine 1 in the range 700– 1000 cm^{-1}, the measurement conditions are under vacuum condition at +10 and -20 °C.
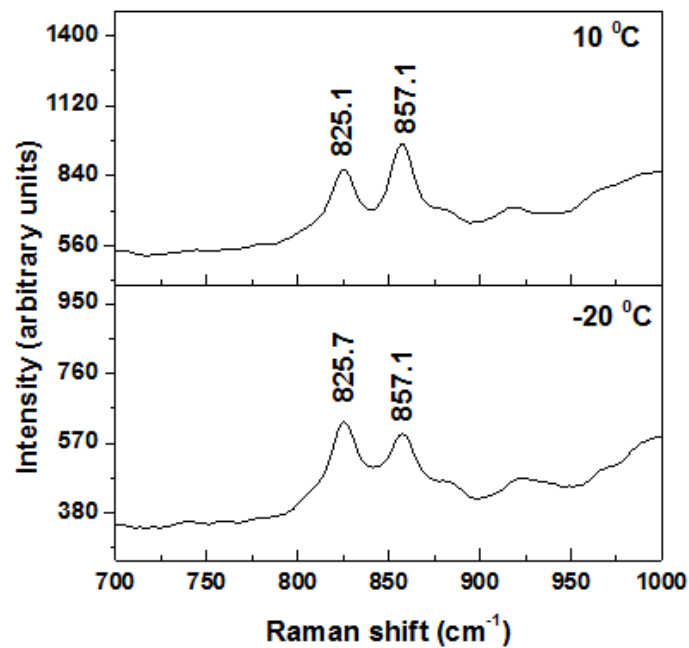
Figure 7. RLS Raman spectra of olivine 2 in the range 700– 1000 cm^{-1}, the measurement conditions are under vacuum condition at +10 and -20 °C.
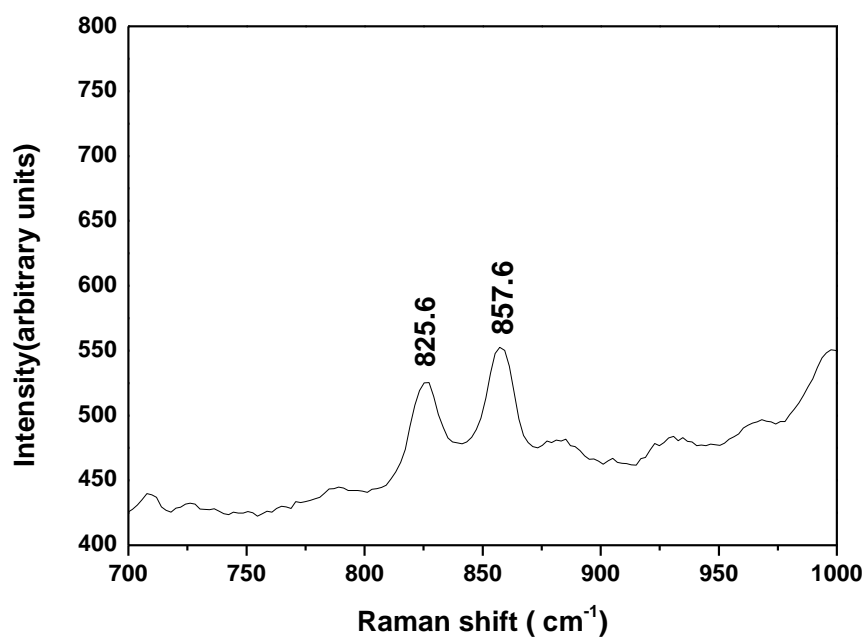
Figure 8. RLS Raman spectra of olivine 2 in the range 700– 1000 cm^{-1}, the measurement condition is CO_2 atmosphere with -20 °C.
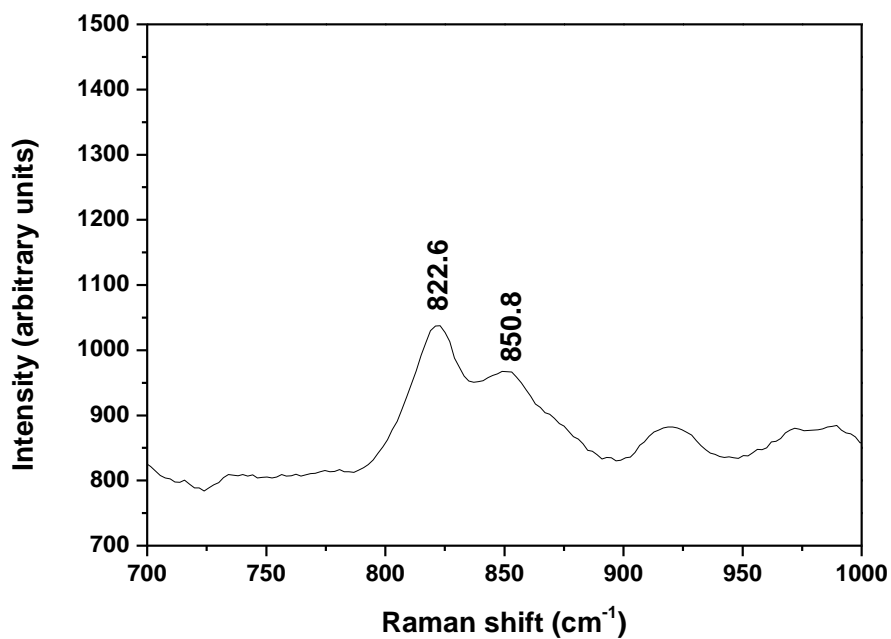
Figure 9. RLS Raman spectra of olivine 1 in the range 700– 1000 cm^{-1}, the measurement condition is CO_2 atmosphere with -20 °C.
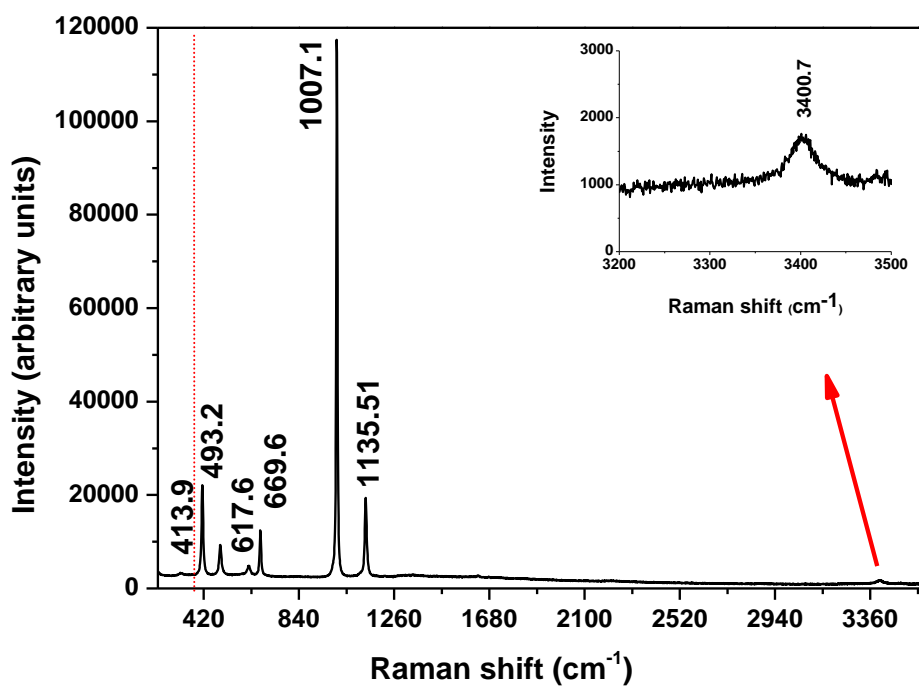
Figure 10. Gypsum Raman spectrum taken with the Renishaw InVia Reflex confocal Raman microscope. The peak at 3400.7 cm^{-1} is attributed to O−H vibration mode of water in the gypsum structure. The Raman spectrum of gypsum is separated into two parts, external vibrations (<400 cm^{-1}) and internal vibrations (400−1200 cm^{-1}) of the sulphate groups.
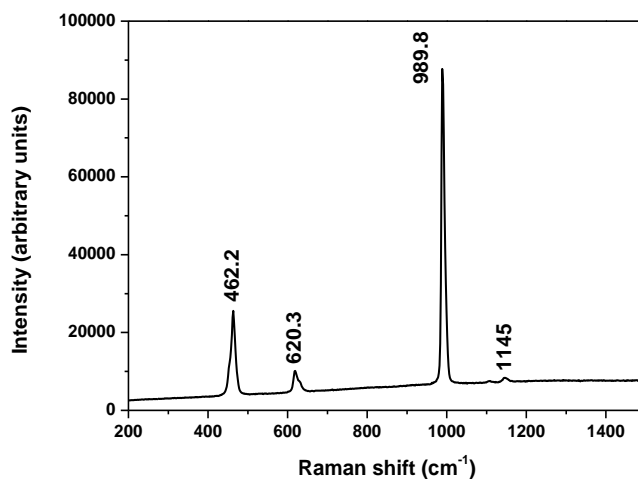
Figure 11. Barite Raman spectrum taken with the Renishaw InVia Reflex confocal Raman microscope.
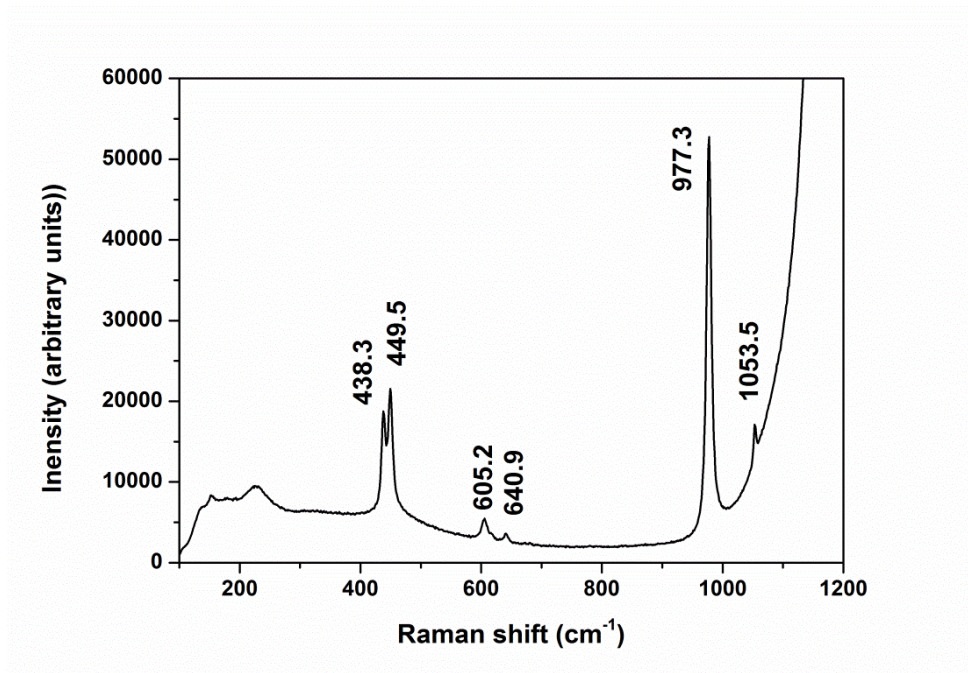
Figure 12. Anglesite Raman spectrum taken with the Renishaw InVia Reflex confocal Raman microscope.
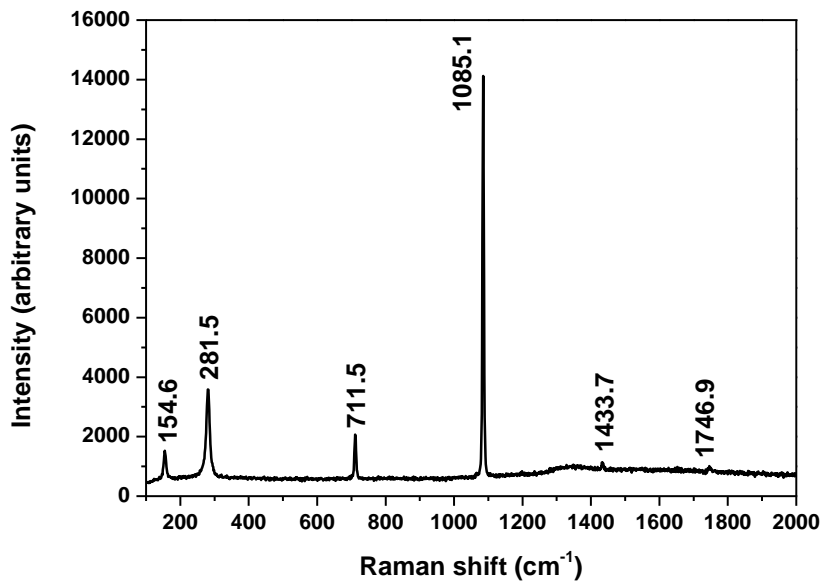
Figure 13. Calcite Raman spectrum taken with the Renishaw InVia Reflex confocal Raman microscope.
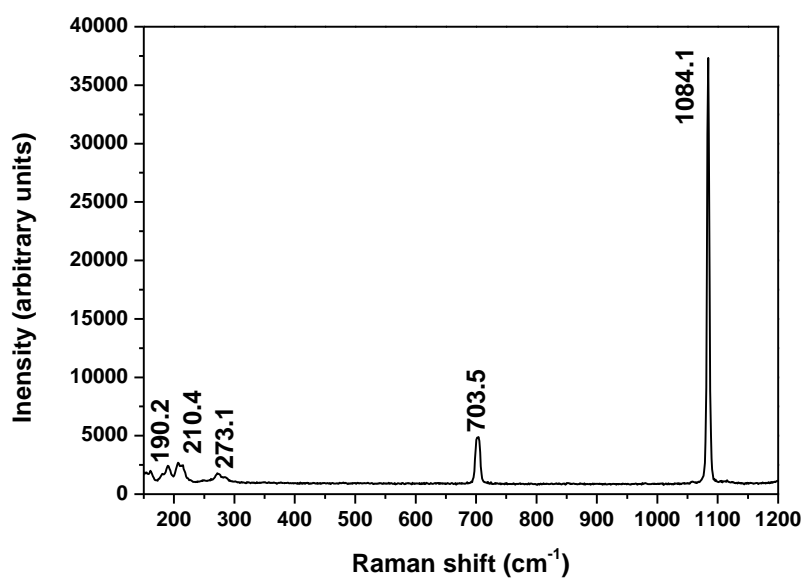
Figure 14. Aragonite Raman spectrum taken with the Renishaw InVia Reflex confocal Raman microscope.
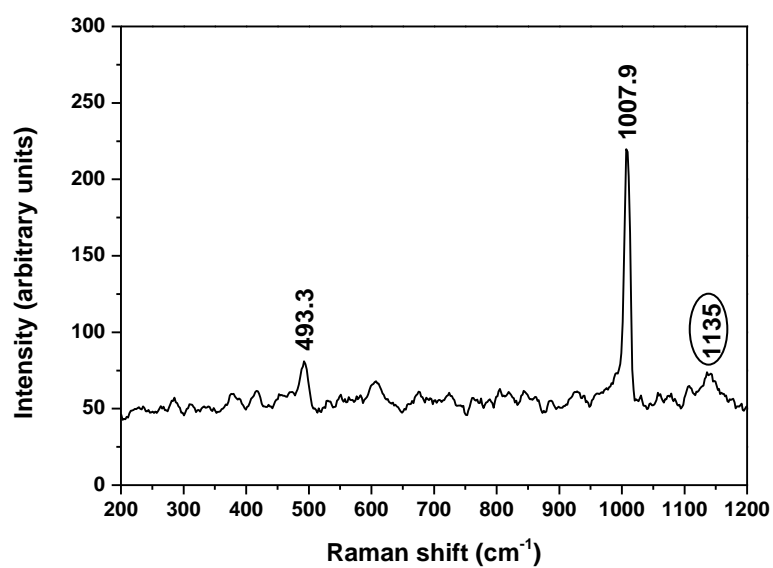
Figure 15. Gypsum RLS Raman spectrum under vacuum at 10 °C. The peak at ~ 1135 cm^{-1} is poorly resolved from the background noise.
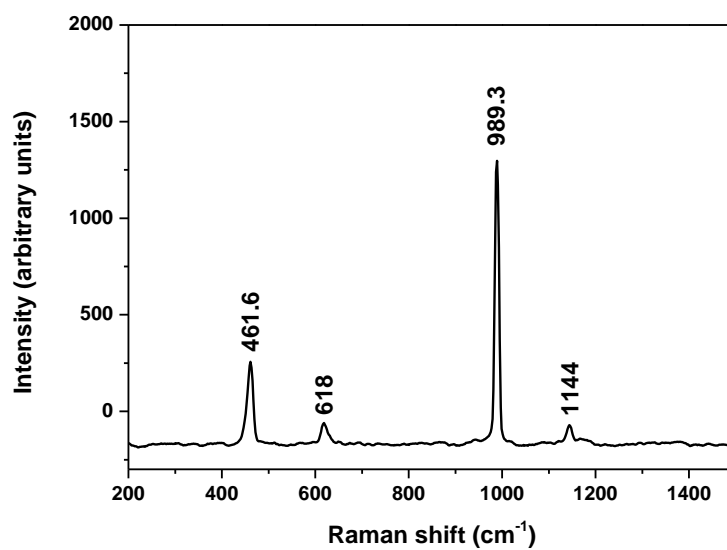
Figure 16. RLS Barite Raman spectrum under vacuum at 10 °C.
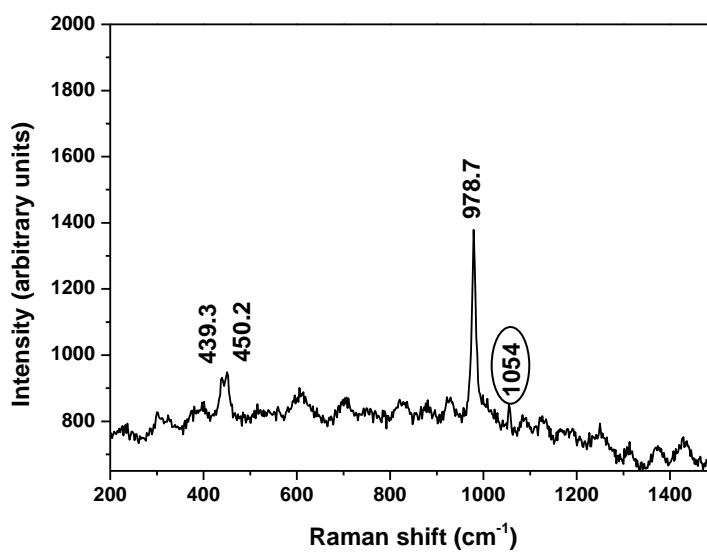
Figure 17. RLS anglesite Raman spectrum under vacuum at 10 °C. The possible peak at 1054 cm^{-1} was poorly resolved from the background at 10 °C.
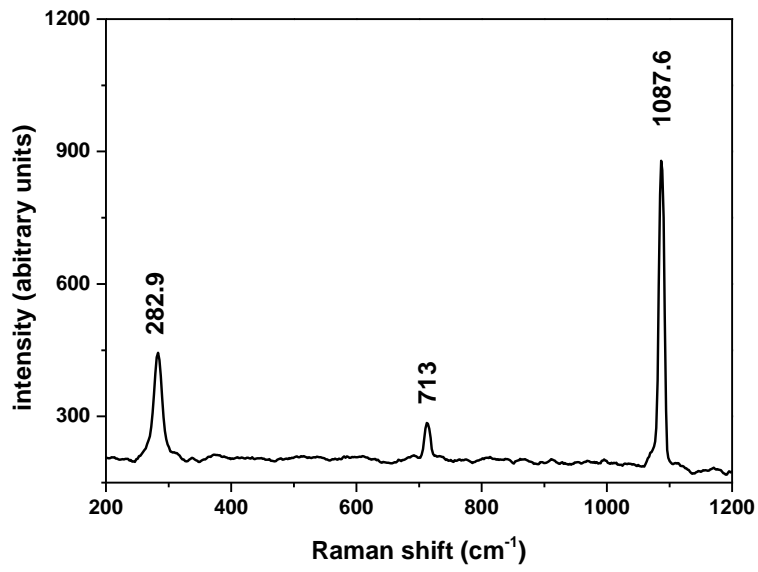
Figure 18. RLS calcite spectrum under vacuum at 10 °C.
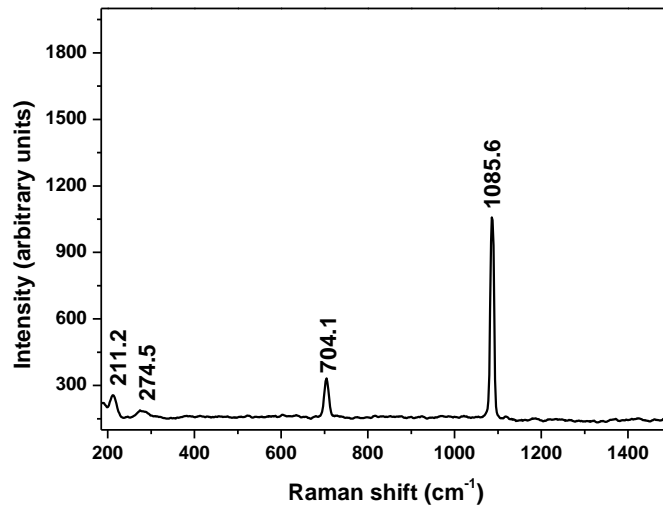
Figure 19. RLS aragonite Raman spectrum under vacuum at 10 °C.
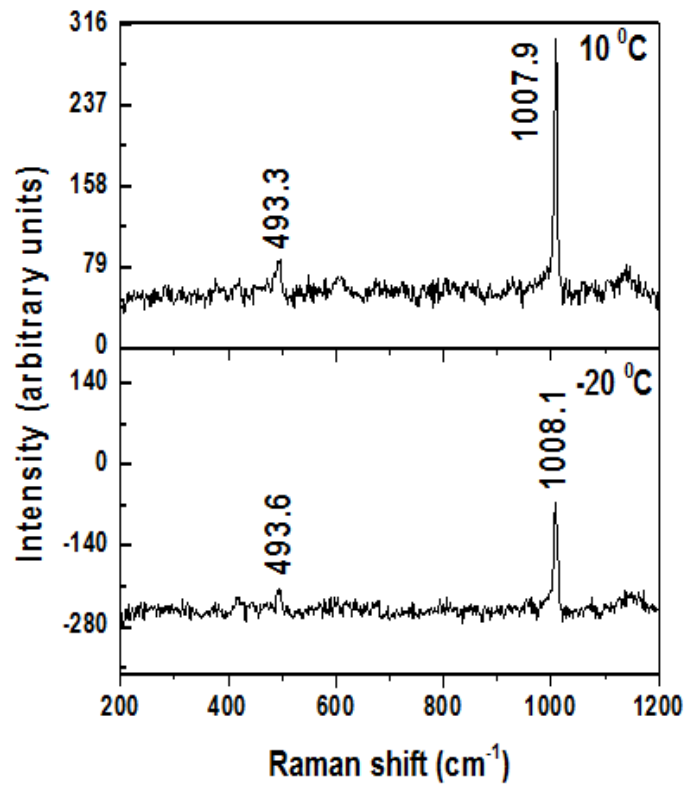
Figure 20. Raman spectra of gypsum in the range 200– 1000 cm^{-1}, the measurement conditions are vacuum at +10 and -20 °C.
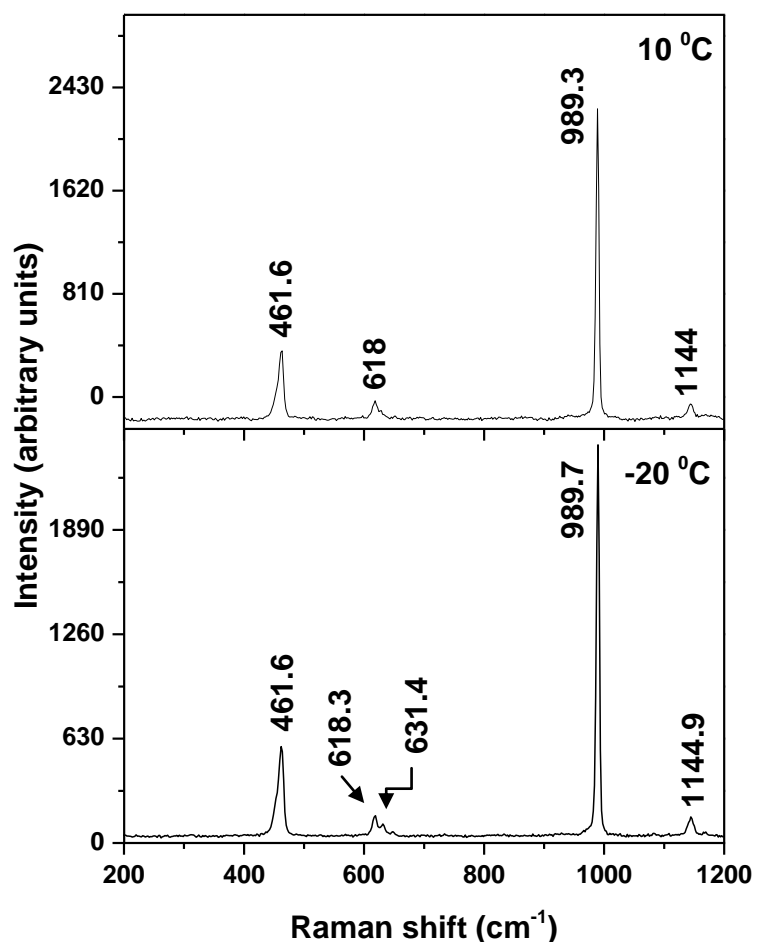
Figure 21. Raman spectra of barite in the range 200– 1000 cm^{-1}, the measurement conditions are vacuum at +10 and -20 °C.
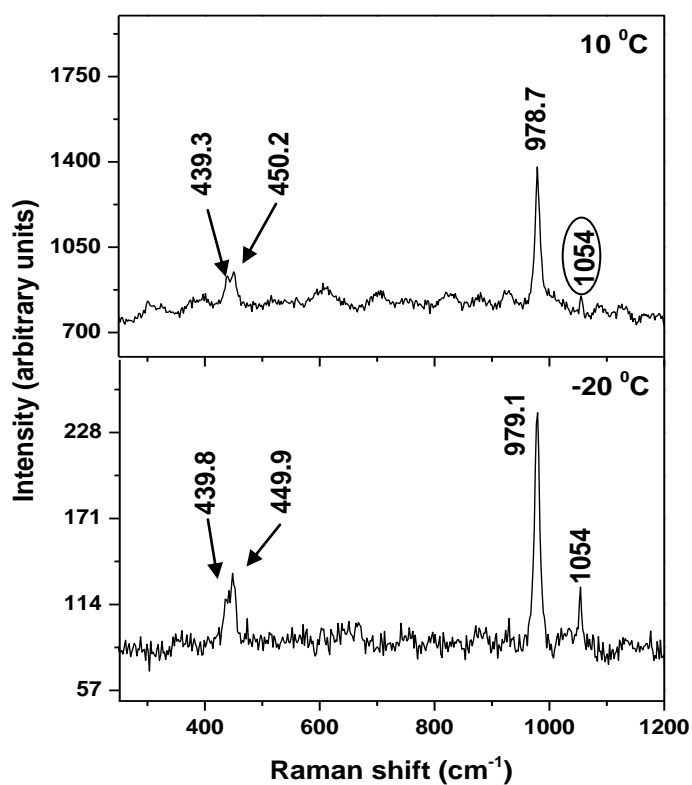
Figure 22. Raman spectra of anglesite in the range 200– 12000 cm^{-1}, the measurement conditions are vacuum at +10 and -20 °C. The possible peak at 1054 cm^{-1} was poorly resolved from the background at 10 °C.
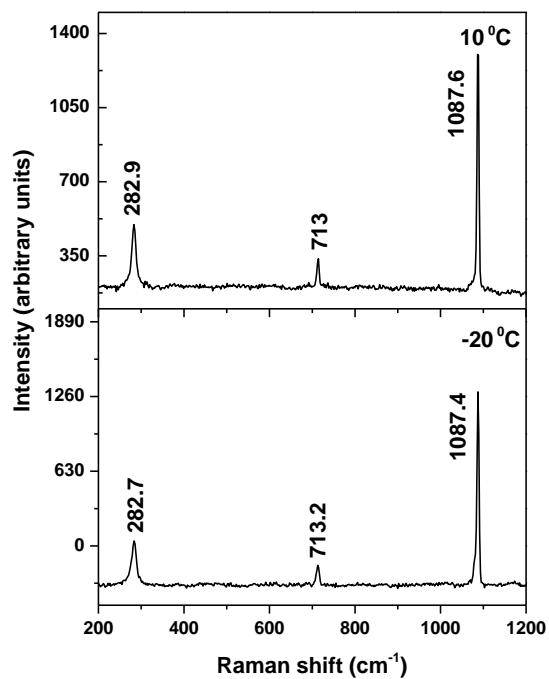
Figure 23. Raman spectra of calcite in the range 200– 12000 cm^{-1}, the measurement conditions are vacuum at +10 and -20 °C.
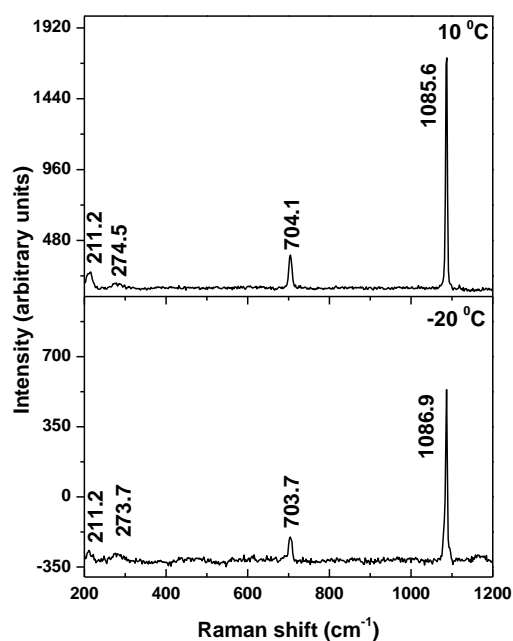
Figure 24. Raman spectra of aragonite in the range 200– 12000 cm^{-1}, the measurement conditions are vacuum at +10 and -20 °C.
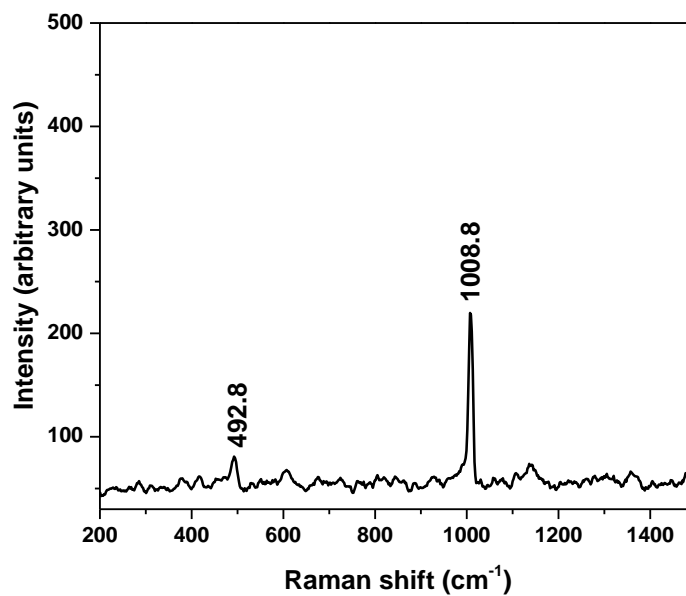
Figure 25. RLS gypsum Raman spectrum under 8 mbar CO_2 atmosphere at -20 °C.
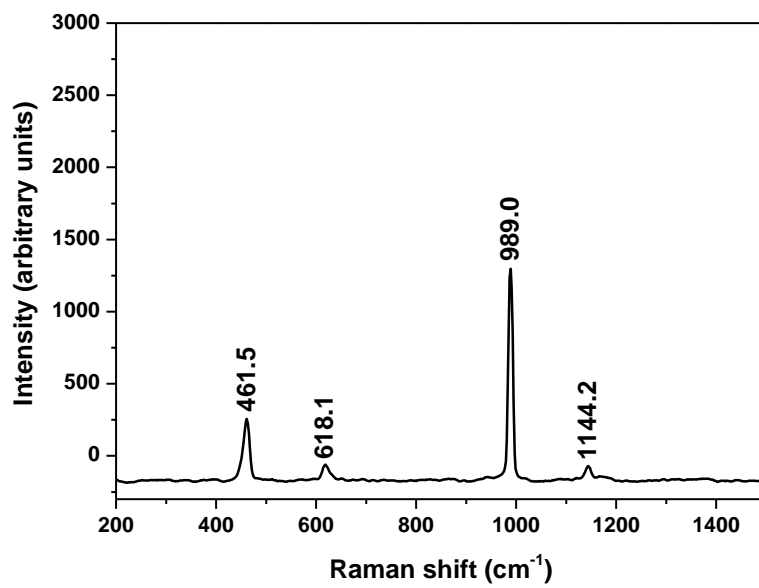
Figure 26. RLS barite Raman spectrum under 8 mbar CO_2 atmosphere at -20 °C.
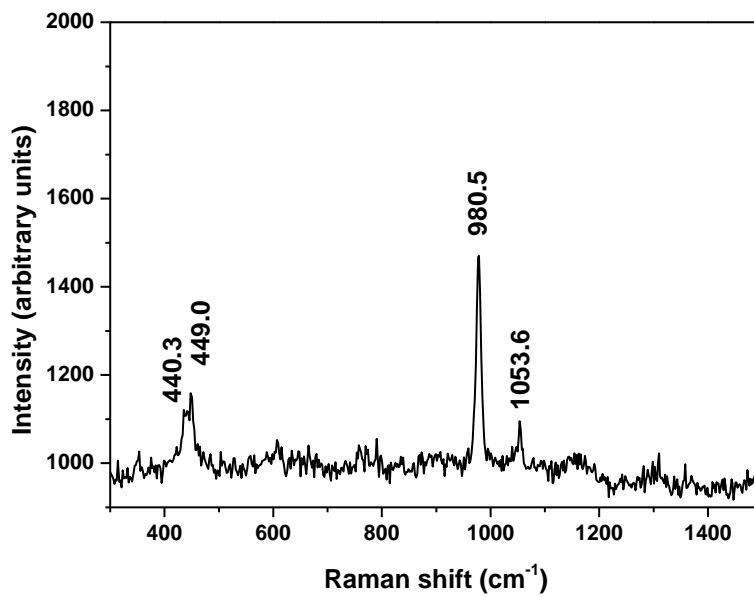
Figure 27. RLS anglesite Raman spectrum under 8 mbar CO_2 atmosphere at -20 °C.
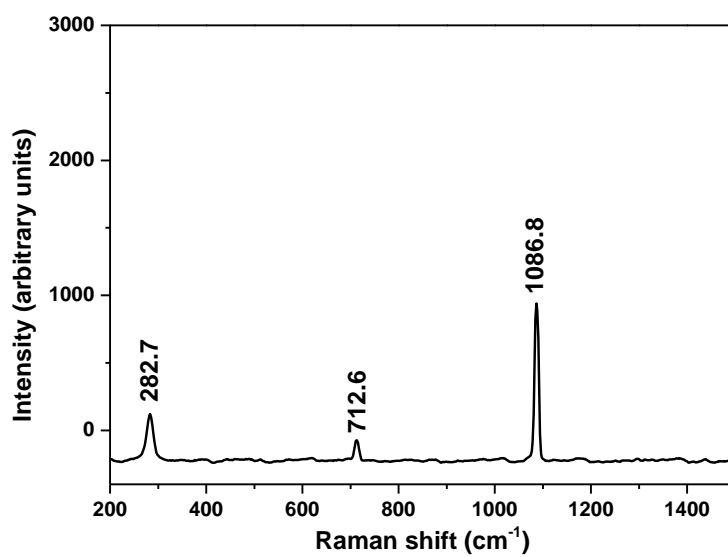
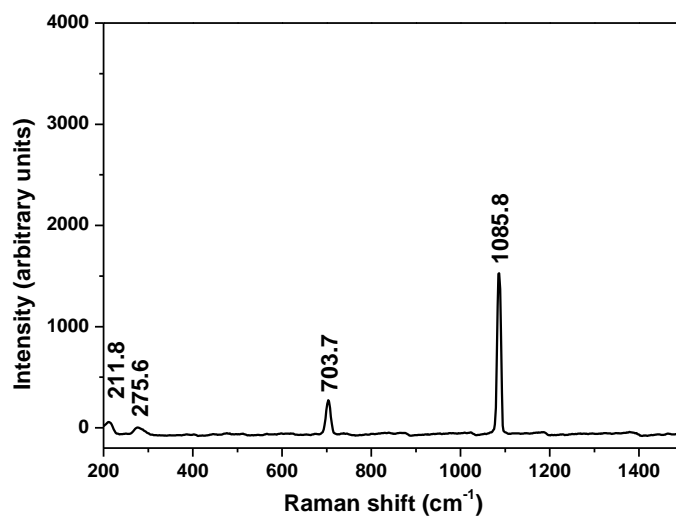Figure 28. RLS calcite Raman spectrum at -20 °C under 8 mbar CO_2 atmosphere.

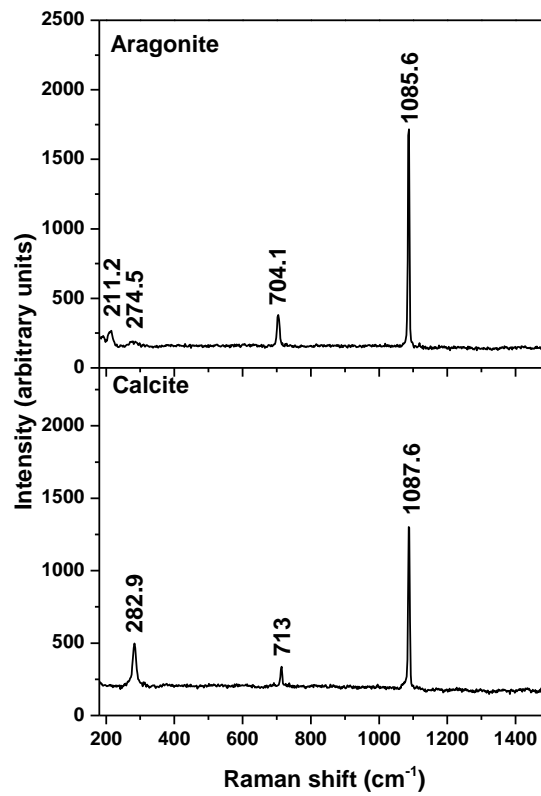Figure 29. RLS aragonite Raman spectrum at -20 °C under 8 mbar CO_2 atmosphere.

Figure 30. RLS Raman spectra of aragonite and calcite under vacuum at 10 °C in order to classify their mineral structure.
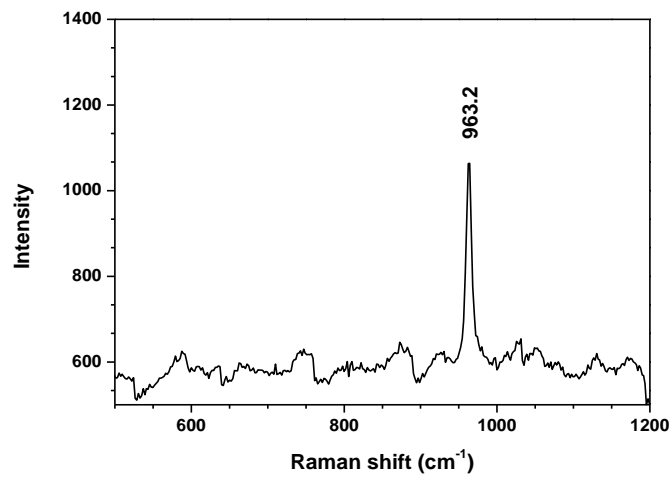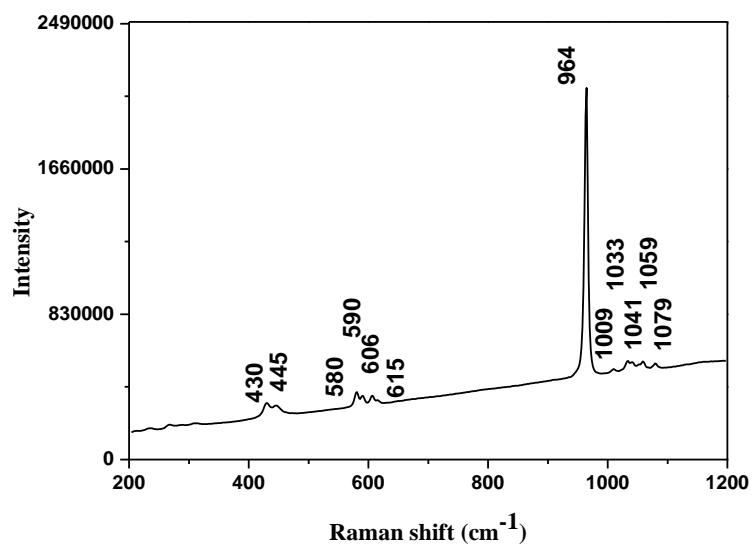

Figure 31. RLS Raman spectra of apatite
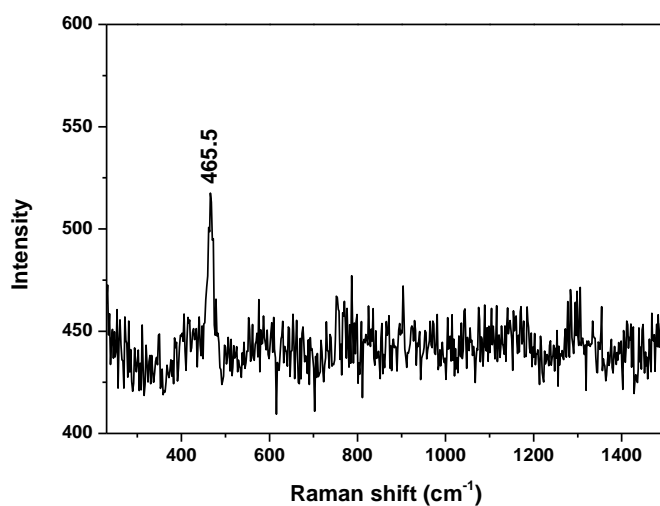
Figure 32. Renishaw Raman spectrum of apatite.
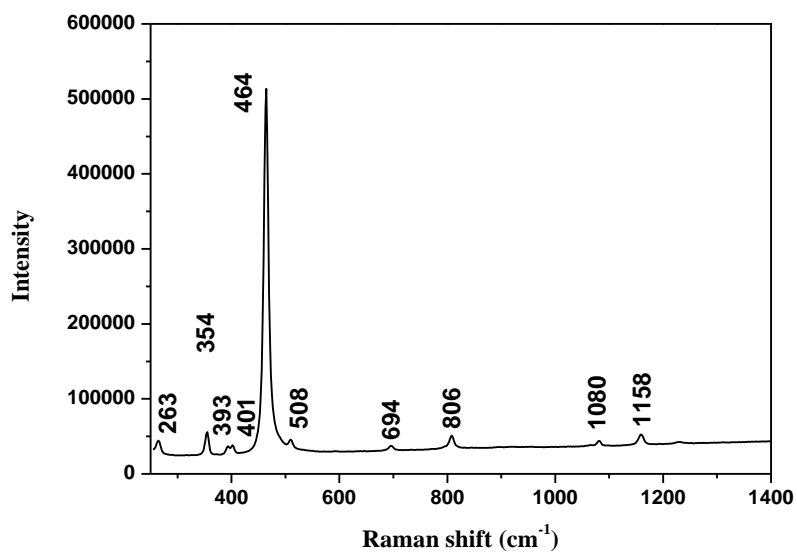

Figure 33. RLS Raman spectra of rose quarts.

Figure 34. Renishaw Raman spectrum of rose quartz.

Acknowledgements:

Professor Davies has been the main supervisor of this PhD research. I would like to thank him first of all. The time he spent on this research is appreciated. He introduced me to the people from the ExoMars programme, who proved to be very important and so helpful; thanks to Berit, Erik, Ian and Richard because I learned different aspects of my research from them. Maria deserves a special message as she was readily available. I appreciated our collaboration and that she were available even over the phone.

I had the privilege to work in a pleasant environment in the Petrology-Deep Earth and Planetary Science department. For this I would like to thank my colleagues; Elodie, Daphne Jelle, Laura, Mirjam, Nachiketa, Sonja, Jane, Janne, Jeilie, Jessica and Josepha. Furthermore, I would like to thank Wim, Fraukje, Wynanda, Bas, Peiter, Frank, Richard and Roel for their support and great friendship during my stay in the department.

Extra special and heart-felt thanks go out to:

- Esther, we shared our office and accompanied each other on a daily basis. She was not only my office mate but also a good friend.

- Aurelia, she was a great help in my research as she made a major contribution in the calibration of the CCD and also developed several matlab programs. For these and many other reasons I appreciate her time and support.

 - The Vrije University technical staff, most notably Onno, Ron, Daniel, Rob, Nick and other colleagues. With their input and guidance in this entire project I could make it to the finish line.

- Fenny, she gave me such useful support and guidance both for my career and private life.

- Jan-Hein, Freek and other colleagues and technicians at the Laser Centre at the Vrije University, with whom I shared the challenges of an unstable laser and many other technical challenges.

- My friends Irene, Stephan and Javier; they were some of the people that pulled me through in rough times.

- The ones standing closest to me are my family such as my sister Razi, my brothers Reza and Roozbeh. They provide their moral support and encouragement. My mother has been a particularly inspiring role model who always stimulated me to continue my study in times that I was struggling. An extra special mention to Emile Gerard for being the one that always stood right next to me in the final years of my research.

Finally I would like to dedicate this thesis to my father, who unfortunately can no longer be with us.

Curriculum vitae

Raheleh motamedi was born in Esfahan, on June 23th 1980. She gained her diploma in mathematics from Beheshtian high school, Esfahan, Iran in 1999. Having a strong interest in physics, she started her bachelor program in applied physics at the Azad University, Shahreza, Iran and graduated in 2003. After that she followed her master program in atomic and molecular physics in Azad University, Tehran, Iran and graduated in 2007. In 2008 she started her PhD on the subject of "Validating the performance of a Raman laser spectrometer (RLS) instrument under Martian conditions" at the Petrology-Deep Earth and Planetary Science department. Five years of research have resulted in this thesis.